Summer 8-15-2019

A modular approach for modeling, detecting, and tracking freezing of gait in Parkinson disease using inertial sensors

Prateek Gundannavar Vijay
Washington University in St. Louis

WASHINGTON UNIVERSITY IN ST. LOUIS

School of Engineering and Applied Science

Department of Electrical & Systems Engineering

Dissertation Examination Committee:
Arye Nehorai, Chair
ShiNung Ching
Gammon Earhart
Matthew Lew
Neal Patwari
Heinz Schaettler

A Modular Approach for Modeling, Detecting, and Tracking Freezing of Gait in Parkinson Disease using Inertial Sensors

by

Prateek Gundannavar Vijay

A dissertation presented to
The Graduate School
of Washington University in
partial fulfillment of the
requirements for the degree
of Doctor of Philosophy

August 2019
Saint Louis, Missouri

Contents

List of Figures . . . . . **v**

List of Tables . . . . . **ix**

Acknowledgments . . . . . **x**

Abstract . . . . . **xiv**

1 Introduction: Model, Detect, and Track Freezing of Gait **1**
1.1 Research Significance 7
1.1.1 Scientific Premise 7
1.1.2 Expected Research Outcomes 8
1.2 Contributions of this Work 9
1.3 Organization of this Dissertation 11
1.3.1 Publications 13
1.4 Notations 14

2 Sensor Module: Inertial Measurement Unit **15**
2.1 Introduction 15
2.2 Frames of Reference 17
2.3 Inertial Measurement Unit 18
2.3.1 Accelerometers 19
2.3.2 Gyroscopes 20
2.3.3 Error Characteristics 22
2.3.4 Sensor Specifications 24
2.4 Inertial System Configurations 24

3 Detection Module: Zero-velocity and Trembling Event Intervals **27**
3.1 Introduction 28
3.2 Signal Model and Statistics 30
3.3 Detectors 32
3.3.1 Detector-I 33
3.3.2 Detector-II 35
3.4 Parameters of the Detectors 37
3.4.1 Metrics 37

3.4.2 Detector-I . . . 39
3.4.3 Detector-II . . . 41
3.5 Illustrative Examples . . . 44
3.5.1 Detector-I . . . 44
3.5.2 Detector-II . . . 46
3.5.3 Estimated Tremor Axis . . . 47
3.6 Chapter Summary . . . 49

4 Navigation Module: Zero-velocity aided Inertial Navigation System . . 50
4.1 Introduction . . . 51
4.2 Preliminaries . . . 52
4.2.1 Rotation Matrix . . . 52
4.3 ZVEI-Aided Inertial Navigation System . . . 55
4.3.1 Navigation Mechanization Equations . . . 56
4.4 Numerical Results . . . 63
4.4.1 Illustrative Example . . . 64
4.4.2 Data Analysis . . . 69
4.5 Chapter Summary . . . 70

5 Filtering Module: Trembling Event aided Point-Process Filter 73
5.1 Introduction . . . 74
5.2 Preliminaries . . . 76
5.2.1 Conditional Intensity Function . . . 76
5.3 Point-Process Filter . . . 77
5.4 Illustrative Example . . . 82
5.4.1 Detector-II and INS . . . 82
5.4.2 Point-Process Filter . . . 85
5.5 Experimental Evaluation . . . 85
5.6 Chapter Summary . . . 89

6 Validation Module: A Sparsity-based Gait Cycle Validation Algorithm 91
6.1 Introduction . . . 92
6.2 Preliminaries . . . 95
6.2.1 Gait Events . . . 95
6.2.2 Zero-velocity Events Intervals . . . 95
6.3 Gait Cycle Validation and Segmentation . . . 97
6.3.1 Discrete Wavelet Transform . . . 98
6.3.2 Zero-Phase Filters as Matrices . . . 99
6.3.3 Sparsity-Assisted Wavelet Denoising (SAWD) . . . 100
6.3.4 Gait Cycle Validation and Segmentation . . . 104
6.4 Illustrative Example . . . 106
6.4.1 Data Collection and Hardware . . . 107

6.4.2 Experiment . . . 107
6.4.3 Template Generation . . . 108
6.4.4 Validation and Segmentation . . . 112
6.5 Numerical Results . . . 116
6.5.1 Fixed Sampling Rate (Excluding Turns) . . . 119
6.5.2 Variable Sampling Rate (Including Turns) . . . 124
6.6 Chapter Summary . . . 126

7 System Integration: A Modular Approach . . . 128
7.1 Introduction . . . 129
7.2 Adaptive Approach . . . 134
7.2.1 Average Foot Speed . . . 134
7.2.2 Weighted Average of Gait Parameters . . . 136
7.3 Illustrative Example . . . 141
7.4 Experimental Results . . . 147
7.5 Chapter Summary . . . 149

8 Conclusions and Future Work . . . 151
8.1 Summary . . . 151
8.2 Future Directions . . . 154

Bibliography . . . 156

Appendix A . . . 171
A.1 Openshoe Database . . . 171
A.2 Opal APDM Database . . . 173

Appendix B . . . 174
B.1 Derivation of Detector-I . . . 174
B.2 Derivation of Detector-II . . . 179

Appendix C . . . 182
C.1 Derivation of Navigation Mechanization Equations . . . 182
C.2 Perturbation Analysis . . . 185

Appendix D . . . 189
D.1 Derivation of Point-Process Filter . . . 189
D.2 Summary: PID TT027 . . . 191
D.3 Experimental Evaluation: Fixed Thresholds . . . 195

Appendix E . . . 198
E.1 Module Parameters . . . 198

List of Figures

1.1 A system overview of the proposed modularity-based approach to detect and track freezing of gait in Parkinson disease. ZVEI: Zero-velocity event intervals; TREI: Trembling event intervals. 4
1.2 Overview of the dissertation. 11

2.1 An illustration of the different frames of reference. 17
2.2 The IMU consists of a three-axis accelerometer and a three-axis gyroscope. The accelerations and angular velocities measured by the accelerometer and gyroscope are denoted by $\tilde{\boldsymbol{s}}^{\mathrm{b}} = [[\tilde{\boldsymbol{s}}^{\mathrm{b}}]_x, [\tilde{\boldsymbol{s}}^{\mathrm{b}}]_y, [\tilde{\boldsymbol{s}}^{\mathrm{b}}]_z]^{\mathsf{T}}$ and $\tilde{\boldsymbol{\omega}}^{\mathrm{b}} = [[\tilde{\boldsymbol{\omega}}^{\mathrm{b}}]_x, [\tilde{\boldsymbol{\omega}}^{\mathrm{b}}]_y, [\tilde{\boldsymbol{\omega}}^{\mathrm{b}}]_z]^{\mathsf{T}}$, respectively. 18
2.3 Electromechanical schematic of an accelerometer. 19
2.4 Electromechanical schematic of a gyroscope. 20
2.5 Stationary accelerometer and gyroscope histogram plots. (a) Histogram of accelerometer measurements for 17 seconds of data from a stationary sensor, along with a Gaussian fit to the data. (b) Histogram of gyroscope measurements for 17 seconds of data from a stationary sensor, with a Gaussian fit to the data. 23
2.6 Stable platform inertial navigation algorithm. 25
2.7 Strapdown platform inertial navigation algorithm. 25

3.1 The goal of the first detector is to detect zero-velocity and trembling events, and filter out gait patterns that are not associated with FOG. The goal of the second detector is to distinguish zero-velocity events from trembling events. . 30
3.2 Gait event intervals 31
3.3 Using the accelerometer data, we develop an energy-based detector to filter gait patterns that are neither ZVEI nor TREI. 33
3.4 To identify ZVEI based on the region identified by the first detector, we develop a second detector which uses information from the gyroscope. 35
3.5 An illustration of FAL, DL, and MDL. The overlapping region between the video and inertial sensor method is the detection length (gray color). The region detected by the video but not by the inertial sensor method is the missed detection length (light orange color). The region detected by the inertial sensor method but not by the video is the false alarm length (light blue color). 38

3.6 Average value of TPR and $1-\text{FAR}$ curves for different values of Detector-I threshold γ'_{D_1}. 40
3.7 Sensitivity of gyroscope: Image plots of average value of TPR and $1-\text{FAR}$ for ZVEI across different values of Detector-II threshold and standard deviation of the gyroscope. 42
3.8 Performance of the foot-mounted inertial navigation system plot across different value of the threshold. 43
3.9 ZVEI and TREI detected by Detector-I for TT004–BLOCK task. 45
3.10 Detector-II separates ZVEI from TREI. 46
3.11 State diagram of Detector-I and Detector-II for PID TT004–BLOCK task with an overlay of the video data. 47
3.12 Tremor axis plot. (a) Trajectory plot of the gait during initiation freeze with an overlay of the tremor-axis for PID–TT027. The initiation gait freeze was observed before the second EIGHT trial. The tremor-axis is shown in magenta color only for the detected trembling event intervals. (b) An illustration of the accelerometer sensor data during a tremor where $\boldsymbol{u}^{\text{a}}$ is the tremor axis, $\boldsymbol{v}^{\text{a}}$ is the gravity vector, α_k^{a} is the magnitude of tremor, and g is the earth's gravity. 48
3.13 A schematic of the two-step detection algorithm in the detection module. . 49

4.1 Euler angles. $z-y'-x''$ sequence (intrinsic rotations; N coincides with y'). The angle rotation sequence is ϕ, θ, ψ. Note that in this case $\psi > 90^\circ$ and θ is a negative angle. Image source: Wikipedia. 53
4.2 Block diagram implementation of navigational mechanization equations in a strapdown inertial system. 57
4.3 Complementary feed-forward implementation of the navigation equations, using the Kalman filter. 60
4.4 Inertial sensor data. (a) Three-axis accelerometer. (b) Three-axis gyroscope. 65
4.5 Left foot roll, pitch, and yaw angles obtained during the TUG trial for PID 08. 65
4.6 Zero-velocity event intervals, speed, and height (z-axis) of the left foot extracted using the zero-velocity aided INS for the TUG trail datasets. 66
4.7 2D trajectory plot of the TUG trial for the left foot inertial sensor data. . . 67
4.8 Error covariances of the position, velocity, and orientation estimates. 67
4.9 Boxplots of average values of the gait parameters during valid gait cycles (VGC) and freezing of gait (FOG) events. 72

5.1 System design. 75
5.2 Detector-II separates ZVEI from TREI. 83
5.3 Detection of FOG using the point-process filter. 84

6.1 Gait cycle validation and segmentation algorithm overview. The proposed modularity-based approach consists of three modules: a) sensor module, b) detection module, and c) validation module. The detection and validation modules are used to identify midstance, and toe-off and heel-strike phase of a gait cycle, respectively. 106
6.2 Scaled and interpolated gyroscope signal segments measured in the sagittal plane, with corresponding DWT coefficients. The solid line indicates the mean value, and the shaded region indicates one standard deviation variance. . . . 107
6.3 Spectrum plot of the scaled and interpolated gyroscope signal segments. The solid line indicates the spectral mean value. The dashed blue line indicates the normalized cutoff frequency $\omega_0 = 0.025$ of the low-pass signal. 109
6.4 The solid lines indicate the average value of the cost function for different values of $\mu \in \{0.01, 0.1, 1\}$. The convergence rate varies with the value of μ, however, it does not affect the cost function. 111
6.5 Scaled and interpolated gyroscope signal segments measured in the sagittal plane and its corresponding DWT coefficients. The solid line indicates the mean value, and the shaded region indicates one standard deviation variance. 112

7.1 Overview of the proposed system design to detect and track FOG in Parkinson disease. 131
7.2 Gaussian kernel functions with zero mean and standard deviation equal to the participant-specific tunable parameter σ_s. The parameter σ_s is initialized to 0.40. 136
7.3 Boxplots of average values of the gait parameters during valid gait cycles (VGC) and freezing of gait (FOG) events. 138
7.4 Exponential kernel function used in generating weights based on the average value of the pitch angle and freeze index of the foot. 139
7.5 Sensor module. (a) Three-axis accelerometer measurements. (b) Three-axis gyroscope measurements. 142
7.6 Detection module. (a) Zero-velocity event intervals (ZVEI). (b) Trembling event intervals (TREI). 142
7.7 Navigation module and freeze index. (a) Speed of the foot. (b) Pitch angle of the foot. (c) Freeze index of the foot. 143
7.8 Validation module. (a) Gyroscope signal in the sagittal plane with an overlay of the valid gait cycles detected using the validation module. 143
7.9 Filtering module. (a) pFOG computed using a point-process filter with a fixed participant-specific tunable parameter, $\sigma_s = 0.40$. 143
7.10 Filtering module. (a) The value of σ_s changes based on the average value of the speed of the foot in the last valid gait cycle. (b) pFOG computed using a point-process filter with an adaptive σ_s 144

7.11 Filtering module. (a) The value of the background spiking rate α_k changes based on the density of the edges of the trembling event intervals. (b) pFOG computed using a point-process filter with a weighted average function. . . 144

C.1 Transformation of $\boldsymbol{r}^{\mathrm{i}}$ to $\boldsymbol{r}^{\mathrm{a}}$. 182

D.1 Summary of TT027. (a) TPR, (b) FAR, and (c) FOG events detected. 192

D.2 PID TT027–BLOCK. (a) Freeze-Index plot with FI-threshold set to 6.0. (b) pFOG plot with $\sigma_{\mathrm{s}} = 0.29$. (c) and (d) Yaw angle plot with an overlay of DL, MDL, and FAL. FOG region was marked using video data the following video commentary: Froze when stood up from chair to walk to block. Froze when turning to go back to cones after second trial. Froze during turn in the fourth, fifth, and sixth trials. Questionable left foot freeze in turn for seventh and eighth trials. Froze after trials over while walking away. 194

D.3 PID TT027–BACK. (a) Freeze-Index plot with FI-threshold set to 6.0. (b) pFOG plot with $\sigma_{\mathrm{s}} = 0.29$. (c) and (d) Yaw angle plot with an overlay of DL, MDL, and FAL. FOG region marked using the following video commentary: Froze turning after first backward trial. Froze turning after second backward trial. Froze at the end of third backward trial into a turn. 194

D.4 PID TT027–EIGHT. (a) Freeze-Index plot with FI-threshold set to 6.0. (b) pFOG plot with $\sigma_{\mathrm{s}} = 0.29$. (c) and (d) Yaw angle plot with an overlay of DL, MDL, and FAL. FOG region was marked using the following video commentary: Gait initiation freeze when standing up to start figure EIGHT trial, and first and second figure EIGHT trials. Froze during turn after second figure EIGHT trial. Froze when lining up for third and fourth figure EIGHT trials. The first two FOG events were not recorded in the IMU data. 195

D.5 PID TT027–NARROW. (a) Freeze-Index plot with FI-threshold set to 6.0. (b) pFOG plot with $\sigma_{\mathrm{s}} = 0.29$. (c) and (d) Yaw angle plot with an overlay of DL, MDL, and FAL. FOG region was marked using the following video commentary: Froze when standing up and initiating gait to measure NARROW chair width. Froze during turn after first and third NARROW trials. Froze before side-step to line up for third NARROW trial. The first FOG event was not recorded in the IMU data. 195

D.6 PID TT027–TURN. (a) Freeze-Index plot with FI-threshold set to 6.0. (b) pFOG plot with $\sigma_{\mathrm{s}} = 0.29$. (c) and (d) Yaw angle plot with an overlay of DL, MDL, and FAL. FOG region was marked using the following video commentary: Froze during first turn, twice during second turn, and third TURN trials. Froze turning wrong way in fourth TURN trial and then froze again turning correct way. Froze in the fifth and sixth TURN trials. 196

D.7 PID TT007–BACK. (a) Freeze-Index plot with FI-threshold set to 6.56. (b) pFOG plot with $\sigma_{\mathrm{s}} = 0.30$. (c) and (d) Yaw angle plot with an overlay of DL, MDL, and FAL. FOG region marked using the following video commentary: Festination backwards into freeze in the middle of first trial. Festination backwards into freeze at the end of the second trial. Six instances of festination backwards into freeze in the third trial. 196

List of Tables

2.1 Features of the low-cost IMU used in this work. 24

4.1 Gait parameters extracted using the MLBS and ZV-INS. 71

5.1 Point-process filter parameters. 84
5.2 Number of FOG events detected for different participants across the gait tasks. 87
5.3 Detection performance for different types of FOG events.. 88
5.4 Average value of TPR and FAR. 89

6.1 Reconstruction error and non-zero coefficients 111
6.2 Validation of toe-off, heel-strike, swing as percentage of gait cycle using the GCVS method. 113
6.3 Performance of MLBS and GCVS algorithms 116
6.4 Performance of the proposed and existing methods for the 40 meter walk task. 122
6.5 Performance of the proposed and existing methods for the free walk task. . 123
6.6 Performance of the existing and proposed methods for the free walk task [1]. 125

7.1 Performance of existing and proposed methods. 146

A.1 Experiment 1: Balance assessment tasks and their descriptions. 172
A.2 Experiment 2: Balance assessment tasks and their descriptions. 173

D.1 Number of FOG events detected for different participants across the gait tasks. 193
D.2 Detection performance for different types of FOG events.. 197

E.1 Detection module parameters. 198
E.2 Navigation module parameters. 198
E.3 Validation module parameters. 199
E.4 Point-process filter parameters for the pFOG and pFOG-AFS. 199
E.5 Point-process filter parameters for the pFOG-WA. 199

Acknowledgments

I would like to express my sincere gratitude to my research advisor, Dr. Arye Nehorai, for his guidance, support, and encouragement during my research and life at Washington University in St. Louis. Dr. Nehorai was instrumental in introducing me to the field of statistical signal processing, which helped me explore and contribute to such research areas as passive radars, gait analysis, signal denoising, and pattern recognition.

I also had the opportunity to work with excellent physicians and researchers at the Washington University School of Medicine. The collaborative research experiences during my PhD study have helped me expand my ability to understand and solve complex problems in the field of medicine. I would like to thank Dr. Gammon Earhart and the members of the Locomotor Lab – Dr. Pietro Mazzoni, Dr. Marie McNeely, Dr. Ryan Duncan, and Dr. Kerri Rawson, – for their discussions, feedback, contributions, and the data that were used in this thesis. I also thank Dr. Yo-El Ju for her support, insightful discussions, and collaboration on identifying sleep-electroencephalography biomarkers in Alzheimer disease project. I would also like to convey my gratitude to Dr. Isaac Skog and Dr. Martin Hurtado for their technical discussions, careful review, and constructive suggestions for improving the quality of the manuscript.

I would like to thank my dissertation defense committee members, Dr. Gammon Earhart, Dr. ShiNung Ching, Dr. Neal Patwari, Dr. Matthew Lew, and Dr. Heinz Schaettler for their insightful feedback and suggestions on improving this dissertation. I wish to thank Dr. Shi-Nung Ching and Dr. Heinz Schaettler for being part of my research committee during my preliminary research exam. I am also grateful to all the faculty members at the Department of Electrical and Systems Engineering, Department of Mathematics and Statistics, and Department of Computer Science Engineering, for their teachings which helped me gain a good background knowledge required to pursue research in the field of statistical signal processing.

My former and current labmates – Zhao, Keyong, Alex, Jichuan, Mengxue, Mianzhi, Zhen, Yijian, Hesam, Zhenqi, Yiqi, Eric, Bing, Uri, Jie, and Feng – who have always been supportive and helpful, and made my journey at Washington University a rich memory. I thank my friends both in St. Louis, USA, and in India, who were constant sources of support in my life. My special thanks go to Mr. James Ballard at the Engineering Communication Center, Washington University in St. Louis, for proofreading my manuscripts and making suggestions on improving the quality the manuscript.

I also owe thanks to my former mentors, Dr. K.V.S. Hari and Dr. V. Umapathi Reddy, at the Indian Institute of Science, Bangalore, and International Institute of Information Technology, Hyderabad, respectively, for instilling in me the foundations and motivation needed to pursue research. Finally, I owe my sincerest and deepest appreciation to my parents, Shri. Vijay Gundannavar and Smt. Asha Gundannavar, and my sister, Ms. Shradha

Gundannavar, for their support, confidence, patience, trust, and love, and being a constant source of inspiration throughout these years.

Prateek Gundannavar Vijay

Washington University in Saint Louis

August 2019

Dedicated to my teachers and parents

ABSTRACT OF THE DISSERTATION

A Modular Approach for Modeling, Detecting, and Tracking Freezing of Gait in Parkinson Disease using Inertial Sensors

by

Prateek Gundannavar Vijay

Doctor of Philosophy in Electrical Engineering

Washington University in St. Louis, 2019

Professor Arye Nehorai, Chair

Parkinson disease, the second most common neurodegenerative disorder, is caused by the loss of dopaminergic subcortical neurons. Approximately 50% of people with Parkinson disease experience freezing of gait (FOG), a brief, episodic absence or marked reduction of forward progression of the feet despite the intention to walk. FOG causes falls and is resistant to medication in more than 50% of cases. FOG episodes can often be interrupted by mechanical interventions (e.g., a verbal reminder to march), but it is often not practical to apply these interventions on demand (e.g., there is not usually another person to detect an FOG episode and provide the reminder).

Wearable sensors offer the possibility of detecting FOG episodes in real time and thus developing a "closed-loop" treatment: real-time detection can be coupled with on-demand interventions. Objective evaluation methods using wearable sensor technology to monitor

and assess FOG have met with varying success. They do not use a signal model that captures FOG patterns explicitly, and they are of limited help in understanding the underlying mechanisms in the structure of the sensor data captured during FOG. In this dissertation, we first develop physically-based signal models for the sensor data, design statistical signal processing methods to detect FOG based on its patterns, and compute the probability of FOG. Then, we proceed to validate the system, using data from experimental gait assessment in a group of people with Parkinson disease.

We further develop a modular approach to model, detect, and track FOG in Parkinson disease, using four modules, namely the detection, navigation, validation, and filtering modules. To capture the gait motion, we use an inertial measurement unit (IMU) consisting of a three-axis accelerometer and a three-axis gyroscope. We first build physically-based signal models that describe "no movement" and "trembling motion" during FOG events. In the detection module, we design a generalized likelihood ratio test framework to develop a two-stage detector for determining the zero-velocity event intervals (ZVEI) and trembling event intervals (TREI) that are associated with FOG. However, not all the detected TREI are associated with FOG. Therefore, to filter out the TREI which are not associated with FOG, we consider the fact that the alternating trembling motion in FOG is associated with low foot speeds and small pitch angles. Next, to estimate these gait parameters, we employ a zero-velocity aided inertial navigation system (ZV-INS) in the navigation module. The ZV-INS uses the ZVEI as pseudo measurements, along with a Kalman filter, to estimate the position, velocity, and orientation angles of the foot.

To track the degradation of the gait parameters prior to the incidence of FOG, we detect valid gait cycles in the validation module. We first identify the non-stationary segments of the gyroscope signal in the sagittal plane, using ZVEI. Next, we preprocess the non-stationary

segments by scaling and interpolating the signal. Finally, we validate the preprocessed non-stationary segment of the gyroscope signal in the sagittal plane as a valid gait cycle, using an optimization framework called sparsity-assisted wavelet denoising (SAWD). In the SAWD algorithm, we simultaneously combine low-pass filtering, multiresolution representations (wavelets), and a sparsity-inducing norm to obtain a sparse representation of the gyroscope signal in the sagittal plane for valid gait cycles, in the form of a discrete wavelet transform coefficient vector. We compute the root-mean-square error between the generated template and the sparse representation of the non-stationary segment of the gyroscope data in the sagittal plane, obtained using the SAWD algorithm. If the root-mean-square error is less than a fixed threshold, then the gait cycle is considered valid.

Finally, to detect the onset and duration of FOG, we develop a point-process filter that computes the probability of FOG (pFOG). We model the edges of the TREI as a point-process, then assign weights to the edges, which depend on a participant-specific tunable parameter and the average value of the gait parameters observed in the bin containing the edge. To compute pFOG, we develop a Bayesian recursive filter and integrate the weights assigned to the edges of the TREI over a time window. To adaptively adjust the participant-specific tunable parameter, we develop two novel approaches that assign weights to the edges of the TREI based on the gait parameters extracted from the last valid gait cycle and the foot motion dynamics. We validate the performance of the modular system design using real data obtained from people with Parkinson disease who performed a battery of gait tasks known to trigger FOG. The results indicate improved performance, with an average accuracy greater than 85% and an average false positive rate of less than 14%. Altogether, we not only improve the accuracy of FOG detection but also open new avenues towards the development of low-cost remote health monitoring systems, which will help provide insights

into the frequency and patterns of FOG that affect the quality of daily life in people with Parkinson disease.

Chapter 1

Introduction: Model, Detect, and Track Freezing of Gait

Parkinson disease is the second most common neurodegenerative disorder, affecting 1-1.5 million people in the United States alone. The main pathological process in Parkinson disease is a loss of dopaminergic subcortical neurons, which leads to various motor impairments [2]. Approximately 50% of people with Parkinson disease experience freezing of gait [3,4] (FOG), a brief, episodic absence or marked reduction of forward progression of the feet despite the intention to walk. FOG causes falls and is resistant to medication in more than 50% of cases [5,6]. FOG episodes can often be interrupted by mechanical interventions or strategies (e.g., a verbal reminder to march), but it is often not practical to apply these interventions on demand (e.g., there is not usually another person to detect an FOG episode and provide the reminder). Wearable sensors offer the possibility of detecting FOG episodes in real time and thus developing a "closed-loop" approach to treatment: real-time detection could be coupled with on-demand interventions to reduce the duration of FOG episodes.

In the last decade, objective evaluation methods using wearable sensor technology to monitor and assess FOG have been developed with varying success [7–9]. Experiments have primarily

been conducted for understanding the bilateral coordination [10–13] of steps during gait, using force resistive sensors embedded in the sole of the shoe. They have also employed through analysis of the spectral characteristics of the accelerometry signal [14–16] from devices attached to the lower extremities, or have used methods from machine learning [17–21] to classify features extracted from inertial sensor data. However, these methods do not present a signal model that captures the FOG patterns explicitly, and they provide limited utility for understanding the potential underlying mechanisms revealed by the structure of the sensor data during FOG.

Our long-term goal is to develop a valid and reliable system which will enable effective personalized treatment for mitigating FOG. The objectives of this thesis are to design a system to automatically detect and track FOG in real-time, and translate to the developed methodology to into individual patient application. To detect FOG, we will develop physically-based signal models for the sensor data associated with the FOG patterns. Based on these models, we will design statistical signal processing methods that detect the onset and duration of the FOG events in real-time.

FOG patterns are known to include (i) alternating trembling in the lower extremities (including the hip, knee, and ankle joints, and the bones of the thigh, leg, and foot), and (ii) no movement of the limbs and trunk [3,22]. FOG events are a reflection of the patterns described in both (i) and (ii), and are characterized by small foot speeds [23, 24], low pitch angles, and high spectral power ratios [14]. To detect and track FOG in real-time, we will use a modular approach system design shown in Fig. 1.1. To capture gait motion, we use a MEMS-based inertial measurement unit (IMU) that consists of a three-axis accelerometer and a three-axis gyroscope. The system design consists of four modules, specifically for detecting, tracking, validating, and filtering. The detection module contains two fixed-threshold detectors to

determine instances of alternating trembling intervals and no-movement (zero-velocity) intervals. We consider these thresholds as fixed because they are not sensitive to the individual gait patterns. To identify FOG gait patterns involving alternating trembling in the lower extremities, we exploit the fact that these events are associated with alternating trembling motion of the sensor about a fixed axis and model them as trembling event intervals. Similarly, to identify FOG gait patterns such as no movement of limbs, we use the fact that these events are associated with zero-velocity and model them as zero-velocity event intervals. However, not all trembling and zero-velocity event intervals detected are associated with FOG. For example, trembling intervals are associated with heel lift-off and heel strike phase of a gait cycle, and zero-velocity event intervals are associated with the flat foot phase of a gait cycle. Therefore, to filter out the gait events that are not associated with FOG, we use a navigation module to extract gait parameters such as the speed and orientation angles of the foot because FOG is associated with small foot speeds and low pitch angles. Further, to filter out gait cycles detected in trembling event intervals, we develop a gait cycle validation and segmentation module.

In the gait cycle validation and segmentation module, we develop a novel approach that employs pattern matching and thresholding to validate and detect three gait events in the gait cycle, namely midstance, toe-off, and heel-strike. To identify the data as stationary or moving, we first use physical models that describe zero-velocity events or stationary events of the sensor data obtained from a foot-mounted inertial system. Next, to generate a sparse representation of the moving segments of the gyroscope measurements in the sagittal plane for valid gait cycles, we develop a computationally efficient algorithm called sparsity-assisted wavelet denoising (SAWD). In SAWD, we simultaneously combine linear time-invariant filters, wavelets, and sparsity-based methods to extract a discrete wavelet transform (DWT)

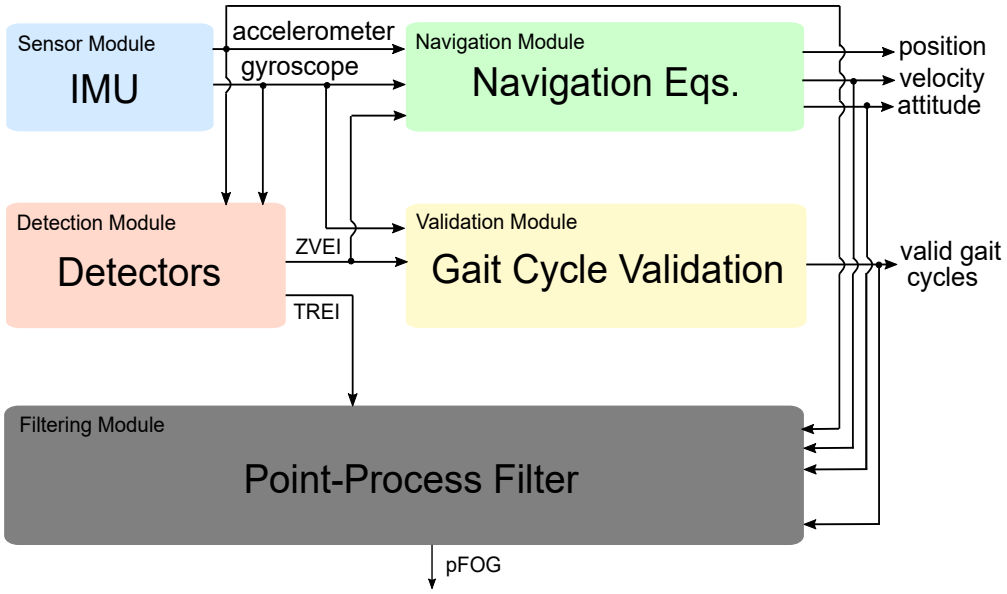

Figure 1.1: A system overview of the proposed modularity-based approach to detect and track freezing of gait in Parkinson disease. ZVEI: Zero-velocity event intervals; TREI: Trembling event intervals.

coefficient vector as a sparse representation of the moving segment of the gyroscope measurements in the sagittal plane. The reconstructed signal obtained from the extracted DWT coefficient vector is smooth and preserves the typical observable patterns, such as "valleys" and "peaks," of a valid gait cycle for the non-stationary segments of the gyroscope signal in the sagittal plane. We generate a template of the DWT coefficient vector by taking the average of the DWT coefficient vectors obtained using the SAWD algorithm for all valid gait cycles of a given trial. Thereafter, to validate any moving segment as a gait cycle, we compute the root-mean-square error between the generated template and the sparse representation of the moving segment of the gyroscope data in the sagittal plane, obtained using the SAWD algorithm. If the root-mean-square error is less than a fixed threshold, then the gait cycle is valid, i.e., not associated with FOG.

Finally, to filter out gait patterns that are not associated with FOG, we develop a point-process filter in the filtering module, which computes the probability of FOG. We first assign weights to the edges of the trembling interval, which depend on the selected gait parameters mapped to a kernel function. In addition, we use the information about the validity of a gait cycle from the validation module to reset the point-process filter and remove gait patterns associated with valid gait cycles. Then, we integrate these weights over a time window using a Bayesian recursive filter. Our central hypothesis is that regions in the space of sensor data that are assigned high values of pFOG indicate FOG with high likelihood. The successful completion of our objectives will contribute to the development of precision measurement through gait analysis adapted to individual gait patterns for detecting FOG. The automatic nature of our system will enable use in a home setting, thus lowering cost of treatment and providing access to larger amounts of sensor data to accurately evaluate disease progression, including evolution of FOG patterns and frequency. These in turn will be useful in the development of effective, personalized treatment methodologies to reduced FOG and thereby improve the quality of life of individuals with Parkinson disease. We will pursue the objectives via the following specific aims:

- **Aim 1**: **Develop a statistically-based adaptive system to automatically detect and track FOG.**

  We hypothesize that through use of gait parameters and parametric modeling of gait during FOG, we can develop a novel system to compute pFOG in real time, by applying a conditional intensity function to data from commercial wearable sensors. The resulting system will first automatically adjust a patient-specific tunable parameter depending on the foot-motion dynamics, and then will detect the onset and duration of FOG.

- **Aim 2**: **Validate the system using data from experimental gait assessment in a group of people with Parkinson disease.**

  We will validate the results obtained using the system designed in *Aim 1* by comparing the algorithm's pFOG with detection of FOG by trained gait analysis experts using video review. We hypothesize that the sensor-based FOG system will detect FOG at least as reliably as human experts. Validation of this sensor-based method would allow for the immediate application of the methodology in gait laboratories, and will pave the way for measuring FOG in clinical practice and everyday life.

Completion of these specific aims will enable researchers to study FOG in the lab using commercially available wearable inertial sensors. Once validated, the system design can be translated into clinical practice, improving the quality of health care and also ensure rapid dissemination of future advances. An enhanced understanding of FOG can spur novel treatment approaches to address FOG events. Real-time detection of FOG will allow the development and study of on-demand interventions and the possible development of closed-loop event-based treatment of FOG. The impact of our work will make it possible to develop clinical systems to study FOG on a large scale, and potentially improve the quality of life for people who experience FOG by paving the way for development of novel intervention strategies to tackle this disabling symptom of Parkinson disease.

1.1 Research Significance

1.1.1 Scientific Premise

The gold standard of FOG assessment involves evaluation of video recordings of ambulating participants by expert raters of FOG [25]. The inter-rater reliability varies, ranging from low to good [26]. However, this approach offers limited information about the frequency and patterns of FOG away from the laboratory environment, requires substantial training of raters, and consumes much time in off-line data analysis [27]. The use of consumer wearable technology developed using inertial sensors offers a potentially more efficient alternative approach to monitoring and assessment of FOG, and is becoming more common [28]. An inertial sensor consists of a three-axis accelerometer and a three-axis gyroscope, which respectively measure acceleration due to motion and gravity, and angular velocity. Automated methods developed for objective evaluation of FOG using these sensors either use information about the spectral characteristics of the accelerometer signal [14–16] or perform exploratory data analysis using tools from machine learning [17–21]. However, these methods do not consider a physically-based signal model that captures the FOG events explicitly, and they provide limited utility for understanding the structure of the sensor data and detecting FOG. Further, methods based on spectral characteristics of the accelerometry signal completely ignore the effect of various sources of error in the sensor [29]. Finally, the use long window lengths to extract features from the sensor data often lead to delays in determining the onset of the FOG event, thus hindering use in a real-time framework.

The most commonly prescribed medication to improve symptoms in people with Parkinson disease is levodopa. This medication is effective in only 50% of patients with FOG [5, 6].

Even when levodopa is effective, its dose-effect is highly complex and nonlinear, and remains a great therapeutic challenge [4]. Surgical treatments, such as deep brain stimulation, have mixed results and limited effectiveness [30–33]. Clinicians have also developed non-pharmaceutical and non-surgical intervention strategies for FOG, such as cueing [34–36], which involves using external auditory or visual stimuli to abort FOG episodes [37, 38]. While these strategies can be effective, they can be used only in an open-loop mode (e.g., metronome cueing), or by requiring patients to engage in the cueing strategy when they experience an FOG episode (e.g., reminding themselves to march). When delivered in this manner, cueing strategies rapidly lose their effectiveness. For cueing to be effective, the external stimulus should ideally be carefully delivered to match an actual or impending FOG event, i.e., in an automatic closed-loop approach. Such an approach has not been possible due to the lack of a method to automatically detect FOG. Therefore, a system that can automatically identify FOG in real time, and can possibly even predict the onset of FOG in advance of an episode, would pave the way for development of novel intervention strategies to reduce or prevent FOG and associated falls.

1.1.2 Expected Research Outcomes

The proposed method promises to develop a personalized healthcare gait analysis system using inertial sensors. The method will adapt to individual gait patterns and automatically detect FOG patterns explicitly in real time. This contribution is expected to have translational importance which could lead to development of novel treatment methodologies to target FOG. The proposed method will not only improve the accuracy of FOG detection but also open new avenues towards the development of low-cost remote health monitoring systems, which will help provide insights into the frequency and patterns of FOG that affect

the quality of daily life in people with Parkinson disease. The development of a personalized healthcare gait analysis patient application could provide enhanced care and improve outcomes. Unlike existing methods, our proposed system design offers a modular approach, which will allow researchers to isolate, test, and make improvements to each module of the system design, and thus increase the effectiveness of the overall application. Moreover, the proposed system design establishes logical connections between the underlying mechanisms of FOG and the physical properties measured by the sensors, which are potentially useful in understanding the control mechanisms underlying FOG and in developing rehabilitative interventions to reduce the incidence of FOG.

1.2 Contributions of this Work

FOG has been reported as the most disabling and distressing symptom of Parkinson disease. The health-related impact of FOG is concerning as it leads to increased risk of falling, reduced quality of life, and cognitive impairments. Further, the episodic nature of FOG makes it difficult to study in laboratory settings. Despite challenges in detecting FOG, the continuous improvement in the development of low-cost wearable sensors and the increased computing power of inexpensive microcontrollers have created opportunities to collect and process rich sensor data sets for specific symptoms of Parkinson disease. However, there is a need for algorithms that can extract FOG episodes from sensor data automatically, reliably, and in real-time.

The work done in this dissertation is innovative in several ways:

a) We developed the first personalized gait analysis system that adapt to individual gait patterns and automatically detect FOG in real-time.

b) Unlike existing methods, the proposed approach automatically adjusted the tunable system parameters of an individual participant depending on the dynamics of the foot and sampling rate of the sensors, thereby reducing the overall time required for manually tuning the system parameters to improve the FOG detection accuracy.

c) The modularity of the proposed system design allow researchers to separately isolate, test, and improve each of its modules, potentially resulting in the development of new patient applications that can improve patient outcomes.

d) The proposed project is a unique multidisciplinary collaboration that integrated methods from statistical signal processing and optimization with clinical expertise and movement science.

e) We implemented our proposed system as an open-source Python-based toolbox to help clinicians validate and use the proposed system design with commercial off-the-shelf wearable inertial sensors.

In the clinical setting, the use of a valid and reliable wearable system will not only enhance protocol adherence and patient compliance but also decrease the need for outpatient visits while maintaining high-quality care. In addition, the ability to detect the frequency and patterns of FOG in daily life, and thus to to optimize treatment strategies, has the potential to address current obstacles to mitigating FOG.

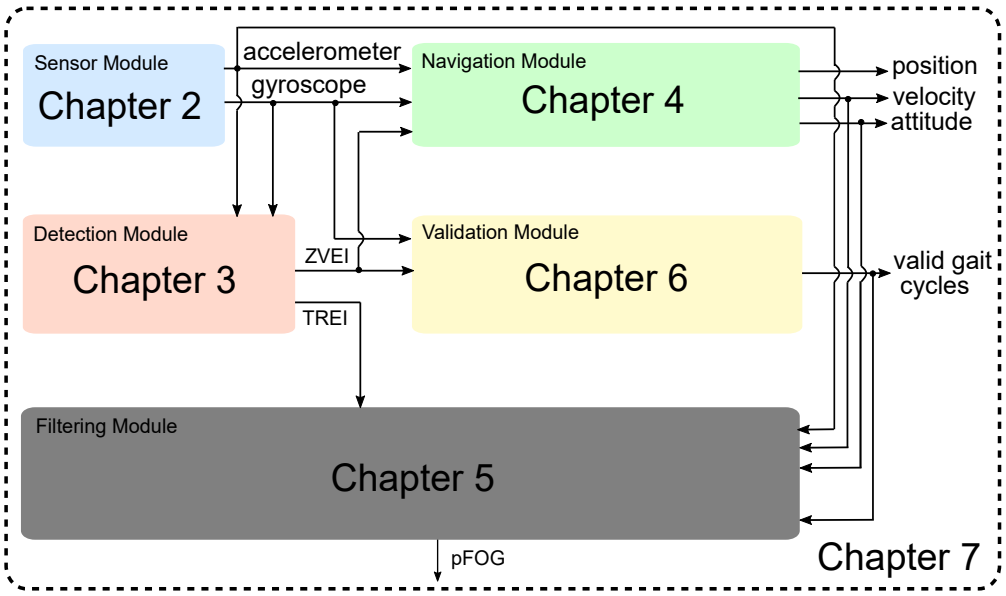

Figure 1.2: Overview of the dissertation.

1.3 Organization of this Dissertation

The dissertation applies a modular approach to modeling, detecting, and tracking freezing of gait in Parkinson disease participants. In **Chapter 2**, we present a brief overview of the MEMS-based inertial sensors (accelerometers and gyroscopes) used in this work. In **Chapter 3**, we develop a two-step detection algorithm to determine instances of zero-velocity event intervals (ZVEI) and trembling event intervals (TREI). We model the inertial sensor data for the gait patterns observed during FOG, and detect ZVEI and TREI. The goal of the first detector is to filter out gait patterns that cannot be classified as ZVEI or TREI. To distinguish ZVEI from TREI, we use the information from the gyroscope and develop the second detector. The second detector detects only ZVEI and cannot filter out those gait patterns identified as TREI, which are not associated with FOG. Therefore, to detect the FOG region, which is a reflection of both ZVEI and TREI, we use the fact that FOG is characterized by gait parameters, such as small foot speeds, low pitch angles, and high

freeze indices. In **Chapter 4**, we present a tutorial on implementing the zero-velocity-aided inertial navigation system that computes the position, velocity, and orientation estimates of the sensor during gait. The INS uses the ZVEI as pseudo-measurements to correct the state estimates of a dynamic system that tracks the position, velocity, and orientation estimates of the foot.

In **Chapter 5**, to detect the onset and duration of FOG events, we develop a point-process filter which computes the probability of FOG. We first assign weights to the edges of the trembling interval which depend on the speed of the foot at the edges and a participant-specific tunable parameter. Then, we integrate these weights over a time window using a Bayesian recursive filter. To maximize the accuracy of the FOG detection, the participant-specific tunable parameter is adjusted manually for every participant based on the foot speeds. However, this step requires a thorough grid search operation which is tedious and computationally expensive. In addition, a value of the tunable parameter that is participant-specific but fixed over time is unlikely to be adequate. Ideally the parameter should be adapted to specific gait patterns, which are subject to change depending on the participant's gait, symptoms, and treatment strategy.

To filter the TREI that are not associated with FOG, we develop a gait cycle validation and segmentation module in **Chapter 6**. In the validation module, we use ZVEI, along with the non-stationary segments of the gyroscope signal in the sagittal plane, to identify if the non-stationary segment of the inertial sensor represents a valid gait cycle. To validate any non-stationary segment of the gyroscope signal in the sagittal plane as a valid gait cycle, we develop an optimization framework called sparsity-assisted wavelet denoising. In **Chapter 7**, we integrate the different modules and develop a statistically-based adaptive system to automatically detect and track FOG. We develop two novel methods to automatically adjust

the participant-specific tunable parameter based on the foot motion dynamics. We validate the performance of the proposed system design using real data obtained from people with Parkinson disease who performed a set of gait tasks. In **Chapter 8**, we draw conclusions and propose potential future directions.

1.3.1 Publications

The following is a list of journal publications completed during my Ph.D. studies and included in the dissertation:

- **G. V. Prateek**, I. Skog, M. E. McNeely, R. P. Duncan, G. M. Earhart, and A. Nehorai, "Modeling, detecting, and tracking freezing of gait in Parkinson disease using inertial sensors," in *IEEE Transactions on Biomedical Engineering*, vol. 65, no. 10, pp. 2152-2161, Oct. 2018. (Chapters 3 and 5)

- **G. V. Prateek**, P. Mazzoni, G. M. Earhart, and A. Nehorai, "Gait cycle validation and segmentation using inertial sensors," in revision *IEEE Transactions on Biomedical Engineering*. (Chapter 6)

- **G. V. Prateek**, P. Mazzoni, G. M. Earhart, and A. Nehorai, "A modular approach for tracking freezing of gait in Parkinson disease using inertial sensors," in preparation, 2019. (Chapter 7)

The following is a list of journal publications completed during my Ph.D. studies, but excluded from the dissertation for thematic reasons:

- **G. V. Prateek**, M. Hurtado, and A. Nehorai, "Target detection using weather radars and electromagnetic vector sensors," *Signal Processing*, vol. 137, pages 387-397, Aug 2017.

- **G. V. Prateek**, Y. E. Ju, and A. Nehorai, "Sparsity-assisted signal denoising and pattern recognition in time-series data," submitted to *IEEE Transactions on Signal Processing*.

1.4 Notations

The following general notation will be used throughout the thesis. Bold uppercase and lowercase letters denote a matrix and vector, respectively. Superscript/subscript a and ω represent accelerometer and gyroscope signals, respectively. Uppercase letters that are not bold denote scalars. For any matrix $\boldsymbol{A}$, $\boldsymbol{A}^{\mathsf{T}}$, $\boldsymbol{A}^{-1}$, and $\mathrm{Tr}\{\boldsymbol{A}\}$ respectively denote the transpose, inverse, and trace of $\boldsymbol{A}$. $\boldsymbol{I}_N$ represents an $N \times N$ identity matrix. The norms $\|\cdot\|_2$ and $\|\cdot\|_1$ indicate the ℓ_2 and ℓ_1 norms, respectively.

Chapter 2

Sensor Module: Inertial Measurement Unit

In this chapter, we briefly review the inertial sensors used in tracking the foot motion dynamics of Parkinson disease participants. An inertial sensor consists of accelerometer and gyroscope, which measure specific force and angular rate, respectively. We provide an overview of micro-electro-mechanical systems (MEMS) based inertial sensors, including their working principle, and briefly talk about the different types of errors which arise in MEMS technology. In addition, we provide the specifications of the different types of inertial sensors that were used in this work. We also briefly discuss two different inertial system configurations commonly used in commercial applications.

2.1 Introduction

In the last decade, inertial sensor technology has been rapidly incorporated in many consumer electronic products, including smart phones, tablets, gaming systems, TV remotes, and toys.

The rapid growth is mainly due to the steep reductions in cost, enabled by highly integrated silicon micro electromechanical systems (MEMS)/complementary metal oxide semiconductor (CMOS) technologies, coupled with an expanding awareness of the benefits of applying motion tracking capability to enhance user interaction with various devices [39]. MEMS technology is of particular interest because the sensors are relatively small and lightweight, and can easily be incorporated into electronic devices. As a result, many industries, such as, gaming, robotics, health care, defense, and automotive manufacturing, have seen a tremendous growth in the number of applications using these sensors [40]. For instance, in 2017, MEMS-based systems were reported to have a total value of $12.5 billion, a figure which is expected to grow to $58.7 billion in 2024[1].

A MEMS-based inertial sensor consists of an accelerometer and gyroscope which measure specific forces and angular rates, respectively. An inertial measurement unit (IMU) combines multiple accelerometers and gyroscopes, usually three axes aligned orthogonally in a 3D-plane, to capture full motion dynamics of the system. This chapter presents a brief overview of the MEMS-based technology used in inertial sensors. Section 2.2 describes the different frames of reference useful in modeling inertial sensor data. Section 2.3 presents the signal model of the accelerometer and gyroscope inertial sensor data, and the different type of errors associated with these sensors. Section 2.4 outlines different inertial system configurations that are commonly used in the various applications listed above. Section 2.4 lists the inertial system configurations that are commonly used in commercial applications.

[1] Worldwide Micro-Electro-Mechanical Systems (MEMs) Sensors Market 2018-2024: Total Value is $12.5 Billion in 2017, Up from $10.35 Billion in 2016, and Will Grow to $58.7 Billion in 2024. https://markets.businessinsider.com/news/stocks/worldwide-micro-electro-mechanical-systems-mems-sensors-market-2018-2

2.2 Frames of Reference

To estimate position, velocity, and orientation, inertial navigation systems often must transform measurements from one frame of reference to another. The three frames of reference shown in Fig. 2.1 are most commonly used in the inertial navigation literature. Not shown is a fourth frame, the body frame, which describes the motion of the foot of the participant's.

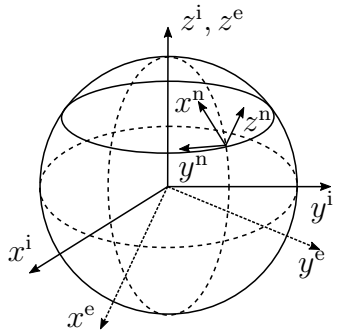

Figure 2.1: An illustration of the different frames of reference.

- The *inertial frame*, denoted by i, is a stationary frame. The IMU measures linear acceleration and angular velocity with respect to this frame. The frame's origin is at the center of the earth, and the inertial x and z axes point toward the vernal equinox and along the Earth's spin axis, respectively.

- The *earth frame*, denoted by e, coincides with the i-frame, but rotates with the earth, i.e., it has its origin at the center of the earth and axes which are fixed with respect to the earth. The x-axis passes through the prime meridian (0° longitude) and the equator (0° latitude).

- The *navigation frame*, denoted by n, is the local geographic frame in which we want to navigate. It is also commonly known as the North-East-Down (NED) system. For most applications, it is defined as stationary with respect to the earth. However, in

cases when the sensor is expected to move over large distances, it is customary to move and rotate the n-frame along the surface of the earth.

- The *body frame* (not shown in Fig. 2.1), denoted by b, is the coordinate frame of the moving IMU. Its origin at the center of the accelerometer or gyroscope triad and is horizontally aligned with the casing. All inertial measurements are resolved in this frame.

2.3 Inertial Measurement Unit

An IMU consists of three orthogonal accelerometers and three orthogonal gyroscopes, respectively measuring linear acceleration and angular velocity as shown in Fig. 2.2. In an inertial navigation system, the raw sensor measurements from the IMU are processed using navigation mechanization equations to track the position, velocity, and orientation of the device.

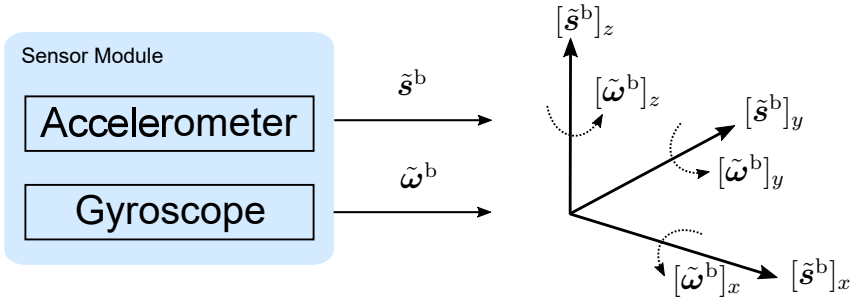

Figure 2.2: The IMU consists of a three-axis accelerometer and a three-axis gyroscope. The accelerations and angular velocities measured by the accelerometer and gyroscope are denoted by $\tilde{\boldsymbol{s}}^{\mathrm{b}} = [[\tilde{\boldsymbol{s}}^{\mathrm{b}}]_x, [\tilde{\boldsymbol{s}}^{\mathrm{b}}]_y, [\tilde{\boldsymbol{s}}^{\mathrm{b}}]_z]^{\mathsf{T}}$ and $\tilde{\boldsymbol{\omega}}^{\mathrm{b}} = [[\tilde{\boldsymbol{\omega}}^{\mathrm{b}}]_x, [\tilde{\boldsymbol{\omega}}^{\mathrm{b}}]_y, [\tilde{\boldsymbol{\omega}}^{\mathrm{b}}]_z]^{\mathsf{T}}$, respectively.

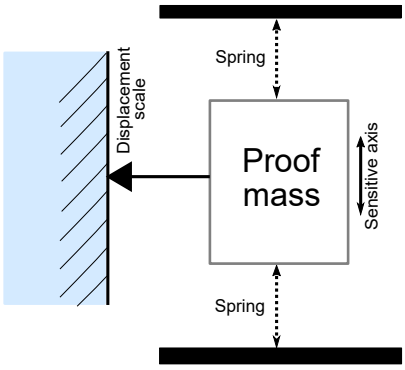

Figure 2.3: Electromechanical schematic of an accelerometer.

2.3.1 Accelerometers

An accelerometer measures linear acceleration in units of gs, where $1g$ is the Earth's gravitational acceleration, given as 9.8 m/s^2. The fundamental concept of an accelerometer can be understood with the help of the electromechanical schematic of spring-mass-damper system as shown in Fig. 2.3. A proof mass is suspended on a mechanical frame and free to move along the accelerometer's sensitive axis. When an input force is applied to the case along the sensitive axis, the mass is displaced from its original position, compressing/stretching the spring, depending on the direction of the force. The resultant position of the mass with respect to the case is proportional to the applied acceleration, which is measured by a change in the capacitance. However, gravitational acceleration acts directly on the proof mass, and not via the spring, and applies the same acceleration to all the components of the accelerometer. Hence, there is no relative motion of the mass with respect to the case. Therefore, the accelerometer measures non-gravitational acceleration, known as *specific force*, and cannot distinguish between inertial and gravitational acceleration. Note that only when the sensitive axis of the case is aligned with the Earth's gravity can linear acceleration be computed by compensating for the Earth's gravity. In other words, during a free fall, the specific force

measured by the accelerometer is zero. Conversely, under zero acceleration, the specific force is equal and opposite to the acceleration due to gravity.

If $\boldsymbol{s}_{\mathrm{ib}}^{\mathrm{b}}$ denotes the specific force, where the superscript b denotes the body frame and the subscript ib denotes the measurement of the body frame with respect to the inertial frame, then

$$\boldsymbol{s}_{\mathrm{ib}}^{\mathrm{b}} = \ddot{\boldsymbol{r}}_{\mathrm{ib}}^{\mathrm{b}} - \boldsymbol{g}_{\mathrm{b}}^{\mathrm{b}}, \tag{2.1}$$

where $\ddot{\boldsymbol{r}}_{\mathrm{ib}}^{\mathrm{b}}$ is the inertial acceleration (second derivative of the position vector) and $\boldsymbol{g}_{\mathrm{b}}^{\mathrm{b}}$ is the gravitational acceleration. The negative sign indicates the direction of gravitational acceleration, which points towards the center of the earth.

2.3.2 Gyroscopes

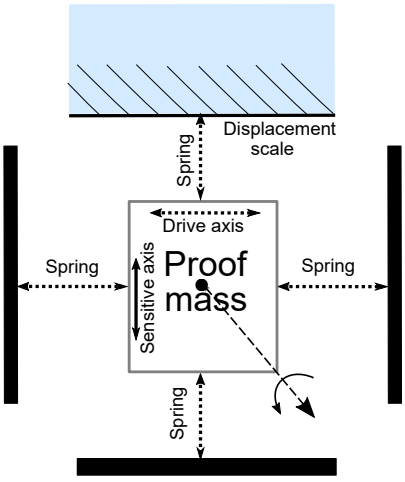

Figure 2.4: Electromechanical schematic of a gyroscope.

A gyroscope is used to measure angular velocities or rotational motion in units of deg/s or rad/s. The fundamental concept of a gyroscope is illustrated by the the electromechanical schematic of a vibratory spring-mass-damper system shown in Fig. 2.4. A proof mass is

suspended so that the mechanical system has two degrees of freedom, one along the sense axis and the other along the drive axis. The proof mass is driven into sinusoidal motion along the drive axis at a known velocity, canceling out any Coriolis acceleration due to linear acceleration [41]. When the gyroscope is rotated along an axis orthogonal to the drive axis, the Coriolis acceleration acting on the vibrating proof mass is proportional to the rate of rotation along an axis orthogonal to the vibrating axis. Assuming that the amplitude of the proof mass's velocity is known, the rate of rotation can be computed by measuring the change in the capacitance caused due to Coriolis acceleration.

The gyroscope measures the angular velocity of the body frame with respect to the inertial frame, expressed in the body frame and denoted by $\boldsymbol{\omega}_{\mathrm{ib}}^{\mathrm{b}}$. The superscript b denotes the measurement frame of reference, whereas the subscript ib indicates that the measurements are relative to the inertial frame of reference. The angular velocity, $\boldsymbol{\omega}_{\mathrm{ib}}^{\mathrm{b}}$, can be expressed as

$$\boldsymbol{\omega}_{\mathrm{ib}}^{\mathrm{b}} = \boldsymbol{R}_{\mathrm{n}}^{\mathrm{b}}(\boldsymbol{\omega}_{\mathrm{ie}}^{\mathrm{n}} + \boldsymbol{\omega}_{\mathrm{en}}^{\mathrm{n}}) + \boldsymbol{\omega}_{\mathrm{nb}}^{\mathrm{b}},$$

where $\boldsymbol{\omega}_{\mathrm{ie}}^{\mathrm{n}}$, $\boldsymbol{\omega}_{\mathrm{en}}^{\mathrm{n}}$, and $\boldsymbol{\omega}_{\mathrm{nb}}^{\mathrm{b}}$ respectively are the angular velocities of earth with respect to the inertial frame, navigation frame with respect to the earth, and body frame with respect to the navigation frame. The earth rotates around its own z-axis in 23.9345 hours with respect to the stars, and its rate is approximately 7.29×10^{-5}rad/s. Further, if the navigation plane, which is a tangential plane on the surface of the earth, is defined as stationary with respect to the earth, then the angular velocity $\boldsymbol{\omega}_{\mathrm{en}}^{\mathrm{n}}$ is zero. Therefore, in the case of pedestrian navigation systems and ambulatory gait analysis, where we assume that the navigation frame is stationary, the angular velocity of the body frame with respect to the inertial frame

is given as

$$\boldsymbol{\omega}_{\mathrm{ib}}^{\mathrm{b}} \approx \boldsymbol{\omega}_{\mathrm{nb}}^{\mathrm{b}}. \tag{2.2}$$

2.3.3 Error Characteristics

The main sources of errors can be broadly classified into five categories [29].

- *Bias* is a constant offset of the sensor measurements from its true value. For example, gyroscope measurements are offset by a constant value when the sensor is not rotating.
- *White noise* is the noise whose amplitude follows a Gaussian distribution of a zero mean and variance σ^2.
- *Temperature effects* are errors due to temperature fluctuations caused by environmental changes, which affect the piezoelectric material used in the MEMS devices.
- *Calibration errors* are due to imperfections in the integrated circuit (packaging) and in the fabrication of the IMU array, scale factors, and misalignment of the sensitivity axes. These errors are observed only when the accelerometer undergo acceleration and the gyroscope is rotated.
- *Flicker noise* is inversely proportional to the bandwidth of the sensor. For a gyroscope, the effect of flicker noise is observed at low frequencies, but it is overshadowed by white noise at high frequencies.

There are several ways to mitigate the different types of errors observed in an inertial sensor. Errors in the gyroscope due to constant bias can be estimated by taking a long term mean

or median of the gyroscope's output when there is no rotational motion. A similar technique cannot applied to the accelerometer, because the component of gravity will appear as bias. Therefore, to cancel the bias, it is necessary to estimate the precise orientation of the device with respect to gravity. Traditional methods of estimating constant bias and scale factors for inertial sensors involve using expensive mechanical rigs [42–44]. Simplified alternatives using manual rotation of the inertial sensor also work well in practice [45–47]. In addition, multiple IMUs (MIMU) or an IMU array can also cancels out the biases and enable estimation of the scale factors [48]. In Fig. 2.5, we plot a histogram of the measurements obtained from a stationary three-axis accelerometer and three-axis gyroscope by using an Openshoe inertial sensor [49]. We also fit a distribution to the histogram plot, using the `histfit` function in MATLAB. As can be seen, the measurement noise resembles a Gaussian curve.

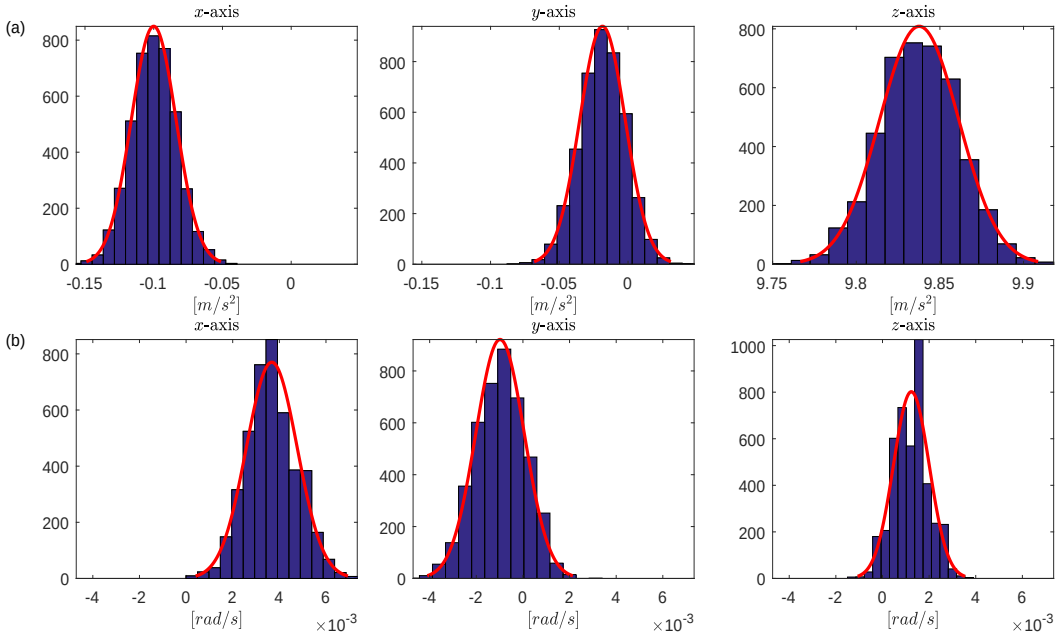

Figure 2.5: Stationary accelerometer and gyroscope histogram plots. (a) Histogram of accelerometer measurements for 17 seconds of data from a stationary sensor, along with a Gaussian fit to the data. (b) Histogram of gyroscope measurements for 17 seconds of data from a stationary sensor, with a Gaussian fit to the data.

2.3.4 Sensor Specifications

We used IMUs manufactured by three different companies in our work. The technical specifications of each IMU are listed in Table 2.1.

Table 2.1: Features of the low-cost IMU used in this work.

Manufacturer	Accelerometer Range	Gyroscope Range	Sampling Rate (Wireless)	Number of IMUs	Cost of Development Kit
Openshoe [49]	±2g, ±4g, ±8g, ±16g	±250deg/s, ±500deg/s, ±1000deg/s, ±2000deg/s	125 Hz	4	$112.00
Opal APDM [50]	±2g, ±6g	±1500deg/s - z-axis ±2000deg/s - x,y-axis	128 Hz	1	$2400.00
Shimmer [51]	±2g	±250deg/s, ±500deg/s, ±1000deg/s, ±2000deg/s	1024 Hz	1	$495.00

2.4 Inertial System Configurations

Inertial system configurations can be broadly classified into two groups depending on the frame of reference in which the rate-gyroscopes and accelerometers operate.

- *Stable Platform Systems*: In these systems, the inertial sensors are mounted on a platform which is isolated from any external rotational motion, i.e., the platform is held in alignment with the global frame. The sensors are mounted on a stable platform and any rotational motion of the platform is canceled out by torque motors. A schematic of the stable platform inertial navigation algorithm is shown in Fig. 2.6.

- *Strapdown inertial navigation algorithm*: In these systems, the inertial sensors are attached or strapped to the device, and therefore the measurements are obtained in

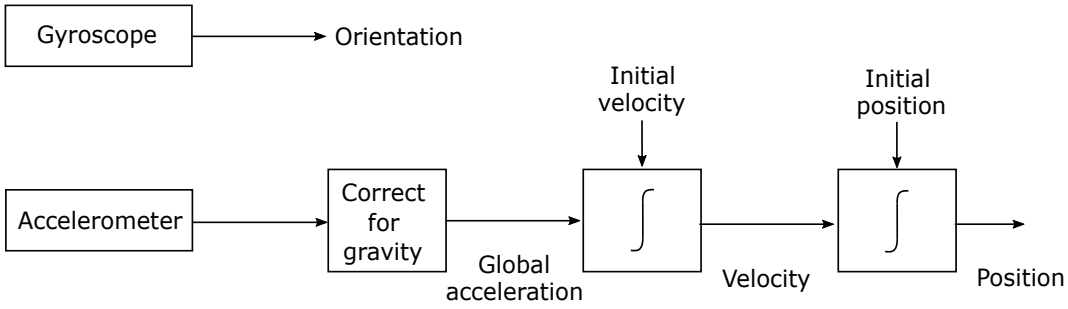

Figure 2.6: Stable platform inertial navigation algorithm.

the body frame. For example, in case of pedestrian navigation systems, the sensors are strapped to the foot or ankle of the person, and raw measurements obtained from the sensors must be rotated from the body frame to the global frame to track the person. The stable platform inertial navigation algorithm is shown schematically in Fig. 2.7.

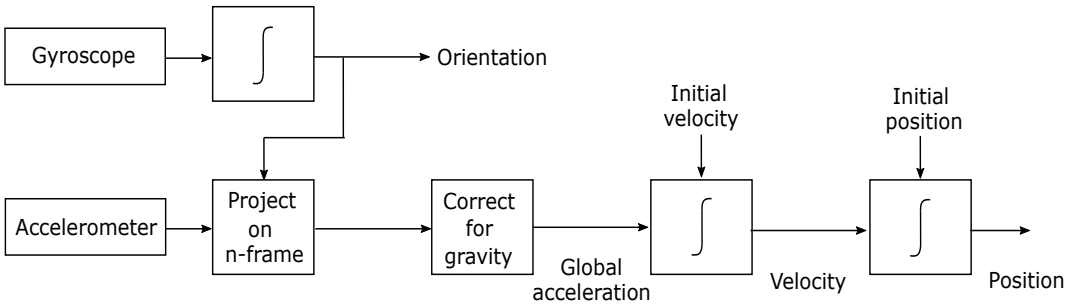

Figure 2.7: Strapdown platform inertial navigation algorithm.

Note that the stable platform and strapdown systems are based on the same underlying navigation mechanization equations. The main difference between the two systems is that strapdown systems tend have reduced mechanical complexity and tend to be physically smaller than stable platform systems, because strapdown systems do not require additional system components to remove external rotation motion. In this work, we use a strapdown inertial system configuration where the sensor is attached to the foot of the Parkinson disease

participant. The mathematical details of implementing the starpdown inertial system are presented in **Chapter 4**.

Chapter 3

Detection Module: Zero-velocity and Trembling Event Intervals

In this chapter, we build a physical model of the inertial sensor data that describes the stationary and trembling motion of the gait during the freezing of gait (FOG) events. Based on broad clinical observations, FOG patterns include alternating trembling in the lower extremities (including the hip, knee, and ankle joints, and the bones of the thigh, leg, and foot), and no movement of the limbs and trunk. We model gait patterns, such as no movement of limbs and alternating trembling in FOG, as zero-velocity event intervals (ZVEI) and trembling event intervals, respectively. We design a generalized likelihood ratio test (GLRT) framework to develop a two-stage detector for detecting ZVEI and TREI. We also develop a methodology to determine the detection module parameters, such as thresholds and scale factors. With the help of an illustrative example, we demonstrate the output of the detector during an FOG event. The results indicate that the detectors can detect ZVEI and TREI; however, not all the TREI are associated with FOG.

3.1 Introduction

Parkinson disease (PD) is a neuro-degenerative disorder that affects 1-1.5 million people in the United States alone. The main cause of PD is a loss of dopaminergic, sub-cortical neurons, which leads to motor impairments [52]. Many individuals with PD experience difficulty walking, the emergence of which is considered as a red flag for onset of disability [53]. Approximately 50% of people with PD experience freezing of gait (FOG), a "brief, episodic absence or marked reduction of forward progression of the feet despite the intention to walk" [4]. FOG events, which are a known risk factors for falls, occur suddenly, generally last for a few seconds, and tend to increase in frequency and duration as the disease progresses.

The most commonly prescribed medication to improve symptoms in people with PD is levodopa. The effective period of the drug varies between two and six hours [15], and decreases as the disease progresses [54]. Recent studies have shown that cueing techniques that apply spatial or temporal external stimuli associated with the motor activity enhance gait and reduce FOG [38,55]. For example, auditory stimulation (see e.g., [35,56]) and visual markers are used as cueing mechanisms to improve locomotor function in people with PD. Currently, to validate the severity of FOG, clinicians use patient questionnaires such as the new FOG-Questionnaire (NFOG-Q) [57] that rely on patient self-report. There is a growing need to develop automated methods for detecting FOG, with the ultimate goal of being able not only to measure but also to predict and prevent episodes of FOG.

In the last decade, methods using wearable technology for monitoring and assessing gait patterns and FOG have been developed with varying success. These methods variously employ a) electromyography (EMG) sensors [58,59]; b) force resistive sensors [60,61]; c) video-based gait analysis [62,63]; or d) inertial sensors (accelerometers and gyroscopes) [15,19,64–70].

In the case of inertial sensors, the spectral characteristics of the accelerometer signal in the vertical direction provide information that is helpful in distinguishing FOG patterns from normal PD gait patterns. For example, researchers use the spectral characteristics of the accelerometer signal to develop a four stage automatic gait detection algorithm [64, 65]. In prior reports, a freeze-index (FI) is defined as the ratio of the square of the power spectrum in two different non-overlapping frequency bands [66]. An extension of the FI method for a variable size window and online detection is presented in [67, 68, 71]. The use of machine learning methods to classify features extracted from the accelerometer signal that capture the uncoordinated nature of the gait, such as trembling of the feet, short stride lengths, and unstable walking, is explored in [19, 69, 70]. However, the preceding methods do not necessarily present a signal model that captures the FOG patterns explicitly, and they use long window lengths to compute the spectral characteristics of the accelerometer signal, which leads to delays when determining the onset of the FOG event. Further, methods developed using machine learning techniques lack explanatory power and provide limited utility for understanding the structure of the data [8].

To overcome these drawbacks, we develop a physical model for the sensor data, design statistical signal processing methods to detect FOG based on its patterns. The detection module includes a two-step detection algorithm to determine instances of zero-velocity event intervals (ZVEI) and trembling event intervals (TREI) (see Fig. 3.1a). In Section 3.3.1, we derive the first detector which can detect ZVEI or TREI; this detector cannot separate these two events. In other words, the goal of the first detector is to filter out gait patterns that cannot be classified as ZVEI or TREI. In Section 3.3.2, we derive the second detector, which uses information from the gyroscope to distinguish ZVEI from TREI. This is necessary because the ZVEI/TREI identified by the first detector contains some gait patterns modeled as trembling events, but not associated with FOG. The second detector only detects ZVEI

and cannot filter out those gait patterns identified as TREI which are not associated with FOG. An illustration of the goals of the different detectors can be found in Fig. 3.1b. To validate the detection module, we use the experimental setup described in Section A.1 of Appendix A. To select the optimal values of the thresholds and scale factors of the detectors, we develop a novel method in Section 3.4.2 and 3.4.3. With the help of illustrative examples, in Section 3.5, we demonstrate the performance of the detector module in Fig. 3.1.

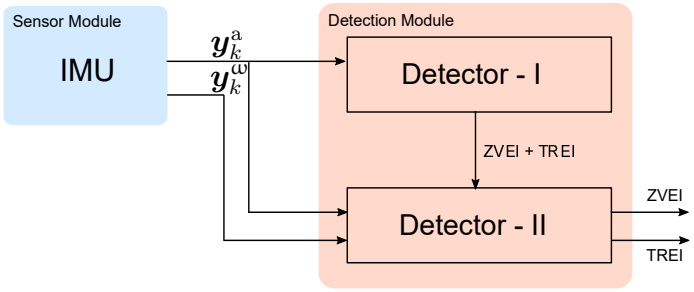

(a) A schematic of the multi hypothesis detection module.

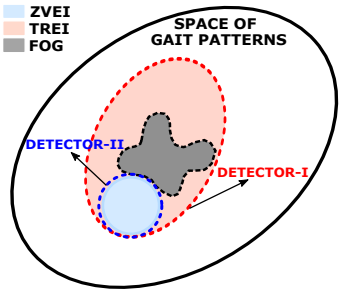

(b) An illustration of the subsets of the gait patterns that the different detectors identify.

Figure 3.1: The goal of the first detector is to detect zero-velocity and trembling events, and filter out gait patterns that are not associated with FOG. The goal of the second detector is to distinguish zero-velocity events from trembling events.

3.2 Signal Model and Statistics

If $\boldsymbol{y}_k^{\mathrm{a}} \in \mathbb{R}^{3\times 1}$ and $\boldsymbol{y}_k^{\omega} \in \mathbb{R}^{3\times 1}$ denote the measurements of a three-axis accelerometer and a three-axis gyroscope, respectively, at time instant k, then these measurements can be modeled as

$$\begin{aligned} \boldsymbol{y}_k^{\mathrm{a}} &= \boldsymbol{s}_k^{\mathrm{a}} + \boldsymbol{e}_k^{\mathrm{a}} \\ \boldsymbol{y}_k^{\omega} &= \boldsymbol{s}_k^{\omega} + \boldsymbol{e}_k^{\omega}. \end{aligned} \tag{3.1}$$

(a) ZVEI (b) TREI

Figure 3.2: Gait patterns. (a) Zero-velocity event intervals (ZVEI) are associated with no movement gait pattern in FOG. (b) Trembling event intervals (TREI) are associated with alternating trembling in the lower extremities gait pattern in FOG.

Here, $\boldsymbol{s}_k^{\mathrm{a}}$ and $\boldsymbol{s}_k^{\omega}$ denote the true specific force and angular velocity experienced by the accelerometer and gyroscope, respectively. Further, $\boldsymbol{e}_k^{\mathrm{a}}$ and $\boldsymbol{e}_k^{\omega}$ denote the measurement errors of the accelerometer and gyroscope, which are assumed to be white, mutually uncorrelated, and Gaussian distributed with zero mean and covariance matrices $\sigma_{\mathrm{a}}^2\boldsymbol{I}_3$ and $\sigma_{\omega}^2\boldsymbol{I}_3$, respectively.

Based on broad clinical observations, FOG patterns include alternating trembling in the lower extremities (includes the hip, knee, and ankle joints, and the bones of the thigh, leg, and foot), and no movement of the limbs and trunk [72,73]. Short, shuffling steps, not specific to or necessarily related to freezing, are observed in parkinsonian gait [74, 75]. Festination is usually associated with a progressive shortening and quickening of steps that often results in a freeze where forward/backward progression ceases [76].

We model gait patterns such as no movement of limbs in FOG, and short, shuffling steps in parkinsonian gait, as ZVEI. These events are associated with the flat foot phase of a gait cycle. ZVEI are defined as the time instances when the IMU is stationary, i.e., the IMU has a constant position and orientation; see Fig. 3.2a for illustration. During ZVEI, the accelerometer measures only the earth's gravitational acceleration, i.e., $g\boldsymbol{v}^{\mathrm{a}}$, where g and

$\boldsymbol{v}^{\mathrm{a}}$ are the magnitude and direction of a unit vector along the gravity. For parkinsonian gait with short, shuffling steps, the duration of the ZVEI are smaller than regular steps during normal PD gait. Further, we model gait patterns such as alternating trembling in FOG, and short, quickening steps on the toes and forepart of the feet in festinating gait, as TREI. These events are associated with heel lift-off and heel strike phase of a gait cycle. TREI are modeled as the motion of the IMU about an unknown fixed axis, and of unknown magnitude which depends on the severity of the trembling; see Fig. 3.2b for illustration. During trembling event, the accelerometer measures the sum of the inertial acceleration and gravitational acceleration, i.e., $\alpha_k^{\mathrm{a}}\boldsymbol{u}^{\mathrm{a}} + g\boldsymbol{v}^{\mathrm{a}}$, where α_k^{a} and $\boldsymbol{u}^{\mathrm{a}}$ are the magnitude and direction of a unit vector along the trembling axis. In this case, the accelerometer cannot distinguish between the axis aligned with the gravity field and trembling.

3.3 Detectors

In this section, we develop a physical model to describe the signal from the inertial sensor during the zero-velocity and trembling event, and design a statistically-based approach to detect these gait patterns. In particular, we develop a two-step detection algorithm to identify zero-velocity and trembling events. We formulate the two-step detection algorithm as a hypothesis testing problem and solve it using the generalized likelihood ratio test (GLRT) framework [77].

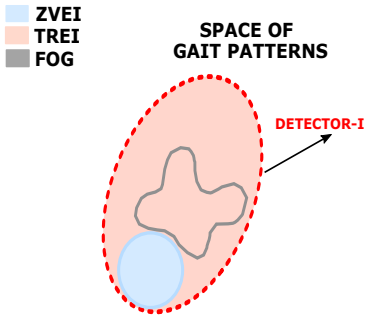

Figure 3.3: Using the accelerometer data, we develop an energy-based detector to filter gait patterns that are neither ZVEI nor TREI.

3.3.1 Detector-I

The goal of the first detector is to detect zero-velocity and trembling events, as illustrated in Fig. 3.3, and filter out gait patterns that are not associated with FOG . The detection problem can be formulated as

$$\begin{aligned} \mathcal{H}_1, \mathcal{H}_2 &\triangleq \text{ IMU is stationary } \textit{or} \text{ experiencing trembling} \\ \mathcal{H}_0 &\triangleq \text{ Otherwise.} \end{aligned} \tag{3.2}$$

For notation, we denote $\mathcal{H}_1$ and $\mathcal{H}_2$ together as $\mathcal{H}_{1,2}$. Under $\mathcal{H}_{1,2}$, the specific force measured by the accelerometers in (3.2), in the time window Ω_N of size N consisting of the time samples $\{k, \ldots, k+N-1\}$, can be modeled as

$$\begin{aligned} \mathcal{H}_1, \mathcal{H}_2 &: \forall k \in \Omega_N : \boldsymbol{s}_k^{\mathrm{a}} = \alpha_k^{\mathrm{a}} \boldsymbol{u}^{\mathrm{a}} + g\boldsymbol{v}^{\mathrm{a}}, \\ \mathcal{H}_0 &: \exists k \in \Omega_N : \boldsymbol{s}_k^{\mathrm{a}} \neq \alpha_k^{\mathrm{a}} \boldsymbol{u}^{\mathrm{a}} + g\boldsymbol{v}^{\mathrm{a}}. \end{aligned} \tag{3.3}$$

Given the signal model in (3.3), it can be shown (see Appendix B.1) that the generalized loglikelihood ratio test for detecting ZVEI and TREI are given by

$$T_{\mathrm{D}_1}(\boldsymbol{y}^{\mathrm{a}}) = \frac{1}{N}\sum_{k\in\Omega_N}\left\{\frac{1}{\sigma_{\mathrm{a}}^2}\|\boldsymbol{y}_k^{\mathrm{a}} - g\hat{\boldsymbol{v}}^{\mathrm{a}}\|^2_{\boldsymbol{P}^{\perp}_{\hat{\boldsymbol{u}}^{\mathrm{a}}}}\right\} \underset{<}{\overset{\mathcal{H}_{12}}{}} \gamma'_{\mathrm{D}_1}, \tag{3.4}$$

where $\hat{\boldsymbol{v}}^{\mathrm{a}}$ and $\hat{\boldsymbol{u}}^{\mathrm{a}}$ denote the estimated unit vectors in the direction of earth's gravitational acceleration vector and the trembling axis, respectively. Here, $\boldsymbol{y}^{\mathrm{a}} = [(\boldsymbol{y}_k^{\mathrm{a}})^{\mathsf{T}}, \ldots, (\boldsymbol{y}_{k+N-1}^{\mathrm{a}})^{\mathsf{T}}]^{\mathsf{T}}$, $\boldsymbol{P}^{\perp}_{\hat{\boldsymbol{u}}^{\mathrm{a}}} = \boldsymbol{I} - \hat{\boldsymbol{u}}^{\mathrm{a}}(\hat{\boldsymbol{u}}^{\mathrm{a}})^{\mathsf{T}}$, and γ'_{D_1} is the detector threshold.

To understand the intuitive meaning of (3.4), let us assume that the measurement error in the accelerometer is zero. When the IMU is stationary, the output from the accelerometer is given as $g\boldsymbol{v}^{\mathrm{a}}$. If the estimate of $\hat{\boldsymbol{v}}^{\mathrm{a}}$ is close to $\boldsymbol{v}^{\mathrm{a}}$, then the weighted norm in (3.4) is close to zero. When the IMU experiences trembling about a fixed axis, $\boldsymbol{u}^{\mathrm{a}}$, then the output of the accelerometer consists of both a gravitational and a trembling component. In Appendix B.1, we show that $\hat{\boldsymbol{u}}^{\mathrm{a}}$ is the eigenvector in the direction of maximum eigenvalue of $\boldsymbol{G}^{\mathrm{a}} = \sum_{k\in\Omega_N}(\boldsymbol{y}_k^{\mathrm{a}} - g\hat{\boldsymbol{v}}^{\mathrm{a}})(\boldsymbol{y}_k^{\mathrm{a}} - g\hat{\boldsymbol{v}}^{\mathrm{a}})^{\mathsf{T}}$. If the estimate of $\hat{\boldsymbol{v}}^{\mathrm{a}}$ closely matches the true direction of the gravitational vector, $\boldsymbol{v}^{\mathrm{a}}$, then, the matrix $\boldsymbol{G}^{\mathrm{a}}$ captures the outer product of the accelerometer output along the trembling axis. The matrix $\boldsymbol{G}^{\mathrm{a}}$ is symmetric and positive semi-definite. For any symmetric and positive semi-definite matrix, the eigenvector corresponding to the maximum eigenvalue represents the direction of the semi-major axis, and its eigenvalue represents the length of the semi-major axis. Therefore, the eigenvector, $\hat{\boldsymbol{u}}^{\mathrm{a}}$, represents the estimated trembling axis. If the estimated trembling axis, $\hat{\boldsymbol{u}}^{\mathrm{a}}$, matches the direction of the true trembling axis, $\boldsymbol{u}^{\mathrm{a}}$, then the weighted norm in (3.4) is zero, because the projection of $\hat{\boldsymbol{u}}^{\mathrm{a}}$ on $\boldsymbol{P}^{\perp}_{\hat{\boldsymbol{u}}^{\mathrm{a}}}$ is zero.

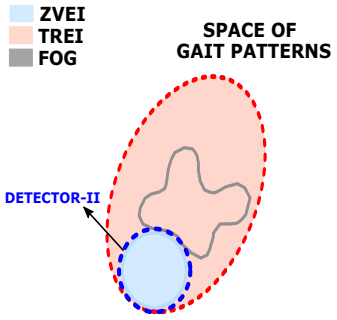

Figure 3.4: To identify ZVEI based on the region identified by the first detector, we develop a second detector which uses information from the gyroscope.

3.3.2 Detector-II

To distinguish ZVEI from TREI, we develop a second detector as illustrated in Fig. 3.4. Based on the hypotheses $\mathcal{H}_1$ and $\mathcal{H}_2$ defined in the previous subsection, we get

$$\begin{aligned} \mathcal{H}_1 &\triangleq \text{ IMU is stationary (ZVEI)} \\ \mathcal{H}_2 &\triangleq \text{ IMU is experiencing trembling (TREI).} \end{aligned} \tag{3.5}$$

Under $\mathcal{H}_1$, the IMU has a constant position and orientation. Because the gyroscopes are highly sensitive to angular motion, we include angular velocity measurements in the hypothesis testing problem in (3.5). Mathematically, under the assumption that the hypothesis $\mathcal{H}_{1,2}$ is true, the signal model for the two hypothesis in (3.5) can be written as

$$\begin{aligned} \mathcal{H}_1 : &\begin{cases} \forall k \in \Omega_N : \boldsymbol{s}_k^{\mathrm{a}} = g\boldsymbol{v}^{\mathrm{a}} \quad \iff \alpha_k^{\mathrm{a}} = 0 \\ \forall k \in \Omega_N : \boldsymbol{s}_k^{\omega} = \boldsymbol{0} \end{cases} \\ \mathcal{H}_2 : &\begin{cases} \exists k \in \Omega_N : \boldsymbol{s}_k^{\mathrm{a}} = \alpha_k^{\mathrm{a}}\boldsymbol{u}^{\mathrm{a}} + g\boldsymbol{v}^{\mathrm{a}}, \quad \iff \alpha_k^{\mathrm{a}} \neq 0 \\ \exists k \in \Omega_N : \boldsymbol{s}_k^{\omega} \neq \boldsymbol{0} \end{cases} . \end{aligned} \tag{3.6}$$

Given the signal model in (3.6), it can be shown (see Appendix B.2) that the generalized loglikelihood ratio test for detecting ZVEI or TREI are given by

$$T_{\mathrm{D}_2}(\boldsymbol{y}) = \frac{1}{N}\sum_{k\in\Omega_N}\left\{\frac{1}{\sigma_\omega^2}\left\|\boldsymbol{y}_k^\omega\right\|^2 + \frac{1}{\sigma_\mathrm{a}^2}\left[\left\|\boldsymbol{y}_k^\mathrm{a} - g\frac{\bar{\boldsymbol{y}}^\mathrm{a}}{\|\bar{\boldsymbol{y}}^\mathrm{a}\|}\right\|^2 - \left\|\boldsymbol{y}_k^\mathrm{a} - g\hat{\boldsymbol{v}}^\mathrm{a}\right\|^2_{\boldsymbol{P}^\perp_{\hat{\boldsymbol{u}}^\mathrm{a}}}\right]\right\} \underset{<}{\overset{\mathcal{H}_1}{}} \gamma'_{\mathrm{D}_2}, \qquad (3.7)$$

where $\boldsymbol{y}$ is the concatenation of the accelerometer and gyroscope measurements given by $[(\boldsymbol{y}^\mathrm{a})^\mathsf{T}, (\boldsymbol{y}^\omega)^\mathsf{T}]^\mathsf{T}$, $\boldsymbol{y}^\omega = [(\boldsymbol{y}_k^\omega)^\mathsf{T}, \ldots, (\boldsymbol{y}_{k+N-1}^\omega)^\mathsf{T}]^\mathsf{T}$, $\bar{\boldsymbol{y}}^\mathrm{a} = (1/N)\sum_{k\in\Omega_N}\boldsymbol{y}_k^\mathrm{a}$, and γ'_{D_2} is the detector threshold.

To understand the intuitive meaning of (3.7), let us again assume that the measurement error is zero for both the accelerometer and gyroscope. When the IMU is stationary, i.e., during zero-velocity event, the first term contains only error measurements, which are set to zero. The last term in (3.7) follows the same explanation as before, i.e., when the estimates of $\hat{\boldsymbol{v}}^\mathrm{a}$ and $\hat{\boldsymbol{u}}^\mathrm{a}$ match the true direction of the gravity vector and trembling axis, respectively, then the last term in (3.7) goes to zero. Further, when the IMU is stationary, the average mean vector of the measured accelerometer data seen in the window Ω_N, denoted as $\bar{\boldsymbol{y}}^\mathrm{a}$, is the same as the measured accelerometer data, which is given as $g\boldsymbol{v}^\mathrm{a}$. Due to this, the second term in (3.7) also goes to zero. Therefore, under the assumption that the IMU is stationary and the measurement error is zero, the test statistic in (3.7) is close to zero. However, during a trembling event in Fig. 3.2 and under the assumptions that the measured errors are zero, the last term in (3.7) goes to zero when the estimates $\hat{\boldsymbol{u}}^\mathrm{a}$ and $\hat{\boldsymbol{v}}^\mathrm{a}$ are close to the true values. The first and second terms are non-zero because gyroscope measurements are non-zero and accelerometer measurements contain both gravitational and specific force components. Therefore, the test statistic in (3.7) is non-zero under $\mathcal{H}_2$.

Observation: The signal model in (3.3) captures a large set of gait patterns that are not associated with FOG. The signal model in (3.6) distinguishes zero-velocity events from trembling events, but cannot filter out gait patterns that are not associated with FOG. In other words, the trembling events identified by the Detector-II also include falsely detected FOG events. Therefore, to filter out these falsely detected events, we use the fact that FOG events are associated with small foot speeds [24, 78]. This is done using a point-process filter, which fuses the output from the detector framework with the speed information provided by a foot-mounted inertial navigation system.

3.4 Parameters of the Detectors

In this subsection, we develop a methodology to select the parameters of the detectors developed in Section 3.3.1 and 3.3.2. In particular, we identify the thresholds of the detectors so that the FOG region in the inertial sensor data is detected. To obtain the optimal value of the thresholds, we define specific metrics and maximize or minimize them depending on the objective used.

3.4.1 Metrics

We define four metric variables that are used to evaluate the performance of the system design. The definition of each metric is as follows:

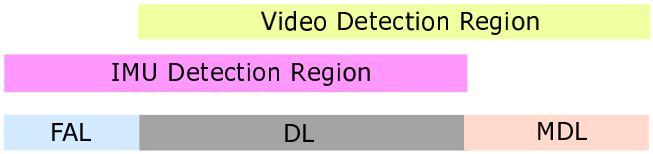

Figure 3.5: An illustration of FAL, DL, and MDL. The overlapping region between the video and inertial sensor method is the detection length (gray color). The region detected by the video but not by the inertial sensor method is the missed detection length (light orange color). The region detected by the inertial sensor method but not by the video is the false alarm length (light blue color).

1) *Detection Length* (DL) is defined as the length of the overlapping regions detected using both video data and the inertial sensor based method, for an episode of FOG. In other words, DL reflects the times when both methods agree that FOG is present.

2) *Missed Detection Length* (MDL) is defined as the length of the non-overlapping regions between the FOG instances detected using video data and the inertial sensor based method, for an episode of FOG. When the inertial sensor based method fails to detect a FOG instance detected by the video data in either foot, then the length of that instance of FOG is also considered as MDL.

3) *False Alarm Length* (FAL) is defined as the length of the non-overlapping region which is detected as a FOG instance by the inertial sensor based method, but not by the experts marking the video data.

4) *Total Length* (TL) is defined as the total length of the IMU data (the same as the duration of the video data).

In Fig. 3.5, we present an illustration of DL, FAL, and MDL. Based on the metric variables, we define two performance metrics, namely, the true positive rate (TPR) or sensitivity, and

the false alarm rate (FAR):

$$\text{TPR} = \frac{\text{DL}}{\text{DL} + \text{MDL}} \quad \text{and} \quad \text{FAR} = \frac{\text{FAL}}{\text{TL}}. \tag{3.8}$$

If TPR is close to one, then the episodes of FOG detected by the IMU match closely with the video data. Similarly, if FAR is close to zero, then the number of falsely detected FOG episodes is small. We say that an inertial sensor based algorithm performs as well as the video-based method if both TPR and $1-\text{FAR}$ are close to one. When $\text{DL} = 0$ and $\text{MDL} = 0$, we say the $\text{TPR} = 1$, because no FOG episodes were detected by the video data nor by the algorithm using the IMU data.

3.4.2 Detector-I

Under $\mathcal{H}_{1,2}$, the distribution of the test statistic in (3.4) follows a chi-square distribution when $\hat{\boldsymbol{u}}^{\text{a}}$ and $\hat{\boldsymbol{v}}^{\text{a}}$ are estimated accurately. Each term in (3.7) follows a χ^2_1 distribution because $\text{rank}(\boldsymbol{P}^{\perp}_{\hat{\boldsymbol{u}}^{\text{a}}}) = 1$ and $\boldsymbol{P}^{\perp}_{\hat{\boldsymbol{u}}^{\text{a}}}$ is an idempotent matrix. The test statistic in (3.7) represents the sum of independent chi-square distributions with $\nu = 1$ degrees of freedom. Hence, (3.7) follows χ^2_N distribution. The exact detection performance is given by $P_{\text{FA}} = \mathcal{Q}_{\chi^2_N}(\gamma'_{D_1})$, where γ'_{D_1} is the detection threshold of Detector-I for a given probability of false alarm, and $\mathcal{Q}_{\chi^2_N}$ is the right-tail probability for a chi-squared distribution with N degrees of freedom.

To obtain the threshold γ'_{D_1}, we consider 5 second IMU data for six different PD participants (TT004–BLOCK, TT006–NARROW, TT013–NARROW, TT015–NARROW, TT021–BLOCK, and TT027–BLOCK). The IMU data consists of either a specific type of FOG pattern (turning freeze for TT004–BLOCK and TT013–NARROW, initiation freeze for TT021–BLOCK and TT027–BLOCK) or no specific FOG pattern. ZVEI, FOG intervals, and other

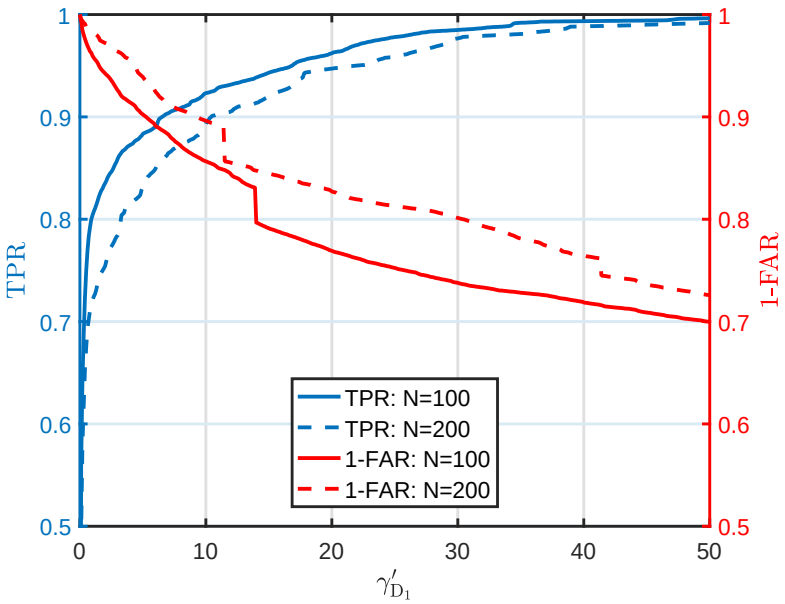

Figure 3.6: Average value of TPR and $1 - \text{FAR}$ curves for different values of Detector-I threshold γ'_{D_1}.

gait patterns are identified in the video and marked as ZVEI (video), FOG (video), and MOVE (video), respectively. The synchronization between the video and IMU data was done manually. We use the definitions of TPR and FAR in (3.8) to evaluate the performance of the Detector-I across different values of threshold γ'_{D_1}. We use ZVEI (video) and FOG (video) regions as ground truth data. In Fig. 3.6, we plot the average value of TPR and $1 - \text{FAR}$ obtained across the six datasets. We observe that, as the Detector-I threshold increases, the average value of TPR increases because Detector-I includes both TREI and ZVEI. However, the average value of $1 - \text{FAR}$ decreases with the increase in the threshold because gait patterns that are modeled as neither ZVEI nor TREI, but contain similar energy information are also identified. Further, in Fig. 3.6, we do not observe a significant improvement in the average value of TPR across different window lengths. Considering these factors, we choose $\gamma'_{D_1} = 34.39$ for $N = 100$ because the average value of the TPR curve

demonstrates a small improvement in the performance on increasing the threshold beyond 34.39.

3.4.3 Detector-II

Under $\mathcal{H}_1$, i.e., when the foot is stationary, the distribution of the test statistic in (3.7) again follows a chi-square distribution when $\hat{\boldsymbol{u}}^{\mathrm{a}}$ and $\hat{\boldsymbol{v}}^{\mathrm{a}}$ are estimated accurately. The difference between the second and third terms in (3.7) is approximately equal to zero, because each term indicates the energy due to the error measurements. The test statistic in (3.7) is the sum of independent chi-squared distributions, with $\nu = 1$. Therefore, the expression of the test statistic under $\mathcal{H}_1$ follows a χ^2_N distribution. The exact detection performance is given by $P_{\mathrm{FA}} = \mathcal{Q}_{\chi^2_N}(\gamma'_{\mathrm{D}_2})$, where γ'_{D_2} is the detection threshold of Detector-II for a given probability of false alarm.

The sensitivity of the gyroscope is characterized σ_ω because it scales the test statistic in (3.7). To determine the sensitivity of the gyroscope signal, we plot the average values of TPR and $1-\mathrm{FAR}$ across different values of threshold γ'_{D_2} and $\sigma_\omega/\sigma_{\mathrm{a}}$ with $\sigma_{\mathrm{a}} = 1.0$. Since the goal of the Detector-II is to distinguish ZVEI from TREI, we compute the average values of TPR and $1-\mathrm{FAR}$ based on (3.8). As the ground truth, we use ZVEI detected in the video. We fix $N = 100$, $\sigma_{\mathrm{a}} = 1.0$, and $\gamma'_{\mathrm{D}_1} = 34.39$ for Detector-I, and evaluate the performance of the second detector. As the value of σ_ω goes to zero, the test statistic tends towards infinity because ZVEI are detected for finite values of the Detector-II threshold. Therefore, for small values of σ_ω, the average value of TPR is close to zero. Similarly, the lower half of Fig. 3.7b detects no ZVEI when σ_ω is small. As the sensitivity of the gyroscope and threshold γ'_{D_2} increase, the average value of TPR increases and $1-\mathrm{FAR}$ decreases. However,

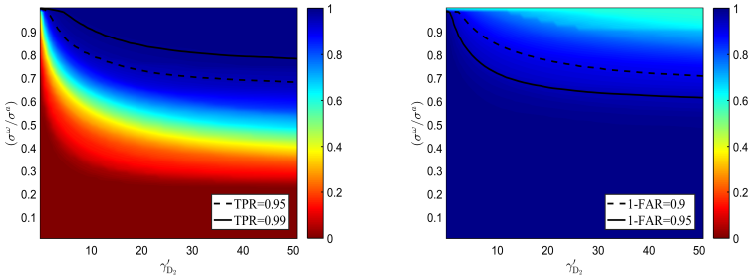

(a) TPR: $N = 100$. (b) $1 - \text{FAR}$: $N = 100$.

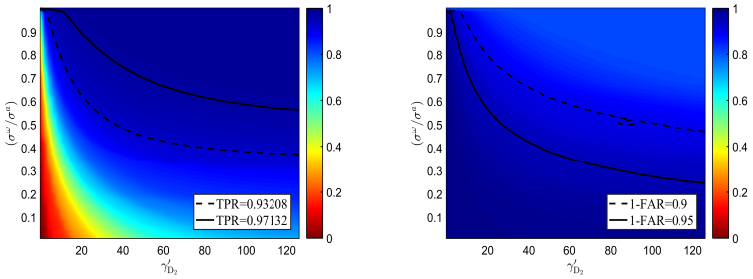

(c) TPR: $N = 200$. (d) $1 - \text{FAR}$: $N = 200$.

Figure 3.7: Sensitivity of gyroscope: Image plots of average value of TPR and $1 - \text{FAR}$ for ZVEI across different values of Detector-II threshold and standard deviation of the gyroscope.

for a fixed large value of σ_ω/σ_a, i.e., $\gamma'_{D_2} \geq 10.0$ the TPR curves begin to saturate (see Fig. 3.7a). This behavior is due to the fact that the maximum region that the Detector-II can detect is bounded by the ZVEI/TREI region detected by the Detector-I. We represent the regions with high average TPR $(95 - 99\%)$ and $1 - \text{FAR}$ $(90 - 95\%)$ values, respectively with solid-line and dashed-line plot. We set $\sigma_\omega/\sigma_a = 0.8$ for $N = 100$ which lies in $95 - 99\%$ region of the average TPR plot and $90 - 95\%$ region of the average $1 - \text{FAR}$ plot. However, due to the saturation behavior of the average value of TPR curve, the threshold γ'_{D_2} can take many finite values.

To determine the optimal threshold γ'_{D_2}, we compute the performance of the foot-mounted inertial navigation system for the calibration task. In the calibration task, the participant was asked to walk forward along a full 6 meter straight path. On reaching the end, the

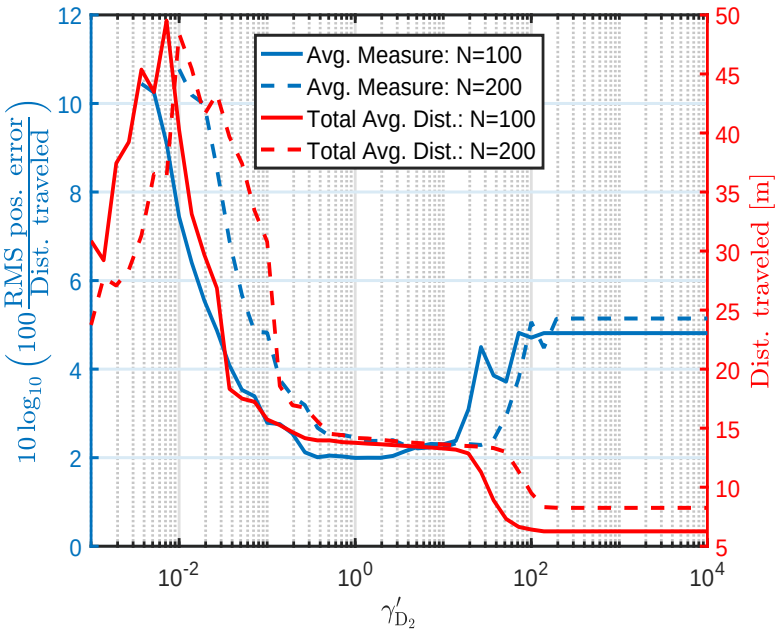

Figure 3.8: Performance of the foot-mounted inertial navigation system plot across different value of the threshold.

participant made a 180° turn and returned to the starting point. Each calibration task contains two datasets where the participant was asked to follow the same trajectory twice. The starting point and ending of the trajectory are the same and the total average distance traveled varied between 13.0-13.5 meters because the participants took an extra step or two beyond the physically marked end-point to complete the first turn. We compute the ratio of the root mean square (RMS) of the position error and distance traveled as follows [79]

$$10\log_{10}\left(100\frac{\text{RMS position error}}{\text{Distance traveled}}\right), \tag{3.9}$$

where the root mean square of the position error is defined as the distance between the starting and ending point of the trajectory during the calibration task, and the distance traveled is defined as the sum of the distances between the position coordinates at the edges of the ZVEI during OFF state. When the threshold of Detector-II is set to a low value, no ZVEI are detected. In this case, the total distance measured by the system sums to zero, and

the performance metric in (3.9) is not defined, as shown in the left half of Fig. 3.8. When the threshold is set to a very high value, zero-velocity update is always ON and the ZVEI detected by Detector-II is equal to the ZVEI/TREI identified by the Detector-I. Due to this, the total distance is a non-zero value close to zero, and thus the curve representing equation (3.9) begins to saturate. Therefore, the optimal value is obtained at the point when the curve in (3.9) attains a minimum value and the estimated total average distance is within an error-bound region of the true average distance. For the calibration task, the total distance traveled by the participants is 12.5 ± 1.5 meters. In Fig. 3.8, for $N = 100$, (3.9) attains a minimum at $\gamma'_{\mathrm{D}_2} = 2.00$ and the average distance traveled is equal to 13.5 meters, which lies within one standard deviation distance of the total average distance traveled by all the participants.

3.5 Illustrative Examples

In this section, with the help of an illustrative example, we demonstrate the output of the detector module of the proposed detection module in Fig. 3.1a. We use the inertial sensor data for participant identity (PID) TT004 and TT027, performing the BLOCK and figure EIGHT task, during which the participant experiences a turning and initiation freeze, respectively. The details of the tasks are listed in Table A.1 of Appendix A.1.

3.5.1 Detector-I

The goal of Detector-I is to detect shuffling or trembling motion intervals, which are modeled as ZVEI and TREI, respectively. In Fig. 3.9a and Fig. 3.9b, we plot the outputs of the

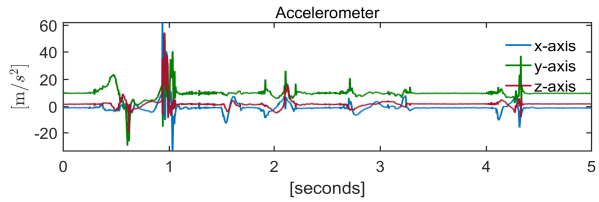

(a) Three axis accelerometer signal

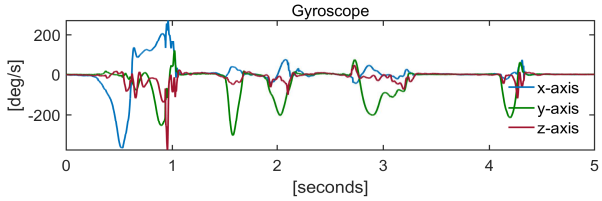

(b) Three axis gyroscope signal

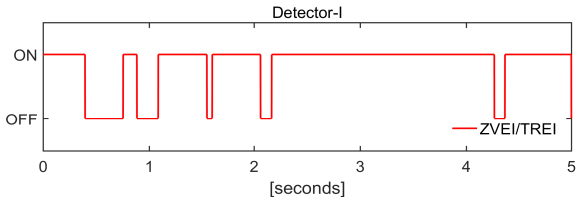

(c) Output of Detector-I (ZVEI/TREI)

Figure 3.9: ZVEI and TREI detected by Detector-I for TT004–BLOCK task.

three-axis accelerometer and the three-axis gyroscope sensor, respectively. In Appendix 3.4.2 of the supplementary material, we demonstrate the procedure to obtain the system parameters for Detector-I, using video data as the reference system. We set the size of the window $\Omega_N = 100$, the standard deviation of the accelerometer signal $\sigma_{\mathrm{a}} = 1.0$, and the threshold of Detector-I $\gamma'_{\mathrm{D}_1} = 34.53$. The output of Detector-I based on the test statistic in (3.4) is shown in Fig. 3.9c. Detector-I in Fig. 3.9c is ON when the angular velocities measured by the gyroscope are zero and the specific force measured by the accelerometer in the y-axis is $9.8\,\mathrm{m}\,/\,\mathrm{s}^2$, indicating ZVEI. Further, Detector-I is also ON at some non-zero velocity instances, indicating possible TREI associated with FOG.

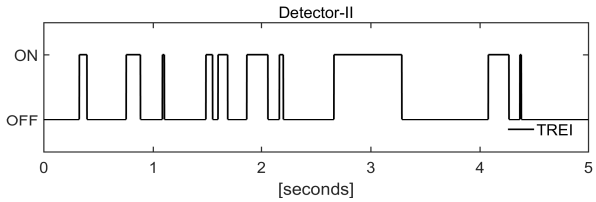

(a) Output of Detector-II (TREI)

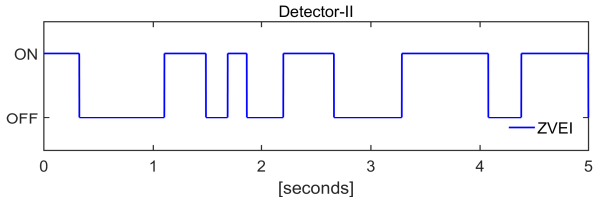

(b) Output of Detector-II (ZVEI)

Figure 3.10: Detector-II separates ZVEI from TREI.

3.5.2 Detector-II

As stated previously, the goal of Detector-II is to distinguish ZVEI from TREI based on the output of Detector-I. We refer to Appendix 3.4.3 of the supplementary material to obtain the design parameters of Detector-II. We use the same window length Ω_N as in Detector-I. In addition, we set the standard deviation of the gyroscope $\sigma_\omega = 0.8$ and the threshold $\gamma'_{\mathrm{D}_2} = 2.00$. The output of Detector-II, based on the test statistic in (3.7), is shown in Fig. 3.10a and Fig. 3.10b. The time periods when ZVEI is ON, the angular velocities are close to zero because no rotational motion is observed when the foot is stationary. Furthermore, the time intervals that are not identified as ZVEI by Detector-II are labeled as TREI, as shown in Fig. 3.10a. However, not all TREI are associated with FOG.

In Fig. 3.11, we overlay the zero-velocity events, freezing of gait, and other gait events detected in the video data, and generate a state diagram of the various outputs of the detection module. The red curve is the output of Detector-I based on the test statistic in (3.4). The goal of Detector-II is to determine the ZVEI when Detector-I is ON. The blue

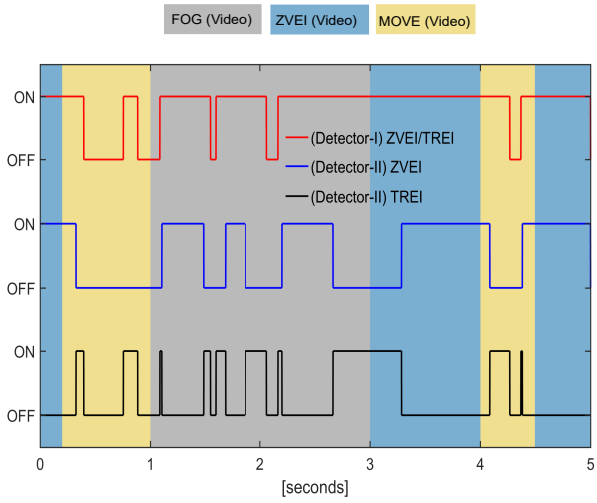

Figure 3.11: State diagram of Detector-I and Detector-II for PID TT004–BLOCK task with an overlay of the video data.

curve is the output of Detector-II for the test statistic in (3.7). In Fig. 3.11, we observe that there is a significant overlap between the ZVEI identified by the Detector-II and ZVEI (video) indicated with a blue background. In addition, the FOG region detected in the video contains both ZVEI and TREI, because a turn freeze includes both trembling and short stride lengths. However, Detector-II also identifies gait patterns that not associated with FOG. Therefore, the detectors alone cannot identify the FOG regions accurately.

3.5.3 Estimated Tremor Axis

In Fig. 3.12a, we plot the 3D trajectory of a single gait cycle for a short shuffling step, obtained for PID–TT027 during the figure EIGHT trial. In this gait cycle, the participant experiences initiation freeze prior to starting the second figure EIGHT trial. We plot the estimate tremor axis, denoted by $\hat{\boldsymbol{u}}^a$, for the detected trembling event intervals. To display the alternating trembling motion of the tremor axis in the navigation plane, we use the orientation angles (roll, pitch, and yaw) to rotate $\hat{\boldsymbol{u}}^a$ from the body frame to the navigation

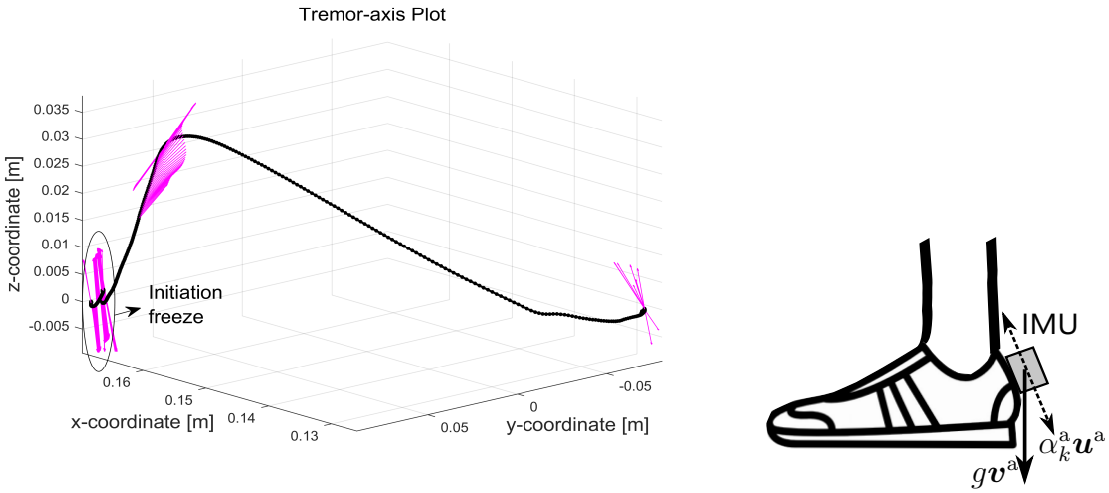

(a) (b)

Figure 3.12: Tremor axis plot. (a) Trajectory plot of the gait during initiation freeze with an overlay of the tremor-axis for PID–TT027. The initiation gait freeze was observed before the second EIGHT trial. The tremor-axis is shown in magenta color only for the detected trembling event intervals. (b) An illustration of the accelerometer sensor data during a tremor where $\boldsymbol{u}^{\mathrm{a}}$ is the tremor axis, $\boldsymbol{v}^{\mathrm{a}}$ is the gravity vector, α_k^{a} is the magnitude of tremor, and g is the earth's gravity.

frame. The vector $\hat{\boldsymbol{u}}^a$, displayed in magenta color in Fig. 3.12a, denotes direction of the tremor axis as illustrated in Fig. 3.12b). The detector thresholds are fixed at $\gamma'_{\mathrm{D}_1} = 34.39$ and $\gamma'_{\mathrm{D}_2} = 2.0$. We observe that during initiation of the gait cycle, the vectors representing the direction of the tremor axis demonstrates trembling motion. This behavior also explains the time invariance of the tremor axis for a small interval of time, i.e., $\alpha_k^{\mathrm{a}}\boldsymbol{u}^{\mathrm{a}} + g\boldsymbol{v}^{\mathrm{a}} \quad \forall k \in \Omega_N$. Furthermore, the TREI identified by Detector-II also detects phases of a gait cycle that are not associated with FOG.

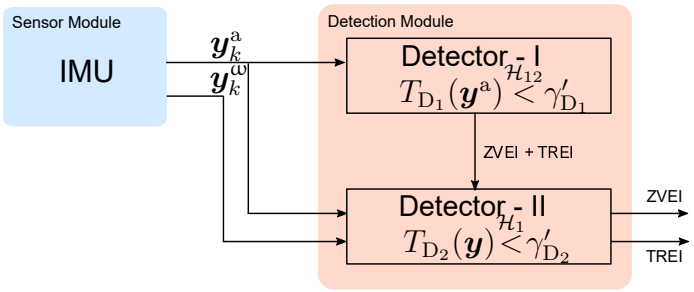

Figure 3.13: A schematic of the two-step detection algorithm in the detection module.

3.6 Chapter Summary

In this chapter, we developed a physical model for the sensor data that describes the trembling motion during FOG events. Next, we designed a generalized likelihood ratio test framework to develop a two-stage detector for determining the zero-velocity and trembling events in the gait. As illustrated in Fig. 3.13, the first detector identified ZVEI and TREI, but could distinguish between them and the second detector identified ZVEI. We also developed a methodology to identify the optimal parameters of the detection module. With the help of illustrative examples using real data from Parkinson disease participants, we showed that the detection module detected ZVEI and TREI; however, not all TREI are associated with FOG. Therefore, to filter out the TREI which are not associated with FOG, we consider the fact that the alternating trembling motion in FOG are associated with low foot speeds and small pitch angles. In the next chapter, to estimate these gait parameters, we employ a zero-velocity aided inertial navigation system in the navigation module.

Chapter 4

Navigation Module: Zero-velocity aided Inertial Navigation System

In this chapter, we explore implementing a strapdown inertial system. To extract the gait parameters associated with freezing of gait (FOG), we employ a zero-velocity aided inertial navigation system (ZV-INS) in the navigation module. The ZV-INS uses the accelerometer and gyroscope sensor measurements along with the zero-velocity event intervals (ZVEI) to estimate the position, velocity, and orientation of the foot via dead reckoning. The ZVEI act as pseudo-measurements, useful in correcting the estimates of the position, velocity, and orientation. We derive the state-space models of a strapdown inertial navigation system, which are commonly used in a pedestrian navigation system. Further, we implement the ZV-INS by using the Kalman filter. Finally, we provide an illustrative example demonstrating the gait parameters extracted using the navigation module.

4.1 Introduction

There has been an increasing demand for a robust and accurate positioning system that works in indoor and outdoor environments. A global positioning system (GPS) provides a whole range of navigation accuracies at very low cost and with low power consumption. Devices that use GPS are portable and well suited for integration with other sensors, communication links, and databases. Still, because GPS does not work in all environments, especially indoors, autonomous positioning systems are needed. The main challenge in developing an infrastructure-free positioning solution is to create a technology that is sufficiently accurate in GPS-limited environments. Since inertial navigation systems (INS) technology can work in almost all environments where GPS has difficulties, micro-electromechanical systems (MEMS) inertial technology is seen as both a possible complement to GPS technology and a potential alternative to GPS. For example, INSs can provide position information whenever GPS signals are unavailable (in tunnels, indoors, in underground facilities), ensuring a seamless provision of position information. Because an INS is low cost, portable, and infrastructure-free, they are well suited for ambulatory gait analysis [15, 19, 64–70].

An INS is a navigation aid that uses a computing platform, accelerometers, and gyroscopes to continuously dead reckon the position, orientation, and velocity (direction and speed of movement) of a moving object without the need for external references [80–82]. The principle of dead reckoning is the process of estimating an object's position by tracking its movements relative to a known starting point. The navigation equations for obtaining the position and velocity estimates are based on the kinematic equations, i.e., the derivative of the position is the velocity, and the derivative of the velocity is the acceleration. Consequently, starting from a stationary point, integrating the acceleration once and twice, respectively, yields the velocity and the change in position. However, to obtain the acceleration measurement,

the body frame (the reference frame of the sensor) must be transformed to the navigation frame (the reference frame of the object/person to be tracked), because the accelerometer measures specific force, and cannot distinguish gravitational and inertial acceleration. The transformation of axis from the body frame to the navigation frame is made possible by a three-axis gyroscope, which measures the angular velocity or rotational motion of the object. Integrating the angular velocities gives the relative orientation of the sensor, which can then be used to transform the accelerometer measurements from the body frame to the navigation frame. An excellent overview of implementing the zero-velocity aided inertial navigation system is also presented in [80–82].

Section 4.2 describes the background required for developing the ZV-INS. Sections 4.3.1 and 4.3.1 respectively develop the state-space models for the navigation mechanization equations and their corresponding perturbation equations, for a strapdown inertial navigation system. Section 4.4 presents the output of the navigation module, using real data from Parkinson disease participants.

4.2 Preliminaries

4.2.1 Rotation Matrix

In the navigation frame (the plane drawn tangential to a point on the surface of the earth), denoted by the North (N), East (E), and Down (D) axes, gravitational acceleration acts downward, and has a magnitude of $9.8\,\mathrm{m}\,/\,\mathrm{s}^2$. The accelerometer in the body frame measures both inertial and gravitation acceleration, and cannot distinguish between the two measurements. To remove the gravitational acceleration, we use a rotation matrix obtained

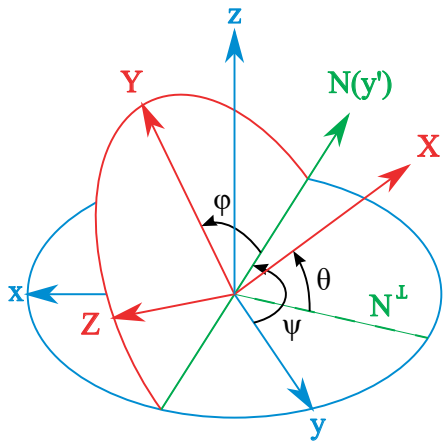

Figure 4.1: Euler angles. $z-y'-x''$ sequence (intrinsic rotations; N coincides with y'). The angle rotation sequence is ϕ, θ, ψ. Note that in this case $\psi > 90°$ and θ is a negative angle. Image source: Wikipedia.

by integrating the angular velocity measurements, to rotate the body frame to the navigation frame. Let $\boldsymbol{R}_{\mathrm{b}}^{\mathrm{n}} \in \mathbb{R}^{3\times 3}$ denote a rotation matrix from the body frame to the navigation frame. The subscript and superscript respectively represent the current and transformed reference frames. If $[\phi, \theta, \psi]^{\mathsf{T}}$ denotes the roll, pitch and yaw angles when the initial axes are aligned with the body frame, then the rotation matrix that transforms the body frame to the navigation frame is given as

$$
\begin{aligned}
\boldsymbol{R}_{\mathrm{b}}^{\mathrm{n}} &= \boldsymbol{R}(\psi)\, \boldsymbol{R}(\theta)\, \boldsymbol{R}(\phi), \\
&= \begin{bmatrix} \cos(\psi) & \sin(\psi) & 0 \\ -\sin(\psi) & \cos(\psi) & 0 \\ 0 & 0 & 1 \end{bmatrix} \begin{bmatrix} \cos(\theta) & 0 & -\sin(\theta) \\ 0 & 1 & 0 \\ \sin(\theta) & 0 & \cos(\phi) \end{bmatrix} \begin{bmatrix} 1 & 0 & 0 \\ 0 & \cos(\phi) & \sin(\phi) \\ 0 & -\sin(\phi) & \cos(\phi) \end{bmatrix},
\end{aligned}
$$

where $\boldsymbol{R}(\psi)$, $\boldsymbol{R}(\theta)$, and $\boldsymbol{R}(\phi)$, respectively, are rotation matrices along z, y', and z'', as shown in Fig. 4.1

Properties of a Rotation Matrix

- *Coordinate Axis Transformation*: Let $\boldsymbol{r}^{\mathrm{b}} \in \mathbb{R}^{3\times 1}$ and $\boldsymbol{r}^{\mathrm{n}} \in \mathbb{R}^{3\times 1}$ respectively denote a position vector in the b-frame and n-frame. Then, any vector in the n-frame can be represented as

$$\boldsymbol{r}^{\mathrm{n}} = \boldsymbol{R}^{\mathrm{n}}_{\mathrm{b}} \boldsymbol{r}^{\mathrm{b}}, \tag{4.1}$$

  where $\boldsymbol{R}^{\mathrm{n}}_{\mathrm{b}} \in \mathbb{R}^{3\times 3}$ is the rotation matrix from the body frame to the navigation frame. Similarly, any position vector in the body frame can be represented as:

$$\boldsymbol{r}^{\mathrm{b}} = \boldsymbol{R}^{\mathrm{b}}_{\mathrm{n}} \boldsymbol{r}^{\mathrm{n}}. \tag{4.2}$$

- *Unitary Matrix*: For any rotation matrix $\boldsymbol{R}^{\mathrm{b}}_{\mathrm{n}}$,

$$(\boldsymbol{R}^{\mathrm{n}}_{\mathrm{b}})^{-1} = (\boldsymbol{R}^{\mathrm{n}}_{\mathrm{b}})^{\mathsf{T}} = \boldsymbol{R}^{\mathrm{b}}_{\mathrm{n}} \quad \text{and} \quad |\boldsymbol{R}^{\mathrm{n}}_{\mathrm{b}}| = 1.$$

- *Derivative*: Consider an arbitrary fixed point in the navigation frame. Let $\boldsymbol{x}^{\mathrm{b}} \in \mathbb{R}^{3\times 1}$ and $\boldsymbol{x}^{\mathrm{n}} \in \mathbb{R}^{3\times 1}$, respectively, be the coordinates of the point in the body frame and the navigation frame. Then, $\boldsymbol{x}^{\mathrm{n}}$ is constant because the point is fixed in the navigation frame. Further, $\boldsymbol{x}^{\mathrm{b}}$ is time-varying because the body frame is rotating with an angular velocity vector $\boldsymbol{\omega}^{\mathrm{b}}_{\mathrm{ib}} = [(\omega^{\mathrm{b}}_{\mathrm{ib}})_x, (\omega^{\mathrm{b}}_{\mathrm{ib}})_y, (\omega^{\mathrm{b}}_{\mathrm{ib}})_z]^{\mathsf{T}}$. Then, we can express $\boldsymbol{x}^{\mathrm{n}}$ as

$$\boldsymbol{x}^{\mathrm{n}} = \boldsymbol{R}^{\mathrm{n}}_{\mathrm{b}} \boldsymbol{x}^{\mathrm{b}}. \tag{4.3}$$

  Since $\dot{\boldsymbol{x}}^{\mathrm{n}} = 0$, taking the derivative on both sides of (4.3), we get

$$\dot{\boldsymbol{x}}^{\mathrm{n}} = \dot{\boldsymbol{R}}^{\mathrm{n}}_{\mathrm{b}} \boldsymbol{x}^{\mathrm{n}} + \boldsymbol{R}^{\mathrm{n}}_{\mathrm{b}} \dot{\boldsymbol{x}}^{\mathrm{b}} \implies -\dot{\boldsymbol{x}}^{\mathrm{b}} = \boldsymbol{R}^{\mathrm{b}}_{\mathrm{n}} \dot{\boldsymbol{R}}^{\mathrm{n}}_{\mathrm{b}} \boldsymbol{x}^{\mathrm{b}}. \tag{4.4}$$

However, the rate of change of a vector, i.e., its derivative, can be represented by using a cross-product. Thus, (4.4) can be expressed as:

$$\dot{\boldsymbol{x}}^{\mathrm{n}} = \dot{\boldsymbol{x}}^{\mathrm{b}} + \boldsymbol{\omega}_{\mathrm{ib}}^{\mathrm{b}} \times \boldsymbol{x}^{\mathrm{b}} \implies -\dot{\boldsymbol{x}}^{\mathrm{b}} = \boldsymbol{\omega}_{\mathrm{ib}}^{\mathrm{b}} \times \boldsymbol{x}^{\mathrm{b}} = \boldsymbol{\Omega}_{\mathrm{ib}}^{\mathrm{b}} \boldsymbol{x}^{\mathrm{b}}. \tag{4.5}$$

Finally, from (4.4) and (4.5), we get

$$\boldsymbol{R}_{\mathrm{b}}^{\mathrm{n}} \dot{\boldsymbol{R}}_{\mathrm{b}}^{\mathrm{n}} = \boldsymbol{\Omega}_{\mathrm{ib}}^{\mathrm{b}} \implies \dot{\boldsymbol{R}}_{\mathrm{b}}^{\mathrm{n}} = \boldsymbol{R}_{\mathrm{b}}^{\mathrm{n}} \boldsymbol{\Omega}_{\mathrm{ib}}^{\mathrm{b}}, \tag{4.6}$$

where $\boldsymbol{\Omega}_{\mathrm{ib}}^{\mathrm{b}}$ is a skew-symmetric matrix given as

$$\boldsymbol{\Omega}_{\mathrm{ib}}^{\mathrm{b}} = \begin{bmatrix} 0 & -[\boldsymbol{\omega}_{\mathrm{ib}}^{\mathrm{b}}]_z & [\boldsymbol{\omega}_{\mathrm{ib}}^{\mathrm{b}}]_y \\ [\boldsymbol{\omega}_{\mathrm{ib}}^{\mathrm{b}}]_z & 0 & -[\boldsymbol{\omega}_{\mathrm{ib}}^{\mathrm{b}}]_x \\ -[\boldsymbol{\omega}_{\mathrm{ib}}^{\mathrm{b}}]_y & [\boldsymbol{\omega}_{\mathrm{ib}}^{\mathrm{b}}]_x & 0 \end{bmatrix}. \tag{4.7}$$

4.3 ZVEI-Aided Inertial Navigation System

In this section, we develop the state-space models for the navigation mechanization equations and their corresponding perturbation equations, for a strapdown inertial navigation system [82, Chapter, 10]. We use the navigation mechanization equations to estimate the position, velocity, and orientation angles. To correct the estimates of position and velocity, we use the zero-velocity event intervals as pseudo measurement updates along with the Kalman filter. We also derive the state-space model for the perturbation equations of a strapdown inertial navigation system, and implement it by employing an extended Kalman filter.

4.3.1 Navigation Mechanization Equations

Naïve Implementation of INS

Let $\boldsymbol{p}^{\mathrm{n}} \in \mathbb{R}^{3\times 1}$ and $\boldsymbol{v}^{\mathrm{n}} \in \mathbb{R}^{3\times 1}$ denote respectively the position and velocity estimates, expressed in the navigational frame. Then, the navigational mechanization equations for a low-cost inertial navigation system can be written as

$$\dot{\boldsymbol{p}}^{\mathrm{n}} = \boldsymbol{v}^{\mathrm{n}}, \tag{4.8}$$

$$\dot{\boldsymbol{v}}^{\mathrm{n}} = \boldsymbol{R}_{\mathrm{b}}^{\mathrm{n}} \boldsymbol{s}^{\mathrm{b}} + \boldsymbol{g}^{\mathrm{n}}, \tag{4.9}$$

$$\dot{\boldsymbol{R}}_{\mathrm{b}}^{\mathrm{n}} = \boldsymbol{R}_{\mathrm{b}}^{\mathrm{n}} \boldsymbol{\Omega}_{\mathrm{nb}}^{\mathrm{b}}, \tag{4.10}$$

where $\boldsymbol{\Omega}_{\mathrm{nb}}^{\mathrm{b}}$ is a skew-symmetric matrix. The derivations of equations (4.8) and (4.9) are presented in Appendix C.1. We get (4.10) from the derivation property of a rotation matrix, as seen in (4.6). Note that in (2.2), we make an approximation, $\boldsymbol{\omega}_{\mathrm{ib}}^{\mathrm{b}} \approx \boldsymbol{\omega}_{\mathrm{nb}}^{\mathrm{b}}$ because the navigation frame is fixed. Equations (4.8) and (4.9) are based on the kinematic equations, i.e., the derivative of the position is the velocity, and the derivative of the velocity is the acceleration. However, to compute acceleration in the navigational frame, the body frame must be rotated to the navigation frame, and the gravitational acceleration must be compensated for. The transformation or rotation matrix of the body frame to the navigation frame is feasible by integrating the the rotation matrix in (4.10). A block diagram illustration of the steps required to compute the navigation mechanization equations described in (4.8)–(4.10) is shown in Fig. 4.2. As can be seen, the naïve implementation of the navigation mechanical implementation requires three integration blocks.

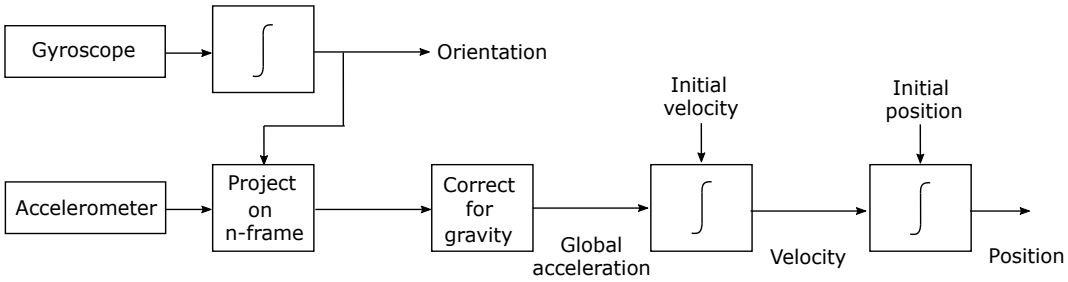

Figure 4.2: Block diagram implementation of navigational mechanization equations in a strapdown inertial system.

We also note that (4.10) is a nonlinear function and that the rotation matrix cannot be estimated directly by plugging (4.10) into a linear recursive filter, such as the Kalman filter. Therefore, to linearize (4.10), we rewrite it in terms of quaternions [82, Appendix D]. If $\boldsymbol{q} \in \mathbb{R}^{4\times 1}$ denotes the quaternion vector equivalent of the rotation matrix $\boldsymbol{R}_{\mathrm{b}}^{\mathrm{n}}$, then (4.10) can be rewritten as

$$\dot{\boldsymbol{q}} = \left(\cos(\|\boldsymbol{w}\|)\boldsymbol{I} + \frac{\sin(\|\boldsymbol{w}\|)}{\|\boldsymbol{w}\|}\boldsymbol{W}\right)\boldsymbol{q}, \tag{4.11}$$

$$= \boldsymbol{\Omega}(\boldsymbol{\omega} dt)\boldsymbol{q}, \tag{4.12}$$

where $W_i = \frac{1}{2}\int_{t_{k-1}}^{t_k} \omega_i(\tau)d\tau, \quad \forall i \in \{1,2,3\}$, and $\boldsymbol{W}$ is the integral of the angular rates over the k-th sampling interval $t \in (t_{k-1}, t_k]$ given as

$$\boldsymbol{W} = \begin{bmatrix} 0 & -\boldsymbol{w}^{\mathsf{T}} \\ \boldsymbol{w} & [\boldsymbol{w}]_{\times} \end{bmatrix} = \begin{bmatrix} 0 & -W_1 & -W_2 & -W_3 \\ W_1 & 0 & -W_3 & W_2 \\ W_2 & W_3 & 0 & -W_1 \\ W_3 & -W_2 & W_1 & 0 \end{bmatrix}. \tag{4.13}$$

By employing quaternions, we can transform the nonlinear function in (4.10) to an affine/linear function expressed as quaternions in (4.11). Because (4.11) is affine, it can be directly plugged

into the Kalman filter along with position and velocity equations. The orientation angles can either be computed directly from the quaternions or from the rotation matrix obtained using the quaternions. An excellent review of the quaternion algebra and the derivation of (4.11) can be found in [82, Appendix D].

Let $\boldsymbol{x}_k = [\boldsymbol{p}_k^\mathsf{T}, \boldsymbol{v}_k^\mathsf{T}, \boldsymbol{q}_k^\mathsf{T}]^\mathsf{T} \in \mathbb{R}^{10\times 1}$ denote the concatenated state vector consisting of the position, velocity, and quaternion estimates at sample time k. By discretizing of the continuous equations in (4.8), (4.9), and (4.11), and dropping the superscript n for notational convenience, the state vector $\boldsymbol{x}_k$ can be expressed as

$$\begin{bmatrix} \boldsymbol{p}_k \\ \boldsymbol{v}_k \\ \boldsymbol{q}_k \end{bmatrix} = \begin{bmatrix} \boldsymbol{p}_{k-1} + \boldsymbol{v}_{k-1} dt_k \\ \boldsymbol{v}_{k-1} + (\boldsymbol{q}_{k-1} \boldsymbol{s}_k^\mathrm{b} \boldsymbol{q}_{k-1}^{-1} - \boldsymbol{g}) dt_k \\ \boldsymbol{\Omega}(\boldsymbol{\omega}_k dt_k) \boldsymbol{q}_{k-1} \end{bmatrix} \tag{4.14}$$

where $\boldsymbol{q}_{k-1} \boldsymbol{s}_k^\mathrm{b} \boldsymbol{q}_{k-1}^{-1}$ is the quaternion equivalent of rotating a vector from one frame to another [82], $\boldsymbol{g} = [0, 0, g]^\mathsf{T}$, $g = 9.8\,\mathrm{m}\,/\,\mathrm{s}^2$, and dt_k is the sampling rate of the sensors.

Observations: We observe that the position and velocity estimates in (4.8) and (4.9) are correlated. Further, as shown in Fig. 4.2, computing the position estimates requires three integration blocks. Therefore, small errors in the measurement of angular velocities can result in cubic errors in the position estimates, because each integration block increases the exponent of the error by a factor of one. As a result, small errors accumulate, and the quality of the position, velocity, and orientation estimates deteriorates swiftly over time.

To mitigate the error growth in an inertial navigation system, several methods have been proposed. These include mitigating the error in the gyroscope measurements by employing high grade IMUs or complementing IMU devices with a global positioning system (GPS)

and odometer to correct the position and velocity estimates. However, there are trade offs involved in using high grade IMUs. For instance, the cost is very high and the size of the sensor also increases with the sensitivity, thereby diminishing its applicability in consumer electronic goods. In contrast, low-cost alternatives, such as the GPS are portable and can estimate the position to within a few centimeters accuracy; however, these estimates become unavailable in indoor environments, especially in the case of a pedestrian navigation system, which results degrades the position, velocity, and orientation estimates. To overcome these drawbacks, we exploit the fact that a foot-mounted IMU shows the foot goes to zero-velocity during ZVEI. In a GPS-aided INS, the INS uses the GPS updates along with the Kalman filter to correct the position updates. Similarly, in the ZV-INS, the INS uses ZVEI as pseudo measurements to correct the estimates of the velocity. Recall that during ZVEI, the velocity of the foot goes to zero, and thus the velocity component of the state vector becomes observable. As a result, the Kalman filter uses the ZVEI to correct the position and velocity estimates. Note that because both position and velocity are correlated, correcting the velocity estimates also corrects the position estimates.

Error Model Implementation of INS

In this subsection, we derive an error model to track the temporal dynamics of the inertial sensor errors. These errors arise due to the uncertainties in the sensors and the gravity field, which often cause the position, velocity, and orientation estimates to drift over time. Therefore, estimating the sensor errors prior to applying the navigation mechanization equations can improve the estimates of the navigation parameters. The error model for a strapdown

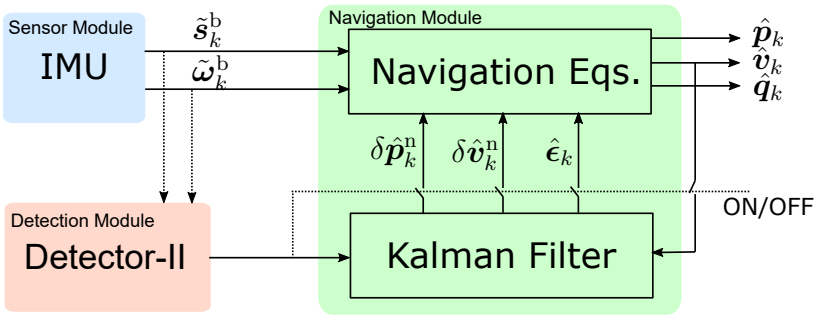

Figure 4.3: Complementary feed-forward implementation of the navigation equations, using the Kalman filter.

inertial navigation system is given as

$$\delta\dot{\boldsymbol{p}}^{\mathrm{n}} = \delta\boldsymbol{v}^{\mathrm{n}}, \tag{4.15}$$

$$\delta\dot{\boldsymbol{v}}^{\mathrm{n}} = \boldsymbol{R}_{\mathrm{b}}^{\mathrm{n}}\delta\boldsymbol{s}^{\mathrm{b}} - \boldsymbol{\Omega}_{\boldsymbol{s}^{\mathrm{n}}}\boldsymbol{\epsilon}, \tag{4.16}$$

$$\dot{\boldsymbol{\epsilon}} = \boldsymbol{R}_{\mathrm{b}}^{\mathrm{n}}\delta\boldsymbol{\omega}_{\mathrm{nb}}^{\mathrm{b}}, \tag{4.17}$$

where $\delta\boldsymbol{p}^{\mathrm{n}}$ and $\delta\boldsymbol{v}^{\mathrm{n}}$, respectively, are the errors in the position and velocity estimates; $\delta\boldsymbol{s}^{\mathrm{b}}$ and $\delta\boldsymbol{\omega}_{\mathrm{nb}}^{\mathrm{n}}$, respectively, are the accelerometer and gyroscope measurement errors in the body frame; and $\boldsymbol{\epsilon}$ denotes the misalignment errors in the orientation angles. The derivation of (4.15)–(4.17) is presented in Appendix C.2. Note that (4.17) is an affine function of $\delta\boldsymbol{\omega}_{\mathrm{nb}}^{\mathrm{b}}$. Thus, we can avoid using quaternion representation for the state-space model of the temporal dynamics of the inertial sensor errors. Because the derivation of (4.15)–(4.17) involves first-order approximations, we implement (4.15)–(4.17) using an extended Kalman filter (EKF). In navigation literature, error models implemented using Kalman filters are also referred to as "complementary feed-forward Kalman filters." Note that, in the case of an EKF implementation of the error models, the errors in the velocity become observable during ZVEI.

In Fig. 4.3, we provide a block digram implementation of the complementary feed-forward Kalman filter used in the navigation module. If $\delta\boldsymbol{x}_k = [\delta\boldsymbol{p}_k^{\mathsf{T}}, \delta\boldsymbol{v}_k^{\mathsf{T}}, \boldsymbol{\epsilon}_k^{\mathsf{T}}]^{\mathsf{T}} \in \mathbb{R}^{9\times 1}$ denotes the concatenation of the error estimates in position, velocity, and orientation at time sample k, then the continuous equations in (4.15)–(4.17), after discretization, can be written as

$$\begin{bmatrix} \delta\boldsymbol{p}_{k+1} \\ \delta\boldsymbol{v}_{k+1} \\ \boldsymbol{\epsilon}_{k+1} \end{bmatrix} = \begin{bmatrix} \boldsymbol{I}_3 & \boldsymbol{I}_3 dt_k & \boldsymbol{0}_3 \\ \boldsymbol{0}_3 & \boldsymbol{I}_3 & \boldsymbol{\Omega}_{\boldsymbol{s}_k^{\mathrm{n}}} dt_k \\ \boldsymbol{0}_3 & \boldsymbol{0}_3 & \boldsymbol{I}_3 \end{bmatrix} \begin{bmatrix} \delta\boldsymbol{p}_k \\ \delta\boldsymbol{v}_k \\ \boldsymbol{\epsilon}_k \end{bmatrix} + \begin{bmatrix} \boldsymbol{0}_3 & \boldsymbol{0}_3 \\ [\boldsymbol{R}_{\mathrm{b}}^{\mathrm{n}}]_k & \boldsymbol{0}_3 \\ \boldsymbol{0}_3 & [\boldsymbol{R}_{\mathrm{b}}^{\mathrm{n}}]_k \end{bmatrix} \begin{bmatrix} \delta\boldsymbol{s}_k^{\mathrm{b}} \\ \delta\boldsymbol{\omega}_k^{\mathrm{b}} \end{bmatrix}, \tag{4.18}$$

$$\delta\boldsymbol{x}_{k+1} = \boldsymbol{F}_k \delta\boldsymbol{x}_k + \boldsymbol{G}_k \delta\boldsymbol{w}_k, \tag{4.19}$$

where $[\boldsymbol{R}_{\mathrm{b}}^{\mathrm{n}}]_k$ is the rotation matrix at the k-th time instance, and

$$\boldsymbol{F}_k = \begin{bmatrix} \boldsymbol{I}_3 & \boldsymbol{I}_3 dt_k & \boldsymbol{0}_3 \\ \boldsymbol{0}_3 & \boldsymbol{I}_3 & \boldsymbol{\Omega}_{\boldsymbol{s}_k^{\mathrm{n}}} dt_k \\ \boldsymbol{0}_3 & \boldsymbol{0}_3 & \boldsymbol{I}_3 \end{bmatrix}, \quad \boldsymbol{G}_k = \begin{bmatrix} \boldsymbol{0}_3 & \boldsymbol{0}_3 \\ [\boldsymbol{R}_{\mathrm{b}}^{\mathrm{n}}]_k & \boldsymbol{0}_3 \\ \boldsymbol{0}_3 & [\boldsymbol{R}_{\mathrm{b}}^{\mathrm{n}}]_k \end{bmatrix}, \tag{4.20}$$

are the state matrices. Equation (4.19) represents the state model of the ZV-INS. The process noise $\delta\boldsymbol{w}_k \in \mathbb{R}^{6\times 1}$ is assumed to be distributed as a Gaussian random vector with a zero mean, and a covariance matrix defined as

$$\begin{aligned} \boldsymbol{Q} &= \mathbb{E}\left(\delta\boldsymbol{w}_k \delta\boldsymbol{w}_k^{\mathsf{T}}\right), \\ &= \begin{bmatrix} \tilde{\sigma}_{\mathrm{a}}^2 \boldsymbol{I}_3 & \boldsymbol{0}_3 \\ \boldsymbol{0}_3 & \tilde{\sigma}_{\omega}^2 \boldsymbol{I}_3 \end{bmatrix}, \end{aligned} \tag{4.21}$$

where $\tilde{\sigma}_{\mathrm{a}}^2$ and $\tilde{\sigma}_{\omega}^2$ are respectively the variances of the process noise of the accelerometer and gyroscope. If $\boldsymbol{P}_k$ denotes the 9-state error covariance matrix for the error model in (4.19),

then the error covariance matrix is updated as follows:

$$\boldsymbol{P}_k = \boldsymbol{F}_k \boldsymbol{P}_{k-1} \boldsymbol{F}_k^{\mathsf{T}} + \boldsymbol{G}_k \boldsymbol{Q} \boldsymbol{G}_k^{\mathsf{T}}. \tag{4.22}$$

Next, the error estimates of the state equation in (4.19) are corrected using the updates from the ZVEI. If $\boldsymbol{y}_k \in \mathbb{R}^{3\times 1}$ denotes the observed velocity error, and $\mathcal{I}_k(\cdot) \in \{0, 1\}$ is an indicator function, such that $\mathcal{I}_k(\cdot) = 1$ if k belongs to a zero-velocity event interval, and $\mathcal{I}_k(\cdot) = 0$ otherwise, then the observed velocity error can be written as

$$\begin{aligned} \boldsymbol{y}_k &= \mathcal{I}_k \left(\begin{bmatrix} \boldsymbol{0}_3 & \boldsymbol{I}_3 & \boldsymbol{0}_{3\times 4} \end{bmatrix} \boldsymbol{x}_k + \delta \boldsymbol{u}_k \right) \\ &= \mathcal{I}_k \left(\boldsymbol{H}_k \boldsymbol{x}_k + \delta \boldsymbol{u}_k \right), \end{aligned} \tag{4.23}$$

where $\boldsymbol{x}_k = [\boldsymbol{p}_k^{\mathsf{T}}, \boldsymbol{v}_k^{\mathsf{T}}, \boldsymbol{q}_k^{\mathsf{T}}]^{\mathsf{T}} \in \mathbb{R}^{10\times 1}$, and $\delta \boldsymbol{u}_k \in \mathbb{R}^{3\times 1}$ is the measurement noise. Equation (4.23) represents the measurement/observation model of the ZV-INS. The measurement noise is assumed to be distributed as a Gaussian random vector with a zero mean, and a covariance matrix defined as

$$\begin{aligned} \boldsymbol{R} &= \mathbb{E}\left(\delta \boldsymbol{u}_k \delta \boldsymbol{u}_k^{\mathsf{T}} \right), \\ &= \sigma_{\mathrm{v}}^2 \boldsymbol{I}_3, \end{aligned} \tag{4.24}$$

where σ_{v}^2 is the variance of the errors in velocity measurements. When the foot is stationary, the velocity component of the state vector $\boldsymbol{x}_k$ becomes observable, and therefore the error estimates $\delta \boldsymbol{x}_k$ are corrected using the Kalman filter. If $\boldsymbol{K}_k$ denotes the Kalman gain, then

$$\boldsymbol{K}_k = \boldsymbol{P}_k \boldsymbol{H}^{\mathsf{T}} (\boldsymbol{H} \boldsymbol{P}_k \boldsymbol{H}^{\mathsf{T}} + \boldsymbol{R})^{-1}. \tag{4.25}$$

The Kalman gain in (4.25) is used to update the error state vector $\delta \boldsymbol{x}_k$ and the error covariance matrix $\boldsymbol{P}_k$, using the following equations:

$$\delta \boldsymbol{x}_k = \boldsymbol{K}_k[\hat{\boldsymbol{x}}_k]_{4:6}, \tag{4.26}$$

$$\boldsymbol{P}_k = (\boldsymbol{I}_9 - \boldsymbol{K}_k \boldsymbol{H})\boldsymbol{P}_k. \tag{4.27}$$

Finally, the navigation parameters are corrected as follows:

$$\begin{bmatrix} \boldsymbol{p}_k \\ \boldsymbol{v}_k \\ \boldsymbol{\epsilon}_k \end{bmatrix} = \begin{bmatrix} \boldsymbol{p}_k \\ \boldsymbol{v}_k \\ \boldsymbol{0} \end{bmatrix} + \boldsymbol{K}_k \boldsymbol{v}_k, \quad \text{and} \tag{4.28}$$

$$\boldsymbol{q}_k = \boldsymbol{\Omega}(\boldsymbol{\epsilon}_k)\boldsymbol{q}_k. \tag{4.29}$$

The details of implementing the foot-mounted inertial navigation system via an extended Kalman filter are presented in Algorithm 1.

4.4 Numerical Results

In this section, with the help of an illustrative example, we extract gait parameters by using the ZV-INS discussed in the previous section. We use inertial sensor data from the TUG1 trial dataset for PID 08. In the TUG trial, the participant stands up, walks 3 meters from the chair, turns, walks back, and returns to a sitting position.

Algorithm 1 Zero-velocity Aided Foot-Mounted INS

procedure ZVEI_INS($\boldsymbol{s}^{\mathrm{b}}$, $\boldsymbol{\omega}^{\mathrm{b}}$, $\boldsymbol{zvei}$)
  initialize:
  MAX $\leftarrow$ len($\boldsymbol{zvei}$), $k \leftarrow 0$
  $\boldsymbol{P}_k$, $\boldsymbol{Q}$, $\boldsymbol{R}$, $\boldsymbol{H}$ $\leftarrow$ initialize filters ▷ From (4.19) and (4.23)
  $\boldsymbol{F}_k$, $\boldsymbol{G}_k$ $\leftarrow$ initialize state model ▷ From (4.19)
  $\hat{\boldsymbol{x}}_k \leftarrow$ initialize navigation equations ▷ From (4.19)
  repeat:
    $k \leftarrow k + 1$
    $\hat{\boldsymbol{x}}_k \leftarrow$ navigation equations ▷ From (4.14)
    $\boldsymbol{F}_k$, $\boldsymbol{G}_k \leftarrow$ update state matrices
    $\delta\boldsymbol{x}_k \leftarrow \boldsymbol{F}_k \delta\boldsymbol{x}_{k-1}$ ▷ From (4.19)
    $\boldsymbol{P}_k \leftarrow \boldsymbol{F}_k \boldsymbol{P}_{k-1} \boldsymbol{F}_k^{\mathsf{T}} + \boldsymbol{G}_k \boldsymbol{Q} \boldsymbol{G}_k^{\mathsf{T}}$ ▷ From (4.22)
    if $\boldsymbol{z}_k$ is ON **then** ▷ If zero-velocity event
      $\boldsymbol{K}_k \leftarrow \boldsymbol{P}_k \boldsymbol{H}^{\mathsf{T}} (\boldsymbol{H} \boldsymbol{P}_k \boldsymbol{H}^{\mathsf{T}} + \boldsymbol{R})^{-1}$ ▷ From (4.25)
      $\delta\boldsymbol{x}_k \leftarrow \boldsymbol{K}_k [\hat{\boldsymbol{x}}_k]_{4:6}$ ▷ From (4.26)
      $\boldsymbol{P}_k \leftarrow (\boldsymbol{I}_9 - \boldsymbol{K}_k \boldsymbol{H}) \boldsymbol{P}_k$ ▷ From (4.22)
      $\hat{\boldsymbol{x}}_k \leftarrow$ correct navigation states ▷ From (4.28) and (4.29)
    end if
  until $k =$ MAX
end procedure

4.4.1 Illustrative Example

In Fig. 4.4, we plot the sensor data obtained from a three-axis accelerometer and a three-axis gyroscope attached to the instep region of the foot of the participant. The sensor data is sampled at $F_{\mathrm{s}} = 128$ Hz.

In Fig. 4.5, we plot the orientation angles estimated using the ZV-INS. The roll and pitch angles are initialized using the accelerometer measurements, whereas the yaw angle is initialized to 0°. The initial heading direction is unknown because we do not use magnetometers. Because the TUG1 trial involves two turns, we note that the yaw angle in Fig. 4.5c starts at 0° and ends at approximately 360°.

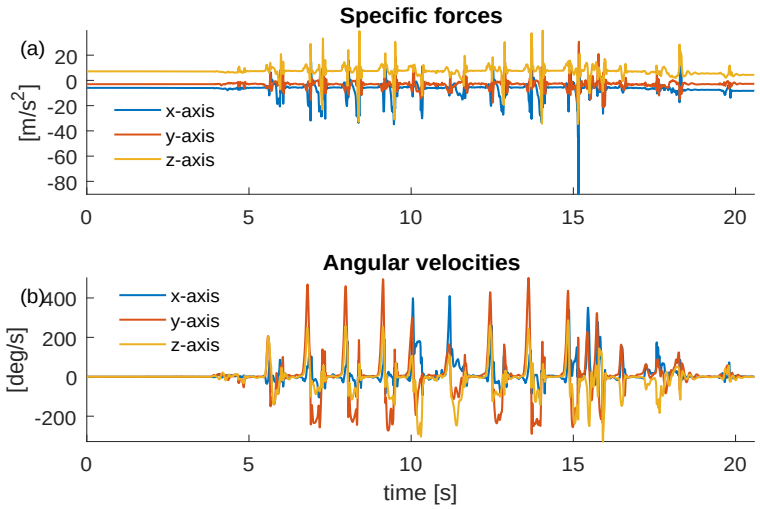

Figure 4.4: Inertial sensor data. (a) Three-axis accelerometer. (b) Three-axis gyroscope.

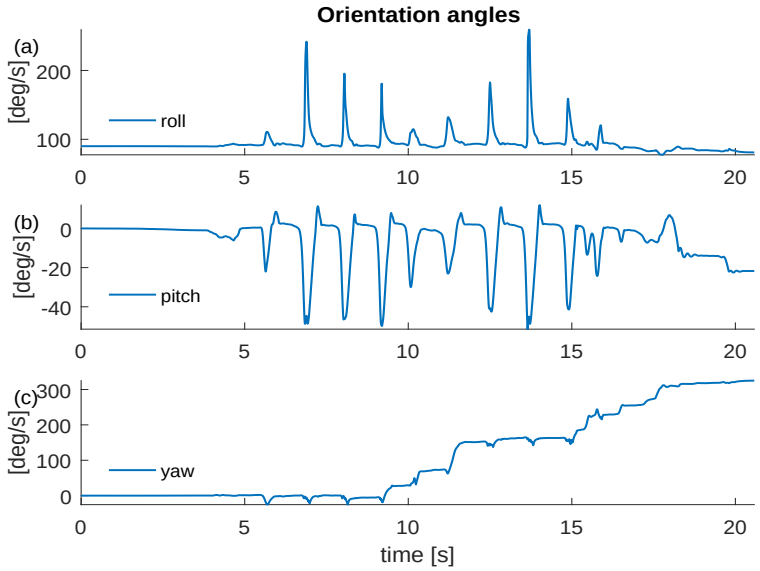

Figure 4.5: Left foot roll, pitch, and yaw angles obtained during the TUG trial for PID 08.

Fig. 4.6 shows the ZVEI, speed, and height of the left foot obtained using ZV-INS. The ZVEI are the outputs of Detector-II. Recall that during the ZVEI, the accelerometer measures the earth's gravitational acceleration and the angular velocities measured by the gyroscope are zero, because no rotational motion is observed. Next, we compute the speed of the foot by taking the ℓ_2-norm of the velocity vector. As can be seen in Fig. 4.6b, the speed of the

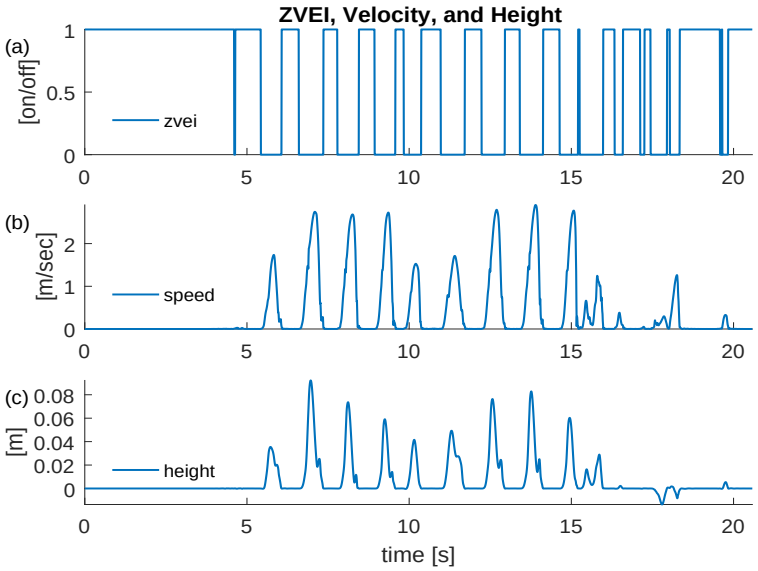

Figure 4.6: Zero-velocity event intervals, speed, and height (z-axis) of the left foot extracted using the zero-velocity aided INS for the TUG trail datasets.

foot goes to zero when the ZVEI in Fig. 4.6a is ON. We also plot the height of the foot or the z-axis component of the position vector. As can be seen in Fig. 4.6c, the height of the foot resets to zero at ZVEI because both the position and velocity are correlated in the navigation mechanization equations in (4.8) and (4.9).

In Fig. 4.7, we plot the trajectory of the left foot in the xy-plane for the TUG trial. Recall that in the TUG1 trial the participant stands up, walks 3 meters from the chair, turns, walks back, and returns to a sitting position. As can be seen in Fig. 4.7, the trajectory of the left foot makes a sharp 180° turn at the 3 meter mark on the y-axis. Further, we also notice that the trajectory tends to drift from the starting point, given that the initial heading direction was set to 0°. The drift in the trajectory occurs because the errors in the heading estimates are not observable, and therefore cannot be contained. To explain this of phenomenon heading drift, we need to look at the temporal dynamics of the diagonal elements of the error covariance matrix $\boldsymbol{P}_k$.

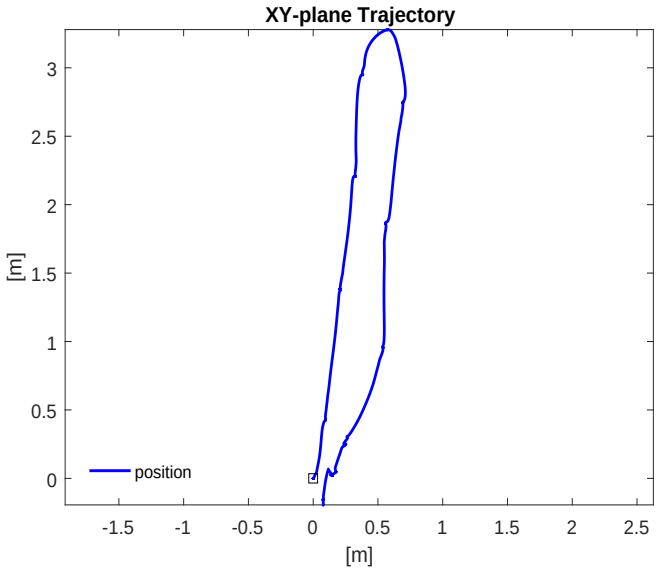

Figure 4.7: 2D trajectory plot of the TUG trial for the left foot inertial sensor data.

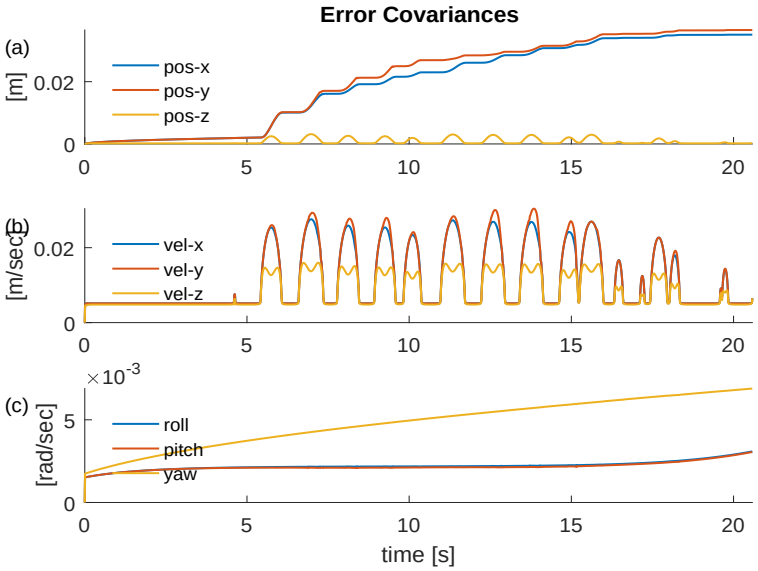

Figure 4.8: Error covariances of the position, velocity, and orientation estimates.

In Fig. 4.8, we plot the square root of the diagonal elements of the error covariance matrix of the navigation parameters. We make two important observations from the error covariance plots.

(1) The error covariances of the velocity vector are reset during ZVEI. Recall that during ZVEI, the velocity component of the error state in (4.16) becomes observable, and thus, the Kalman filter corrects the navigation estimates and its corresponding error covariances. Therefore, the error covariances of the velocity vector are always reset during the ZVEI.

(2) Both the error covariances of the yaw angle and the x and y components of the position vector, drift over time. The drift in the heading is primarily due to the poor observability of INS errors when ZVEI are the only measurements available to the Kalman filter. For simplicity, let us assume that the errors due to accelerometer measurement $\delta \boldsymbol{s}^{\mathrm{b}}$ are zero. Then, from (4.16), the error model for the velocity is given as

$$\delta \dot{\boldsymbol{v}}^{\mathrm{n}} = -\boldsymbol{\Omega}_{\boldsymbol{s}^{\mathrm{n}}} \boldsymbol{\epsilon}, \tag{4.30}$$

where $\boldsymbol{s}^{\mathrm{n}}$ are the specific forces measured by the accelerometer and the superscript n denotes the navigation frame. If we express the individual components of the velocity vector in the navigation frame in terms of the North (N), East (E), and Down (D) axes, then (4.30) can be written as

$$\begin{bmatrix} \delta \dot{\boldsymbol{v}}^{\mathrm{N}} \\ \delta \dot{\boldsymbol{v}}^{\mathrm{E}} \\ \delta \dot{\boldsymbol{v}}^{\mathrm{D}} \end{bmatrix} = - \begin{bmatrix} 0 & -s^{\mathrm{D}} & s^{\mathrm{E}} \\ s^{\mathrm{D}} & 0 & -s^{\mathrm{N}} \\ -s^{\mathrm{E}} & s^{\mathrm{N}} & 0 \end{bmatrix} \begin{bmatrix} \epsilon^{\mathrm{N}} \\ \epsilon^{\mathrm{E}} \\ \epsilon^{\mathrm{D}} \end{bmatrix}. \tag{4.31}$$

During ZVEI, the horizontal acceleration in the north and east axis are zero, and only gravitational acceleration in the down axis is observable and non-zero. Therefore, the orientation errors in the down axis are not observable because the horizontal accelerations along the north and east axes are zero. As a result, there exists no means to correct

the errors in the yaw angle, so they drift over time. Recall that any small measurement error in the orientation angle estimates can result in exponential error in the position estimates (see Fig. 4.2). Because the yaw angle errors drift, the position error also drifts. We observe this phenomenon in Fig. 4.8a and Fig. 4.8c.

Several techniques can mitigate the heading drift. These include employing high grade inertial measurement units, magnetometers, drift compensated inertial measurement units, or position updates from GPS. However, incorporating these techniques is beyond the scope of this work.

4.4.2 Data Analysis

We evaluate the performance of the ZV-INS by extracting gait parameters from Parkinson disease participants for the Opal APDM sensor database, given in Appendix A.2. We compare our results with the gait parameters extracted using Mobility labs software (MLBS), which is compatible with Opal APDM sensors. Note that the implementation details of the INS using the MLBS are unknown because the software is proprietary. We evaluate the performance of the INS algorithm for the two-minute walk task dataset described in Table A.2 of Appendix A.2. We extract the following gait parameters.

1) The *toe-off angle* of the foot is the angle of the foot as it leaves the floor at push-off. The pitch of the foot when flat is zero.

2) The *heel-strike angle* of the foot is the angle at the point of initial contact. The pitch of the foot is zero when the foot is flat, and positive when the heel makes first contact.

3) The *gait cycle* consists of exactly one heel-strike and one toe-off event, in that order, between two consecutive flat foot events.

4) *Swing* is defined as the percentage of the gait cycle during which the foot is not on the ground, i.e., it is the ratio of the time between the last heel-strike and toe-off events to the time of the corresponding gait cycle.

5) The *stride length* is the distance between two consecutive foot falls at the moments of initial contacts.

Note that the gait parameters are extracted only for valid gait cycles. To determine valid gait cycles, and identify the heel-strike and toe-off event of the gait cycles, for the ZV-INS, we use the gait cycle validation and segmentation algorithm described in Chapter 6. As can be seen in Table 4.1, the average values of the gait parameters estimated using the zero-velocity aided INS are within one standard deviation of the existing method's values.

Fig. 4.9 shows the boxplot of the average values of the foot speed and pitch angle, for valid gait cycles (VGC) detected using the validation module and FOG events in the inertial sensor data marked by a trained gait analysis expert for the tasks listed in Table A.2 of Appendix A.2. As can be seen, FOG events are associated with small foot speeds and low pitch angles caused by the alternating trembling motion.

4.5 Chapter Summary

We discussed implementing a zero-velocity aided inertial navigation system, we derived the navigation mechanization equations and their corresponding error models, and used the

Table 4.1: Gait parameters extracted using the MLBS and ZV-INS.

PID #	Toe-off Angle		Heel-Strike Angle		Swing as %GCT		Stride Length	
	MLBS	ZV-INS	MLBS	ZV-INS	MLBS	ZV-INS	MLBS	ZV-INS
01	$39° \pm 1.0°$	$37.1° \pm 4.4°$	$-25° \pm 1.2°$	$-20.9° \pm 2.4°$	$42\% \pm 0.5\%$	$40.3\% \pm 11.7\%$	1.30 ± 0.02	1.24 ± 0.29
02	$18° \pm 1.2°$	$18.7° \pm 2.4°$	$-9° \pm 1.0°$	$-9.9° \pm 1.5°$	$32\% \pm 1.0\%$	$31.1\% \pm 6.2\%$	0.69 ± 0.04	0.68 ± 0.14
03	$36° \pm 0.8°$	$33.3° \pm 3.9°$	$-14° \pm 1.7°$	$-12.7° \pm 2.1°$	$39\% \pm 1.1\%$	$38.4\% \pm 10.0\%$	1.20 ± 0.03	1.13 ± 0.29
05	$38° \pm 0.8°$	$34.6° \pm 4.9°$	$-23° \pm 1.3°$	$-20.6° \pm 2.1°$	$39\% \pm 0.7\%$	$39.5\% \pm 10.0\%$	1.20 ± 0.03	1.22 ± 0.20
08	$32° \pm 1.5°$	$27.5° \pm 5.5°$	$-16° \pm 2.6°$	$-16.6° \pm 1.9°$	$36\% \pm 1.1\%$	$36.4\% \pm 8.1\%$	1.00 ± 0.03	0.83 ± 0.37
09	$40° \pm 1.9°$	$38.4° \pm 9.9°$	$-23° \pm 2.4°$	$-18.4° \pm 4.2°$	$40\% \pm 1.3\%$	$36.9\% \pm 11.3\%$	1.40 ± 0.08	1.15 ± 0.50
10	$35° \pm 1.1°$	$30.7° \pm 4.8°$	$-14° \pm 3.0°$	$-16.9° \pm 2.2°$	$40\% \pm 1.3\%$	$37.9\% \pm 10.9\%$	1.20 ± 0.05	1.15 ± 0.50

MLBS: Mobility labs software; ZV-INS: Zero-velocity inertial navigation system.

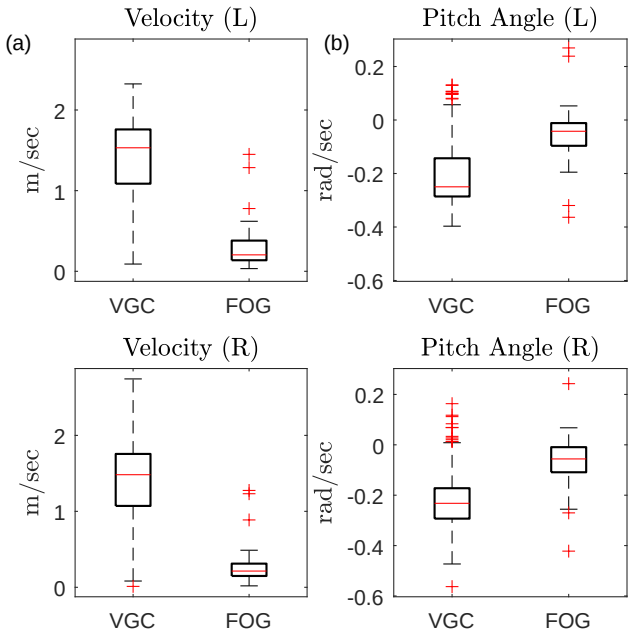

Figure 4.9: Boxplots of average values of the gait parameters during valid gait cycles (VGC) and freezing of gait (FOG) events.

Kalman filter to estimate the position, velocity, and orientation angles. We validated our implementation by comparing the gait parameters extracted using the ZV-INS with an existing proprietary software compatible with the APDM Opal sensors. We also demonstrated that FOG events are associated with small foot speeds and low pitch angles. In the next chapter, we will develop an estimation filter that combines the trembling event intervals with the gait parameters associated with FOG, and computes probability of FOG.

Chapter 5

Filtering Module: Trembling Event aided Point-Process Filter

In this chapter, to detect the onset and duration of freezing of gait (FOG), we develop a point-process filter, which computes the probability of FOG (pFOG). We model the edges of the trembling event intervals (TREI) as a point-process, assign weights to the edges, which depend on the average value of the speed of the foot at the edge and a participant-specific tunable parameter. The participant-specific tunable parameter determines the weight, which is inversely proportional to the average value of the speed of the foot. Then, we integrate these weights over a time window, using a Bayesian recursive filter. We adjust the participant-specific tunable parameter manually for every participant based on their gait patterns. We validate the performance of the proposed system design using real data obtained from people with Parkinson disease who performed a set of gait tasks. We compare our FOG detection results with an existing method that only uses accelerometer data. The results indicate that our method yields 81.03% accuracy in detecting FOG events, and a three-fold decrease in the false-alarm rate relative to the existing method.

5.1 Introduction

A temporal point-process is a stochastic set of localized process composed of events or instances that occur in continuous time. Because these processes are localized at a finite set of time points, they are widely employed in several disciplines including economics, computational neuroscience, seismology, astronomy, and others [83]. For example, point-processes are commonly used as models for random events in time, such as the arrival rate of customers in a queue (queuing theory) [84], impulses generated by a neuron (computational neuroscience) [85–87], particles in a Geiger counter (measuring ionizing radiation) [88], characterize the timing and regularity of heart beats [89], and searchers on the world-wide web (data analytics) [90]. For each of these processes, there is an underlying continuous process that is evolving in time and the associated point-process occurs when the time-series representing the continuous process is above or below certain fixed threshold.

Point-processes are characterized into different classes based on the probability of firing an event in a small time interval. The simplest form of a point-process is the *Poisson process*. In this process, the probability of firing an event is independent of the firing activity of the past spiking activity. In addition, if the probability of firing an event is independent of time, then the process is called *homogeneous Poisson process*. For any time interval in a homogeneous Poisson process, the point-process increment follows a Poisson distribution and the increments from non-overlapping intervals are independent [83]. Note that the homogeneous Poisson process demonstrates a stationary distribution of a Markov chain. However, in many practical scenarios, the point-process is non-stationary, i.e., the firing activity changes with time. For example, if we were to count the number of cars crossing an intersection near a workplace, then rate of crossing the intersection increases during peak office hours. In other words, the firing rate function that defines the probability of observing

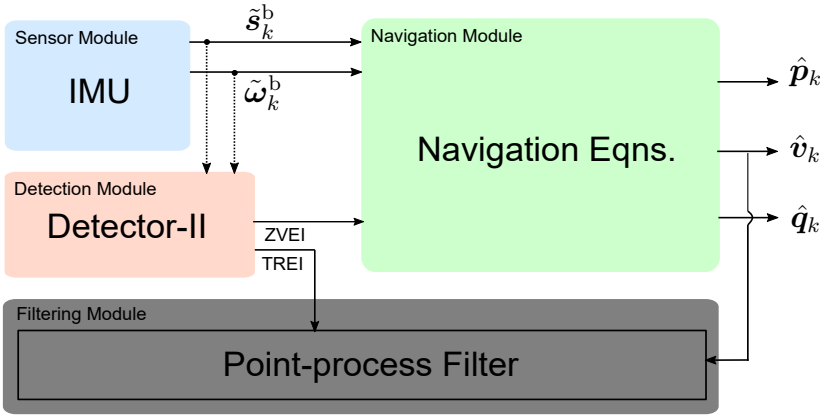

Figure 5.1: System design.

an event is dependent on time. We call such processes as *inhomogeneous Poisson process*. Both homogeneous and inhomogeneous Poisson processes are independent of the past events. Several systems that produce point-processes are not only dependent on time but also on past data. To characterize the probability of firing an event that depends on historical data, we use the *conditional intensity function*, and the resulting point-process is called as a *doubly stochastic point-process* [91].

In this work, develop a system design to detect and track freezing of gait (FOG) as shown in Fig. 5.1. Recall that the goal of Detector-II is to distinguish zero-velocity event intervals (ZVEI) from trembling event intervals (TREI). We model the edges of the TREI as a doubly stochastic point-process. We assign weights to the edges, which depend on the average value of the speed of the foot at the edge and a participant-specific tunable parameter. The participant-specific tunable parameter determines the weight, which is inversely proportional to the average value of the speed of the foot. Then, we characterize the weights and the edges of the trembling event intervals, using a conditional intensity function. To compute the probability of freezing of gait (pFOG), we integrate these weights over a time window using a Bayesian recursive filter. To maximize the number of freezing of gait events detected,

we adjust the participant-specific tunable parameter manually for every participant based on the gait patterns.

Section 5.2 describes the background required for developing the point-process. Section 5.3 develops the TREI-aided point-process filter for computing pFOG. Section 5.4 provides an example to demonstrate the output of the each module in Fig. 5.1, using real data from Parkinson disease participants. Section 5.5 presents the experimental results.

5.2 Preliminaries

5.2.1 Conditional Intensity Function

Given an observation $(0, T]$, let $N(t)$ be a counting process which is the total number of events in $(0, t]$, for $t \in (0, T]$. We define *conditional intensity function* for $t \in (0, T]$ as

$$\lambda(t|H(t)) = \lim_{\Delta t \to 0} \frac{P(N(t+\Delta) - N(t) = 1|H(t))}{\Delta t} \tag{5.1}$$

where $P(\cdot)$ is a conditional probability, and $H(t)$ is the history of the sample path and of any covariates up to time t [92]. Conditional intensity function is also referred as *stochastic intensity* or *hazard function*. It follows that the conditional intensity function $\lambda(t|H(t))$ can also be defined in terms of the inter-event probability density at time t, denoted by $P(t|H(t))$, as

$$\lambda(t|H(t)) = \frac{P(t|H(t))}{1 - \int_0^t P(u|H(t))du}. \tag{5.2}$$

The probability of an event in $[t, t+\Delta)$ given $H(t)$ and no other event is observed in $(0, t)$ is given as:

$$\begin{aligned} P(u \in [t, t+\Delta) | u > t, H(t)) &= \frac{P(u \in [t, t+\Delta) \cap u > t | H(t))}{P(u > t | H(t))} \\ &= \frac{\int_t^{t+\Delta} P(u|H(u))du}{1 - \int_0^t P(u|H(u))du} = \frac{P(t|H(t))\Delta}{1 - \int_0^t P(u|H(t))du} + o(\Delta) \\ &= \lambda(t|H(t))\Delta + o(\Delta) \end{aligned} \tag{5.3}$$

where Δ is a small bin measured in seconds or samples and $o(\Delta)$ refers to all events smaller than Δ, such as observing two or more events in the interval Δ [92]. The intuitive explanation of (5.3) is that the conditional intensity function characterizes the stochastic structure of the event train. In other words, $\lambda(t|H(t))\Delta$ defines the probability of an event given the history up to time t. In the next Section, we model the edges of the TREI as a point-process and define a suitable conditional intensity function to compute the probability of FOG.

5.3 Point-Process Filter

In this section, we describe the filtering module in the system design in Fig. 5.1. We develop a point-process which is characterized by the conditional intensity function [93], whose parameters are modeled as a Gaussian autoregressive model [87,94–96]. By combining the information about the speed of the foot with the detected TREI via a conditional intensity function, we compute the probability of FOG (pFOG).

Recall that Detector-I identifies the zero-velocity and trembling events, and Detector-II only separates zero-velocity events from trembling events. The edges of the TREI also contain information of either the beginning or ending of ZVEI, which represents FOG patterns, characterized by small foot speeds. Therefore, we detect the edges of the TREI and model them as spikes generated from a point-process. The spikes are divided into equal segments or bins of length $B = \Delta F_{\mathrm{s}}$ samples, where Δ is the width of the bin interval in seconds and F_{s} is the sampling rate of the IMU. Let δB_k and b_k denote an indicator variable[2] and the number of spikes in the interval $((k-1)\Delta, k\Delta], k \in \mathbb{N}$, respectively. Further, let w_k denote a weight associated with each bin interval. FOG patterns such as trembling and short shuffling steps are characterized by small foot speeds [78]. To identify bins with small foot speeds, we first compute the average bin speed for the bin intervals $((k-1)\Delta, k\Delta]$. Then, we use a Gaussian kernel with zero mean and σ_{s} standard deviation to assign larger weights to bins with smaller average foot speeds. In our proposed method, the system parameter σ_{s} is considered as a participant-specific tunable parameter. As σ_{s} decreases, the bin weights corresponding to smaller foot speeds increase.

Let $\delta\boldsymbol{B}_{1:k} = [\delta B_1, \cdots, \delta B_k]$, $\boldsymbol{b}_{1:k} = [b_1, \cdots, b_k]$, and $\boldsymbol{w}_{1:k} = [w_1, \cdots, w_k]$ denote the activity of observable parameters up to time $k\Delta$. Let $\boldsymbol{H}_k = [\delta\boldsymbol{B}_{k-\ell-1:k-1}, \boldsymbol{b}_{k-\ell-1:k-1}, \boldsymbol{w}_{k-\ell-1:k-1}]$ denote the history of the activity of the spikes observed in the interval $((k-\ell-1)\Delta, (k-1)\Delta]$, where ℓ represents length of the history. Let $\boldsymbol{\theta}_k = [\theta_{k,0}, \cdots, \theta_{k,\ell-1}]^{\mathsf{T}} \in \mathbb{R}^{\ell}$ denote a latent parameter vector. We model the number of spikes observed in the k-th interval as a binomial distribution with probability mass function given by

$$f(b_k|\boldsymbol{\theta}_k, \boldsymbol{H}_k) = \binom{B}{n_k} p_k^{b_k} (1-p_k)^{(B-b_k)}, \tag{5.4}$$

[2] $\delta B_k = 1$, if $b_k \neq 0$ and $\delta B_k = 0$, if $b_k = 0$.

where

$$p_k = \frac{\exp\left(\lambda_k(\boldsymbol{\theta}_k, \boldsymbol{H}_k)\right)}{1 + \exp\left(\lambda_k(\boldsymbol{\theta}_k, \boldsymbol{H}_k)\right)} \quad \text{and} \tag{5.5}$$

$$\lambda_k(\boldsymbol{\theta}_k, \boldsymbol{H}_k) = \alpha + \beta \left(\sum_{i=0}^{\ell-1} \theta_{k,i}^2 w_{k-i} \delta B_{k-i} \right) = \alpha + \beta(\boldsymbol{\theta}_k^{\mathsf{T}} \boldsymbol{W}_k \boldsymbol{\theta}_k), \tag{5.6}$$

and $\boldsymbol{W}_k = \text{diag}\{w_k \delta B_k, \ldots, w_{k-\ell+1} \delta B_{k-\ell+1}\} \in \mathbb{R}^{\ell \times \ell}$. In (5.5), p_k is a sigmoid function that represents instantaneous pFOG in the interval $((k-1)\Delta, k\Delta]$, α denotes a fixed background firing rate, and β is a fixed scaling parameter. The exponential term is defined as the conditional intensity function [93] and the log-exponential is denoted as $\lambda_k(\boldsymbol{\theta}_k, \boldsymbol{H}_k)$. In (5.6), we model the history of spikes as an auto-regressive process where $\theta_{k,i}$ represents the auto-regressive coefficients. The parameters that define the conditional intensity function in (5.6) are either fixed or observable, except for $\boldsymbol{\theta}_k$ (a latent parameter vector), which is modeled as a linear evolution process with Gaussian errors [87, 94–97]. We define the evolution process of the latent parameter as

$$\boldsymbol{\theta}_{k+1} = \boldsymbol{A}_k \boldsymbol{\theta}_k + \boldsymbol{n}_k, \tag{5.7}$$

where $\boldsymbol{A}_k$ is the system evolution matrix and $\boldsymbol{n}_k$ is zero-mean additive Gaussian noise with covariance $\boldsymbol{N}_k$. The probability of freezing of gait (pFOG) is given as

$$p'_k = \frac{1}{l} \sum_{i=0}^{l-1} p_{k-i}. \tag{5.8}$$

Applying Bayes' rule to (5.4) and (5.7), the posterior density of the parameter vector in the k-th interval is given as

$$f(\boldsymbol{\theta}_k|b_k, \boldsymbol{H}_k) = \frac{f(b_k|\boldsymbol{\theta}_k, \boldsymbol{H}_k)f(\boldsymbol{\theta}_k|\boldsymbol{H}_k)}{f(b_k|\boldsymbol{H}_k)}, \tag{5.9}$$

where

$$\begin{aligned} f(\boldsymbol{\theta}_k|\boldsymbol{H}_k) &= \int f(\boldsymbol{\theta}_k|\boldsymbol{\theta}_{k-1}, \boldsymbol{H}_k)f(\boldsymbol{\theta}_{k-1}|b_{k-1}, \boldsymbol{H}_{k-1})d\boldsymbol{\theta}_{k-1} \\ &= \int f(\boldsymbol{\theta}_k|\boldsymbol{\theta}_{k-1})f(\boldsymbol{\theta}_{k-1}|b_{k-1}, \boldsymbol{H}_{k-1})d\boldsymbol{\theta}_{k-1}. \end{aligned} \tag{5.10}$$

The last equality comes from (5.7), where $\boldsymbol{\theta}_k$ does not depend on the aggregate history of the spikes, $\boldsymbol{H}_k$. Based on (5.7), we assume that the latent parameter vector, $\boldsymbol{\theta}_k$, follows a Gaussian distribution. There is no closed form expression for the Bayesian recursive filter in (5.9) and (5.10). Therefore, we develop the approximate filters based on the Gaussian approximations. The Gaussian approximation of the posterior density of the latent parameter vector in (5.7) can be motivated by the fact that the Binomial distribution in (5.4) converges towards a Gaussian distribution as the number of samples in each bin, B, increase. Let $\boldsymbol{\theta}_{k|k-1} = \mathbb{E}[\boldsymbol{\theta}_k|\boldsymbol{H}_k]$ and $\boldsymbol{J}_{k|k-1} = \mathrm{Cov}[\boldsymbol{\theta}_k|\boldsymbol{H}_k]$ denote the mean and the covariance of one-step prediction density. Similarly, let $\boldsymbol{\theta}_{k|k} = \mathbb{E}[\boldsymbol{\theta}_k|b_k, \boldsymbol{H}_k]$ and $\boldsymbol{J}_{k|k} = \mathrm{Cov}[\boldsymbol{\theta}_k|b_k, \boldsymbol{H}_k]$ denote the mean and the covariance of the posterior distribution. Then, using the Laplace

Gaussian filter approximation method [96,97], the point-process filter equations are given as

$$\boldsymbol{\theta}_{k|k-1} = \boldsymbol{F}_k \boldsymbol{\theta}_{k-1|k-1}, \tag{5.11a}$$

$$\boldsymbol{P}_{k|k-1} = \boldsymbol{F}_k \boldsymbol{J}_{k-1|k-1} \boldsymbol{F}_k^{\mathsf{T}} + \boldsymbol{N}_k, \tag{5.11b}$$

$$\boldsymbol{\theta}_{k|k} = \boldsymbol{\theta}_{k|k-1} + \boldsymbol{J}_{k|k} \left[(b_k - Bp_k) \lambda_k'(\boldsymbol{\theta}_k, \boldsymbol{H}_k) \right]_{\boldsymbol{\theta}_{k|k-1}}, \tag{5.11c}$$

$$(\boldsymbol{J}_{k|k})^{-1} = \boldsymbol{J}_{k|k-1}^{-1} + \left[(Bp_k - b_k) \lambda_k''(\boldsymbol{\theta}_k, \boldsymbol{H}_k) + Bp_k(1-p_k) \lambda_k'(\boldsymbol{\theta}_k, \boldsymbol{H}_k) (\lambda_k'(\boldsymbol{\theta}_k, \boldsymbol{H}_k))^{\mathsf{T}} \right]_{\boldsymbol{\theta}_{k|k-1}}, . \tag{5.11d}$$

where the first derivative and second derivative of $\lambda_k(\boldsymbol{\theta}_k, \boldsymbol{H}_k)$, denoted as $\lambda_k'(\boldsymbol{\theta}_k, \boldsymbol{H}_k)$ and $\lambda_k''(\boldsymbol{\theta}_k, \boldsymbol{H}_k)$, are given as $2\beta \boldsymbol{W}_k \boldsymbol{\theta}_k$ and $2\beta \boldsymbol{W}_k$, respectively. We provide the details of the derivation of (5.11a)-(5.11d) in Appendix D.1 of the supplementary material. Equations (5.11a) and (5.11b) are the mean and covariance of a one-step prediction distribution. Similarly, equations (5.11c) and (5.11d) are the mean and covariance of the posterior distribution, respectively. The second term in (5.11c) is the learning rate, analogous to the the posterior update step of a Kalman filter. The term $(b_k/B - p_k)$ in (5.11c) is the innovation term, because b_k/B represents the probability of spikes in the measurement model and p_k is the probability of spikes in the state model, observed in the k-th time interval. However, unlike the Kalman filter posterior update step, here the posterior update step depends on the posterior update covariance matrix instead of the prediction covariance matrix. We compute p_k in (5.5), evaluated at $\boldsymbol{\theta}_k = \boldsymbol{\theta}_{k|k}$ at every time instance $k\Delta$, to obtain the instantaneous pFOG. The details of implementing the pFOG algorithm are listed in Algorithm 2.

Algorithm 2 TREI Aided Point-Process Filter

procedure pFOG($\boldsymbol{v}$, $\boldsymbol{t}$, σ_{s})
  initialize:
  $k \leftarrow 0$, $\Delta \leftarrow \lceil f_s/8 \rceil$, $\ell \leftarrow$ length of history process
  $\boldsymbol{\theta}_{0|0}, \boldsymbol{J}_{0|0} \leftarrow$ initialize point-process filter
  MAX $\leftarrow \lceil \mathrm{len}(\boldsymbol{t})/\Delta \rceil$,
  repeat:
    $k \leftarrow k + 1$
    $\boldsymbol{b}_{k-\ell-1:k-1}, \Delta\boldsymbol{B}_{k-\ell-1:k-1} \leftarrow$ generate point-process($\boldsymbol{t}$)
    $\boldsymbol{W}_k \leftarrow$ generates weights($\boldsymbol{v}, \sigma_{\mathrm{s}}$)
    $\boldsymbol{\theta}_{k|k-1} \leftarrow \boldsymbol{A}_k \boldsymbol{\theta}_{k-1|k-1}$ ▷ From (5.11a)
    $\boldsymbol{J}_{k|k-1} \leftarrow \boldsymbol{A}_k \boldsymbol{J}_{k-1|k-1} \boldsymbol{A}_k^T + \boldsymbol{N}_k$ ▷ From (5.11b)
    $p_k \leftarrow 1/(1 + \exp(-\lambda_k(\boldsymbol{\theta}_k, \boldsymbol{H}_k)))$ ▷ From (5.5)
    $\boldsymbol{\theta}_{k|k} \leftarrow \boldsymbol{\theta}_{k|k-1} + \boldsymbol{J}_{k|k} \left[(b_k - Bp_k)\lambda'_k(\boldsymbol{\theta}_k, \boldsymbol{H}_k)\right]_{\boldsymbol{\theta}_{k|k-1}}$ ▷ From (5.11d)
    $\boldsymbol{J}_{k|k}^{-1} \leftarrow \boldsymbol{J}_{k|k-1}^{-1} + \left[(Bp_k - b_k)\lambda''_k(\boldsymbol{\theta}_k, \boldsymbol{H}_k) + Bp_k(1-p_k)\lambda'_k(\boldsymbol{\theta}_k, \boldsymbol{H}_k)(\lambda'_k(\boldsymbol{\theta}_k, \boldsymbol{H}_k))^{\mathsf{T}}\right]_{\boldsymbol{\theta}_{k|k-1}}$ ▷ From (5.11c)
    $p'_k = (1/l)\sum_{i=0}^{\ell-1} p_{k-i}$ ▷ From (5.8)
  until $k =$ MAX
end procedure

5.4 Illustrative Example

In this section, with the help of an illustrative example, we demonstrate the output of each module of the proposed system design in Fig. 5.1. In particular, we use the inertial sensor data for participant identity (PID) TT004, performing the BLOCK task, during which the participant experiences a turning freeze.

5.4.1 Detector-II and INS

As stated previously in Chapter 3, the goal of Detector-II is to distinguish ZVEI from TREI based on the output of Detector-I. We use the same window length Ω_N as in Detector-I. In addition, we set the standard deviation of the gyroscope $\sigma_\omega = 0.8$ and the threshold

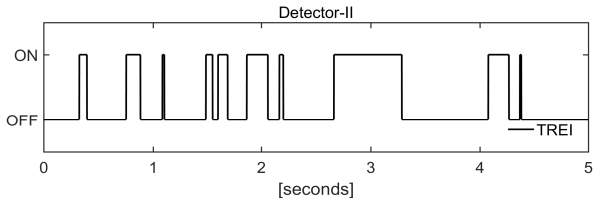

(a) Output of Detector-II (TREI)

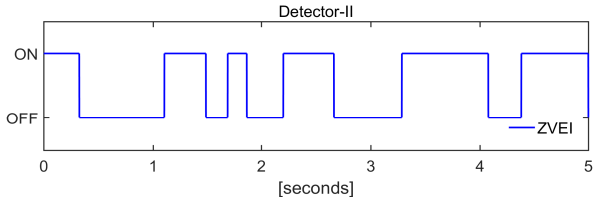

(b) Output of Detector-II (ZVEI)

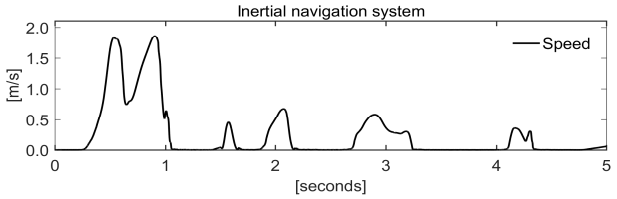

(c) Output of the INS (speed of the foot)

Figure 5.2: Detector-II separates ZVEI from TREI.

$\gamma'_{D_2} = 2.00$. The output of Detector-II, based on the test statistic in (3.7), is shown in Fig. 5.2a and Fig. 5.2b. In Fig. 5.2b, Detector-II detects ZVEI which can be verified with the information about the speed of the foot shown in Fig. 5.2c. When zero-velocity updates are ON, the speed of the foot is close to zero. The time intervals that are not identified as ZVEI by Detector-II are considered as TREI, as shown in Fig. 5.2a. However, not all the TREI are associated with FOG. Hence, to filter out falsely detected TREI that are not associated with FOG, we use the proposed point-process filter.

Table 5.1: Point-process filter parameters.

Parameters of the point-process filter	**Assigned value**
Width of each bin, Δ	0.1 seconds
Length of each bin, ΔF_{s}	100 samples
Length of the history of spikes, ℓ	10
Background firing rate, α	-15
Fixed scaling parameter, β	35
State transition matrix, $\boldsymbol{A}_k$	$\boldsymbol{I}_\ell$
Process noise covariance matrix, $\boldsymbol{N}_k$	$10^{-14}\boldsymbol{I}_\ell$
Initial state of the parameter vector, $\boldsymbol{\theta}_{0\vert 0}$	$0.351\!\!1_\ell$
Initial covariance matrix, $\boldsymbol{P}_{0\vert 0}$	$10^2\boldsymbol{N}_k$
Participant-specific tunable parameter, σ_{s}	0.4

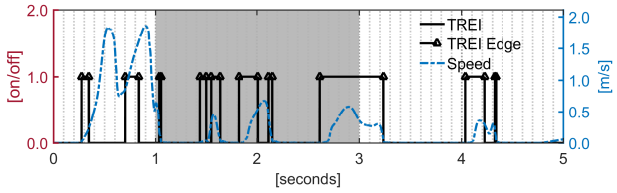

(a) Spikes with an overlay of foot speed

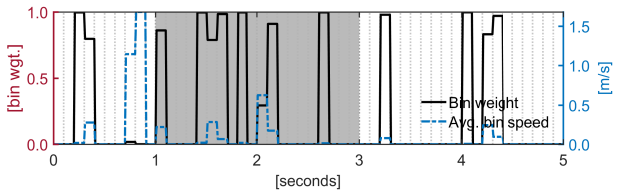

(b) Bin weights with $\Delta = 0.1$ seconds and $\sigma_{\mathrm{s}} = 0.4$

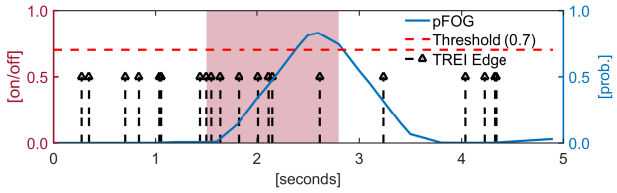

(c) pFOG output of the point-process filter

Figure 5.3: Detection of FOG using the point-process filter.

5.4.2 Point-Process Filter

Recall that the goal of the point-process filter is to filter out the falsely detected FOG events in the TREI. The edges in the TREI contain information about both ZVEI and TREI which represents FOG patterns characterized by small foot speeds. In Fig. 5.3a, we model the edges of TREI as spikes and overlay the speed of the foot obtained from the inertial navigation system. In Table 5.1, we list the values assigned to the parameters of the point-process filter. The participant-specific tunable parameter σ_s assigns a unit weight to bin interval with average bin speed zero, as shown in Fig. 5.3b. In Fig. 5.3c, the region consisting of high density of spikes with small foot speeds corresponds to an increase in the pFOG curve with some delay. We set the pFOG threshold as 0.7. When the pFOG is greater than 0.7, we determine the local minimum of the pFOG curve and denote it as the onset time of FOG. The duration of freezing is determined by subtracting the instant when the pFOG curve goes below 0.7 from the onset time, as indicated with red background in Fig. 5.3c. Further, on computing the onset and duration of FOG event, we notice a significant overlap between the FOG region detected by processing the IMU data using our proposed system design (represented with red background) and the video data in the reference system (represented with gray background). The mismatch between the FOG region detected using the video and the inertial sensor data in Fig. 5.3c is also attributed to the difference in the temporal resolution of the two systems under consideration.

5.5 Experimental Evaluation

In this section, we analyze the performance of the system design in Fig. 5.1, using real data from 16 people with Parkinson disease, given in Appendix A.1. We also compare our

results with an existing method that determines FOG events based on the FI method [66], computed using the vertical axis measurements of the accelerometer data. To calculate the FI [66], we downsample the accelerometer data by a factor of 10 and compute the ratio of the square of the area of the power spectrum in the 'freeze-band' and 'loco-band', using a moving window of 6 seconds. The FI is normalized by multiplying by 100 and taking the natural logarithm.

Out of the sixteen participants, only eight (PID TT003, TT004, TT005, TT007, TT013, TT017, TT021, and TT027) demonstrated FOG. In total, 58 events of FOG were detected using the video data, of which 38 events were categorized as turning freeze, 12 events as initiation or gait freeze, and 8 events as festinating gait with freezing. For each participant, we first identified the task with the greatest number of FOG events to determine the tunable parameters, i.e., the FI-threshold and kernel parameter σ_s. The FI-threshold and kernel parameter were tuned such that the number of FOG events detected was maximized for the identified task. In the proposed method, the system parameters such as detector thresholds, size of the window, standard deviation of the accelerometer and gyroscope, and point-process filter variables remain fixed for all participants across all tasks. Only the participant-specific tunable parameter is adjusted for every participant and remains fixed across all tasks. For participants who demonstrated FOG in the video-based reference system, the individual FI-threshold ranged from 4.5 to 10.0 (mean=6.56 and s.d.=1.67), and the kernel parameter σ_s ranged from 0.24 to 0.4 (mean=0.30 and s.d.=0.06). We present a detailed analysis of our proposed approach for PID TT027 in Appendix D.2. In Tables 5.2 and 5.3, we summarize the number of FOG events detected using FI and our method, respectively. For simplicity, we call our method the pFOG method. Overall, the pFOG method obtained an accuracy of 81.03%, i.e., 47/58 FOG events were detected using a tuned participant-specific kernel parameter (see Table 5.2). Further, when compared with the FI method, our method shows

Table 5.2: Number of FOG events detected for different participants across the gait tasks.

PID	**PARAMETER**		**BACK**		**BLOCK**		**EIGHT**		**NARROW**		**TURN**		**TOTAL**	
	FI	pFOG	FI	pFOG	FI	pFOG	FI	pFOG	FI	pFOG	FI	pFOG	FI	pFOG
TT003	7.0	0.40	(0/0)	(0/0)	(0/1)	(0/1)	(0/0)	(0/0)	(0/0)	(0/0)	(0/0)	(0/0)	(0/1)	(0/1)
TT004	4.5	0.24	(0/2)	(2/2)	(5/6)	(5/6)	(0/0)	(0/0)	(0/0)	(0/0)	(0/0)	(0/0)	(5/8)	(7/8)
TT005	7.0	0.35	(0/1)	(1/1)	(0/0)	(0/0)	(0/0)	(0/0)	(0/1)	(1/1)	(0/0)	(0/0)	(0/2)	(2/2)
TT007	10.0	0.24	(5/8)	(6/8)	(0/0)	(0/0)	(0/1)	(1/1)	(0/1)	(0/1)	(0/0)	(0/0)	(5/10)	(7/10)
TT013	6.0	0.25	(0/0)	(0/0)	(1/3)	(2/3)	(0/0)	(0/0)	(2/2)	(1/2)	(0/0)	(0/0)	(3/5)	(3/5)
TT017	7.0	0.40	(0/0)	(0/0)	(1/1)	(0/1)	(0/0)	(0/0)	(0/0)	(0/0)	(0/0)	(0/0)	(1/1)	(0/1)
TT021	5.0	0.30	(1/1)	(1/1)	(3/3)	(3/3)	(1/2)	(1/2)	(0/0)	(0/0)	(1/1)	(1/1)	(6/7)	(6/7)
TT027	6.0	0.29	(3/3)	(3/3)	(7/8)	(7/8)	(4/4)	(3/4)	(2/3)	(3/3)	(5/6)	(6/6)	(21/24)	(22/24)
TOTAL	6.56	0.30	(9/15)	(13/15)	(17/22)	(17/22)	(5/7)	(5/7)	(4/7)	(5/7)	(6/7)	(7/7)	(41/58)	**(47/58)**

Table 5.3: Detection performance for different types of FOG events..

Event type (No. of events)	(tuned) FI	(tuned) pFOG
Turn Freeze (38)	71.05% (27)	84.21% (32)
Initiation/Gait Freeze (12)	75.00% (9)	75.00% (9)
Festination with Freeze (8)	62.50% (5)	75.00% (6)
Overall (58)	70.68% (41)	**81.03**% (47)

either an improvement or equivalent performance in detecting different types of FOG events (see Table 5.3). We also compared our proposed approach with the FI method for a fixed value of participant-specific tunable parameter and FI-threshold. These values were obtained by taking the average of these parameters across all FOG participants (see Table 5.2). The results are presented in Appendix D.3. For a fixed value of the participant-specific tunable parameter, the pFOG method obtained an accuracy of 72.41% whereas the FI method obtained an accuracy of 56.68% (see Table D.1 of the Appendix D.3). This observation motivates the need to develop methods that can automatically adjust the participant-specific tunable parameter based on individual gait patterns.

Next, we compute the TPR and FAR for all participants across all tasks, using video as the reference system. For participants who did not exhibit FOG, the FI-threshold is set to the mean value of the FI-threshold obtained for FOG participants, rounded to the nearest integer. Similarly, for non-FOG participants, the kernel parameter $\sigma_s = 0.4$, a value which assigns a unit weight if the average speed in the bin is zero. We call this the 'baseline setting'. In Table 5.4, we summarize the average values of TPR and FAR for all tasks across all participants. We first notice that the proposed method demonstrates a low average FAR for non-FOG participants using the baseline setting. Next, we observe that the average value of TPR for FOG participants using the proposed and existing method are nearly the same. However, the proposed method demonstrates an overall accuracy of 81.03% (see Tables 5.2 and 5.3). Further, the proposed method shows a more than three-fold decrease in the average

Table 5.4: Average value of TPR and FAR.

Performance Metric	FI	pFOG
Avg. FAR (non-FOG participants)	0.07	**0.03**
Avg. TPR (FOG participants)	0.66	0.73
Avg. FAR (FOG participants)	0.21	**0.07**
Avg. TPR (all participants)	0.82	0.86
Avg. FAR (all participants)	0.15	**0.05**

value of FAR for FOG participants. A similar trend is also observed in the average values of TPR and FAR for all tasks across all participants using the pFOG method, displaying an overall improvement in the accuracy of determining the onset and duration of FOG.

5.6 Chapter Summary

In this chapter, we developed a point-process filter which was characterized by a conditional intensity function. We modeled the edges of the TREI as a point-process, and assigned weights to the edges of the TREI. The weights assigned depended on a participant-specific tunable parameter and the average value of the speed of the foot in the bin containing the edge. We considered the average value of the foot speed as a gait parameter because freezing of gait is associated with small foot speeds. Finally, we integrated these weights over a time window, using a Bayesian recursive filter called as the TREI-aided point-process filter, and computed the pFOG. We demonstrated that regions in the inertial sensor that contain FOG demonstrated high pFOG. We manually tuned the participant-specific tunable parameter for individual participant, and maximized the number of FOG events detected. Our results demonstrated an overall improvement in detecting the number of FOG events and also a three-fold decrease in the false alarm rate when compared with an existing method. The price payed is an increased computational load and the need for additional sensors (gyroscopes).

However, considering that ultra-low-cost IMUs today can be manufactured at cost less than one dollar and that powerful floating point micro-controllers are readily available, advanced signal processing strategies such as that proposed in the paper are practical and feasible for most applications.

The participant-specific tunable parameter was adjusted manually for every participant based on their gait patterns. This adjustment required a thorough grid search operation, which was a tedious and computationally expensive task. In addition, a value of the tunable parameter that was participant-specific but fixed over time was unlikely to be adequate. Ideally, the parameter should be adapted to specific gait patterns, which are subject to change depending on the participant's gait, symptoms, and treatment strategy. To automatically adjust the participant-specific tunable parameter, we first detect valid gait cycles and then adjust the parameter based on the gait parameters in the valid gait cycle.

Chapter 6

Validation Module: A Sparsity-based Gait Cycle Validation Algorithm

In this chapter, we develop an algorithm to automatically validate and segment a gait cycle in real time into three gait events, namely midstance, toe-off, and heel-strike, using inertial sensors. We first use the physical models of sensor data obtained from a foot-mounted inertial system to differentiate stationary and moving segments of the sensor data. Next, we develop an optimization routine called sparsity-assisted wavelet denoising (SAWD), which simultaneously combines linear time invariant filters, orthogonal multiresolution representations such as wavelets, and sparsity-based methods, to generate a sparse template of the moving segments of the gyroscope measurements in the sagittal plane for valid gait cycles. Thereafter, to validate any moving segment as a gait cycle, we compute the root-mean-square error between the generated sparse template and the sparse representation of the moving segment of the gyroscope data in the sagittal plane obtained using SAWD. Finally, we find the local minima for the stationary and moving segments of a valid gait cycle to detect the gait events. We compare our proposed method with existing methods, for a fixed threshold, using real data obtained from three groups, namely controls, participants with Parkinson

disease, and geriatric participants. Our proposed method demonstrates an average F1 score of 87.78% across all groups for a fixed sampling rate, and an average F1 score of 92.44% across all Parkinson disease participants for a variable sampling rate.

6.1 Introduction

Movement disorders are common in the general elderly population, and the prevalence increases with age, from 10% between 60 to 69 years to more than 60% in those over 80 years [98, 99]. The evaluation of movement disorders includes clinical observations and assessment of gait, both of which may guide the choice of therapies and rehabilitation strategies [100].

In the last decade, gait analysis has moved away from equipment-intensive, laboratory-based analyses toward the use of wearable sensors. Several gait segmentation methods for ambulatory gait analysis using wearable technology have been developed, with varying success [101, 102]. These methods employ sensing modalities such as electromyography (EMG) sensors [103], force-sensitive resistor (FSR) sensors [104–106], pressure sensors [107, 108], inertial sensors [109–113], or a combination of two or more sensing modalities [114–119]. Note that the granularity of a gait segmentation method, i.e., the number of phases of a gait cycle detected, varies with the choice of sensing modalities. In the case of inertial sensors, the existing methods are based on thresholding sensor measurements [109–111, 114–116, 118], template matching via dynamic time warping [113], or machine learning based methods such as hidden Markov models [112, 119]. Across all these methods, gyroscope measurements in the sagittal plane are the best choice for gait segmentation because the measurements contain typical time-series patterns such as "valleys," "peaks," and "plateaus." These patterns are

respectively, toe-off and heel-strike, mid-swing, and midstance. While thresholding methods work well in practice, these methods do not have a mechanism to verify and validate the observable patterns of the gyroscope signal in the sagittal plane, which leads to low precision. As an alternative, dynamic time warping is a pattern matching method that computes a similarity measure between a template representing a valid gait cycle and an input sequence [120]. However, the threshold required to validate an input sequence as a gait cycle is not fixed and exhibits a large variance [121]. Yet another alternative, machine learning methods, requires large samples of training data across many participants and manual segmentation of gait phases, depending on the granularity of the task, to label the training data. Moreover, it is computationally expensive to learn the parameters of the machine learning task.

To overcome these drawbacks, we propose a modular approach that employs pattern matching and thresholding, to validate and detect three gait events in the gait cycle, namely midstance, toe-off, and heel-strike. To identify the data as stationary or moving, we first use physical models that describe zero-velocity events or stationary events of the sensor data obtained from a foot-mounted inertial system. Next, to generate a sparse representation of the moving segments of the gyroscope measurements in the sagittal plane for valid gait cycles, we develop a computationally efficient algorithm called sparsity-assisted wavelet denoising (SAWD). In SAWD, we simultaneously combine linear time-invariant filters, wavelets, and sparsity-based methods to extract a discrete wavelet transform (DWT) coefficient vector as a sparse representation of the moving segment of the gyroscope measurements in the sagittal plane. The reconstructed signal obtained from the extracted DWT coefficient vector is smooth and preserves the typical observable patterns, such as "valleys" and "peaks," of a valid gait cycle for the nonstationary segments of the gyroscope signal in the sagittal plane.

We generate a template of the DWT coefficient vector by taking the average of the DWT coefficient vectors obtained using the SAWD algorithm for all valid gait cycles of a given trial. Thereafter, to validate any moving segment as a gait cycle, we compute the root-mean-square error between the generated template and the sparse representation of the moving segment of the gyroscope data in the sagittal plane, obtained using the SAWD algorithm. If the root-mean-square error is less than a fixed threshold, then the gait cycle is valid. Finally, we find the local minima for the stationary and moving segments of a valid gait cycle to identify toe-off and heel-strike gait events. To demonstrate the robustness of our proposed method, we herein generate the DWT coefficient vector using inertial sensor data from a healthy participant and evaluate the method's performance on data obtained from controls, participants with Parkinson disease, geriatric participants. In addition, we also show the threshold-invariance property of our proposed method across different sampling rates.

There are several advantages of developing a modularity-based approach for validating and segmenting a gait cycle in real time. These include the ability to incorporate the gait cycle validation and segmentation module into the existing zero-velocity aided foot-mounted inertial navigation systems to accurately identify phases of the gait that are affected [49,122] and the development of novel cueing strategies for mitigating disabling motor symptoms such as freezing of gait in Parkinson disease [37, 123, 124]. Section 6.2 describes the background required for detecting zero-velocity or stationary segments of sensor data from a foot-mounted inertial system. Section 6.3 develops an algorithm to validate a gait cycle and detect toe-off and heel-strike events using the non-stationary gyroscope measurements in the sagittal plane. Section 6.4 presents an illustrative example to demonstrate the robustness of our proposed method. Section 6.5 compares the results of our proposed method with some existing methods. Section 6.6 presents the conclusions.

6.2 Preliminaries

6.2.1 Gait Events

There are two main components of a gait cycle: stance and swing. A typical gait cycle for a healthy adult consists of 62% stance and 38% swing phase [125]. These two gait phases are further divided into eight events: Five (heel-strike, flat-foot, midstance, heel-off, and toe-off) during the stance phase, and three (acceleration, midswing, and deceleration) occur during the swing phase [125]. In this work, we use gyroscope measurements in the sagittal plane to detect toe-off and heel-strike events of the stance phase of a gait cycle. The location of the toe-off and heel-strike events detected using the gyroscope signal in the sagittal plane vary depending on the location of the sensor on the foot [109–119]. With the help of FSR and inertial sensors, it was verified in [109, 110] that the local minima of the gyroscope signal in the sagittal plane represent the toe-off and heel-strike events when the sensor is attached to the instep region of the foot.

6.2.2 Zero-velocity Events Intervals

In this subsection, we provide a brief background of the physical models of the inertial sensor data obtained from a foot-mounted inertial system to segment the data as stationary or moving. If $\boldsymbol{y}_k^{\mathrm{a}} \in \mathbb{R}^{3\times 1}$ and $\boldsymbol{y}_k^{\omega} \in \mathbb{R}^{3\times 1}$ denote the measurements of a three-axis accelerometer and a three-axis gyroscope, respectively, at time instant k, then these measurements can be

modeled as

$$\begin{aligned} \boldsymbol{y}_k^{\mathrm{a}} &= \boldsymbol{s}_k^{\mathrm{a}} + \boldsymbol{e}_k^{\mathrm{a}} \\ \boldsymbol{y}_k^{\omega} &= \boldsymbol{s}_k^{\omega} + \boldsymbol{e}_k^{\omega}. \end{aligned} \tag{6.1}$$

Here, $\boldsymbol{s}_k^{\mathrm{a}}$ and $\boldsymbol{s}_k^{\omega}$ denote the true specific force and angular velocity experienced by the accelerometer and gyroscope, respectively. Further, $\boldsymbol{e}_k^{\mathrm{a}}$ and $\boldsymbol{e}_k^{\omega}$ denote the measurement errors of the accelerometer and gyroscope, which are assumed to be white, mutually uncorrelated, and Gaussian distributed with zero mean and covariance matrices $\sigma_{\mathrm{a}}^2 \boldsymbol{I}_3$ and $\sigma_{\omega}^2 \boldsymbol{I}_3$, respectively. To distinguish stationary from non-stationary instances, we use the zero-velocity detector. We define two hypotheses, $\mathcal{H}_0$ and $\mathcal{H}_1$, as follows:

$$\begin{aligned} \mathcal{H}_0 &\coloneqq \text{ Sensor is moving} \\ \mathcal{H}_1 &\coloneqq \text{ Sensor is stationary.} \end{aligned} \tag{6.2}$$

Mathematically, the signal model for the two hypotheses in (6.2) can be written as

$$\begin{aligned} \mathcal{H}_0 : &\begin{cases} \exists k \in \Omega_W : \boldsymbol{s}_k^{\mathrm{a}} \neq g\boldsymbol{v}^{\mathrm{a}} \\ \exists k \in \Omega_W : \boldsymbol{s}_k^{\omega} \neq \boldsymbol{0} \end{cases} \\ \mathcal{H}_1 : &\begin{cases} \forall k \in \Omega_W : \boldsymbol{s}_k^{\mathrm{a}} = g\boldsymbol{v}^{\mathrm{a}}, \\ \forall k \in \Omega_W : \boldsymbol{s}_k^{\omega} = \boldsymbol{0} \end{cases} \end{aligned}, \tag{6.3}$$

where g is the Earth's gravity, $\boldsymbol{v}^{\mathrm{a}}$ is the direction of the gravity vector (which is unknown), and Ω_W is a window of size W consisting of the time samples $\{k, \ldots, k+W-1\}$. Given the signal model in (6.3), it can be shown that the generalized loglikelihood ratio test, denoted

by $T_k(\boldsymbol{y}^{\mathrm{a}}, \boldsymbol{y}^{\omega})$ at time index k, for detecting zero-velocity event intervals is given by

$$\frac{1}{W}\sum_{k\in\Omega_W}\left\{\frac{1}{\sigma_{\omega}^2}\left\|\boldsymbol{y}_k^{\omega}\right\|_2^2+\frac{1}{\sigma_{\mathrm{a}}^2}\left\|\boldsymbol{y}_k^{\mathrm{a}}-g\frac{\bar{\boldsymbol{y}}^{\mathrm{a}}}{\|\bar{\boldsymbol{y}}^{\mathrm{a}}\|}\right\|_2^2\right\}\underset{<}{\overset{\mathcal{H}_1}{}}\gamma_{\mathrm{D}}, \tag{6.4}$$

where $\boldsymbol{y}^{\mathrm{a}}=[(\boldsymbol{y}_k^{\mathrm{a}})^T,\ldots,(\boldsymbol{y}_{k+W-1}^{\mathrm{a}})^T]^T\in\mathbb{R}^{3N\times 1}$, $\boldsymbol{y}^{\omega}=[(\boldsymbol{y}_k^{\omega})^T,\ldots,(\boldsymbol{y}_{k+W-1}^{\omega})^T]^T\in\mathbb{R}^{3N\times 1}$, $\bar{\boldsymbol{y}}^{\mathrm{a}}=(1/W)\sum_{k\in\Omega_W}\boldsymbol{y}_k^{\mathrm{a}}\in\mathbb{R}^{3\times 1}$, and γ_{D} is the detector threshold. The derivation of (6.4) can be found in [79] and [1, Appendix B]. It is also possible to use only gyroscope measurements to identify foot-mounted inertial sensor data as stationary or non-stationary regions [126–128]. In this work, we define a midstance event as the time instance under $\mathcal{H}_1$ when $T_k(\boldsymbol{y}^{\mathrm{a}}, \boldsymbol{y}^{\omega})$ is minimum, i.e., if Ω_{M_i} is a segment of inertial sensor data of variable length $M_i > 0.1$ seconds, for the i-th stride under $\mathcal{H}_1$, then the midstance event is mathematically expressed as

$$\mathrm{MS}_i \leftarrow \arg\min_{k,k\in\Omega_{M_i}} T_k(\boldsymbol{y}^{\mathrm{a}}, \boldsymbol{y}^{\omega}). \tag{6.5}$$

We choose the time index when $T_k(\boldsymbol{y}^{\mathrm{a}}, \boldsymbol{y}^{\omega})$ is minimum as the midstance event because during a midstance event the foot is completely stationary.

6.3 Gait Cycle Validation and Segmentation

In this section, we develop a new approach to validate a gait cycle and detect gait events such as toe-off and heel-strike, using the gyroscope sensor data in the sagittal plane. The proposed algorithm is applied only to the regions of the sensor data when the sensor is moving, i.e., when hypothesis $\mathcal{H}_0$ in (3.5) is true. Our goal is to extract a sparse representation of the segments of the gyroscope signal for valid gait cycles.

6.3.1 Discrete Wavelet Transform

Multiresolution orthogonal representations, such as discrete wavelet transform (DWT), are widely used in a variety of signal and image processing applications [129]. Wavelet coefficients are computed by integrating the product of a signal and oscillating functions obtained by stretching and translating a locally oscillating basis function, referred to as a wavelet [130]. Because of their low computational complexity and high accuracy in representing signals, wavelets are used in many applications, such as compression, denoising, and pattern recognition [130].

Let $\boldsymbol{x} \in \mathbb{R}^{N\times 1}$ be an N-dimensional vector. To model $\boldsymbol{x}$ in wavelet-domain, we use windowed discrete wavelet transform (WDWT). The WDWT coefficients, denoted by $\boldsymbol{k} \in \mathbb{R}^{U\times V}$, depend on the window length, the windows overlap factor, and the number of levels of the wavelet decomposition. In our work, we define $\boldsymbol{\Psi} : \mathbb{R}^{U\times V} \rightarrow \mathbb{R}^{N}$ (the synthesis equation of WDWT) as

$$\boldsymbol{\Psi k} \coloneqq \mathrm{WDWT}^{-1}(\boldsymbol{k}), \tag{6.6}$$

whereas $\boldsymbol{\Psi}^{\mathsf{T}} : \mathbb{R}^{N} \rightarrow \mathbb{R}^{U\times V}$ (the analysis equation of WDWT) is defined as

$$\boldsymbol{\Psi}^{\mathsf{T}}\boldsymbol{x} \coloneqq \mathrm{WDWT}(\boldsymbol{x}). \tag{6.7}$$

In this work, the length of the window U depends on the sampling frequency $\mathrm{F_s}$, and is given as $U = 2^J$, where J is the smallest positive integer for which $U \geq \mathrm{F_s}$. The value of J determines the maximum levels of wavelet decomposition. The length of V depends on the percentage of overlap between two consecutive windows and generates an overcomplete

dictionary, $\boldsymbol{k}$. If $V = 1$, then WDWT is the same as DWT. Furthermore, WDWT in (6.6) and (6.7) satisfies a generalized version of Parseval's identity [130, 131], i.e., $\|\boldsymbol{\Psi k}\| = \|\boldsymbol{x}\|$, and demonstrates the perfect reconstruction property, i.e., $\boldsymbol{\Psi\Psi}^{\mathsf{T}} = \boldsymbol{I}$.

6.3.2 Zero-Phase Filters as Matrices

Linear time-invariant filters are easy to implement and are also efficient, especially when the frequency band of the signal of interest is known. However, when designed as matrices and used in batch-mode processing, these filters are computationally expensive where the complexity increases as the number of samples increase. To overcome the computational load, the authors in [132, 133] developed computationally efficient zero-phase noncausal high-pass and low-pass recursive filter designs as banded Toeplitz matrices. The banded Toeplitz allows using fast solvers for a banded system of linear equations. Further, the zero-phase property allows employing these filters in an optimization framework as matrix operators, without introducing any phase distortions from the filter. We denote the zero-phase low-pass filter matrix operator as $\mathsf{LPF}_{\omega_0}(\cdot)$, where

$$\mathsf{LPF}_{\omega_0}(\boldsymbol{x}) \coloneqq \boldsymbol{Lx} = \boldsymbol{A}^{-1}\boldsymbol{Cx}. \tag{6.8}$$

Here, $0 \leq \omega_0 \leq 1/2$ is the normalized 3dB cutoff frequency of the low-pass filter, and $\boldsymbol{A} \in \mathbb{R}^{N\times N}$ and $\boldsymbol{C} \in \mathbb{R}^{N\times N}$ are banded Toeplitz matrices [132, 133].

6.3.3 Sparsity-Assisted Wavelet Denoising (SAWD)

Let $\boldsymbol{y}^{\omega_s} \in \mathbb{R}^{N\times 1}$ denote the measured gyroscope signal segment under hypothesis $\mathcal{H}_0$, where the superscript ω_s indicates measurement in the sagittal plane. The length of the signal N depends on the speed of the foot and the threshold γ_D of the zero-velocity event interval detector in (6.4), and varies with every gait cycle. We begin by scaling $\boldsymbol{y}^{\omega_s}$ so that its amplitude $\in [-1, 1]$. If $\boldsymbol{y}^s$ denotes the scaled gyroscope signal, then

$$\boldsymbol{y}^s = 2\left[\frac{\boldsymbol{y}^{\omega_s} - \max\left(\boldsymbol{y}^{\omega_s}\right)}{\max(\boldsymbol{y}^{\omega_s}) - \min(\boldsymbol{y}^{\omega_s})}\right] - 1, \tag{6.9}$$

where $\max(\cdot)$ and $\min(\cdot)$ are the maximum and minimum of the input vector. In the next step, we use a 1D linear interpolation filter on $\boldsymbol{y}^s$ so that the length of the interpolated signal is equal to the sampling rate. Let $\boldsymbol{y}$ denote the 1D linear interpolated signal, and then

$$\boldsymbol{y} = \text{interp1}(\boldsymbol{y}^s, \boldsymbol{t}_1, \boldsymbol{t}_2), \tag{6.10}$$

where `interp1` is the 1D linear interpolation function in MATLAB or Python, and $\boldsymbol{t}_1$ and $\boldsymbol{t}_2$ are vectors containing sample points of length N and F_s, respectively. The scaling step follows the interpolation step, and these two steps cannot be interchanged. Note that in the signal preprocessing step (scaling and interpolating), the gyroscope signal preserves the patterns of interest of a valid gait cycle. The preprocessed signal is only used for validating a gait cycle whereas the scaled non-stationary segment is used for for determining the toe-off and heel-strike events because interpolation does not preserve the location of local minima. In the next step, we minimize a cost function to extract the DWT coefficients of a smoothed segment of a valid gait cycle so that it preserves the typical observable patterns. In particular,

we solve the following optimization problem:

$$\arg\min_{\boldsymbol{k}}\Big\{\frac{1}{2}\left\|\boldsymbol{L}(\boldsymbol{y}-\boldsymbol{\Psi k})\right\|_2^2\Big\}, \tag{6.11}$$

where $\boldsymbol{L}$ is the low-pass filter in (6.8) with a normalized cutoff frequency ω_0, and $\boldsymbol{\Psi k}$ is the synthesis equation of the WDWT in (6.6). Note that the optimization problem in (6.11) is the standard least-squares problem and has a closed-form expression. Solving (6.11) gives the set of DWT coefficients required to reconstruct the low-frequency signal of the scaled gyroscope measurement vector. However, many entries of the DWT coefficient matrix $\boldsymbol{k}$ are close to zero and do not significantly contribute in the reconstruction of the low-frequency signal. Therefore, we introduce a regularization term to reduce the number of DWT coefficients required to represent the low-frequency signal. The cost function of the modified optimization problem, denoted by $C(\boldsymbol{y},\boldsymbol{k})$, is given as

$$C(\boldsymbol{y},\boldsymbol{k}) = \arg\min_{\boldsymbol{k}}\Big\{\frac{1}{2}\left\|\boldsymbol{L}(\boldsymbol{y}-\boldsymbol{\Psi k})\right\|_2^2 + \lambda\left\|\boldsymbol{k}\right\|_1\Big\}, \tag{6.12}$$

where $\lambda > 0$ is the regularization parameter. The first term in (6.12) is the data fidelity term, which is same as (6.11), whereas the second term is the regularization term on the dictionary, $\boldsymbol{k}$, of DWT coefficients representing the low-frequency signal. In (6.12), we simultaneously combine low-pass filtering, wavelet representation, and a sparsity-inducing norm. We apply the alternative direction method of multipliers (ADMM) [134, Chapter 3] to iteratively minimize the cost function in (6.12). We begin by decoupling the cost function in (6.12) using the Douglas-Rachford variable splitting method [135]. The cost can be rewritten

as

$$\begin{aligned} &\arg\min_{\boldsymbol{k},\boldsymbol{u}} \Big\{ \frac{1}{2} \left\| \boldsymbol{L}(\boldsymbol{y} - \boldsymbol{\Psi}\boldsymbol{u}) \right\|_2^2 + \lambda \left\| \boldsymbol{k} \right\|_1 \Big\}, \\ &\text{such that} \quad \boldsymbol{u} = \boldsymbol{k}. \end{aligned} \tag{6.13}$$

Applying the augmented Lagrangian [134] to (6.13) we get the following iterative optimization routine:

repeat :

$$\boldsymbol{u} \leftarrow \arg\min_{\boldsymbol{u}} \Big\{ \frac{1}{2} \left\| \boldsymbol{L}(\boldsymbol{y} - \boldsymbol{\Psi}\boldsymbol{u}) \right\|_2^2 + \frac{\mu}{2} \left\| \boldsymbol{u} - \boldsymbol{k} - \boldsymbol{d} \right\|_2^2 \Big\}, \tag{6.14a}$$

$$\boldsymbol{k} \leftarrow \arg\min_{\boldsymbol{k}} \Big\{ \lambda \left\| \boldsymbol{k} \right\|_1 + \frac{\mu}{2} \left\| \boldsymbol{u} - \boldsymbol{k} - \boldsymbol{d} \right\|_2^2 \Big\}, \tag{6.14b}$$

$$\boldsymbol{d} \leftarrow \boldsymbol{d} - (\boldsymbol{u} - \boldsymbol{k}), \tag{6.14c}$$

until convergence,

where $\mu > 0$ determines the rate of convergence and does not affect the final value of the cost function in (6.12). The equation (6.14a) is the standard least-squares problem, whose solution is given as

$$\boldsymbol{u} \leftarrow (\boldsymbol{\Psi}^\mathsf{T}\boldsymbol{L}^\mathsf{T}\boldsymbol{L}\boldsymbol{\Psi} + \mu\boldsymbol{I}_N)^{-1}(\boldsymbol{\Psi}^\mathsf{T}\boldsymbol{L}^\mathsf{T}\boldsymbol{L}\boldsymbol{y} + \mu(\boldsymbol{k} + \boldsymbol{d})), \tag{6.15}$$

where we use the perfect reconstruction property of wavelets, i.e., $\boldsymbol{\Psi}\boldsymbol{\Psi}^\mathsf{T} = \boldsymbol{I}_N$. Expanding $(\boldsymbol{\Psi}^\mathsf{T}\boldsymbol{L}^\mathsf{T}\boldsymbol{L}\boldsymbol{\Psi} + \mu\boldsymbol{I})^{-1}$ using the matrix inversion lemma [136], we can further simplify (6.15)

as

$$(\boldsymbol{\Psi}^{\mathsf{T}}\boldsymbol{L}^{\mathsf{T}}\boldsymbol{L}\boldsymbol{\Psi} + \mu\boldsymbol{I}_N)^{-1} = (\boldsymbol{\Psi}^{\mathsf{T}}\boldsymbol{C}^{\mathsf{T}}(\boldsymbol{A}\boldsymbol{A}^{\mathsf{T}})^{-1}\boldsymbol{C}\boldsymbol{\Psi} + \mu\boldsymbol{I}_N)^{-1}$$
$$= \frac{1}{\mu}\left(\boldsymbol{I} - \boldsymbol{\Psi}^{\mathsf{T}}\boldsymbol{C}^{\mathsf{T}}\boldsymbol{G}^{-1}\boldsymbol{\Psi}\boldsymbol{C}\right), \tag{6.16}$$

where $\boldsymbol{G} = (\mu\boldsymbol{A}\boldsymbol{A}^{\mathsf{T}} + \boldsymbol{C}\boldsymbol{C}^{\mathsf{T}})$ is a banded matrix. Therefore, (6.15) can be written as

$$\boldsymbol{u} \leftarrow \frac{1}{\mu}\left[\boldsymbol{I} - \boldsymbol{\Psi}^{\mathsf{T}}\boldsymbol{C}^{\mathsf{T}}\boldsymbol{G}^{-1}\boldsymbol{\Psi}\boldsymbol{C}\right](\boldsymbol{\Psi}^{\mathsf{T}}\boldsymbol{L}^{\mathsf{T}}\boldsymbol{L}\boldsymbol{y} + \mu(\boldsymbol{k} + \boldsymbol{d})). \tag{6.17}$$

The least-squares solution in (6.17) can be further simplified as a two-step iterative problem and is given as

$$\boldsymbol{g} \leftarrow \frac{1}{\mu}\boldsymbol{\Psi}^{\mathsf{T}}(\boldsymbol{C}^{\mathsf{T}}(\boldsymbol{A}\boldsymbol{A}^{\mathsf{T}})^{-1}\boldsymbol{C}\boldsymbol{y}) + (\boldsymbol{k} + \boldsymbol{d}) \tag{6.18a}$$

$$\boldsymbol{u} \leftarrow \boldsymbol{g} - \boldsymbol{\Psi}^{\mathsf{T}}(\boldsymbol{C}^{\mathsf{T}}\boldsymbol{G}^{-1}\boldsymbol{C}\boldsymbol{\Psi}(\boldsymbol{g})). \tag{6.18b}$$

The solution to (6.14b) is the solution to the least absolute shrinkage and selection operator (LASSO) problem [137] and is expressed as

$$\boldsymbol{k} \leftarrow \text{soft}(\boldsymbol{u} - \boldsymbol{d}, \lambda/\mu), \tag{6.19}$$

where the soft-threshold function is defined as

$$\text{soft}(x, T) \coloneqq \begin{cases} x - T(x/|x|), & |x| > T \\ 0, & |x| \leq T \end{cases}. \tag{6.20}$$

Algorithm 3 Sparsity-Assisted Wavelet Denoising (6.12)

procedure SAWD($\boldsymbol{y}$, $\boldsymbol{A}$, $\boldsymbol{C}$, λ, μ)
  initialize:
  $\boldsymbol{G} \leftarrow (\mu \boldsymbol{A}\boldsymbol{A}^{\mathsf{T}} + \boldsymbol{C}\boldsymbol{C}^{\mathsf{T}})$
  $\boldsymbol{k} \leftarrow \boldsymbol{\Psi}^{\mathsf{T}}(\boldsymbol{A}^{-1}\boldsymbol{C}\boldsymbol{y})$
  $\boldsymbol{d} \leftarrow \boldsymbol{0}$
  $\boldsymbol{b} \leftarrow (1/\mu)\boldsymbol{\Psi}^{\mathsf{T}}(\boldsymbol{C}^{\mathsf{T}}(\boldsymbol{A}\boldsymbol{A}^{\mathsf{T}})^{-1}\boldsymbol{C}\boldsymbol{y})$
  repeat:
    $\boldsymbol{g} \leftarrow \boldsymbol{b} + \boldsymbol{k} + \boldsymbol{d}$ ▷ From (6.18a)
    $\boldsymbol{u} \leftarrow \boldsymbol{g} - \boldsymbol{\Psi}^{\mathsf{T}}(\boldsymbol{C}^{\mathsf{T}}\boldsymbol{G}^{-1}\boldsymbol{C}\boldsymbol{\Psi}(\boldsymbol{g}))$ ▷ From (6.18b)
    $\boldsymbol{k} \leftarrow \mathrm{soft}(\boldsymbol{u} - \boldsymbol{d}, \lambda/\mu)$ ▷ From (6.19)
    $\boldsymbol{d} \leftarrow \boldsymbol{d} - (\boldsymbol{u} - \boldsymbol{k})$ ▷ From (6.14c)
  until convergence
  return $\boldsymbol{\Psi}\boldsymbol{k}$, $\boldsymbol{k}$
end procedure

The complete algorithm is called sparsity-assisted wavelet denoising and is listed as *Algorithm 3*. Note that the matrix $\boldsymbol{G}$ is always invertible when the degree of the low-pass filter is of the third-order or lower [132, 133, 138].

Remark: The convergence of the Douglas-Rachford splitting and the alternating direction of multipliers demonstrates a linear convergence rate [139]. Because of the linear convergence rate of the ADMM approach, the computational complexity of our proposed method does not depend on the length of the signal or the sampling rate, unlike existing methods.

6.3.4 Gait Cycle Validation and Segmentation

We generate a template of the DWT coefficients by taking the average of the DWT coefficients obtained by solving (6.12) for valid gait cycle segments of gyroscope data in the

sagittal plane. If $\boldsymbol{k}_{\mathrm{T}}$ denotes the template of the DWT coefficients, then

$$\boldsymbol{k}_{\mathrm{T}} = \frac{1}{M}\sum_{i=1}^{M}\boldsymbol{k}_i, \tag{6.21}$$

where M represents the number of valid gait cycles and $\boldsymbol{k}_i$ represents the DWT coefficients obtained by solving (6.12) for the i-th valid gait cycle. Next, we compute the root-mean-square error, denoted by RMSE_i, between the extracted DWT coefficients for a moving segment of the gyroscope data and the template DWT coefficients as follows:

$$\mathrm{RMSE}_i = \left[\frac{1}{\mathrm{F_s}}\sum_{j=1}^{\mathrm{F_s}}(\boldsymbol{k}_{\mathrm{T},j} - \boldsymbol{k}_{i,j})^2\right]^{1/2}. \tag{6.22}$$

A segment of the gyroscope signal measured in the sagittal plane under hypothesis $\mathcal{H}_0$ is a valid gait cycle if

$$\mathrm{RMSE}_i < \gamma_{\mathrm{GCVS}}, \tag{6.23}$$

where γ_{GCVS} is the template matching threshold. In our work, we set γ_{GCVS} as one standard deviation distant from the mean of the RMSE computed during the template generation task. If (6.23) is true, then we determine the toe-off and heel-strike events for the i-th stride, denoted by TO_i and HS_i, respectively, by finding the local minima of the scaled gyroscope signal $\boldsymbol{y}^{\mathrm{s}}$. The first local minimum represents the toe-off event, whereas the second represents the heel-strike event. We segment the scaled gyroscope signal $\boldsymbol{y}^{\mathrm{s}}$ in (6.9) into two or more segments, depending on the smoothness of the signal, with a fixed threshold of 0.5. If Ω_{T_i} and Ω_{H_i} represent, respectively, the first segment and the union of the remaining segments

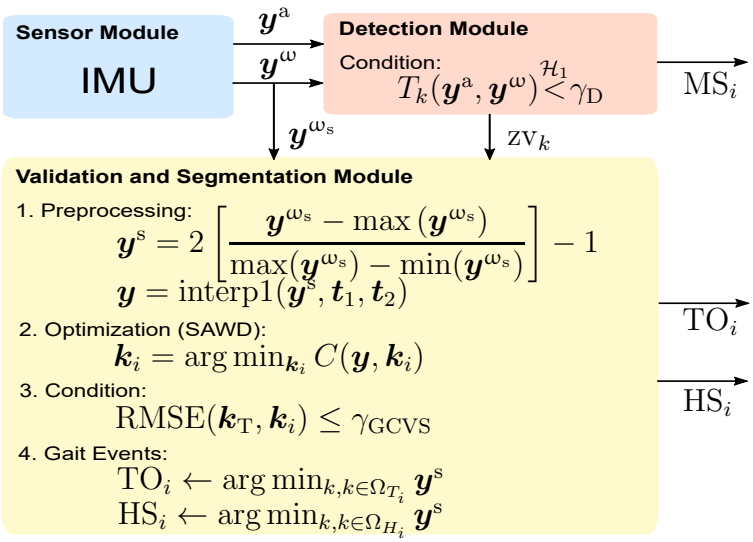

Figure 6.1: Gait cycle validation and segmentation algorithm overview. The proposed modularity-based approach consists of three modules: a) sensor module, b) detection module, and c) validation module. The detection and validation modules are used to identify midstance, and toe-off and heel-strike phase of a gait cycle, respectively.

of $\boldsymbol{y}^{\mathrm{s}}$ that are below the threshold, then

$$\mathrm{TO}_i \leftarrow \arg \min_{k, k\in\Omega_{T_i}} \boldsymbol{y}^{\mathrm{s}}, \tag{6.24}$$

$$\mathrm{HS}_i \leftarrow \arg \min_{k, k\in\Omega_{H_i}} \boldsymbol{y}^{\mathrm{s}}, \tag{6.25}$$

where T_i and H_i are the lengths of the segments of Ω_{T_i} and Ω_{H_i}.

6.4 Illustrative Example

In this section, with the help of an illustrative example, we demonstrate our proposed method. We develop methods to identify the cutoff frequency ω_0 of the low-pass filter in (6.8) and tune the parameter μ to improve the rate of convergence of the SAWD algorithm.

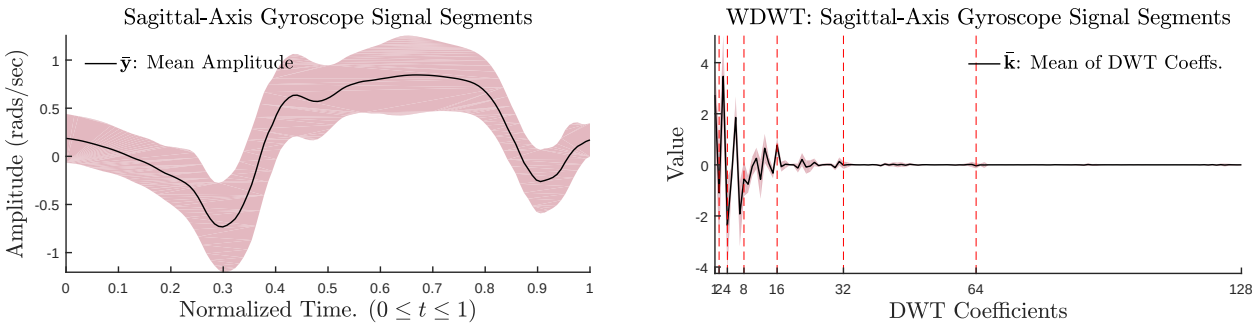

(a) Gyroscope signal segments in the sagittal plane.

(b) DWT coefficients of the gyroscope signal segments.

Figure 6.2: Scaled and interpolated gyroscope signal segments measured in the sagittal plane, with corresponding DWT coefficients. The solid line indicates the mean value, and the shaded region indicates one standard deviation variance.

6.4.1 Data Collection and Hardware

We used APDM Opal sensors [50] to collect accelerometer and gyroscope sensor data for a participant walking on a treadmill. The sensors operate at a sampling frequency of $F_s = 128$ Hz and are firmly attached to the instep region of the foot with the help of elastic Velcro straps. Data from the sensors was transmitted in wireless mode to a laptop and stored in HDF5 format. As a reference system, we used a GoPro camera placed a few feet away from the treadmill. In addition, a digital clock was also placed next to the treadmill, so that the readings on the clock were clearly captured in the video data. The digital clock readings were used to manually synchronize the video data with the inertial sensor data.

6.4.2 Experiment

To validate and segment a gait cycle, a healthy male participant of age 30 was recruited. The participant stood on the treadmill, with his feet in comfortable stance width. When a tone sounded, the participant began to walk, slowly accelerating at a comfortable pace and

reaching gait speed of 1.34 m/s (3 miles/hr) in the first 15 seconds of the trial. Then, for the next 15 seconds, the participant walked at a steady pace of 1.34 m/s, which was maintained with the help of the speed indicator on the treadmill. Finally, in the last 15 seconds of the trial, the participant began to slowly decelerate from a steady pace of 1.34 m/s to a standstill. Each trial lasted for 45 seconds and was repeated seven times. To generate the template of the DWT coefficient vector $\boldsymbol{k}_{\mathrm{T}}$, we used datasets from the treadmill walking experiment because the dataset contains inertial sensor data with variable walking speeds.

6.4.3 Template Generation

To detect midstance events, we set the zero-velocity detector threshold $\gamma_{\mathrm{D}} = 2.0$ in (6.4). The size of the window is set to one-eighth of the sampling rate $\mathrm{F_s}$, i.e., $W = 16$. Further, the standard deviations of the accelerometer and gyroscope are set to $\sigma_{\mathrm{a}} = 1.0$ and $\sigma_{\omega} = 0.8$, respectively. The details of the steps for obtaining the parameter of the zero-velocity detector are presented in [1, Appendix D and E]. Next, using the zero-velocity detector, we segment the gyroscope measurements in the sagittal plane and detect the regions when the IMU is not stationary, i.e., when hypothesis $\mathcal{H}_0$ is true in (3.5). The segments of the gyroscope measurements in the sagittal plane under hypothesis $\mathcal{H}_0$ are scaled and interpolated employing (6.10) and (6.9), respectively. To design the WDWT in (6.6) and (6.7), we select a Daubechies wavelet (`db4` or `D8`) as the mother wavelet because it closely resembles the shape of the gyroscope signal in the sagittal plane for a valid gait cycle. We use a window length of the next highest power of the sampling rate $\mathrm{F_s}$, expressed as a power of 2, i.e., $U = 2^7 = 128$. Further, we use non-overlapping windows, i.e., $V = 1$, because the length of the scaled segment $N \leq \mathrm{F_s}$ for all valid gait cycles across varying gait speeds of the treadmill walking trial [140]. In Fig. 6.2a and 6.2b, we plot the scaled and interpolated gyroscope

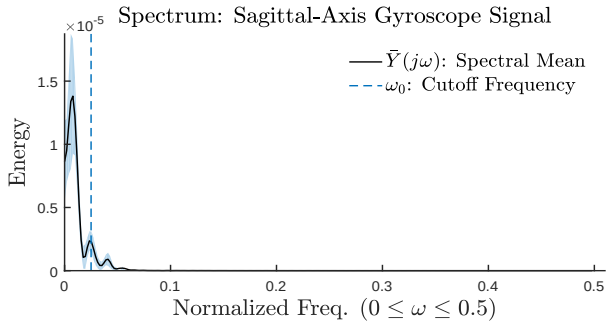

Figure 6.3: Spectrum plot of the scaled and interpolated gyroscope signal segments. The solid line indicates the spectral mean value. The dashed blue line indicates the normalized cutoff frequency $\omega_0 = 0.025$ of the low-pass signal.

signal segments and corresponding DWT coefficients for valid gait cycles of the fifth trial of the treadmill experiment, selected at random. As can be seen in Fig. 6.2a, each segment consist of observable patterns of interest, i.e. , "valleys" and "peaks." Further, we notice that the DWT coefficients in Fig. 6.2b consist of large coefficients in the lower frequency scales $[2^{j-1}, 2^j), j \in \{1, 2, 3\}$, small coefficients in the mid frequency scales $[2^{j-1}, 2^j), j \in \{4, 5\}$, and coefficients close to zero in the high frequency scales $[2^{j-1}, 2^j), j \in \{6, 7\}$. The DWT coefficients in the lower frequency scales represent the low-frequency signal. Therefore, it is sufficient to retain these coefficients to reconstruct a template of the gait cycle that preserves the observable patterns of interest.

To determine the cutoff frequency of the low-frequency signal, we compute the Fourier transform of each segment and select the cutoff frequency ω_0 such that the range of frequencies representing the dominant energy regions are retained. In Fig. 6.3, we plot the N-point discrete Fourier transform (DFT) of the scaled and interpolated gyroscope signal segments on a normalized frequency scale $0 \leq \omega_0 \leq 0.5$, where the length of DFT is set to $N = 512$. As can be seen, the energy of the segments resides in the lower frequency range of the normalized frequency scale. Therefore, to obtain a smoothed template of the input signal such that preserves its shape, we select $\omega_0 = 0.025$, equivalent to 3.2 Hz, as shown in Fig. 6.3 with

a dashed blue vertical line. The cutoff frequency ω_0 and the length of the interpolated signal are used to construct the banded matrices $\boldsymbol{A}$ and $\boldsymbol{C}$. Using (6.8), we design a zero-phase low-pass filter as a banded matrix [133].

In Fig. 6.4, we demonstrate the rate of convergence of the SAWD algorithm across different values of μ. Note that μ affects only the rate of convergence and not the final value of the cost function. We plot the average value of the cost function for $\mu \in \{0.01, 0.1, 1\}$ obtained for valid gait cycle segments of the fifth trial of the treadmill experiment. As can be seen in Fig. 6.4, the SAWD algorithm converges in less than five iterations on average for $\mu = 0.1$. Further, the SAWD algorithm takes 0.02 ± 0.01 seconds per gait cycle to converge on a Windows computer (2.7 GHz Intel Core i7) running MATLAB 2016b, and thus making it feasible to implement the algorithm in real time.

In Table 6.1, we report the results of the average reconstruction error and the average number of non-zero DWT coefficients across different values of λ. The reconstruction error is defined as the root-mean-square error between the reconstructed signal $\boldsymbol{\Psi k}_{\mathrm{T}}$ (see Fig. 6.5a) and the signal obtained by averaging the low-frequency segments of valid gait cycles (see Fig. 6.5c). The cutoff frequency of the low-frequency signal is same as the cutoff frequency of the low-pass filter used in the SAWD algorithm. Table 6.1 shows that, as the λ value increases, the reconstruction error increases, but, the number of non-zero DWT coefficients decreases. To find a good balance between the reconstruction error and the number of non-zero DWT coefficients, we select $\lambda = 0.05$.

We plot the outputs of the SAWD algorithm, $\boldsymbol{\Psi k}$ and $\boldsymbol{k}$, in Fig. 6.5a and 6.5b, respectively. We notice that the low-frequency signal $\boldsymbol{\Psi k}$ obtained by solving (6.12) in Fig. 6.5a is smooth and preserves the observable patterns of interest of a valid gait cycle. Further, as shown in Fig. 6.5b, the dominant DWT coefficients in the lower frequency scales $[2^{j-1}, 2^j), j \in \{1, 2, 3\}$

Table 6.1: Reconstruction error and non-zero coefficients

λ	Reconstruction Error (Avg.)	Non-Zero Coefficients (Avg.)
0.01	0.007685	13.764706
0.03	0.015022	10.852941
0.05	0.022069	10.323529
0.07	0.029112	9.558824
0.09	0.036047	9.000000

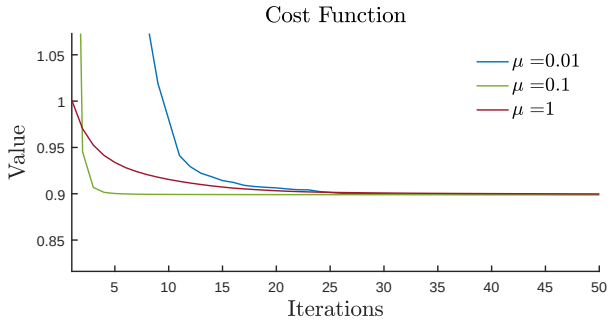

Figure 6.4: The solid lines indicate the average value of the cost function for different values of $\mu \in \{0.01, 0.1, 1\}$. The convergence rate varies with the value of μ, however, it does not affect the cost function.

remain unaffected whereas the DWT coefficients in higher frequency scales $[2^{j-1}, 2^j), j \in \{4, 5, 6, 7\}$ are either zero or nearly zero. The template of the DWT coefficients $\boldsymbol{k}_{\mathrm{T}}$ is obtained using (6.21). It is shown as a solid line in Fig. 6.5b, which is a sparse representation of the scaled and interpolated gyroscope segment. In the fifth trial of the treadmill walking task, a total of 31 gait cycles were identified from the video data, i.e., $M = 31$. In Fig. 6.5c and 6.5d, we plot the scaled and interpolated low-frequency signal for $\omega_0 = 0.025$ and the corresponding DWT coefficients without applying the SAWD algorithm. We notice that the shapes of the two smoothed signals in Fig. 6.5a and 6.5c are quite similar. However, the DWT coefficients obtained using the SAWD algorithm contain fewer non-zero coefficients than the DWT coefficients obtained using only the low-pass filter. Further, the RMSE in (6.22) for the SAWD algorithm is small (0.246418 ± 0.229323) in comparison to that of the low-pass filtering method (0.465160 ± 0.118028). Thus, the SAWD algorithm can extract

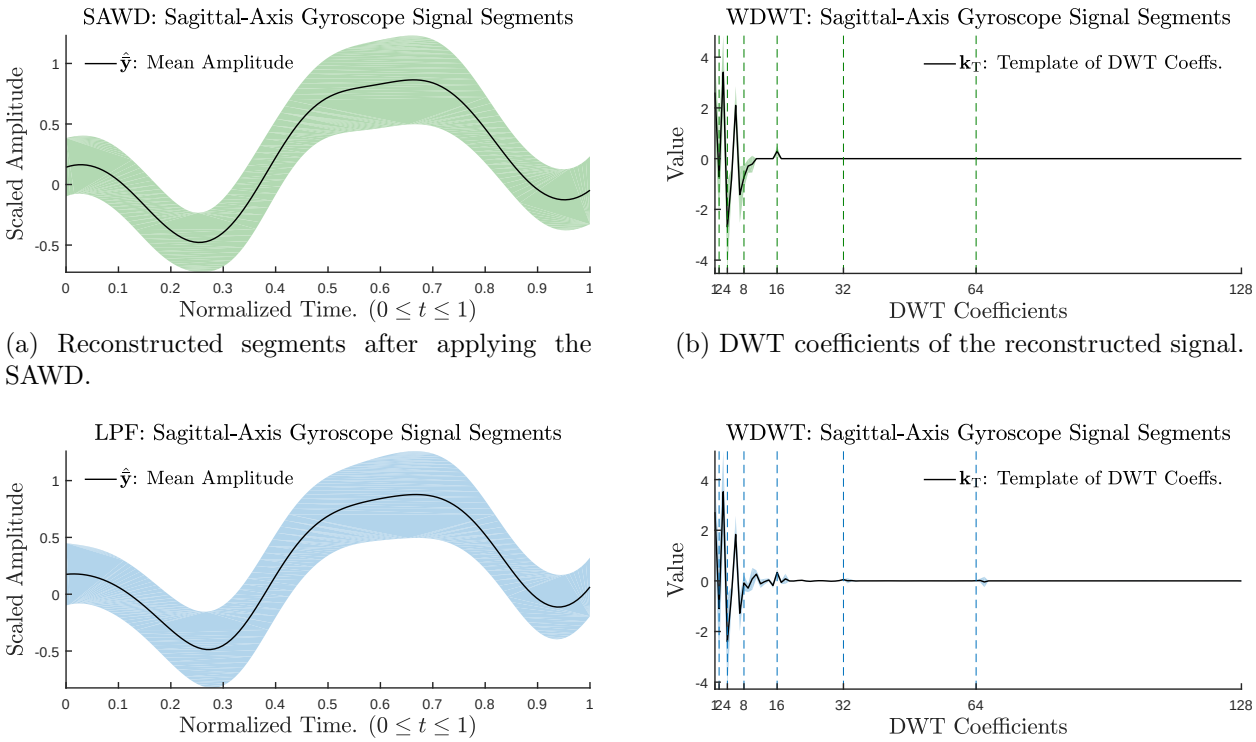

(a) Reconstructed segments after applying the SAWD.

(b) DWT coefficients of the reconstructed signal.

(c) Reconstructed segments after applying low-pass filtering.

(d) DWT coefficients of the reconstructed signal.

Figure 6.5: Scaled and interpolated gyroscope signal segments measured in the sagittal plane and its corresponding DWT coefficients. The solid line indicates the mean value, and the shaded region indicates one standard deviation variance.

a sparse representation of a valid gait cycle in the form of DWT coefficients with minimum RMSE.

6.4.4 Validation and Segmentation

To validate a moving segment of the inertial sensor data as a gait cycle, we use the generated DWT coefficient template $\boldsymbol{k}_{\mathrm{T}}$ and the DWT coefficients $\boldsymbol{k}$ obtained using the SAWD algorithm for any moving segment of the gyroscope signal in sagittal plane, and compute the RMSE in (6.22). The threshold in (6.23), γ_{GCVS}, is set to the maximum of one standard

Table 6.2: Validation of toe-off, heel-strike, swing as percentage of gait cycle using the GCVS method.

Trial #	Toe-off Angle (mean ± std)		Heel-Strike Angle (mean ± std)		Swing as %GCT (mean ± std)		Gait Cycles (detect/actual)	
	MLBS	GCVS	MLBS	GCVS	MLBS	GCVS	MLBS	GCVS
2	$30° \pm 3.2°$	$35.3° \pm 5.6°$	$-14° \pm 2.2°$	$-12.9° \pm 3.0°$	$39\% \pm 1.2\%$	$38.6\% \pm 9.3\%$	22/27	25/27
3	$31° \pm 5.3°$	$32.9° \pm 7.3°$	$-15° \pm 2.4°$	$-18.3° \pm 3.1°$	$40\% \pm 2.1\%$	$41.7\% \pm 2.4\%$	29/31	29/31
4	$33° \pm 3.5°$	$32.6° \pm 6.2°$	$-17° \pm 2.6°$	$-17.5° \pm 2.3°$	$40\% \pm 2.0\%$	$42.1\% \pm 3.0\%$	23/30	27/30
5	$32° \pm 5.1°$	$31.4° \pm 6.9°$	$-18° \pm 2.7°$	$-20.0° \pm 2.7°$	$40\% \pm 0.9\%$	$42.6\% \pm 2.5\%$	27/31	28/31
6	$33° \pm 3.2°$	$33.4° \pm 5.6°$	$-18° \pm 2.5°$	$-19.4° \pm 2.5°$	$40\% \pm 1.7\%$	$42.7\% \pm 3.0\%$	29/31	30/31
7	$33° \pm 4.8°$	$31.8° \pm 5.2°$	$-18° \pm 2.6°$	$-18.4° \pm 2.5°$	$40\% \pm 1.1\%$	$43.2\% \pm 3.1\%$	26/30	29/30
Overall	$32° \pm 4.1°$	$32.9° \pm 6.1°$	$-16.6° \pm 2.5°$	$-17.7° \pm 2.6°$	$40\% \pm 1.5\%$	$41.8\% \pm 3.8\%$	156/180	168/180

deviation of the RMSE values obtained for the valid gait cycles of the treadmill walking experiment, i.e., $\gamma_{\text{GCVS}} = 0.50$. If a segment is a valid gait cycle, then we compute the toe-off and heel-strike events using (6.24) and (6.25), respectively. Table[3] 6.2 compares the performance our proposed method with an existing method implemented by Mobility Lab software (MLBS) [50]. The MLBS gait segmentation algorithm is based on a fixed thresholding method developed in [109]. To evaluate the performance of our proposed method, we define four metrics [50].

1) The *toe-off angle* of the foot is the angle of the foot as it leaves the floor at push-off. The pitch of the foot when flat is zero.

2) The *heel-strike angle* of the foot is the angle at the point of initial contact. The pitch of the foot is zero when the foot is flat, and positive when the heel makes first contact.

3) The *gait cycle* consists of exactly one heel-strike and one toe-off event, in that order, between two consecutive flat foot events.

4) *Swing* is defined as the percentage of the gait cycle during which the foot is not on the ground, i.e., it is the ratio of the time between the last heel-strike and toe-off events to the time of the corresponding gait cycle.

When computing the number of valid gait cycles using video data, we ignore the first stride because the foot starts from a midstance event. A gait cycle in the video data is defined as a valid gait cycle if it if it consists of exactly one heel-strike and one toe-off event, in that order, between two consecutive midstance events. In Table 6.2, we use the DWT template $\boldsymbol{k}_{\text{T}}$ generated in the fifth trial and evaluate the performance of our method in

[3]Results obtained in the first trial were not included because no video was available

the remaining trials. We use a zero-velocity aided foot-mounted inertial navigation system (INS) described in [49, 122, 141] to estimate the pitch angle of the foot during the gait. The INS uses the accelerometer and gyroscope sensor measurements along with the zero-velocity event intervals [1, 79, 142] to estimate the position, velocity, and orientation of the foot via dead reckoning [143]. As can be seen in Table 6.2, our proposed method detects equal or more number of gait cycles than the existing method across all trials, except the second, of the treadmill walking task. In addition, the average values of the estimated toe-off and heel-strike angles are within one standard deviation of the existing method values.

To demonstrate the robustness of our proposed approach, we use the left foot DWT template generated in the fifth trial of the treadmill experiment for a healthy participant, and compute the number of gait cycles detected for inertial sensor data collected in Appendix A.2. In Table 6.3, we report the performance of our proposed method for two tasks whose descriptions are as follows:

1) Timed up and go (TUG): The participant stands up, walks 3 meters from the chair, turns, walks back, and returns to a sitting position.

2) Stand and walk (SAW): The participant stands at one end of the walkway, with their feet comfortably apart and their hands on their hips, for 30 seconds, when a tone sounds. Then the participant walks 7 meters, turns, walks back, and stops, now facing the opposite direction of their starting position.

The ground truth was again determined using video data. We ignored the open-ended walk task dataset because the participant's gait was not captured in the video data during some instances of the trial. As can be seen in Table 6.3, our proposed method demonstrates an improved performance in detecting valid gait cycles across different tasks. In addition,

Table 6.3: Performance of MLBS and GCVS algorithms

PID #	TUG1		TUG2		SAW	
	MLBS	GCVS	MLBS	GCVS	MLBS	GCVS
01	1/3	3/3	1/4	4/4	7/10	9/10
02	5/13	13/13	7/13	10/13	18/20	19/20
03	0/6	6/6	0/7	7/7	5/8	8/8
05	0/4	3/4	1/5	5/5	0/8	7/8
08	1/6	6/6	0/6	6/6	7/12	11/12
09	0/6	5/6	0/7	7/7	7/10	10/10
10	0/3	2/3	0/5	5/5	5/8	8/8
Overall	7/41	38/41	9/47	44/47	49/76	72/76

our proposed method also detected gait cycles during turns when the gait did not involve pivoting using either of the two feet.

6.5 Numerical Results

In this section, we compare our proposed method with existing methods based on either thresholding or template matching and thresholding. We use the prefixes online (ON) and offline (OFF) to indicate if an existing method can be implemented in real time. The details of implementing the existing methods are as follows:

- The peak detection (OFF-PDT) algorithm is an offline implementation of the gait cycle validation and segmentation algorithm which works on the principle of thresholding the gyroscope signal in the sagittal plane [109]. In the first step, the gyroscope signal is filtered using a high-pass IIR filter with cutoff frequency 0.25 Hz. Next, the mid-swing area is determined by finding the local maxima of the gyroscope signal. Only peaks that are greater than 50°/sec are considered. In addition, if multiple adjacent peaks within 500 millisecond are detected, the peak with the highest amplitude is

selected. In the final step, the local minimum peaks within a ± 1.5 millisecond interval around the local maxima are searched such that the amplitudes of the local minima are less than $-20°$/sec, and the two local minimums on either side of the mid-swing peak, representing the toe-off and heel-strike events, are separated by at least 200 milliseconds.

- The subsequence dynamic time warping (OFF-SDTW) is an offline implementation of the gait cycle validation and segmentation algorithm which works on the principle of thresholding and template matching [113]. To generate a template of a valid gait stride, the gyroscope measurement in the sagittal plane obtained from 25 elderly individuals performing a 40 meter walk protocol, is manually segmented, scaled, and interpolated. Given an input sequence of gyroscope measurements in the sagittal plane, the OFF-SDTW algorithm scales the amplitude of the gyroscope measurements, and constructs a distance matrix which captures the similarity measurements between the input sequence and template. Note that the method proposed in [113] can also be extended to multidimensional axes, however, in this work we only considered the sagittal axis of the gyroscope. In the next step, matrix which represents the accumulated cost of warping the template to parts of the input sequence is constructed. Thereafter, the local minima of the top row of the accumulated cost matrix, which represents the starting points of the warping paths are determined using a fixed threshold $\gamma_{\text{OFF-SDTW}}$. Finally, a monotonically decreasing path, called the "warping path," is traced from the local minima in the first row of the accumulated cost matrix to the last row of the accumulated cost matrix. Additional constraints based on the duration and overlapping regions of the warping paths are also applied to remove outliers. In our work, we determined the optimal value of the threshold $\gamma_{\text{OFF-SDTW}}$ by manually incrementing

its value in steps of five and selected the one that gave the best results. We used a fixed threshold of $\gamma_{\mathrm{OFF-SDTW}} = 20.0$ in all our simulations.

- Dynamic time warping (ON-DTW) is a real-time implementation of the gait cycle validation and segmentation algorithm which constructs a distance grid between the given input sequence and the template signal, and finds the shortest path through the grid which minimizes the total distance between the two sequences [120]. The total distance of the shortest path is the measure of similarity between the two sequences. For example, if the input sequence is exactly same as the template sequence, then the measure of similarity is zero. However, in many practical scenarios, it is very rare for the input sequence to match the template sequence. Therefore, in practice, a certain fixed threshold $\gamma_{\mathrm{ON-DTW}}$ is used to determine sequences that match closely with the template sequence. In addition, we applied a fourth-order zero-phase low-pass Butterworth filter with a cutoff frequency of 15 Hz to smooth and reduce the variance of the similarity measure of the input sequence. To generate a template signal, we scaled, interpolated, and computed the average of the non-stationary segments gyroscope signal in the sagittal plane for the second experiment of the treadmill walking task. Analogous to the GCVS algorithm, a similarity metric is computed between the template signal, and the scaled and interpolated non-stationary segment of the gyroscope signal in the sagittal plane. If the similarity metric is less than a fixed threshold $\gamma_{\mathrm{ON-DTW}}$, then the non-statioanry segment represents a valid gait cycle. In our work, we set $\gamma_{\mathrm{ON-DTW}}$ as two standard deviations from the mean value of the similarity measure obtained across all valid gait segments of the second trial of the treadmill walking experiment, i.e., we use a fixed threshold of $\gamma_{\mathrm{ON-DTW}} = 4.0$ in all our simulations.

We did not include the MLBS in our analysis because the proprietary software supports sensor data from APDM Opal sensors only. However, the MLBS uses OFF-PDT to validate and segment a gait cycle.

6.5.1 Fixed Sampling Rate (Excluding Turns)

Data Collection, Tasks, and Manual Segmentation

We evaluate the proposed and existing methods using a publicly available inertial sensor database [113, 144]. The database consists of 45 participants, equally divided into three groups, namely control participants, participants with Parkinson disease, and geriatric participants. More details about the participants included in the study can be found in [113, Table I]. Inertial measurement units manufactured by Shimmer Sennsing were mounted laterally to the heel of the participant's right and left shoe to acquire inertial sensor data from both feet simultaneously [51]. The data was recorded at a sampling rate of 102.4 Hz. The participants were asked to perform two tasks:

- 40 meter walk: In this task, the participant walks along a 10 meter straight path at a comfortable self-selected speed, turns, walks back, returns to the starting position, and repeats this routine two times.
- Free walk: In this task, the participant walks for two minutes at a comfortable self-selected speed around the University Erlangen Hospital where the study was conducted.

Only strides from straight walking were identified and labeled as ground truth. Turning movements with more than 45° per stride were excluded in the free walk protocol. We refer to the video data as gold standard data.

Metrics

To evaluate the proposed and existing gait cycle validation and segmentation algorithms, we define three variables. The definition of each variable is as follows:

- *Detection positives*: The number of strides identified by the selected gait cycle validation and segmentation algorithm.
- *True positives*: The number of strides identified by the selected gait cycle validation and segmentation algorithm, and also labeled as valid stride in the gold standard data.
- *False negatives*: The number of strides not identified by the selected gait cycle validation and segmentation algorithm.

Based on these variables, we define three performance metrics namely precision, recall, and F1 score. Precision is defined as the ratio of the number of true positives to the number of detection positives. Precision is equal to one if all the strides identified by the selected algorithm are labeled in the gold standard data. Recall is defined as the ratio of the number of true positives to the sum of the number of true positives and false negatives. Recall is equal to one if no false negatives are identified, i.e., no stride is missed. F1 score is the harmonic mean of precision and recall, and takes into account missing strides and wrongly detected strides.

Data Analysis

In Table 6.4 and 6.5, we present the average value of the performance metrics for the proposed and existing methods. The best results are obtained for the OFF-SDTW algorithm [113]. However, the OFF-SDTW algorithm cannot be implemented in real time because the accumulated cost matrix requires access to the entire input sequence. Furthermore, the OFF-SDTW algorithm is also computationally expensive because identifying the warping path requires a grid search operation of complexity $\mathcal{O}(PQ)$, where P and Q are the lengths of the template and input sequence, respectively. In contrast, the OFF-PDT algorithm is computationally inexpensive, but the performance varies depending on the task selected. In addition, the precision values of the OFF-PDT algorithm are lower than the OFF-SDTW method because turns were neglected in the gold standard. The ON-DTW algorithm performs poorly for geriatric participants because there is a significant mismatch between the template of a valid gait cycle of a healthy and geriatric participant. The proposed ON-GCVS algorithm demonstrates high recall values across control participants and participants with Parkinson disease. However, the precision is slightly lower because our proposed method can also detect gait cycles during turns which were not included in the gold standard for database in [113]. In the case of geriatric participants, our proposed method performs significantly better than the ON-DTW algorithm even when there is a mismatch between the template of a valid gait cycle of a healthy and geriatric participant.

Table 6.4: Performance of the proposed and existing methods for the 40 meter walk task.

Method	40 Meters WALK												
	Controls				PD Patients				Geriatric Patients				Average
	Precision	Recall	F1 Score	Time	Precision	Recall	F1 Score	Time	Precision	Recall	F1 Score	Time	F1 Score
OFF-PDT	79.91%	97.57%	87.78%	0.036	80.07%	98.61%	88.32%	0.035	80.23%	100.0%	88.93%	0.050	88.34%
OFF-SDTW	83.66%	100.0%	90.98%	0.611	81.85%	100.0%	89.98%	0.628	92.01%	97.40%	94.56%	1.506	91.84%
ON-DTW	84.71%	93.14%	88.20%	0.001	82.69%	86.41%	83.16%	0.001	93.59%	62.49%	68.23%	0.002	79.86%
ON-GCVS	79.12%	100.0%	88.25%	0.020	79.10%	100.0%	88.28%	0.018	84.72%	91.40%	86.34%	0.017	87.62%

Table 6.5: Performance of the proposed and existing methods for the free walk task.

Method	Free WALK												Average
	Controls				PD Patients				Geriatric Patients				
	Precision	Recall	F1 Score	Time	Precision	Recall	F1 Score	Time	Precision	Recall	F1 Score	Time	F1 score
OFF-PDT	73.46%	100.0%	84.68%	0.219	76.43%	100.0%	86.57%	0.190	76.13%	99.47%	86.13%	0.178	85.79%
OFF-SDTW	79.00%	99.83%	88.13%	4.161	84.04%	99.81%	91.18%	5.250	86.86%	97.42%	91.76%	6.571	90.35%
ON-DTW	90.00%	98.08%	93.86%	0.003	81.85%	80.32%	80.08%	0.003	93.65%	66.67%	70.22%	0.002	81.38%
ON-GCVS	77.65%	100.0%	87.39%	0.019	80.08%	98.70%	88.17%	0.019	82.91%	95.30%	88.27%	0.020	87.94%

6.5.2 Variable Sampling Rate (Including Turns)

Data Collection, Tasks, and Manual Segmentation

We evaluate the threshold invariance property of the proposed and existing methods using real data collected from 16 participants with Parkinson disease [1], given in Appendix A.1. To assess gait, we assigned the participants several tasks one of which was the 12 meter walk task. In the 12 meter walk task, the participant was asked to walk forward along a full 6 meter straight path. On reaching the end, the participant made a 180° turn and returned to the starting point. The ground truth or gold standard was obtained using video data. For the database in Appendix A.1, turning movements were also included in the gold standard.

Template Generation

Generating a template is essential in both the ON-DWT and ON-GCVS algorithms especially when the sampling rate varies. To select training data for template generation, we used two criteria: a) the participant did not exhibit freezing of gait or any abnormal gait pattern during the trial, and b) the number of valid gait segments was maximum across all participants. Only participant TT022 matched the criteria for data selection, and the sensor data from valid gait cycle segments was used to generate the DWT coefficient template $\boldsymbol{k}_{\mathrm{T}}$ and DTW template sequence.

Table 6.6: Performance of the existing and proposed methods for the free walk task [1].

Method	12 Meters WALK												Average
	$F_s = 125$ Hz				$F_s = 250$ Hz				$F_s = 500$ Hz				
	Precision	Recall	F1-Score	Time	Precision	Recall	F1-Score	Time	Precision	Recall	F1-Score	Time	F1 Score
OFF-PDT	86.88%	98.80%	92.26%	0.112	86.94%	99.52%	92.75%	0.107	86.16%	99.52%	92.25%	0.196	92.42%
OFF-SDTW	88.89%	90.69%	89.93%	0.754	84.58%	88.38%	86.25%	1.421	77.32%	81.86%	79.43%	2.982	85.20%
ON-DTW	92.53%	90.14%	91.48%	0.001	64.58%	26.00%	36.64%	0.001	00.00%	00.00%	00.00%	0.001	42.70%
ON-GCVS	90.87%	100.0%	95.19%	0.020	88.77%	99.28%	93.65%	0.128	79.53%	100.0%	88.48%	0.054	92.44%

Data Analysis

In Table 6.6, we present the results of the average values of precision, recall, and F1 score for the 12 meters walk task, for the proposed and existing methods. The thresholds of the proposed and existing methods are held constant and only the sampling rate of the sensors are varied. We used the same performance metrics as defined in Section V-A. As can be seen in Table 6.6, the performance of the OFF-SDTW algorithm decreases as the sampling rate of the sensors increases because the entries of the accumulated cost matrix vary based on the sampling rate. Further, the computational cost of identifying the warping path also increases with the sampling rate. A like trend in the computational cost is also observed for the OFF-PDT algorithm. However, the performance of the OFF-PDT algorithm remains consistent across varying sampling rate because the amplitude of the signal remains unaffected by changing the sampling rate. The ON-DTW performs poorly on increasing the sampling rate because the similarity metric value between the template and the input sequence increases on increasing the sampling rate. In contrast, the proposed ON-GCVS method is computationally inexpensive and takes approximately 0.067 seconds on an average per dataset. Furthermore, the F1 score of the proposed method is as good as the offline implementation of the PDT algorithm and significantly better than the existing real time method.

6.6 Chapter Summary

We developed a robust and computationally efficient framework to validate and segment a gait cycle in real time. We first used the physical models of sensor data from a foot-mounted inertial system to detect the stationary and moving segments in the sensor data. Thereafter,

to validate a moving segment of sensor data as a gait cycle, we developed an optimization routine called sparsity-assisted wavelet denoising. In SAWD, we combined low-pass filtering, wavelets, and sparsity-based methods to extract a sparse template of a valid gait cycle in the form of DWT coefficients with minimum RMSE. Finally, we detected midstance, toe-off, and heel-strike by finding the local minima of the stationary and non-stationary regions of a valid gait cycle. We demonstrated the robustness of our proposed approach by extracting a DWT coefficient template from a healthy participant, and applying it to sensor data obtained from control participants, participants with Parkinson disease, and geriatric participants. Our results showed a consistent performance, with an average F1 score of 87.78% across all groups for a fixed sampling rate. In addition, we also demonstrated the threshold invariance property of our proposed method by keeping the threshold fixed and varying the sampling rate. Our proposed method yielded an average F1 score of 92.44% across all Parkinson disease participants for a variable sampling rate.

In the next chapter, we integrate the gait cycle validation and segmentation module with our existing system design to detect and track freezing of gait in Parkinson disease, and improve the accuracy of detecting and/or predicting freezing of gait.

Chapter 7

System Integration: A Modular Approach

In this chapter, we develop a modular approach to track freezing of gait (FOG). The proposed method adapts to individual gait patterns and automatically detects FOG patterns explicitly in real time. Our modular approach consists of four modules, namely detection, navigation, validation, and filtering. We begin by detecting gait patterns associated with FOG, such as alternating trembling and no movements, by using the physical models of the inertial sensor data that describe these gait patterns during the FOG events. Thereafter, to filter falsely detected FOG events, we use the navigation and validation module to extract information about the gait. In the navigation module, we use a zero-velocity aided inertial navigation system to estimate the position, velocity, and orientation angles of the foot. In the validation module, we identify non-stationary segments of the inertial sensor data as valid gait cycles. Finally, the filtering module combines the output of the detection module with the weights generated using a participant-specific tunable parameter, the extracted gait parameters, and the information from the valid gait cycles, and computes the probability of FOG (pFOG). We develop two novel methods to automatically adjust the participant-specific tunable parameter

based on the foot motion dynamics. We validate the performance of the proposed system design using real data obtained from people with Parkinson disease who performed a set of gait tasks. The results indicate improved performance, with an average accuracy greater than 85% and an average false positive rate of less than 14%.

7.1 Introduction

Parkinson disease is the second most common neurodegenerative disorder, affecting 1-1.5 million people in the United States alone. The main pathological process in Parkinson disease is a loss of dopaminergic subcortical neurons, which leads to various motor impairments [2]. Approximately 50% of people with Parkinson disease experience freezing of gait [3,4] (FOG), a brief, episodic absence or marked reduction of forward progression of the feet despite the intention to walk. FOG causes falls and is resistant to medication in more than 50% of cases [5,6]. FOG episodes can often be interrupted by mechanical interventions or strategies (e.g., a verbal reminder to march), but it is often not practical to apply these interventions on demand (e.g., there is not usually another person to detect an FOG episode and provide the reminder). Wearable sensors offer the possibility of detecting FOG episodes in real time and thus developing a "closed-loop" approach to treatment: real-time detection could be coupled with on-demand interventions to reduce the duration of FOG episodes.

The gold standard of FOG assessment involves evaluation of video recordings of ambulating participants by expert raters of FOG [25], with a variable inter-rater reliability, ranging from low to good [26]. However, this approach offers limited information about the frequency and patterns of FOG away from the laboratory environment and requires substantial training of raters and time-consuming off-line data analysis [27]. In the last decade, objective evaluation

methods using wearable sensor technology to monitor and assess FOG have been developed with varying success [7–9]. Experiments have primarily been conducted for understanding the bilateral coordination [10–13] of steps during gait, using force resistive sensors embedded in the sole of the shoe. They have also employed analysis of the spectral characteristics of the accelerometry signal [14–16] from devices attached to the lower extremities, or have used methods from machine learning [17–21] to classify features extracted from inertial sensor data. For example, researchers extracted spectral characteristics of the accelerometer signal and demonstrated that the power of the signal belongs to two non-overlapping spectral bands during FOG and normal gait [14]. The use of machine learning methods to classify features extracted from the accelerometer signal that capture the uncoordinated nature of the gait, such as trembling of the feet, short stride lengths, and unstable walking, is explored in [17–21, 145]. However, these methods do not present a signal model that captures the FOG patterns explicitly, and they provide limited utility for understanding the potential underlying mechanisms revealed by the structure of the sensor data during FOG. Further, methods based on spectral characteristics of the accelerometry signal completely ignore the effect of various sources of error in the sensor [29]. Finally, the use of long window lengths to extract features from the sensor data often lead to delays in determining the onset of the FOG event, thus hindering use in a real-time framework.

To address these shortcomings, we developed physically-based signal models for the sensor data associated with the FOG patterns. Based on these models, we designed statistical signal processing methods that detect the onset and duration of the FOG events. The three modules of our system are detection, tracking, and filtering. The detection module contains two fixed-threshold detectors to determine instances of alternating trembling intervals and no-movement (zero-velocity) intervals. We considered these thresholds as fixed because they are not sensitive to the individual gait patterns. To identify FOG gait patterns involving

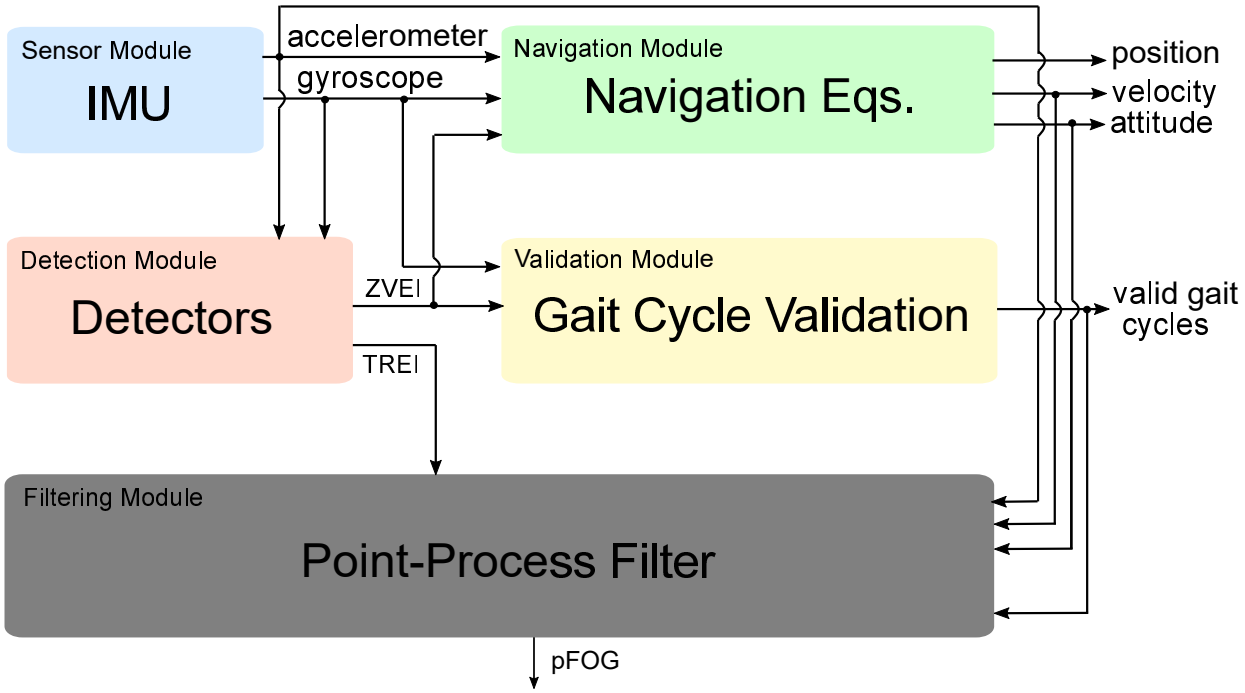

Figure 7.1: Overview of the proposed system design to detect and track FOG in Parkinson disease.

alternating trembling in the lower extremities, and quickening steps on the toes and ball of the feet in festinating gait, we exploited the fact that these events are associated with alternating trembling motions of the sensor about a fixed axis and modeled them as trembling event intervals (TREI). Similarly, to identify FOG gait patterns such as no movement of limbs, we used the fact that these events are associated with zero-velocity and modeled them as zero-velocity event intervals (ZVEI). In Chapter 3, we modeled the inertial sensor data for the gait patterns observed during FOG, and detected ZVEI and TREI. However, not all trembling and zero-velocity event intervals detected are associated with FOG. For example, trembling intervals are associated with the heel lift-off and heel strike phases of a gait cycle, and zero-velocity event intervals are associated with the flat foot phase of a gait cycle. Therefore, to filter out gait events not associated with FOG, we considered the fact that FOG is associated with small foot speeds [78]. We used a zero-velocity aided inertial navigation

system and estimated the speed of the foot. In Chapter 4, we briefly described the navigation mechanization equations of a zero-velocity aided foot-mounted inertial navigation system (ZV-INS), which estimated the position, velocity, and orientation angles of the foot during gait. To detect the onset and duration of the FOG events, we developed a point-process filter which computed the probability of FOG (pFOG). We first modeled the edges of the TREI as point-process, and assigned weights to the edges, which depended on the average value of the speed of the foot at the edge and a participant-specific tunable parameter. The participant-specific tunable parameter determined the weight, which was inversely proportional to the average value of the speed of the foot. Then, we integrated these weights over a time window, using a Bayesian recursive filter. In Chapter 5, we derived a point-process filter which combined the TREI with the weights assigned, and computed pFOG. Note that, in our previous work, the participant-specific tunable parameter was adjusted manually for every participant based on their gait patterns. This adjustment required a thorough grid search operation, which was a tedious and computationally expensive task. In addition, a value of the tunable parameter that was participant-specific but fixed over time was unlikely to be adequate. Ideally, the parameter should be adapted to specific gait patterns, which are subject to change depending on the participant's gait, symptoms, and treatment strategy.

To overcome the need to manually tune the participant-specific parameter, here we propose a modular approach to detect and track FOG in Parkinson disease. In our previous work, our system design comprised of three modules: detection, navigation, and filtering [1]. Our main contribution in this works involves incorporating a gait cycle validation module, and using the information from the gait cycle validation module to adaptively tune the participant-specific parameter. In particular, we use the output of the validation module and modify the point-process filter in the filtering module. In Chapter 6, we developed the gait cycle validation and segmentation algorithm. We propose two new methods to automatically adapt

the participant-specific tunable parameter, using the gait information extracted from the last valid gait cycle. In the first approach, we extend our previous method [1] by automatically tuning the participant-specific tunable parameter based on the average value of the foot speed observed in the last valid gait cycle. We modify the weights assigned to the edges of the trembling event intervals dynamically using the average value of the speed of the foot in the last valid gait cycle. In the second approach, to automatically select the participant-specific tunable parameter, we first evaluate three gait parameters, namely speed, pitch angle, and freeze index [14] of the foot, by computing their average values during valid gait cycles and FOG events. The weight assigned to the edge of the trembling event interval is a weighted average of the selected gait parameters. In addition, we also modify the conditional intensity function of the point-process filter by dynamically adapting the background spiking rate, based on the density of the spikes due to the edges of the trembling event intervals. Finally, we use the output of the gait cycle validation module to reset the point-process filter and also filter those edges of the trembling event intervals that do not belong to a FOG event. In other words, if the trembling event interval belongs to a valid gait cycle, then the weights assigned to the edges of the trembling event intervals that belong to the valid gait cycle event are set to zero because they do not contribute to FOG. To demonstrate the capabilities of the proposed modular approach, we will present an illustrative example using real data. We evaluate the method's performance on data obtained from participants with Parkinson disease. The proposed method promises to speed the development of a personalized healthcare gait analysis system using inertial sensors.

Sections 7.2.1 and 7.2.2 propose two novel methods to automatically select the participant-specific tunable parameter, based on the foot motion dynamics. With the help of an illustrative example, in Section 7.3 we demonstrate the output of each system module. In Section 7.4, we present the experimental results. Our conclusions are presented in Section 7.5.

7.2 Adaptive Approach

In this section, we propose two novel methods to automatically select the participant-specific tunable parameter. Developing a closed-loop system design involves dynamically adjusting the weights assigned to the edges of the trembling event intervals based on the information extracted from the gait in the last valid gait cycle and the gait parameters observed at the edges of the trembling event intervals at the current time.

7.2.1 Average Foot Speed

In the first approach, we assign weights to the edges of the trembling event intervals based on the average value of the foot speed observed in the last valid gait cycle. Because degradation of gait occurs prior to a FOG episode [146] and FOG is associated with small foot speeds [78], we use the average value of the speed of the foot in the last valid gait cycle.

In Chapter 5, we modeled the edges of TREI as a point-process. We assigned weights to the edges of the trembling event intervals by computing the average value of the speed of the foot in the bin intervals $((k-1)\Delta, k\Delta]$, where $k \in \mathbb{N}$ is the bin number and Δ is the bin width in seconds or samples [1]. Here, to assign weights to bins, we used a Gaussian kernel with zero mean and σ_{s} standard deviation, defined as the participant-specific tunable parameter, and given as

$$w_k = (1/\sqrt{2\pi\sigma_{\mathrm{s}}^2}) \exp\left(-x^2/(2\sigma_{\mathrm{s}}^2)\right), \tag{7.1}$$

where w_k is the weight assigned and x is the average value of the speed of the foot observed in a bin containing a rising or falling edge of the trembling event interval. The main purpose

of using a Gaussian kernel was to bound the weights assigned to the edges of the trembling event intervals. Bins with small foot speeds were assigned large weights, and vice versa. The participant-specific tunable parameter was adjusted manually for every participant, based on their gait patterns, so that the number of FOG events detected was maximized. However, a value of the tunable parameter that was fixed is unlikely to be adequate because gait patterns change with the participant's gait symptoms and treatment intervention strategies.

To overcome the need for manual tuning, we use the average value of the speed of the foot from the last valid gait cycle and automatically tune the participant-specific tunable parameter. We use the same Gaussian kernel as before. If $\bar{v}$ denotes the average value of the speed of the foot in the last valid gait cycle, then the participant-specific tunable parameter σ_{s} is adjusted as shown in Fig. 7.2. In other words, the algorithm dynamically selects one Gaussian probability density function among those shown in Fig. 7.2 and generates weights using equation (7.1) for the edges of the trembling event intervals in the current bin. We initialize the participant-specific tunable parameter σ_{s} to 0.40 because a unit weight is assigned to the edge of the trembling event interval if the average speed of the foot in the current bin is close to zero. Further, if $\sigma_{\mathrm{s}} = 0.40$, then the average foot speeds belong to $(1.00, 1.25]$ m/sec. This range of average foot speeds overlaps with the walking speeds of the healthy controls who belong to the same age group as participants selected in this experiment [147]. Starting at an initial value of $\sigma_{\mathrm{s}} = 0.40$, the participant-specific tunable parameter automatically adjusts itself based on the average value of the speed of the foot in the last valid gait cycle. We call our proposed method as "pFOG via average foot speed" (pFOG-AFS). The details of implementing the pFOG-AFS algorithm are same as Algorithm 2 in Chapter 5, except that the weights assigned to the TREI are updated every time the bin interval $((k-1)\Delta, k\Delta]$ belongs to the trailing edge of a valid gait cycle event. Furthermore, we use the information about the validity of the gait cycle to reset the point-process filter,

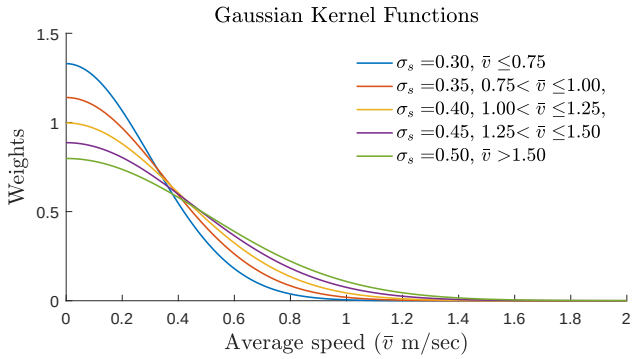

Figure 7.2: Gaussian kernel functions with zero mean and standard deviation equal to the participant-specific tunable parameter σ_{s}. The parameter σ_{s} is initialized to 0.40.

i.e., when the bin $((k-1)\Delta, k\Delta]$ contains information about the trailing edge of a valid gait cycle event, then

$$\boldsymbol{\theta}_{k|k} = \boldsymbol{\theta}_{0|0}, \tag{7.2}$$

$$\boldsymbol{J}_{k|k} = \boldsymbol{J}_{0|0}. \tag{7.3}$$

7.2.2 Weighted Average of Gait Parameters

In the second approach, we modify the conditional intensity function in (5.6) by dynamically adapting the background spiking rate. We also use a multi parameter model to assign weights to the bins containing edges of the trembling event intervals. To modify the conditional intensity function, we first consider a variable background spiking rate of the trembling event intervals, i.e., α is not longer fixed and it varies with k, where k denotes the index of the bin interval $((k-1)\Delta, k\Delta]$. Let $\boldsymbol{\eta}_k = [\alpha_k, \boldsymbol{\theta}_k^{\mathsf{T}}]^{\mathsf{T}}$ denote the latent parameter, then the modified conditional intensity function is given as

$$\lambda_k(\boldsymbol{\eta}_k, \boldsymbol{H}_k) = \alpha_k + \beta(\boldsymbol{\theta}_k^T \boldsymbol{W}_k \boldsymbol{\theta}_k), \tag{7.4}$$

where $\boldsymbol{\theta}_k = [\theta_{k,0}, \cdots, \theta_{k,\ell-1}]^T \in \mathbb{R}^{\ell \times 1}$ is the latent parameter vector, $\boldsymbol{W}_k = \text{diag}\{w_k \delta B_k, \ldots, w_{k-\ell+1} \delta B_{k-\ell+1}\} \in \mathbb{R}^{\ell \times \ell}$ denotes the matrix containing the weights observed in $((k-\ell-1)\Delta, (k-1)\Delta]$, $\boldsymbol{H}_k = [\delta \boldsymbol{B}_{k-\ell-1:k-1}, \boldsymbol{b}_{k-\ell-1:k-1}, \boldsymbol{w}_{k-\ell-1:k-1}]$ is the history of the activity of the spikes modeled as the edges of the trembling event intervals observed in $((k-\ell-1)\Delta, (k-1)\Delta]$, and ℓ is the length of the history. The parameters $\delta \boldsymbol{B}_{k-\ell-1:k-1} = [\delta B_{k-\ell-1}, \cdots, \delta B_{k-1}]$, $\boldsymbol{b}_{k-\ell-1:k-1} = [b_{k-\ell-1}, \cdots, b_{k-1}]$, and $\boldsymbol{w}_{k-\ell-1:k-1} = [w_{k-\ell-1}, \cdots, w_{k-1}]$ denote the activity of observable parameters of TREI up to time $k\Delta$, where δB_k and b_k denote an indicator variable[4] and the number of spikes in the interval $((k-\ell-1)\Delta, (k-1)\Delta]$, respectively.

We use the same approach as described in Appendix D.1 and derive the point-process filter. The equations of the point-process filter are same as (5.11a)-(5.11d), however, we replace $\boldsymbol{\theta}_k$ with $\boldsymbol{\eta}_k$. In addition, the first and second derivative of $\lambda_k(\boldsymbol{\eta}_k, \boldsymbol{H}_k)$, denoted by $\lambda'_k(\boldsymbol{\eta}_k, \boldsymbol{H}_k)$ and $\lambda''_k(\boldsymbol{\eta}_k, \boldsymbol{H}_k)$, respectively are given as $[1, 2\beta \boldsymbol{\theta}_k^T \boldsymbol{W}_k^T]^T$ and $\text{diag}\{0, 2\beta \boldsymbol{W}_k\}$. Note that by including the background spiking rate in the latent parameter vector $\boldsymbol{\eta}_k$, the size of the system evolution matrix $\boldsymbol{A}_k$, noise covariance $\boldsymbol{N}_k$, state prediction matrix $\boldsymbol{J}_{k|k-1}$, and state update matrix $\boldsymbol{J}_{k|k}$ all increase by one. Furthermore, we use the information about the validity of the gait cycle to reset the point-process filter, i.e., when the bin $((k-1)\Delta, k\Delta]$ contains information about the trailing edge of a valid gait cycle event, then

$$\boldsymbol{\eta}_{k|k} = \boldsymbol{\eta}_{0|0}, \tag{7.5}$$

$$\boldsymbol{J}_{k|k} = \boldsymbol{J}_{0|0}. \tag{7.6}$$

Note that resetting the point-process filter also resets the background spiking rate α_k to its initial value.

[4] $\delta B_k = 1$, if $b_k \neq 0$ and $\delta B_k = 0$, if $b_k = 0$.

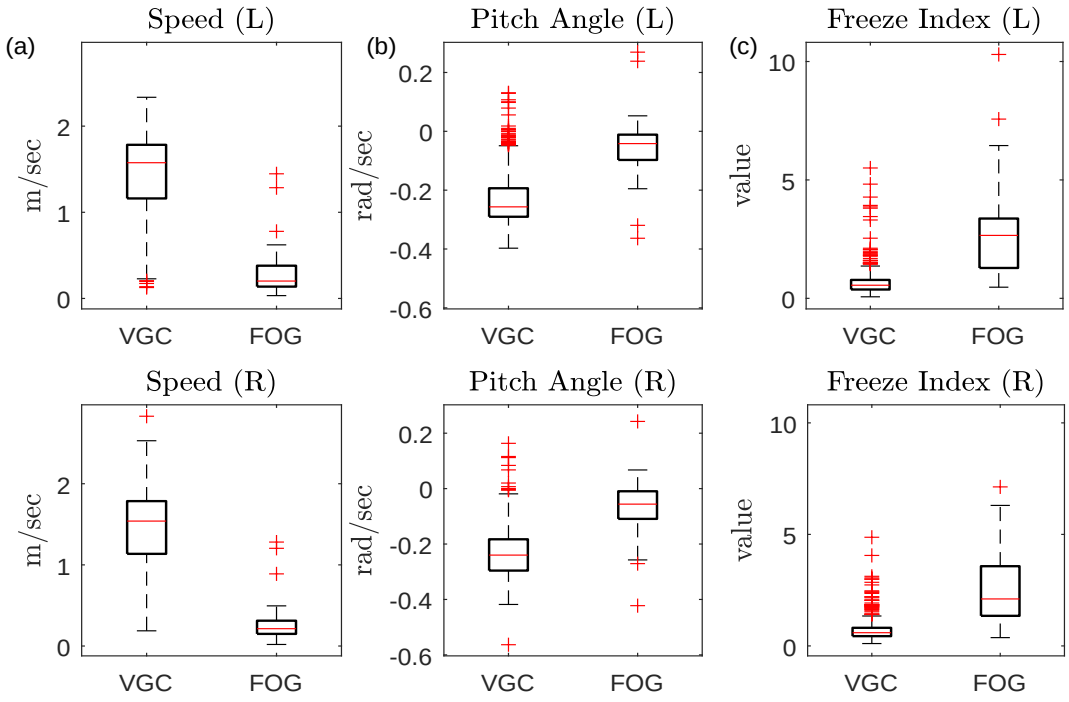

Figure 7.3: Boxplots of average values of the gait parameters during valid gait cycles (VGC) and freezing of gait (FOG) events.

Next, we assign weight to an edge of the trembling event interval, based on the weighted average of the observable gait parameters in the bin containing the edge of the trembling event interval. In our approach we consider three different gait parameters: a) speed, b) pitch, and c) freeze index [14]. Both speed and pitch are extracted from the navigation module. To calculate the "freeze index", we compute the ratio of the square of the area of the power spectrum in the 'freeze-band' and 'loco-band', using a moving window of 4 seconds. Fig. 7.3 shows the boxplot of the average values of the foot speed, pitch angle, and freeze index, for valid gait cycles (VGC) detected using the validation module and FOG events in the inertial sensor data marked by a trained gait analysis expert for the tasks listed in Appendix A.2. As can be seen, FOG is associated with small foot speeds, low pitch angles, and high freeze indices. Further, among all the selected gait parameters, the average value of the speed of the foot demonstrates less overlap between VGC and FOG events.

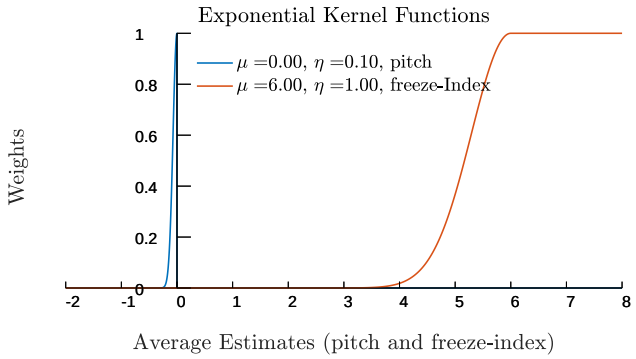

Figure 7.4: Exponential kernel function used in generating weights based on the average value of the pitch angle and freeze index of the foot.

Let $w_k^{(\mathrm{i})}$ denote the generated weight based on the selected gait parameter $\mathrm{i} \in \{\mathrm{s}, \mathrm{p}, \mathrm{f}\}$, where the superscripts $\mathrm{s}, \mathrm{p}, \mathrm{f}$, respectively denote the speed, pitch, and freeze-index of the foot. To generate a weight $w_k^{(\mathrm{s})}$ corresponding to the speed of the foot, we follow the same approach as discussed in Section 7.2.1; i.e., the weights assigned to the edges of the trembling event intervals depend on the speed of the foot in the last valid gait cycle. To generate weights for the pitch angle and freeze index of the foot, we use a squared exponential kernel function, which is defined as

$$w_k^{(\mathrm{i})} = \exp\left(-(x-\mu)^2/\tau^2\right), \tag{7.7}$$

where μ and τ respectively are the mean and characteristic length scales. Our main purpose in using the kernel function is to bound the value of the gait parameters. In Fig. 7.4, we plot the kernel functions that are mapped to the pitch angle and freeze-index of the foot. The values of μ and τ for the exponential kernel functions are determined from the boxplots in Fig. 7.3. For instance, the weights generated for pitch angles greater than zero are set to zero. Note that the weights generated are inversely proportional to the average value of the speed and pitch angle of the foot, and directly proportional to the freeze index of the foot. Finally, the weight assigned to the edge of the trembling event interval is computed as

the weighted average of the weights obtained from the selected gait parameters mapped to a corresponding kernel function, i.e., if w_k is the weight assigned to the edge of a trembling event interval, then

$$w_k = \sum_{\mathrm{i}\in\{\mathrm{s,p,f}\}}^{3} c_{\mathrm{i}} w_k^{(\mathrm{i})}, \quad \text{where} \sum_{\mathrm{i}\in\{\mathrm{s,p,f}\}}^{3} c_{\mathrm{i}} = 1, \tag{7.8}$$

and $0 \leq c_{\mathrm{i}} \leq 1$. In our work, we set $c_{\mathrm{i}} = 1/3 \quad \forall \mathrm{i} \in \{\mathrm{s,p,f}\}$. We call our proposed method "pFOG via weighted average" (pFOG-WA). The details of implementing pFOG-WA is listed in Algorithm 4.

Algorithm 4 TREI Aided Point-Process Filter

procedure pFOG_WA($\boldsymbol{v}$, $\boldsymbol{p}$, $\boldsymbol{f}$, $\boldsymbol{t}$)
  initialize:
  $k \leftarrow 0$, $\Delta \leftarrow$ bin size, $\ell \leftarrow$ length of history process
  $\boldsymbol{\eta}_{0|0}, \boldsymbol{J}_{0|0} \leftarrow$ initialize point-process filter
  MAX $\leftarrow \lceil \mathrm{len}(\boldsymbol{t})/\Delta \rceil$,
  repeat:
    $k \leftarrow k+1$
    $\boldsymbol{b}_{k-\ell-1:k-1}, \Delta\boldsymbol{B}_{k-\ell-1:k-1} \leftarrow$ generate point-process($\boldsymbol{t}$)
    $\boldsymbol{W}_k \leftarrow$ generates weights($\boldsymbol{v}, \boldsymbol{p}, \boldsymbol{f}, \sigma_s$)
    $\boldsymbol{\eta}_{k|k-1} \leftarrow \boldsymbol{A}_k \boldsymbol{\eta}_{k-1|k-1}$
    $\boldsymbol{J}_{k|k-1} \leftarrow \boldsymbol{A}_k \boldsymbol{J}_{k-1|k-1} \boldsymbol{A}_k^T + \boldsymbol{N}_k$
    $p_k \leftarrow 1/(1+\exp(-\lambda_k(\boldsymbol{\eta}_k, \boldsymbol{H}_k)))$
    $\boldsymbol{\theta}_{k|k} \leftarrow \boldsymbol{\theta}_{k|k-1} + \boldsymbol{J}_{k|k}\left[(b_k - Bp_k)\lambda_k'(\boldsymbol{\eta}_k, \boldsymbol{H}_k)\right]_{\boldsymbol{\eta}_{k|k-1}}$
    $\boldsymbol{J}_{k|k}^{-1} \leftarrow \boldsymbol{J}_{k|k-1}^{-1} + \left[(Bp_k - b_k)\lambda_k''(\boldsymbol{\eta}_k, \boldsymbol{H}_k) + Bp_k(1-p_k)\lambda_k'(\boldsymbol{\eta}_k, \boldsymbol{H}_k)(\lambda_k'(\boldsymbol{\eta}_k, \boldsymbol{H}_k))^{\mathsf{T}}\right]_{\boldsymbol{\eta}_{k|k-1}}$
    $p_k' = (1/l)\sum_{i=0}^{\ell-1} p_{k-i}$
    if $((k-1)\Delta, k\Delta]$ contains trailing edge of valid gait cycle **then**
      updates weights($\boldsymbol{v}, \boldsymbol{p}, \boldsymbol{f}, \sigma_s$)
      reset point-process filter
    end if
  until $k =$ MAX
end procedure

7.3 Illustrative Example

In this section, with the help of an illustrative example, we demonstrate the output of each module of the proposed system, shown in Fig. 7.1. We use the inertial sensor data from participant identity (PID) 08, performing a two-minute WALK task (see Table A.2 for details). During this task, the participant takes seven turns in total, and experiences turning freeze in five of the seven turns. The true instance of FOG events detected in the video data are indicated with a red background in all the figures. In Fig. 7.5(a) and 7.5(b), we plot the outputs of the three-axis accelerometer and three-axis gyroscope obtained from the right foot IMU of PID 08 for the two-minute WALK trial. Recall that the goal of Detector-I is to detect no movement or trembling motion intervals, which are modeled as ZVEI and TREI, respectively. The goal of Detector-II is to distinguish ZVEI from TREI based on the output of Detector-II. In Fig. 7.6(a) and 7.6(b), we plot those outputs of the Detector-II that are either ZVEI or TREI. The system parameters of the detection module are given in Table E.1 of the Appendix E.1. As can be seen, the density of ZVEI and TREI during FOG events increases because of the alternating trembling motion of the foot. However, Detector-II also detects TREI during straight walk. Therefore, to detect the FOG region, which is a reflection of both ZVEI and TREI, we use the fact that FOG is characterized by small foot speeds, low pitch angles, and high freeze indices.

To extract the gait parameters, such as the speed and pitch angle of the foot, we use the navigation module. The goal of the navigation module is to estimate the position, velocity, and orientation angles of the foot. In Fig. 7.7(a) and 7.7(b), we plot the speed and pitch angle of the foot, respectively. The parameters of the navigation module used to compute the speed and pitch angle of the foot are given in Table E.2 of Appendix E.1. The speed of the foot goes to zero at ZVEI. Furthermore, from Fig. 7.7(a) and 7.7(b), we can verify that

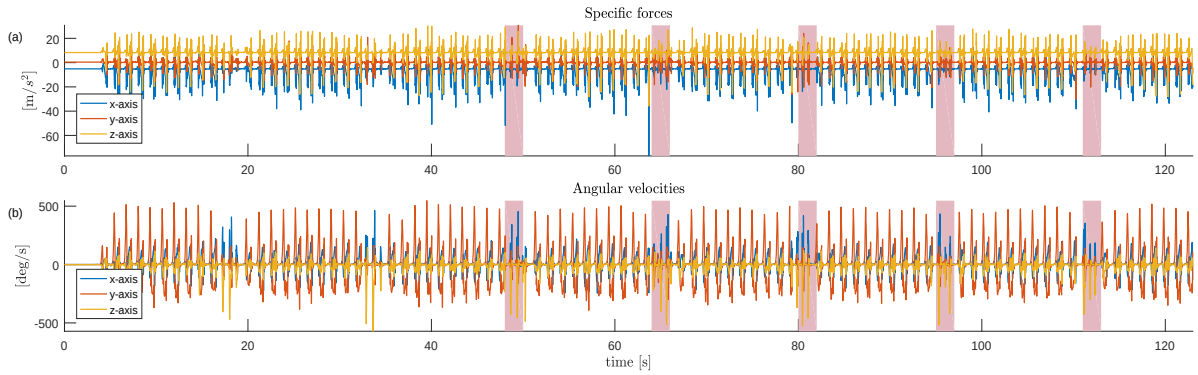

Figure 7.5: Sensor module. (a) Three-axis accelerometer measurements. (b) Three-axis gyroscope measurements.

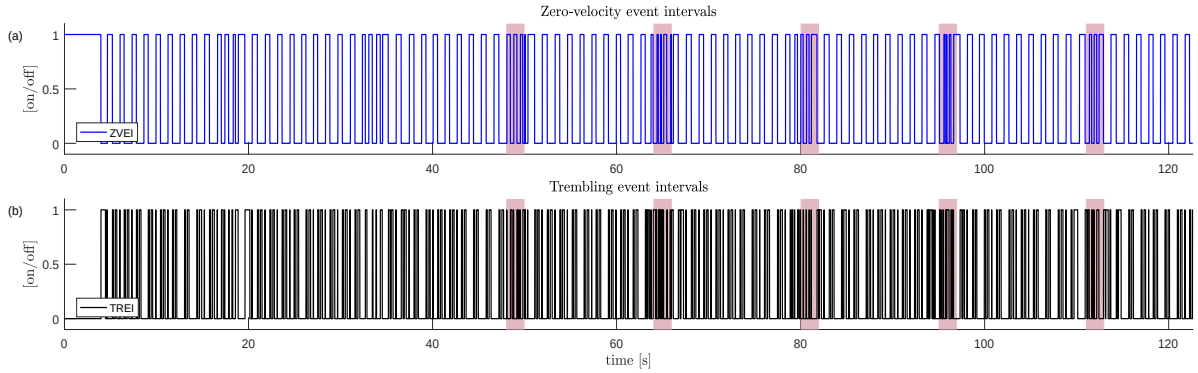

Figure 7.6: Detection module. (a) Zero-velocity event intervals (ZVEI). (b) Trembling event intervals (TREI).

FOG is indeed associated with small foot speeds and low pitch angles. We also compute the freeze index as one of the gait parameters to predict FOG. Note that the freeze index is not an output of the navigation module, but it is computed separately, using the z-axis measurements of the accelerometer signal. To calculate the freeze index, we compute the ratio of the square of the area of the power spectrum in the 'freeze-band' (3-8 Hz) and 'loco-band' (0.5-3 Hz), using a moving window of 4 seconds. The freeze index is normalized by multiplying by 100 and taking the natural logarithm [14]. In Fig. 7.7(c), we plot the freeze index value of the right foot, during FOG events, the foot demonstrates high freeze index values.

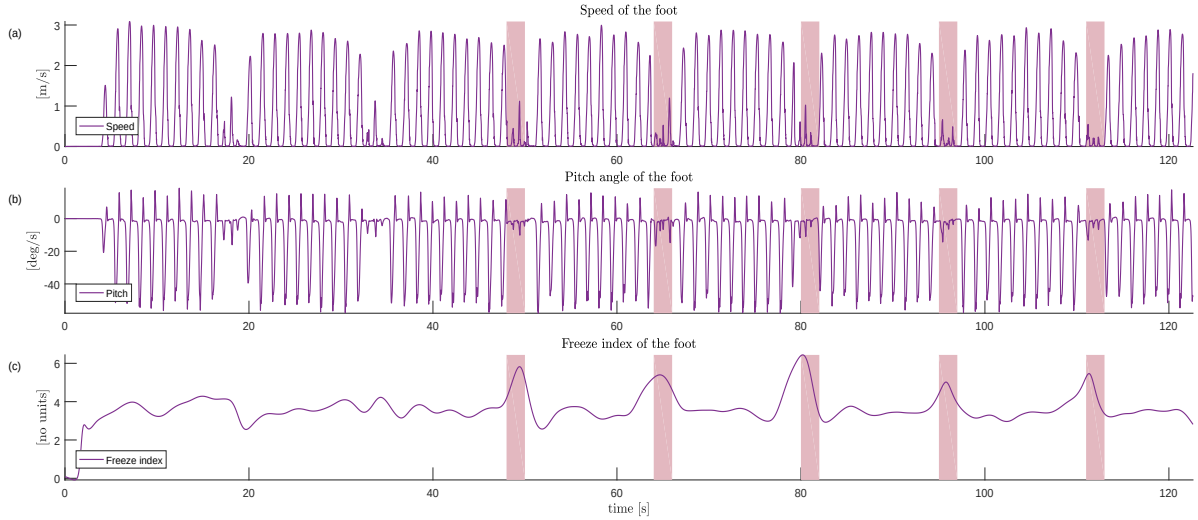

Figure 7.7: Navigation module and freeze index. (a) Speed of the foot. (b) Pitch angle of the foot. (c) Freeze index of the foot.

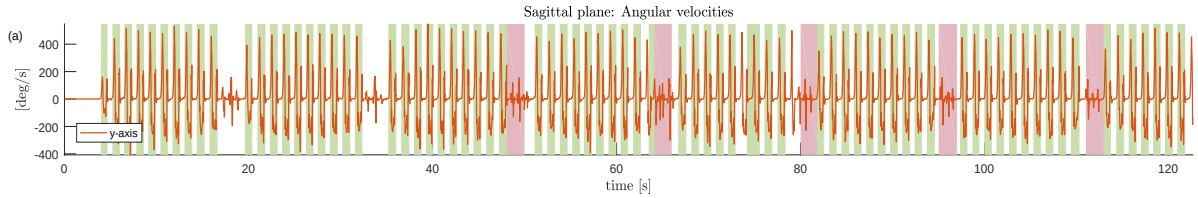

Figure 7.8: Validation module. (a) Gyroscope signal in the sagittal plane with an overlay of the valid gait cycles detected using the validation module.

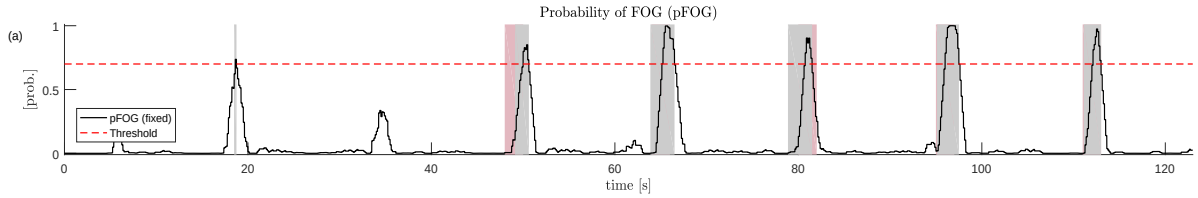

Figure 7.9: Filtering module. (a) pFOG computed using a point-process filter with a fixed participant-specific tunable parameter, $\sigma_s = 0.40$.

To filter TREI associated with valid gait cycles, we use the validation module to identify non-stationary segments of the gyroscope signal in the sagittal plane that are associated with gait cycles. In Fig. 7.8(a), we plot the gyroscope signal in the sagittal plane with an overlay of the valid gait cycles detected using the validation module. The non-stationary segments

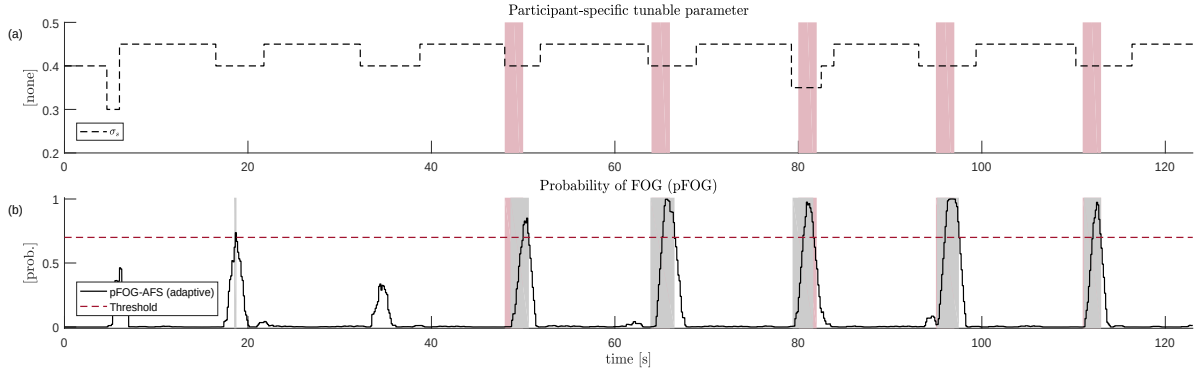

Figure 7.10: Filtering module. (a) The value of σ_{s} changes based on the average value of the speed of the foot in the last valid gait cycle. (b) pFOG computed using a point-process filter with an adaptive σ_{s}

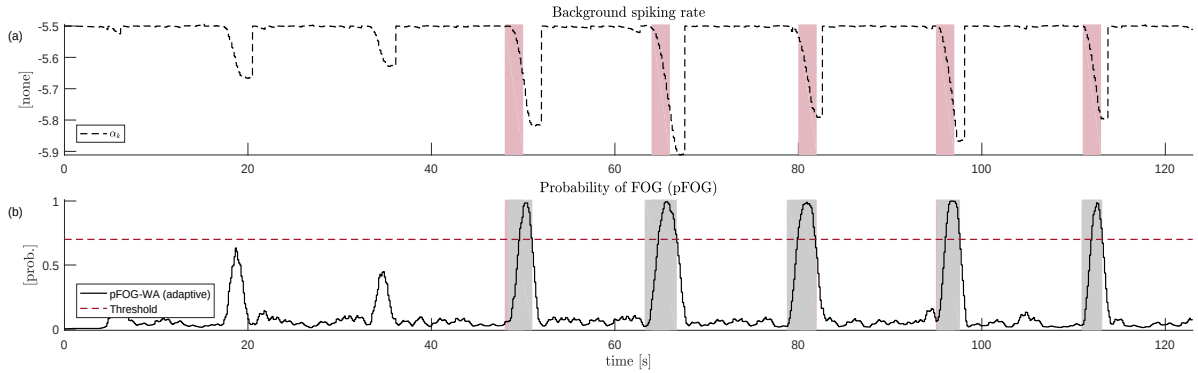

Figure 7.11: Filtering module. (a) The value of the background spiking rate α_k changes based on the density of the edges of the trembling event intervals. (b) pFOG computed using a point-process filter with a weighted average function.

of the gait which represent a valid gait cycle are highlighted with a green background. The parameters used in the validation module are given in Table E.3 of Appendix E.1. We observe that the validation module detects gait cycles when the participant walks along a straight path, but not during turns, because the gyroscope signal in the sagittal plane do not contain typical patterns such as "valleys," "peaks," and "plateaus" during turning movements.

To detect the onset and duration of FOG, we use the point-process filter. The edges in the TREI contain information about both ZVEI and TREI, a combination which represents FOG

patterns. In Fig. 7.9(a), we plot the pFOG, computed using a fixed value of the participant-specific tunable parameter $\sigma_s = 0.40$, which represents $(1.25, 1.50]$ m/sec range of the average value of the foot speed. The parameters of the filtering module used to compute pFOG of the foot are given in Table E.4 of Appendix E.1. We set the pFOG threshold as 0.7, so that the binomial distribution in (5.4) approximate a Gaussian distribution. Note that a binomial distribution can be approximated as a Gaussian distribution if B is sufficiently large, such that $Bp \geq 5$ and $B(1-p) \geq 5$, where p is the probability of an event. In our work, $B = 16$ and $p = 0.7$ (minimum probability to detect FOG), which implies $Bp \geq 5$ and $B(1-p) \approx 5$. When the pFOG is greater than 0.7, we determine the local minimum of the pFOG curve and denote it as the onset time of FOG. The duration of freezing is determined by subtracting the instant when the pFOG curve goes below 0.7 from the onset time, as indicated with gray background in Fig. 7.9(a). As can be seen in Fig. 7.9(a), the point-process filter with a fixed participant-specific tunable parameter detects all episodes of FOG. In addition, the algorithm also falsely detects an FOG event.

In Fig. 7.10, we plot the output of the point-process filter, using the adaptive pFOG-AFS algorithm. In this case, the participant-specific tunable parameter σ_s is tuned based on the average value of the speed of the foot observed in the last valid gait cycle. In Fig. 7.10(a), we plot the value of σ_s, which changes based on the average value of the speed of the foot in the last valid gait cycle, according to the Gaussian kernel function in Fig. 7.2. As can be seen in Fig. 7.10(a), the participant-specific tunable parameter demonstrates variation under two scenarios: a) at the beginning of the gait when the participant slowly begins to accelerate to reach a comfortable pace, and b) prior to the 180°, turn when the participant decelerates to maintain balance and complete the turning movement. In Fig. 7.10(b), we plot the output of the point-process filter for the adaptive participant-specific tunable parameter. We observe that the FOG events detected by the experts and the adaptive pFOG-AFS algorithm match.

Table 7.1: Performance of existing and proposed methods.

Method	Adaptive	Gait Parameters of Interest	Accuracy of Events Detected	False Positive Rate	Number of Events Detected	Number of False Detections
Freeze Index (window = 4 sec, threshold = 5.5)	No	Ratio of spectral powers	65.70%	39.63%	36/60 (60.00%)	75
Freeze Index (window = 4 sec, threshold = 6.0)	No	Ratio of spectral powers	72.59%	31.11%	33/60 (55.00%)	67
pFOG ($\sigma_s = 0.35$, threshold = 0.7)	No	Speed	87.99%	11.16%	49/60 (81.66%)	38
pFOG ($\sigma_s = 0.40$, threshold = 0.7)	No	Speed	90.13%	7.79%	47/60 (78.33%)	37
pFOG-AFS (threshold = 0.7)	Yes	Speed	87.81%	11.01%	49/60 (81.66%)	40
pFOG-WA (threshold = 0.7)	Yes	Speed, pitch, and ratio of spectral power	85.12%	14.14%	53/60 (88.33%)	40

In Fig. 7.11, we plot the output of the point-process filter by using the adaptive pFOG-WA algorithm. The weights assigned to the edges of the trembling event intervals are obtained from the gait parameters mapped to the corresponding kernel function, as shown in Figs. 7.2 and 7.4. Further, the background spiking rate of the conditional intensity function is no longer fixed. The parameters of the filtering module used to compute pFOG by employing pFOG-WA are given in Table E.5 of Appendix E.1. In Fig. 7.11(a), we plot the background spiking rate α_k for the point-process generated using the edges of the TREI in Fig. 7.6(b). As can be seen, the background spiking rate varies depending on the density of the edges of the TREI, and demonstrates variation during turns. Because the point-process filter is reset at every valid gait cycle event, the background spiking rate also resets at these events. In Fig. 7.11(b), we plot the output of the point-process filter for the multi-parameter adaptive point-process filter. We observe that the FOG events detected by the experts and the adaptive pFOG-WA algorithm again match closely.

7.4 Experimental Results

In this section, we analyze the performance of the different modules of the proposed system shown in Fig. 7.1, using real data from seven people with Parkinson disease. The details of our sample size and data collection, and a list of tasks performed by the participants, can be found in Appendix A.2.

We compare our proposed method with existing open-loop methods based on either the freeze index method [14] or the fixed participant-specific tunable parameter [1]. To evaluate the performance of the existing and proposed methods, we define four metric variables.

- *Accuracy* is the ratio of the true positives and true negatives to the total length (in samples) of the dataset.
- *False positive rate* is the ratio of the false positives to the sum of false positives and true negatives.
- A *detected event* occurs if the regions detected using both the inertial sensor based method and video data overlap.
- A *falsely detected event* occurs if the region detected using the inertial sensor based method does not overlap with the region detected using the video data.

In Table 7.1, we present the results of the proposed and existing methods. For the inertial sensor based methods, we take the union of the binary vectors representing the detected events for each foot and compute the metric variables. While the existing methods use fixed thresholds and participant-specific tunable parameters, the proposed methods are adaptive. A total of 60 FOG events were identified in the gold standard video data for the tasks listed in Table A.2. The minimum and maximum durations of the FOG events detected in the video data are 1 and 8 seconds, respectively. A fixed threshold scheme for the freeze index method demonstrates few events and has low accuracy, with a high false positive rate. Further, the number of false detections increases when the threshold is decreased. In contrast, the pFOG method with a fixed participant-specific tunable parameter demonstrates improved performance over the freeze index method. For example, the pFOG method demonstrates a fourfold decrease in the false positive rate. A similar trend was also observed in [1]. Further, increasing the participant-specific tunable parameter from $\sigma_{\mathrm{s}} = 0.35$ to $\sigma_{\mathrm{s}} = 0.40$ decreases the number of events detected and the false positive rate. Comparing the proposed adaptive methods with the existing methods, we see that the adaptive methods perform as well as

or better than the existing methods. For the adaptive pFOG-AFS and pFOG-WA, the participant-specific tunable parameter is adjusted automatically. As can be seen in Table 7.1, the performance of the pFOG-AFS method matches closely with the performance of the pFOG method with a fixed participant-specific tunable parameter $\sigma_s = 0.35$. However, the number of false detections is lower for the adaptive pFOG-AFS method, as seen in Fig. 7.9(a) and 7.10(b). The pFOG-WA method detects the highest number of FOG events. However, the accuracy and false positive rate, respectively, are slightly lower and higher, than for the adaptive pFOG-AFS method. Note that the weight assigned to the edge of a trembling event interval in the pFOG-WA method is a weighted average of the weights generated using the speed, pitch angle, and freeze index of the foot in the bin containing the trembling event interval. Because the freeze index demonstrates poor accuracy and a high false positive rate, it also affects the performance of the pFOG-WA method.

7.5 Chapter Summary

We developed an adaptive modular approach to track FOG in Parkinson disease participants in real time. In the detection module, we first used the physical models of sensor data from a foot-mounted inertial system to detect two FOG-related gait patterns, ZVEI and TREI. The detector could not filter out those gait patterns identified as TREI, which are not associated with FOG. To filter out TREI, in the navigation module, we first extracted gait parameters, such as the speed and pitch angle of the foot using zero-velocity aided inertial navigation system. Next, in the validation module, we identified the non-stationary segments of the sensor data that represent valid gait cycles. Finally, in the filtering module, we combined the output of the detectors with weights generated from the extracted gait

parameters and information from the valid gait cycles, and computed pFOG. We developed two novel methods to automatically tune the participant-specific tunable parameter used to generate the weights of the point-process filter. We validated the modular system using data from experimental gait assessment in a group of people with Parkinson disease. Our proposed methods yielded an average accuracy of greater than 85%, with an average false positive rate of less than 14%.

Chapter 8

Conclusions and Future Work

8.1 Summary

In this dissertation, we developed a modular approach to model, detect, and track freezing of gait (FOG) in Parkinson disease. Our system design consisted of four modules, namely the detection, navigation, validation, and filtering modules. To capture the gait motion, in the sensor module we used a MEMS-based inertial measurement unit (IMU), which consists of a three-axis accelerometer and a three-axis gyroscope. The IMU is strapped to the heel or instep region of the foot of the participant. Based on broad clinical observations, FOG patterns included alternating trembling in the lower extremities (including the hip, knee, and ankle joints, and the bones of the thigh, leg, and foot), and no movement of the limbs and trunk. We modeled stationary FOG gait patterns, such as no limb movement, as zero-velocity event intervals (ZVEI). These events are associated with the midstance phase of a gait cycle. Further, we modeled non-stationary FOG gait patterns, such as alternating trembling in FOG, and short, quickening steps on the toes and forepart of the feet in festinating gait, as trembling event intervals (TREI). These events are associated with the heel lift-off and heel strike phases of a gait cycle. TREI are modeled as the motion of the IMU about an

unknown fixed axis and are of an unknown magnitude which depends on the severity of the trembling. In the detection module, we developed a two-step detection algorithm to identify ZVEI and TREI. The goal of the first detector was to filter out gait patterns that cannot be classified as ZVEI or TREI. To distinguish ZVEI from TREI, we used information from the gyroscope and developed the second detector. The second detector detected only ZVEI and could not filter out those gait patterns identified as TREI, which are not associated with FOG. To filter out gait patterns not associated with FOG, we considered the fact that FOG events are associated with small foot speeds and low pitch angles, which are caused by the alternating trembling motion. To extract gait parameters, such as the speed and pitch angle of the foot, we employed a navigation module. In the navigation module, we estimated the position, velocity, and orientation angles of the foot, using the navigation mechanization equations. We used the ZVEI as pseudo measurements to correct the estimates of the navigation parameters and contain the error growth. We also validated our implementation of the zero-velocity aided inertial navigation system by computing the gait parameters for the valid gait cycles and comparing the estimated parameters with an existing method.

To filter out TREI related to valid gait cycles, we used the gait cycle validation module. We first identified the non-stationary segments of the gyroscope signal in the sagittal plane, using ZVEI. Gyroscope measurements in the sagittal plane were considered as the best choice for gait segmentation because these measurements contained typical time-series patterns such as "valleys," "peaks," and "plateaus." Next, we preprocessed the non-stationary segments by scaling and interpolating the signal. Finally, we validated any preprocessed non-stationary segment of the gyroscope signal in the sagittal plane as a valid gait cycle, using an optimization framework called sparsity-assisted wavelet denoising (SAWD). In the SAWD algorithm, we simultaneously combined low-pass filtering, multiresolution representations (wavelets), and a sparsity-inducing norm to obtain a sparse representation of the gyroscope signal in

the sagittal plane for valid gait cycles, in the form of a discrete wavelet transform coefficient vector. We computed the root-mean-square error between the generated template and the sparse representation of the moving segment of the gyroscope data in the sagittal plane, obtained using the SAWD algorithm. If the root-mean-square error was less than a fixed threshold, then the gait cycle was valid.

To detect the onset and duration of freezing of gait FOG, we developed a point-process filter that computed the probability of FOG (pFOG). We first modeled the edges of the TREI as a point-process, then assigned weights to the edges, which depended on the average value of the gait parameters observed in the bin containing the edge and a participant-specific tunable parameter. Then, we integrated these weights over a time window, using a Bayesian recursive filter, and computed pFOG. We considered three different approaches to generate the weights assigned to the edges of the TREI. In the first approach, we considered a fixed value of the participant-specific tunable parameter and assigned weights based on the average value of the speed of the foot in the bin containing an edge of the TREI. We used a Gaussian kernel function with a zero mean and standard deviation equal to the participant-specific tunable parameter. In the second approach, we automatically adjusted the participant-specific tunable parameter based on the average value of the foot speed observed in the last valid gait cycle. As a result, we modified the weights assigned to the edges of the TREI dynamically, using the average value of the speed of the foot in the last valid gait cycle. In the third approach, the weight assigned to the edge of the TREI was a weighted average of the selected gait parameters. We considered three gait parameters, namely speed, pitch angle, and the freeze index of the foot, and a corresponding kernel function to dynamically assign weights. In addition, we also modified the conditional intensity function of the point-process filter by dynamically adapting the background spiking rate, based on the density of the spikes caused by the edges of the TREI. We used the output of the gait cycle validation

module to reset the point-process filter and also filter those edges of the TREI that did not belong to a FOG event.

We validated the performance of the proposed system design using real data obtained from people with Parkinson disease who performed a battery of gait tasks known to trigger FOG. The results indicated improved performance, with an average accuracy greater than 85% and an average false positive rate of less than 14%.

8.2 Future Directions

In the future, we can potentially extend our research in the following directions:

Improving the detection module with adaptive thresholds: In this dissertation, we considered the thresholds of the detectors in the detection module to be fixed. Ideally, the optimal value of these thresholds varies with the participant's walking speed, i.e., lower thresholds are required to detect ZVEI when the participant is jogging or running. We plan to develop an adaptive framework to dynamically adjust the threshold of the ZVEI detector so that the edges of the ZVEI correspond to the heel-off and flat-foot events. As a result, we can increase the granularity of the gait cycle validation and segmentation algorithm, which can provide an improved understanding of the affected phases of the gait cycle.

Generating a valid gait cycle template online: In this dissertation, to validate a gait cycle, we used a fixed template obtained from a healthy participant. The fixed template contained inertial sensor data with variable walking speeds. If the same template were used on other patients, such as patients with limited knee and ankle movement, then it would be difficult to identify valid gait cycles because there would be a mismatch between the

templates generated by the two groups. We plan to design a system which can use the first S strides to dynamically generate the template signal in real-time, and then use the online generated template along with a fixed threshold to validate and segment the remaining strides.

Integrating physical models with machine learning: In this dissertation, we developed physically-based signal models for the sensor data associated with the FOG patterns and designed statistical signal processing methods to detect the onset and duration of the FOG events in real-time. We employed a point-process filter to compute the probability of FOG. We plan to combine the physical models of the sensor data with data driven techniques, such as neural networks, to compute the probability of FOG.

Mitigating FOG using a closed-loop approach: In this dissertation, we developed a modular approach to model, detect, and track FOG in real time. Clinicians have also developed non-pharmaceutical and non-surgical intervention strategies for FOG, such as cueing, which involves using external auditory or visual stimuli to avert FOG episodes. For cueing to be effective, the external stimulus should ideally be carefully delivered to match an actual or impending FOG event. In addition, the choice of modality selected to deliver the external stimuli also plays a prominent role. We plan to explore different modalities that can deliver external cues, andthen integrate the best intervention strategy with our existing method.

Bibliography

[1] G. V. Prateek, I. Skog, M. E. McNeely, R. P. Duncan, G. M. Earhart, and A. Nehorai, "Modeling, detecting, and tracking freezing of gait in Parkinson disease using inertial sensors," *IEEE Transactions on Biomedical Engineering*, vol. 65, no. 10, pp. 2152–2161, Oct 2018.

[2] H. Braak, E. Ghebremedhin, U. Rüb, H. Bratzke, and K. Del Tredici, "Stages in the development of Parkinson's disease-related pathology," *Cell and Tissue Research*, vol. 318, no. 1, pp. 121–134, Oct 2004.

[3] B. R. Bloem, J. M. Hausdorff, J. E. Visser, and N. Giladi, "Falls and freezing of gait in Parkinson's disease: A review of two interconnected, episodic phenomena," *Movement Disorders*, vol. 19, no. 8, pp. 871–884, 2004.

[4] N. Giladi and A. Nieuwboer, "Understanding and treating freezing of gait in Parkinsonism, proposed working definition, and setting the stage," *Movement Disorders*, vol. 23, no. S2, pp. S423–S425, 2008.

[5] N. Giladi, D. McMahon, S. Przedborski, E. Flaster, S. Guillory, V. Kostic, and S. Fahn, "Motor blocks in Parkinson's disease," *Neurology*, vol. 42, no. 2, pp. 333–333, 1992.

[6] J. D. Schaafsma, Y. Balash, T. Gurevich, A. L. Bartels, J. M. Hausdorff, and N. Giladi, "Characterization of freezing of gait subtypes and the response of each to levodopa in Parkinson's disease," *European Journal of Neurology*, vol. 10, no. 4, pp. 391–398, 2003.

[7] A. J. Espay, P. Bonato, F. B. Nahab, W. Maetzler, J. M. Dean, J. Klucken, B. M. Eskofier, A. Merola, F. Horak, A. E. Lang, R. Reilmann, J. Giuffrida, A. Nieuwboer, M. Horne, M. A. Little, I. Litvan, T. Simuni, E. R. Dorsey, M. A. Burack, K. Kubota, A. Kamondi, C. Godinho, J.-F. Daneault, G. Mitsi, L. Krinke, J. M. Hausdorff, B. R. Bloem, S. Papapetropoulos, and on behalf of the Movement Disorders Society Task Force on Technology, "Technology in Parkinson's disease: Challenges and opportunities," *Movement Disorders*, vol. 31, no. 9, pp. 1272–1282, 2016.

[8] K. J. Kubota, J. A. Chen, and M. A. Little, "Machine learning for large-scale wearable sensor data in Parkinson's disease: Concepts, promises, pitfalls, and futures," *Movement Disorders*, vol. 31, no. 9, pp. 1314–1326, 2016.

[9] A. Vienne, R. P. Barrois, S. Buffat, D. Ricard, and P.-P. Vidal, "Inertial sensors to assess gait quality in patients with neurological disorders: A systematic review of technical and analytical challenges," *Frontiers in Psychology*, vol. 8, p. 817, 2017.

[10] M. Plotnik, N. Giladi, Y. Balash, C. Peretz, and J. M. Hausdorff, "Is freezing of gait in Parkinson's disease related to asymmetric motor function?" *Annals of Neurology*, vol. 57, no. 5, pp. 656–663, 2005.

[11] M. Plotnik, N. Giladi, and J. M. Hausdorff, "A new measure for quantifying the bilateral coordination of human gait: effects of aging and Parkinson's disease," *Experimental Brain Research*, vol. 181, no. 4, pp. 561–570, Aug 2007.

[12] ——, "Bilateral coordination of walking and freezing of gait in Parkinson's disease," *European Journal of Neuroscience*, vol. 27, no. 8, pp. 1999–2006, 2008.

[13] M. Plotnik and J. M. Hausdorff, "The role of gait rhythmicity and bilateral coordination of stepping in the pathophysiology of freezing of gait in Parkinson's disease," *Movement Disorders*, vol. 23, no. S2, pp. S444–S450, 2008.

[14] S. T. Moore, H. G. MacDougall, and W. G. Ondo, "Ambulatory monitoring of freezing of gait in Parkinson's disease," *Journal of Neuroscience Methods*, vol. 167, no. 2, pp. 340 – 348, 2008.

[15] M. Bachlin, M. Plotnik, D. Roggen, I. Maidan, J. M. Hausdorff, N. Giladi, and G. Troster, "Wearable assistant for Parkinson's disease patients with the freezing of gait symptom," *IEEE Transactions on Information Technology in Biomedicine*, vol. 14, no. 2, pp. 436–446, March 2010.

[16] Y. Zhao, K. Tonn, K. Niazmand, U. M. Fietzek, L. T. D'Angelo, A. Ceballos-Baumann, and T. C. Lueth, "Online fog identification in Parkinson's disease with a time-frequency combined algorithm," in *Proceedings of 2012 IEEE-EMBS International Conference on Biomedical and Health Informatics*, Jan 2012, pp. 192–195.

[17] E. E. Tripoliti, A. T. Tzallas, M. G. Tsipouras, G. Rigas, P. Bougia, M. Leontiou, S. Konitsiotis, M. Chondrogiorgi, S. Tsouli, and D. I. Fotiadis, "Automatic detection of freezing of gait events in patients with Parkinson's disease," *Computer Methods and Programs in Biomedicine*, vol. 110, no. 1, pp. 12 – 26, 2013.

[18] S. Mazilu, M. Hardegger, Z. Zhu, D. Roggen, G. Tröster, M. Plotnik, and J. M. Hausdorff, "Online detection of freezing of gait with smartphones and machine learning techniques," in *2012 6th International Conference on Pervasive Computing Technologies for Healthcare (PervasiveHealth) and Workshops*, May 2012, pp. 123–130.

[19] S. Mazilu, U. Blanke, M. Hardegger, G. Tröster, E. Gazit, and J. M. Hausdorff, "Gaitassist: A daily-life support and training system for Parkinson's disease patients

with freezing of gait," in *Proceedings of the SIGCHI Conference on Human Factors in Computing Systems*, ser. CHI '14. New York, NY, USA: ACM, 2014, pp. 2531–2540.

[20] L. di Biase, J.-S. Brittain, S. A. Shah, D. J. Pedrosa, H. Cagnan, A. Mathy, C. C. Chen, J. F. Martín-Rodríguez, P. Mir, L. Timmerman, P. Schwingenschuh, K. Bhatia, V. Di Lazzaro, and P. Brown, "Tremor stability index: a new tool for differential diagnosis in tremor syndromes," *Brain*, vol. 140, no. 7, pp. 1977–1986, 04 2017.

[21] T. T. Pham, S. T. Moore, S. J. G. Lewis, D. N. Nguyen, E. Dutkiewicz, A. J. Fuglevand, A. L. McEwan, and P. H. W. Leong, "Freezing of gait detection in Parkinson's disease: A subject-independent detector using anomaly scores," *IEEE Transactions on Biomedical Engineering*, vol. 64, no. 11, pp. 2719–2728, Nov 2017.

[22] J. G. Nutt, B. R. Bloem, N. Giladi, M. Hallett, F. B. Horak, and A. Nieuwboer, "Freezing of gait: Moving forward on a mysterious clinical phenomenon," *The Lancet Neurology*, vol. 10, no. 8, pp. 734 – 744, 2011.

[23] A. Nieuwboer, R. Dom, W. De Weerdt, K. Desloovere, S. Fieuws, and E. Broens-Kaucsik, "Abnormalities of the spatiotemporal characteristics of gait at the onset of freezing in Parkinson's disease," *Movement Disorders*, vol. 16, no. 6, pp. 1066–1075, 2001.

[24] R. Iansek, F. Huxham, and J. McGinley, "The sequence effect and gait festination in parkinson disease: Contributors to freezing of gait?" *Movement Disorders*, vol. 21, no. 9, pp. 1419–1424, 2006.

[25] E. Heremans, A. Nieuwboer, and S. Vercruysse, "Freezing of gait in Parkinson's disease: Where are we now?" *Current Neurology and Neuroscience Reports*, vol. 13, no. 6, p. 350, Apr 2013.

[26] T. R. Morris, C. Cho, V. Dilda, J. M. Shine, S. L. Naismith, S. J. Lewis, and S. T. Moore, "A comparison of clinical and objective measures of freezing of gait in Parkinson's disease," *Parkinsonism & Related Disorders*, vol. 18, no. 5, pp. 572 – 577, 2012.

[27] A. H. Snijders, M. J. Nijkrake, M. Bakker, M. Munneke, C. Wind, and B. R. Bloem, "Clinimetrics of freezing of gait," *Movement Disorders*, vol. 23, no. S2, pp. S468–S474, 2008.

[28] S. Majumder, T. Mondal, and M. J. Deen, "Wearable sensors for remote health monitoring," *Sensors*, vol. 17, no. 1, 2017.

[29] O. J. Woodman, "An introduction to inertial navigation," *University of Cambridge, Computer Laboratory, Tech. Rep. UCAMCL-TR-696*, vol. 14, p. 15, 2007.

[30] P. Krack, A. Batir, N. Van Blercom, S. Chabardes, V. Fraix, C. Ardouin, A. Koudsie, P. D. Limousin, A. Benazzouz, J. F. LeBas, A.-L. Benabid, and P. Pollak, "Five-year follow-up of bilateral stimulation of the subthalamic nucleus in advanced Parkinson's disease," *New England Journal of Medicine*, vol. 349, no. 20, pp. 1925–1934, 2003.

[31] C. Moreau, L. Defebvre, A. Destée, S. Bleuse, F. Clement, J. L. Blatt, P. Krystkowiak, and D. Devos, "STN-DBS frequency effects on freezing of gait in advanced Parkinson disease," *Neurology*, vol. 71, no. 2, pp. 80–84, 2008.

[32] M. U. Ferraye, B. Debû, V. Fraix, L. Goetz, C. Ardouin, J. Yelnik, C. Henry-Lagrange, E. Seigneuret, B. Piallat, P. Krack, J.-F. Le Bas, A.-L. Benabid, S. Chabardès, and P. Pollak, "Effects of pedunculopontine nucleus area stimulation on gait disorders in Parkinson's disease," *Brain*, vol. 133, no. 1, pp. 205–214, 09 2009.

[33] M. E. McNeely and G. M. Earhart, "Medication and subthalamic nucleus deep brain stimulation similarly improve balance and complex gait in Parkinson disease," *Parkinsonism & Related Disorders*, vol. 19, no. 1, pp. 86 – 91, 2013.

[34] T. C. Rubinstein, N. Giladi, and J. M. Hausdorff, "The power of cueing to circumvent dopamine deficits: A review of physical therapy treatment of gait disturbances in Parkinson's disease," *Movement Disorders*, vol. 17, no. 6, pp. 1148–1160, 2002.

[35] Y. Okuma, "Freezing of gait in Parkinson's disease," *Journal of Neurology*, vol. 253, no. 7, pp. vii27–vii32, Dec 2006.

[36] T. Hashimoto, "Speculation on the responsible sites and pathophysiology of freezing of gait," *Parkinsonism & Related Disorders*, vol. 12, pp. S55 – S62, 2006, proceedings of the 1st International Symposium on Dopaminergic and Nondopaminergic Mechanisms in Parkinson's Disease (ISDNMPD).

[37] A. Nieuwboer, G. Kwakkel, L. Rochester, D. Jones, E. van Wegen, A. M. Willems, F. Chavret, V. Hetherington, K. Baker, and I. Lim, "Cueing training in the home improves gait-related mobility in parkinson's disease: The RESCUE trial," *Journal of Neurology, Neurosurgery & Psychiatry*, vol. 78, no. 2, pp. 134–140, 2007.

[38] A. Nieuwboer, "Cueing for freezing of gait in patients with Parkinson's disease: A rehabilitation perspective," *Movement Disorders*, vol. 23, no. S2, pp. S475–S481, 2008.

[39] D. K. Shaeffer, "MEMS inertial sensors: A tutorial overview," *IEEE Communications Magazine*, vol. 51, no. 4, pp. 100–109, April 2013.

[40] J. B. Richard H. Dixon, "Markets and applications for MEMS inertial sensors," 2006.

[41] J. A. Geen, S. J. Sherman, J. F. Chang, and S. R. Lewis, "Single-chip surface micromachined integrated gyroscope with 50/spl deg//h allan deviation," *IEEE Journal of Solid-State Circuits*, vol. 37, no. 12, pp. 1860–1866, Dec 2002.

[42] S. Y. Cho and C. G. Park, "A calibration technique for a redundant IMU containing low-grade inertial sensors," *ETRI Journal*, vol. 27, no. 4, pp. 418–426, 2005.

[43] M. E. Pittelkau, "Cascaded and decoupled RIMU calibration filters," *The Journal of the Astronautical Sciences*, vol. 54, no. 3, pp. 449–466, Dec 2006.

[44] T. Beravs, J. Podobnik, and M. Munih, "Three-axial accelerometer calibration using kalman filter covariance matrix for online estimation of optimal sensor orientation," *IEEE Transactions on Instrumentation and Measurement*, vol. 61, no. 9, pp. 2501–2511, Sep. 2012.

[45] G. Panahandeh, I. Skog, and M. Jansson, "Calibration of the accelerometer triad of an inertial measurement unit, maximum likelihood estimation and cramér-rao bound," in *2010 International Conference on Indoor Positioning and Indoor Navigation*, Sep. 2010, pp. 1–6.

[46] Z. F. Syed, P. Aggarwal, C. Goodall, X. Niu, and N. El-Sheimy, "A new multi-position calibration method for MEMS inertial navigation systems," *Measurement Science and Technology*, vol. 18, no. 7, pp. 1897–1907, may 2007.

[47] I. Skog and P. Händel, "Calibration of a MEMS inertial measurement unit," in *XVII IMEKO world congress*, 2006, pp. 1–6.

[48] J. Nilsson, I. Skog, and P. Händel, "Aligning the forces—eliminating the misalignments in IMU arrays," *IEEE Transactions on Instrumentation and Measurement*, vol. 63, no. 10, pp. 2498–2500, Oct 2014.

[49] J. O. Nilsson, A. K. Gupta, and P. Händel, "Foot-mounted inertial navigation made easy," in *2014 International Conference on Indoor Positioning and Indoor Navigation (IPIN)*, Oct 2014, pp. 24–29.

[50] F. Horak, L. King, and M. Mancini, "Role of Body-Worn Movement Monitor Technology for Balance and Gait Rehabilitation," *Physical Therapy*, vol. 95, no. 3, pp. 461–470, 03 2015.

[51] A. Burns, B. R. Greene, M. J. McGrath, T. J. O'Shea, B. Kuris, S. M. Ayer, F. Stroiescu, and V. Cionca, "SHIMMER – a wireless sensor platform for noninvasive biomedical research," *IEEE Sensors Journal*, vol. 10, no. 9, pp. 1527–1534, Sep. 2010.

[52] H. Braak, E. Ghebremedhin, U. Rüb, H. Bratzke, and K. Del Tredici, "Stages in the development of Parkinson's disease-related pathology," *Cell and Tissue Research*, vol. 318, no. 1, pp. 121–134, 2004.

[53] L. M. Shulman, A. L. Gruber-Baldini, K. E. Anderson, C. G. Vaughan, S. G. Reich, P. S. Fishman, and W. J. Weiner, "The evolution of disability in Parkinson disease," *Movement Disorders*, vol. 23, no. 6, pp. 790–796, 2008.

[54] N. Giladi, M. P. McDermott, S. Fahn, S. Przedborski, J. Jankovic, M. Stern, C. Tanner, and T. P. S. Group, "Freezing of gait in Parkionson's disease: Prospective assessment in the DATATOP cohort," *Neurology*, vol. 56, no. 12, pp. 1712–1721, 2001.

[55] T. C. Rubinstein, N. Giladi, and J. M. Hausdorff, "The power of cueing to circumvent dopamine deficits: A review of physical therapy treatment of gait disturbances in Parkinson's disease," *Movement Disorders*, vol. 17, no. 6, pp. 1148–1160, 2002.

[56] G. C. McIntosh, S. H. Brown, R. R. Rice, and M. H. Thaut, "Rhythmic auditory-motor facilitation of gait patterns in patients with Parkinson's disease." *Journal of Neurology, Neurosurgery & Psychiatry*, vol. 62, no. 1, pp. 22–26, 1997.

[57] A. Nieuwboer, L. Rochester, T. Herman, W. Vandenberghe, G. E. Emil, T. Thomaes, and N. Giladi, "Reliability of the new freezing of gait questionnaire: Agreement between patients with Parkinson's disease and their carers," *Gait & Posture*, vol. 30, no. 4, pp. 459 – 463, 2009.

[58] H. Mitoma, R. Hayashi, N. Yanagisawa, and H. Tsukagoshi, "Characteristics of Parkinsonian and ataxic gaits: A study using surface electromyograms, angular displacements and floor reaction forces," *Journal of the Neurological Sciences*, vol. 174, no. 1, pp. 22 – 39, 2000.

[59] A. Nieuwboer, R. Dom, W. De Weerdt, K. Desloovere, L. Janssens, and V. Stijn, "Electromyographic profiles of gait prior to onset of freezing episodes in patients with Parkinson's disease," *Brain*, vol. 127, no. 7, pp. 1650–1660, 2004.

[60] M. Plotnik, N. Giladi, Y. Balash, C. Peretz, and J. M. Hausdorff, "Is freezing of gait in Parkinson's disease related to asymmetric motor function?" *Annals of Neurology*, vol. 57, no. 5, pp. 656–663, 2005.

[61] J. Hausdorff, J. Schaafsma, Y. Balash, A. Bartels, T. Gurevich, and N. Giladi, "Impaired regulation of stride variability in Parkinson's disease subjects with freezing of gait," *Experimental Brain Research*, vol. 149, no. 2, pp. 187–194, 2003.

[62] A. H. Snijders, I. Leunissen, M. Bakker, S. Overeem, R. C. Helmich, B. R. Bloem, and I. Toni, "Gait-related cerebral alterations in patients with Parkinson's disease with freezing of gait," *Brain*, vol. 134, no. 1, pp. 59–72, 2010.

[63] A. Delval, A. H. Snijders, V. Weerdesteyn, J. E. Duysens, L. Defebvre, N. Giladi, and B. R. Bloem, "Objective detection of subtle freezing of gait episodes in Parkinson's disease," *Movement Disorders*, vol. 25, no. 11, pp. 1684–1693, 2010.

[64] J. H. Han, W. J. Lee, T. B. Ahn, B. S. Jeon, and K. S. Park, "Gait analysis for freezing detection in patients with movement disorder using three dimensional acceleration system," in *Engineering in Medicine and Biology Society, 2003. Proceedings of the*

25th Annual International Conference of the IEEE, vol. 2. IEEE, 2003, pp. 1863–1865.

[65] J. Han, H. S. Jeon, B. S. Jeon, and K. S. Park, "Gait detection from three dimensional acceleration signals of ankles for the patients with Parkinson's disease-related," in *Proceedings of the IEEE The International Special Topic Conference on Information Technology in Biomedicine, Ioannina, Epirus, Greece*, vol. 2628, 2006.

[66] S. T. Moore, H. G. MacDougall, and W. G. Ondo, "Ambulatory monitoring of freezing of gait in Parkinson's disease," *Journal of Neuroscience Methods*, vol. 167, no. 2, pp. 340–348, 2008.

[67] E. Jovanov, E. Wang, L. Verhagen, M. Fredrickson, and R. Fratangelo, "deFOG-A real time system for detection and unfreezing of gait of Parkinson's patients," in *Annual International Conference of the IEEE on Engineering in Medicine and Biology Society,*. IEEE, 2009, pp. 5151–5154.

[68] P. Healthcare, "A wearable system to assist walking of Parkinsons disease patients," *Methods Inf Med*, vol. 49, pp. 88–95, 2010.

[69] E. E. Tripoliti, A. T. Tzallas, M. G. Tsipouras, G. Rigas, P. Bougia, M. Leontiou, S. Konitsiotis, M. Chondrogiorgi, S. Tsouli, and D. I. Fotiadis, "Automatic detection of freezing of gait events in patients with Parkinson's disease," *Computer Methods and Programs in Biomedicine*, vol. 110, no. 1, pp. 12–26, 2013.

[70] S. Mazilu, U. Blanke, A. Calatroni, E. Gazit, J. M. Hausdorff, and G. Tröster, "The role of wrist-mounted inertial sensors in detecting gait freeze episodes in Parkinson's disease," *Pervasive and Mobile Computing*, vol. 33, pp. 1 – 16, 2016.

[71] M. Bächlin, M. Plotnik, D. Roggen, I. Maidan, J. M. Hausdorff, N. Giladi, and G. Tröster, "Wearable assistant for Parkinson's disease patients with the freezing of gait symptom," *IEEE Transactions on Information Technology in Biomedicine,*, vol. 14, no. 2, pp. 436–446, 2010.

[72] B. R. Bloem, J. M. Hausdorff, J. E. Visser, and N. Giladi, "Falls and freezing of gait in Parkinson's disease: A review of two interconnected, episodic phenomena," *Movement Disorders*, vol. 19, no. 8, pp. 871–884, 2004.

[73] J. G. Nutt, B. R. Bloem, N. Giladi, M. Hallett, F. B. Horak, and A. Nieuwboer, "Freezing of Gait: Moving forward on a mysterious clinical phenomenon," *The Lancet Neurology*, vol. 10, no. 8, pp. 734–744, 2011.

[74] M. E. Morris, R. Iansek, T. A. Matyas, and J. J. Summers, "Stride length regulation in Parkinson's disease normalization strategies and underlying mechanisms," *Brain*, vol. 119, no. 2, p. 551, 1996.

[75] M. Morris, R. Iansek, T. Matyas, and J. Summers, "Abnormalities in the stride length-cadence relation in parkinsonian gait," *Movement Disorders*, vol. 13, no. 1, pp. 61–69, 1998.

[76] N. Giladi, H. Shabtai, E. Rozenberg, and E. Shabtai, "Gait festination in Parkinson's disease," *Parkinsonism & Related Disorders*, vol. 7, no. 2, pp. 135 – 138, 2001.

[77] S. M. Kay, "Fundamentals of statistical signal processing, vol. ii: Detection theory," *Signal Processing. Upper Saddle River, NJ: Prentice Hall*, 1998.

[78] A. Nieuwboer, R. Dom, W. De Weerdt, K. Desloovere, S. Fieuws, and E. Broens-Kaucsik, "Abnormalities of the spatiotemporal characteristics of gait at the onset of freezing in Parkinson's disease," *Movement Disorders*, vol. 16, no. 6, pp. 1066–1075, 2001.

[79] I. Skog, J. O. Nilsson, and P. Händel, "Evaluation of zero-velocity detectors for foot-mounted inertial navigation systems," in *2010 International Conference on Indoor Positioning and Indoor Navigation (IPIN),*, Sept 2010, pp. 1–6.

[80] E. Foxlin, "Pedestrian tracking with shoe-mounted inertial sensors," *IEEE Computer Graphics and Applications*, vol. 25, no. 6, pp. 38–46, Nov 2005.

[81] C. Fischer, P. Talkad Sukumar, and M. Hazas, "Tutorial: Implementing a pedestrian tracker using inertial sensors," *IEEE Pervasive Computing*, vol. 12, no. 2, pp. 17–27, April 2013.

[82] J. Farrell, *Aided navigation: GPS with high rate sensors*. McGraw-Hill, Inc., 2008.

[83] D. R. Cox, *The theory of stochastic processes*. Routledge, 2017.

[84] S. Asmussen and G. Koole, "Marked point processes as limits of markovian arrival streams," *Journal of Applied Probability*, vol. 30, no. 2, pp. 365–372, 1993.

[85] A. C. Smith and E. N. Brown, "Estimating a state-space model from point process observations," *Neural computation*, vol. 15, no. 5, pp. 965–991, 2003.

[86] L. Paninski, "Maximum likelihood estimation of cascade point-process neural encoding models," *Network: Computation in Neural Systems*, vol. 15, no. 4, pp. 243–262, 2004.

[87] U. T. Eden, L. M. Frank, R. Barbieri, V. Solo, and E. N. Brown, "Dynamic analysis of neural encoding by point process adaptive filtering," *Neural Computation*, vol. 16, no. 5, pp. 971–998, May 2004.

[88] J. F. C. Kingman, "Poisson processes," *Encyclopedia of biostatistics*, vol. 6, 2005.

[89] R. Barbieri and E. N. Brown, "Analysis of heartbeat dynamics by point process adaptive filtering," *IEEE Transactions on Biomedical Engineering*, vol. 53, no. 1, pp. 4–12, Jan 2006.

[90] W. R. West and T. R. Ogden, "Continuous-time estimation of a change-point in a poisson process," *Journal of Statistical Computation and Simulation*, vol. 56, no. 4, pp. 293–302, 1997.

[91] D. J. Daley and D. Vere-Jones, *An introduction to the theory of point processes: General theory and structure*, 2007, vol. II.

[92] E. N. Brown, R. Barbieri, U. T. Eden, and L. M. Frank, "Likelihood methods for neural spike train data analysis," *Computational neuroscience: A comprehensive approach*, pp. 253–286, 2003.

[93] D. R. Cox and V. Isham, *Point Processes*. CRC Press, 1980, vol. 12.

[94] A. C. Smith and E. N. Brown, "Estimating a state-space model from point process observations," *Neural Computation*, vol. 15, no. 5, pp. 965–991, May 2003.

[95] A. Ergun, R. Barbieri, U. T. Eden, M. A. Wilson, and E. N. Brown, "Construction of point process adaptive filter algorithms for neural systems using sequential monte carlo methods," *IEEE Transactions on Biomedical Engineering*, vol. 54, no. 3, pp. 419–428, March 2007.

[96] S. Koyama, U. T. Eden, E. N. Brown, and R. E. Kass, "Bayesian decoding of neural spike trains," *Annals of the Institute of Statistical Mathematics*, vol. 62, no. 1, pp. 37–59, 2009.

[97] S. Koyama, L. C. Pérez-Bolde, C. R. Shalizi, and R. E. Kass, "Approximate methods for state-space models," *Journal of the American Statistical Association*, vol. 105, no. 489, pp. 170–180, 2010.

[98] P. Mahlknecht, S. Kiechl, B. R. Bloem, J. Willeit, C. Scherfler, A. Gasperi, G. Rungger, W. Poewe, and K. Seppi, "Prevalence and burden of gait disorders in elderly men and women aged 60–97 years: A population-based study," *PLOS ONE*, vol. 8, pp. 1–7, 07 2013.

[99] W. Pirker and R. Katzenschlager, "Gait disorders in adults and the elderly," *Wiener klinische Wochenschrift*, vol. 129, no. 3, pp. 81–95, Feb 2017.

[100] W. F. Abdo, B. P. Van De Warrenburg, D. J. Burn, N. P. Quinn, and B. R. Bloem, "The clinical approach to movement disorders," *Nature Reviews Neurology*, vol. 6, no. 1, p. 29, 2010.

[101] S. Sprager and M. B. Juric, "Inertial sensor-based gait recognition: A review," *Sensors*, vol. 15, no. 9, pp. 22 089–22 127, 2015.

[102] J. Taborri, E. Palermo, S. Rossi, and P. Cappa, "Gait partitioning methods: A systematic review," *Sensors*, vol. 16, no. 1, 2016.

[103] R. T. Lauer, B. T. Smith, and R. R. Betz, "Application of a neuro-fuzzy network for gait event detection using electromyography in the child with cerebral palsy," *IEEE Transactions on Biomedical Engineering*, vol. 52, no. 9, pp. 1532–1540, Sep. 2005.

[104] M. M. Skelly and H. J. Chizeck, "Real-time gait event detection for paraplegic FES walking," *IEEE Transactions on Neural Systems and Rehabilitation Engineering*, vol. 9, no. 1, pp. 59–68, March 2001.

[105] B. T. Smith, D. J. Coiro, R. Finson, R. R. Betz, and J. McCarthy, "Evaluation of force-sensing resistors for gait event detection to trigger electrical stimulation to improve walking in the child with cerebral palsy," *IEEE Transactions on Neural Systems and Rehabilitation Engineering*, vol. 10, no. 1, pp. 22–29, March 2002.

[106] V. Agostini, G. Balestra, and M. Knaflitz, "Segmentation and classification of gait cycles," *IEEE Transactions on Neural Systems and Rehabilitation Engineering*, vol. 22, no. 5, pp. 946–952, Sep. 2014.

[107] S. Crea, S. M. M. D. Rossi, M. Donati, P. Reberšek, D. Novak, N. Vitiello, T. Lenzi, J. Podobnik, M. Munih, and M. C. Carrozza, "Development of gait segmentation methods for wearable foot pressure sensors," in *2012 Annual International Conference of the IEEE Engineering in Medicine and Biology Society*, Aug 2012, pp. 5018–5021.

[108] P. Catalfamo, D. Moser, S. Ghoussayni, and D. Ewins, "Detection of gait events using an F-scan in-shoe pressure measurement system," *Gait & Posture*, vol. 28, no. 3, pp. 420 – 426, 2008.

[109] A. Salarian, H. Russmann, F. J. G. Vingerhoets, C. Dehollain, Y. Blanc, P. R. Burkhard, and K. Aminian, "Gait assessment in Parkinson's disease: toward an ambulatory system for long-term monitoring," *IEEE Transactions on Biomedical Engineering*, vol. 51, no. 8, pp. 1434–1443, Aug 2004.

[110] A. M. Sabatini, C. Martelloni, S. Scapellato, and F. Cavallo, "Assessment of walking features from foot inertial sensing," *IEEE Transactions on Biomedical Engineering*, vol. 52, no. 3, pp. 486–494, March 2005.

[111] D. Kotiadis, H. Hermens, and P. Veltink, "Inertial gait phase detection for control of a drop foot stimulator: Inertial sensing for gait phase detection," *Medical Engineering & Physics*, vol. 32, no. 4, pp. 287 – 297, 2010.

[112] A. Mannini and A. M. Sabatini, "Gait phase detection and discrimination between walking–jogging activities using hidden Markov models applied to foot motion data from a gyroscope," *Gait & Posture*, vol. 36, no. 4, pp. 657 – 661, 2012.

[113] J. Barth, C. Oberndorfer, C. Pasluosta, S. Schülein, H. Gassner, S. Reinfelder, P. Kugler, D. Schuldhaus, J. Winkler, J. Klucken, and B. M. Eskofier, "Stride segmentation during free walk movements using multi-dimensional subsequence dynamic time warping on inertial sensor data," *Sensors*, vol. 15, no. 3, pp. 6419–6440, 2015.

[114] I. P. I. Pappas, M. R. Popovic, T. Keller, V. Dietz, and M. Morari, "A reliable gait phase detection system," *IEEE Transactions on Neural Systems and Rehabilitation Engineering*, vol. 9, no. 2, pp. 113–125, June 2001.

[115] K. Aminian, B. Najafi, C. Büla, P.-F. Leyvraz, and P. Robert, "Spatio-temporal parameters of gait measured by an ambulatory system using miniature gyroscopes," *Journal of Biomechanics*, vol. 35, no. 5, pp. 689 – 699, 2002.

[116] I. P. I. Pappas, T. Keller, S. Mangold, M. R. Popovic, V. Dietz, and M. Morari, "A reliable gyroscope-based gait-phase detection sensor embedded in a shoe insole," *IEEE Sensors Journal*, vol. 4, no. 2, pp. 268–274, April 2004.

[117] H. Lau and K. Tong, "The reliability of using accelerometer and gyroscope for gait event identification on persons with dropped foot," *Gait & Posture*, vol. 27, no. 2, pp. 248 – 257, 2008.

[118] J. K. Lee and E. J. Park, "Quasi real-time gait event detection using shank-attached gyroscopes," *Medical & Biological Engineering & Computing*, vol. 49, no. 6, pp. 707–712, Jun 2011.

[119] N. Abaid, P. Cappa, E. Palermo, M. Petrarca, and M. Porfiri, "Gait detection in children with and without Hemiplegia using single-axis wearable gyroscopes," *PLOS ONE*, vol. 8, no. 9, pp. 1–8, 09 2013.

[120] D. J. Berndt and J. Clifford, "Using dynamic time warping to find patterns in time series." in *KDD workshop*, vol. 10, no. 16. Seattle, WA, 1994, pp. 359–370.

[121] N. Haji Ghassemi, J. Hannink, C. F. Martindale, H. Gaßner, M. Müller, J. Klucken, and B. M. Eskofier, "Segmentation of gait sequences in sensor-based movement analysis: A comparison of methods in Parkinson's disease," *Sensors*, vol. 18, no. 1, 2018.

[122] J. O. Nilsson, I. Skog, P. Händel, and K. V. S. Hari, "Foot-mounted INS for everybody - An open-source embedded implementation," in *Proceedings of the 2012 IEEE/ION Position, Location and Navigation Symposium*, April 2012, pp. 140–145.

[123] G. C. McIntosh, S. H. Brown, R. R. Rice, and M. H. Thaut, "Rhythmic auditory-motor facilitation of gait patterns in patients with parkinson's disease." *Journal of Neurology, Neurosurgery & Psychiatry*, vol. 62, no. 1, pp. 22–26, 1997.

[124] E. C. Harrison, A. P. Horin, and G. M. Earhart, "Internal cueing improves gait more than external cueing in healthy adults and people with Parkinson disease," *Scientific reports*, vol. 8, no. 1, p. 15525, 2018.

[125] C. L. Vaughan, B. L. Davis, C. Jeremy *et al.*, "Dynamics of human gait," 1999.

[126] L. Ojeda and J. Borenstein, "Non-GPS navigation for security personnel and first responders," *Journal of Navigation*, vol. 60, no. 3, pp. 391–407, 9 2007.

[127] F. Cavallo, A. M. Sabatini, and V. Genovese, "A step toward GPS/INS personal navigation systems: Real-time assessment of gait by foot inertial sensing," in *2005 IEEE/RSJ International Conference on Intelligent Robots and Systems*, Aug 2005, pp. 1187–1191.

[128] R. Feliz Alonso, E. Zalama Casanova, and J. Gómez García-Bermejo, "Pedestrian tracking using inertial sensors," 2009-01.

[129] S. G. Mallat, "A theory for multiresolution signal decomposition: The wavelet representation," *IEEE Transactions on Pattern Analysis and Machine Intelligence*, vol. 11, no. 7, pp. 674–693, July 1989.

[130] C. S. Burrus, R. A. Gopinath, H. Guo, J. E. Odegard, and I. W. Selesnick, *Introduction to wavelets and wavelet transforms: A primer*. Prentice hall New Jersey, 1998, vol. 1.

[131] S. Mallat, *A wavelet tour of signal processing: The sparse way*. Academic press, 2008.

[132] I. W. Selesnick, H. L. Graber, D. S. Pfeil, and R. L. Barbour, "Simultaneous low-pass filtering and total variation denoising," *IEEE Transactions on Signal Processing*, vol. 62, no. 5, pp. 1109–1124, March 2014.

[133] I. Selesnick, "Sparsity-assisted signal smoothing (revisited)," in *2017 IEEE International Conference on Acoustics, Speech and Signal Processing (ICASSP)*, March 2017, pp. 4546–4550.

[134] S. Boyd, N. Parikh, E. Chu, B. Peleato, and J. Eckstein, "Distributed optimization and statistical learning via the alternating direction method of multipliers," *Foundations and Trends in Machine Learning*, vol. 3, no. 1, pp. 1–122, 2011.

[135] J. Eckstein and D. P. Bertsekas, "On the Douglas—Rachford splitting method and the proximal point algorithm for maximal monotone operators," *Mathematical Programming*, vol. 55, no. 1-3, pp. 293–318, 1992.

[136] D. A. Harville, *Matrix algebra from a statistician's perspective*. Springer, 1997, vol. 1.

[137] D. L. Donoho and I. M. Johnstone, "Adapting to unknown smoothness via wavelet shrinkage," *Journal of the American Statistical Association*, vol. 90, no. 432, pp. 1200–1224, 1995.

[138] I. W. Selesnick, *Sparsity-Assisted Signal Smoothing*. Cham: Springer International Publishing, 2015, pp. 149–176.

[139] R. Nishihara, L. Lessard, B. Recht, A. Packard, and M. I. Jordan, "A general analysis of the convergence of ADMM," in *Proceedings of the 32Nd International Conference on International Conference on Machine Learning - Volume 37*, ser. ICML'15. JMLR.org, 2015, pp. 343–352.

[140] B. Mariani, H. Rouhani, X. Crevoisier, and K. Aminian, "Quantitative estimation of foot-flat and stance phase of gait using foot-worn inertial sensors," *Gait & Posture*, vol. 37, no. 2, pp. 229 – 234, 2013.

[141] D. S. Colomar, J. O. Nilsson, and P. Händel, "Smoothing for ZUPT-aided INSs," in *2012 International Conference on Indoor Positioning and Indoor Navigation (IPIN)*, Nov 2012, pp. 1–5.

[142] I. Skog, J. Nilsson, and P. Händel, "Evaluation of zero-velocity detectors for foot-mounted inertial navigation systems," in *2010 International Conference on Indoor Positioning and Indoor Navigation*, Sep. 2010, pp. 1–6.

[143] J. Farrell, *Aided Navigation: GPS with High Rate Sensors*, 1st ed. New York, NY, USA: McGraw-Hill, Inc., 2008.

[144] A. Rampp, J. Barth, S. Schülein, K. Gaßmann, J. Klucken, and B. M. Eskofier, "Inertial sensor-based stride parameter calculation from gait sequences in geriatric patients," *IEEE Transactions on Biomedical Engineering*, vol. 62, no. 4, pp. 1089–1097, April 2015.

[145] N. Naghavi and E. Wade, "Prediction of freezing of gait in parkinson's disease using statistical inference and lower–limb acceleration data," *IEEE Transactions on Neural Systems and Rehabilitation Engineering*, vol. 27, no. 5, pp. 947–955, May 2019.

[146] L. Palmerini, L. Rocchi, S. Mazilu, E. Gazit, J. M. Hausdorff, and L. Chiari, "Identification of characteristic motor patterns preceding freezing of gait in parkinson's disease using wearable sensors," *Frontiers in Neurology*, vol. 8, p. 394, 2017.

[147] O. Sofuwa, A. Nieuwboer, K. Desloovere, A.-M. Willems, F. Chavret, and I. Jonkers, "Quantitative gait analysis in parkinson's disease: Comparison with a healthy control group," *Archives of Physical Medicine and Rehabilitation*, vol. 86, no. 5, pp. 1007 – 1013, 2005.

[148] S. Godha and G. Lachapelle, "Foot mounted inertial system for pedestrian navigation," *Measurement Science and Technology*, vol. 19, no. 7, p. 075202, 2008.

[149] P. Stromback, J. Rantakokko, S.-L. Wirkander, M. Alexandersson, K. Fors, I. Skog, and P. Handel, "Foot-mounted inertial navigation and cooperative sensor fusion for indoor positioning," *Proceedings of the 2010 International Technical Meeting of The Institute of Navigation*, pp. 89–98, Jan 2010.

[150] H. M. Schepers, H. F. J. M. Koopman, and P. H. Veltink, "Ambulatory assessment of ankle and foot dynamics," *IEEE Transactions on Biomedical Engineering*, vol. 54, no. 5, pp. 895–902, May 2007.

[151] H. M. Schepers*, E. H. F. van Asseldonk, J. H. Buurke, and P. H. Veltink, "Ambulatory estimation of center of mass displacement during walking," *IEEE Transactions on Biomedical Engineering*, vol. 56, no. 4, pp. 1189–1195, April 2009.

[152] S. J. M. Bamberg, A. Y. Benbasat, D. M. Scarborough, D. E. Krebs, and J. A. Paradiso, "Gait analysis using a shoe-integrated wireless sensor system," *IEEE Transactions on Information Technology in Biomedicine*, vol. 12, no. 4, pp. 413–423, July 2008.

[153] J. M. Jasiewicz, J. H. Allum, J. W. Middleton, A. Barriskill, P. Condie, B. Purcell, and R. C. T. Li, "Gait event detection using linear accelerometers or angular velocity transducers in able-bodied and spinal-cord injured individuals," *Gait & Posture*, vol. 24, no. 4, pp. 502 – 509, 2006.

[154] A. M. Sabatini, C. Martelloni, S. Scapellato, and F. Cavallo, "Energy expenditure rate in level and uphill treadmill walking determined from empirical models and foot inertial sensing data," *Electronics Letters*, vol. 40, no. 2, pp. 95–96, Jan 2004.

[155] I. Skog, P. Handel, J.-O. Nilsson, and J. Rantakokko, "Zero-velocity detection – An algorithm evaluation," *IEEE Transactions on Biomedical Engineering*, vol. 57, no. 11, pp. 2657–2666, Nov 2010.

[156] J. P. Imhof, "Computing the distribution of quadratic forms in normal variables," *Biometrika*, vol. 48, no. 3/4, pp. 419–426, 1961.

[157] M. E. Morris, R. Iansek, T. A. Matyas, and J. J. Summers, "Ability to modulate walking cadence remains intact in parkinson's disease." *Journal of Neurology, Neurosurgery & Psychiatry*, vol. 57, no. 12, pp. 1532–1534, 1994.

[158] C. Ramaker, J. Marinus, A. M. Stiggelbout, and B. J. van Hilten, "Systematic evaluation of rating scales for impairment and disability in Parkinson's disease," *Movement Disorders*, vol. 17, no. 5, pp. 867–876, 2002.

[159] S. Katz, "Assessing self-maintenance: activities of daily living, mobility, and instrumental activities of daily living," *Journal of the American Geriatrics Society*, vol. 31, no. 12, pp. 721–727, 1983.

[160] N. Giladi, H. Shabtai, E. Simon, S. Biran, J. Tal, and A. Korczyn, "Construction of freezing of gait questionnaire for patients with Parkinsonism," *Parkinsonism & Related Disorders*, vol. 6, no. 3, pp. 165–170, 2000.

[161] O. Moore, C. Peretz, and N. Giladi, "Freezing of gait affects quality of life of peoples with Parkinson's disease beyond its relationships with mobility and gait," *Movement Disorders*, vol. 22, no. 15, pp. 2192–2195, 2007.

[162] J. Chemali, S. Ching, P. L. Purdon, K. Solt, and E. N. Brown, "Burst suppression probability algorithms: State-space methods for tracking eeg burst suppression," *Journal of Neural Engineering*, vol. 10, no. 5, p. 056017, 2013.

[163] I. Skog, J. O. Nilsson, P. Handel, and A. Nehorai, "Inertial sensor arrays, maximum likelihood, and cramer-rao bound," *IEEE Transactions on Signal Processing*, vol. PP, no. 99, pp. 1–1, 2016.

[164] H. Liu, H. Darabi, P. Banerjee, and J. Liu, "Survey of wireless indoor positioning techniques and systems," *IEEE Transactions on Systems, Man, and Cybernetics, Part C (Applications and Reviews)*, vol. 37, no. 6, pp. 1067–1080, Nov 2007.

[165] MATLAB, *version 9.1.0 (R2016b)*. Natick, Massachusetts: The MathWorks Inc., 2016.

[166] D. L. Donoho and I. M. Johnstone, "Ideal spatial adaptation by wavelet shrinkage," *Biometrika*, vol. 81, no. 3, pp. 425–455, 1994.

[167] A. N. Akansu, R. A. Haddad, and H. Caglar, "The binomial QMF-wavelet transform for multiresolution signal decomposition," *IEEE Transactions on Signal Processing*, vol. 41, no. 1, pp. 13–, January 1993.

[168] C. G. Goetz, B. C. Tilley, S. R. Shaftman, G. T. Stebbins, S. Fahn, P. Martinez-Martin, W. Poewe, C. Sampaio, M. B. Stern, R. Dodel, B. Dubois, R. Holloway, J. Jankovic, J. Kulisevsky, A. E. Lang, A. Lees, S. Leurgans, P. A. LeWitt, D. Nyenhuis, C. W. Olanow, O. Rascol, A. Schrag, J. A. Teresi, J. J. van Hilten, and N. LaPelle, "Movement disorder society-sponsored revision of the unified Parkinson's disease rating scale (MDS-UPDRS): Scale presentation and clinimetric testing results," *Movement Disorders*, vol. 23, no. 15, pp. 2129–2170, 2008.

Appendix A

A.1 Openshoe Database

In this database, we collected real data from 16 people with Parkinson disease. For our sample, there were seven females, the mean age was 70.3 ± 7.9 years, the mean disease duration was 5.0 ± 3.6 years, and the median off medication Movement Disorders Society Unified Parkinson Disease Rating Scale Motor Subsection (MDS_UPDRS_III) Score was 35.5 (first and third quartiles: 30.5, 41.5). The IMU data and video data for all the participants were recorded for the list of gait tasks in Table A.1, with the only exceptions being TT006–NARROW and TT006–EIGHT, which were not recorded due to network issues. The true instances of FOG events detected in the video data are manually marked by a trained gait analysis experts.

We used the Openshoe module to collect the accelerometer and gyroscope sensor data [49]. The sensors operated at a sampling frequency of $F_{\mathrm{s}} = 1000$ Hz. We taped the sensor module to the heel of each shoe firmly, as shown in Fig. 3.2. The choice of the sensor location [15] enabled us to compute gait parameters such as speed of the foot which can be useful in understanding the underlying mechanism of FOG. The sensors were powered by micro-USB cords whose other ends are plugged into a USB-port of a laptop. The laptop, which weighs less than 1.2 kilograms, was placed in a backpack carried by the participant. Cords were

Table A.1: Experiment 1: Balance assessment tasks and their descriptions.

Task	Description of the task
BACK	The participant was asked to walk backwards at a comfortable pace along a 3 meter straight path. On reaching the end, the participant made a 180° turn and re-traversed the path in the next trial.
BLOCK	A wood block 6 inches high, 24 inches wide, and 14.5 inches deep was placed between two cones. The total distance between the center of each cone and the nearest edge of the block was 22.5 inches. The participant was asked to start between one of the cones and the block, step up onto the block and step down between the block and the second cone. The participant made a 180° turn in the small space between the block and the cone, and repeated the trial.
EIGHT	The participant was asked to follow a figure-eight trajectory around two cones placed 1.5 meters apart (cone center to cone center). Two chairs were placed with the backs inward, approximately shoulder width apart at the center of the figure-eight loop to create a narrow space. The participants started next to a cone at one end of the figure-eight loop, completed the figure-eight (traveling through the narrow space), and positioned themselves on the other side of the first cone for the next figure-eight.
NARROW	The participant was asked to walk along a path 3 meters long, with three sets of chairs placed with the backs inward, about shoulder width apart in the middle 1.5 meters of the path. At the end of the 3 meter path, the participant made a 180° turn and re-traversed the path in the next trial.
TURN	The participant was asked to do an in-place 180° turn. The participant began by standing stationary and was told to turn either right or left to face the wall behind them.

firmly strapped around each leg, so that they did not interfere with gait and there are minimal cord movements captured by the sensors.

To assess gait, we assigned five different tasks that are likely to trigger a FOG event. The list of the tasks and their descriptions are given in Table A.1. As a reference system, we use video-based technology to determine the time instances of FOG. With the help of trained gait analysis experts, we mark the instances of FOG observed in the videos with a temporal resolution of one second. The experts watched each video together and came to consensus on the presence and timing of definite or potential freezing episodes. The synchronization of the video and IMU data is done manually.

Table A.2: Experiment 2: Balance assessment tasks and their descriptions.

Task	Description of the task
TUG1	The participant stands up from the chair, walks 3 meters, turns, walks back, and returns to a sitting position.
TUG2	The participant stands up from the chair, walks 3 meters, turns, walks back, and returns to a sitting position, while counting numbers backwards from a starting point given by the instructor in fixed step size.
TURN	The participant is asked to do an in-place 360° turn. The participant begins by standing stationary and is told to turn either right or left. The TURN task is repeated in sets of three or five.
SAW	The participant stands at one end of the walkway, with their feet comfortably apart and their hands on their hips, for 30 seconds, when a tone sounds. Then the participant walks 7 meters, turns, walks back, and stops, now facing the opposite direction of their starting position.
WALK	The participant walks 7 meters at a comfortable pace, turns, walks back, turns again, and repeats this routine until the end of two minutes.

TUG: Timed up and go; SAW: Stand and walk.

A.2 Opal APDM Database

In this database, we collected real data from seven Parkinson disease participants. The mean age 70.57 ± 5.65 years, the mean disease duration was 4.71 ± 4.54 years, and the mean on-medication score on the motor section of the Movement Disorders Society Unified Parkinson Disease Rating Scale (MDS-UPDRS III) [168] was 28.71 ± 11.69. Four of the participants were women. We used APDM Opal sensors [50] to collect accelerometer and gyroscope sensor data. The sensors operated at a sampling frequency of $F_s = 128$ Hz and were firmly attached to the instep region of the foot with the help of elastic Velcro straps. Data from the sensors was transmitted in wireless mode to a laptop and stored in HDF5 format. To assess gait, we assigned five different tasks that are likely to trigger a FOG event. The tasks and their descriptions are listed in Table A.2. As a gold standard, we used video-based technology to determine the time instances of FOG. With the help of trained gait analysis experts, we mark the instances of FOG in the videos with a temporal resolution of one second. The video and IMU data were manually synchronized.

Appendix B

B.1 Derivation of Detector-I

Let $\boldsymbol{y}^{\mathrm{a}}$, $\boldsymbol{u}^{\mathrm{a}}$, $\boldsymbol{v}^{\mathrm{a}}$, and $\boldsymbol{\alpha}^{\mathrm{a}}$ denote the concatenation of the observed accelerometer signal vector, direction of the accelerometer vector without the gravity vector, direction of the gravity vector, and magnitude of the accelerometer vector, respectively. Then,

$$\begin{aligned}
\boldsymbol{y}^{\mathrm{a}} &= [(\boldsymbol{y}_k^{\mathrm{a}})^{\mathsf{T}}, \ldots, (\boldsymbol{y}_{k+N-1}^{\mathrm{a}})^{\mathsf{T}}]^{\mathsf{T}} \in \mathbb{R}^{3N\times 1}, \\
\boldsymbol{u}^{\mathrm{a}} &= [(\boldsymbol{u}_k^{\mathrm{a}})^{\mathsf{T}}, \ldots, (\boldsymbol{u}_{k+N-1}^{\mathrm{a}})^{\mathsf{T}}]^{\mathsf{T}} \in \mathbb{R}^{3N\times 1}, \\
\boldsymbol{v}^{\mathrm{a}} &= [(\boldsymbol{v}_k^{\mathrm{a}})^{\mathsf{T}}, \ldots, (\boldsymbol{v}_{k+N-1}^{\mathrm{a}})^{\mathsf{T}}]^{\mathsf{T}} \in \mathbb{R}^{3N\times 1}, \\
\boldsymbol{\alpha}^{\mathrm{a}} &= [\alpha_k^{\mathrm{a}}, \ldots, \alpha_{k+N-1}^{\mathrm{a}}]^{\mathsf{T}} \in \mathbb{R}^{N\times 1}.
\end{aligned}$$

Under $\mathcal{H}_0$, the conditional probability density function of $\boldsymbol{y}^{\mathrm{a}}$, denoted as $f_0\left(\boldsymbol{y}^{\mathrm{a}}|\boldsymbol{\alpha}^{\mathrm{a}}, \boldsymbol{u}^{\mathrm{a}}, \boldsymbol{v}^{\mathrm{a}}\right)$ factors as

$$f_0\left(\boldsymbol{y}^{\mathrm{a}}|\boldsymbol{\alpha}^{\mathrm{a}}, \boldsymbol{u}^{\mathrm{a}}, \boldsymbol{v}^{\mathrm{a}}\right) = \prod_{k\in\Omega_N} \mathcal{N}(\alpha_k^{\mathrm{a}}\boldsymbol{u}_k^{\mathrm{a}} + g\boldsymbol{v}_k^{\mathrm{a}}, \sigma_{\mathrm{a}}^2\boldsymbol{I}_3)$$

Under $\mathcal{H}_{1,2}$, the conditional probability density function of $\boldsymbol{y}$, denoted as $f_{1,2}\left(\boldsymbol{y}|\boldsymbol{\alpha}^{\mathrm{a}}, \boldsymbol{u}^{\mathrm{a}}, \boldsymbol{v}^{\mathrm{a}}\right)$ factors as

$$f_{1,2}\left(\boldsymbol{y}^{\mathrm{a}}|\boldsymbol{\alpha}^{\mathrm{a}}, \boldsymbol{u}^{\mathrm{a}}, \boldsymbol{v}^{\mathrm{a}}\right) = \prod_{k\in\Omega_N} \mathcal{N}(\alpha_k^{\mathrm{a}}\boldsymbol{u}^{\mathrm{a}} + g\boldsymbol{v}^{\mathrm{a}}, \sigma_{\mathrm{a}}^2\boldsymbol{I}_3)$$

The GLRT based detector replaces the unknown parameters with their maximum likelihood estimates (MLEs). Let $L_0(\boldsymbol{\alpha}^{\mathrm{a}}, \boldsymbol{u}^{\mathrm{a}}, \boldsymbol{v}^{\mathrm{a}}|\boldsymbol{y}^{\mathrm{a}})$ and $L_{1,2}(\boldsymbol{\alpha}^{\mathrm{a}}, \boldsymbol{u}^{\mathrm{a}}, \boldsymbol{v}^{\mathrm{a}}|\boldsymbol{y}^{\mathrm{a}})$ denote the loglikelihood of the probability distribution functions under $\mathcal{H}_0$ and $\mathcal{H}_{1,2}$, respectively. If $L_{\mathrm{D}_1}(\boldsymbol{y}^{\mathrm{a}})$ is the likelihood ratio, and $\hat{\boldsymbol{\alpha}}^a$, $\hat{\boldsymbol{u}}^a$, and $\hat{\boldsymbol{v}}^a$, are the maximum likelihood estimates of the unknown parameters, then the GLRT based detector can be written as

$$\ln L_{\mathrm{D}_1}(\boldsymbol{y}^{\mathrm{a}}) = \max_{\boldsymbol{\alpha}^{\mathrm{a}},\boldsymbol{u}^{\mathrm{a}},\boldsymbol{v}^{\mathrm{a}}} L_0(\boldsymbol{\alpha}^{\mathrm{a}}, \boldsymbol{u}^{\mathrm{a}}, \boldsymbol{v}^{\mathrm{a}}|\boldsymbol{y}^{\mathrm{a}}) - \max_{\boldsymbol{\alpha}^{\mathrm{a}},\boldsymbol{u}^{\mathrm{a}},\boldsymbol{v}^{\mathrm{a}}} L_{1,2}(\boldsymbol{\alpha}^{\mathrm{a}}, \boldsymbol{u}^{\mathrm{a}}, \boldsymbol{v}^{\mathrm{a}}|\boldsymbol{y}^{\mathrm{a}}) \underset{\mathcal{H}_{1,2}}{\overset{\mathcal{H}_0}{\gtrless}} \ln\gamma_{\mathrm{D}_1}. \tag{B.1}$$

The loglikelihood function, $L_0(\boldsymbol{\alpha}^{\mathrm{a}}, \boldsymbol{u}^{\mathrm{a}}, \boldsymbol{v}^{\mathrm{a}}|\boldsymbol{y}^{\mathrm{a}})$, under the hypothesis $\mathcal{H}_0$, is

$$L_0(\boldsymbol{\alpha}^{\mathrm{a}}, \boldsymbol{u}^{\mathrm{a}}, \boldsymbol{v}^{\mathrm{a}}|\boldsymbol{y}^{\mathrm{a}}) = c - \sum_{k\in\Omega_N}\left[\frac{1}{2\sigma_{\mathrm{a}}^2}\left\|\boldsymbol{y}_k^{\mathrm{a}} - \alpha_k^{\mathrm{a}}\boldsymbol{u}_k^{\mathrm{a}} - g\boldsymbol{v}_k^{\mathrm{a}}\right\|^2\right],$$

where c is the normalizing constant. However, the parameters α_k^{a}, $\boldsymbol{u}_k^{\mathrm{a}}$, and $\boldsymbol{v}_k^{\mathrm{a}}$ that define the accelerometer signal are unknown. Hence, the maximum of the $L_0(\boldsymbol{\alpha}^{\mathrm{a}}, \boldsymbol{u}^{\mathrm{a}}, \boldsymbol{v}^{\mathrm{a}}|\boldsymbol{y}^{\mathrm{a}})$ is,

$$\max_{\boldsymbol{\alpha}^{\mathrm{a}},\boldsymbol{u}^{\mathrm{a}},\boldsymbol{v}^{\mathrm{a}}} L_0(\boldsymbol{\alpha}^{\mathrm{a}}, \boldsymbol{u}^{\mathrm{a}}, \boldsymbol{v}^{\mathrm{a}}|\boldsymbol{y}^{\mathrm{a}}) = c. \tag{B.2}$$

The loglikelihood function, $L_{1,2}(\boldsymbol{\alpha}^{\mathrm{a}}, \boldsymbol{u}^{\mathrm{a}}, \boldsymbol{v}^{\mathrm{a}}|\boldsymbol{y})$, under the hypothesis $\mathcal{H}_{1,2}$ is given as:

$$L_{1,2}(\boldsymbol{\alpha}^{\mathrm{a}}, \boldsymbol{u}^{\mathrm{a}}, \boldsymbol{v}^{\mathrm{a}}|\boldsymbol{y}^{\mathrm{a}}) = c - \sum_{k\in\Omega_N}\left[\frac{1}{2\sigma_{\mathrm{a}}^2}\left\|\boldsymbol{y}_k^{\mathrm{a}} - \alpha_k^{\mathrm{a}}\boldsymbol{u}^{\mathrm{a}} - g\boldsymbol{v}^{\mathrm{a}}\right\|^2\right]. \tag{B.3}$$

Let $\hat{\alpha}_k^{\mathrm{a}}$ be the MLE of α_k^{a} that minimizes (B.3). Taking the partial derivative with respect to α_k^{a} and equating it to zero, we get

$$\hat{\alpha}_k^{\mathrm{a}} = \frac{(\boldsymbol{u}^{\mathrm{a}})^{\mathsf{T}}(\boldsymbol{y}_k^{\mathrm{a}} - g\boldsymbol{v}^{\mathrm{a}})}{\|\boldsymbol{u}^{\mathrm{a}}\|^2} = (\boldsymbol{u}^{\mathrm{a}})^{\mathsf{T}}(\boldsymbol{y}_k^{\mathrm{a}} - g\boldsymbol{v}^{\mathrm{a}}). \tag{B.4}$$

Substituting (B.4) in (B.3) gives

$$L_{1,2}(\hat{\boldsymbol{\alpha}}^{\mathrm{a}}, \boldsymbol{u}^{\mathrm{a}}, \boldsymbol{v}^{\mathrm{a}} | \boldsymbol{y}^{\mathrm{a}}) = c - \frac{1}{2\sigma_{\mathrm{a}}^2} \sum_{k \in \Omega_N} \left\| \boldsymbol{y}_k^{\mathrm{a}} - (\boldsymbol{u}^{\mathrm{a}})^{\mathsf{T}}(\boldsymbol{y}_k^{\mathrm{a}} - g\boldsymbol{v}^{\mathrm{a}}) - g\boldsymbol{v}^{\mathrm{a}} \right\|^2. \tag{B.5}$$

Maximizing (B.5) is equivalent solving the following minimization problem:

$$\min_{\boldsymbol{u}^{\mathrm{a}}, \boldsymbol{v}^{\mathrm{a}}} \sum_{k \in \Omega_N} \|\boldsymbol{y}_k^{\mathrm{a}} - g\boldsymbol{v}^{\mathrm{a}}\|^2_{\boldsymbol{P}^{\perp}_{\boldsymbol{u}^{\mathrm{a}}}}, \tag{B.6}$$

where $\boldsymbol{P}^{\perp}_{\boldsymbol{u}^{\mathrm{a}}} = \boldsymbol{I} - \boldsymbol{u}^{\mathrm{a}}(\boldsymbol{u}^{\mathrm{a}})^{\mathsf{T}}$. Note that $\boldsymbol{P}^{\perp}_{\boldsymbol{u}^{\mathrm{a}}}$ is idempotent and symmetric, which makes it an orthogonal projection matrix. The weighted optimization problem in (B.6) is bi-quadratic, i.e., it is quadratic with respect to both $\boldsymbol{u}^{\mathrm{a}}$ and $\boldsymbol{v}^{\mathrm{a}}$. Further, the optimization problem in (B.6) does not have a closed form expression. Here, we use alternative minimization technique to solve (B.6). In alternative minimization, one of the two variables $\boldsymbol{u}^{\mathrm{a}}$ and $\boldsymbol{v}^{\mathrm{a}}$ is fixed, and minimizing the function with respect to the other variable is of low-complexity and high stability. We begin solving the optimization problem by first fixing $\boldsymbol{v}^{\mathrm{a}}$ in (B.6). The minimization problem is formulated as

$$\begin{aligned}
&\min_{\boldsymbol{u}^{\mathrm{a}}} \sum_{k \in \Omega_N} \left\{ \|\boldsymbol{y}_k^{\mathrm{a}} - g\boldsymbol{v}^{\mathrm{a}}\|^2 - (\boldsymbol{y}_k^{\mathrm{a}} - g\boldsymbol{v}^{\mathrm{a}})^{\mathsf{T}} \boldsymbol{u}^{\mathrm{a}} (\boldsymbol{u}^{\mathrm{a}})^{\mathsf{T}} (\boldsymbol{y}_k^{\mathrm{a}} - g\boldsymbol{v}^{\mathrm{a}}) \right\} \\
&= \max_{\boldsymbol{u}^{\mathrm{a}}} \left\{ (\boldsymbol{u}^{\mathrm{a}})^{\mathsf{T}} \sum_{k \in \Omega_N} \left[(\boldsymbol{y}_k^{\mathrm{a}} - g\boldsymbol{v}^{\mathrm{a}})(\boldsymbol{y}_k^{\mathrm{a}} - g\boldsymbol{v}^{\mathrm{a}})^{\mathsf{T}} \right] \boldsymbol{u}^{\mathrm{a}} \right\}.
\end{aligned} \tag{B.7}$$

Let $\boldsymbol{G}^{\mathrm{a}} = \sum_{k\in\Omega_N} \left[(\boldsymbol{y}_k^{\mathrm{a}} - g\boldsymbol{v}^{\mathrm{a}})(\boldsymbol{y}_k^{\mathrm{a}} - g\boldsymbol{v}^{\mathrm{a}})^{\mathsf{T}}\right]$. The matrix $\boldsymbol{G}^{\mathrm{a}}$ is positive definite and symmetric. Let $\hat{\boldsymbol{u}}^{\mathrm{a}}$ denote the eigenvector corresponding to the maximum eigenvalue of $\boldsymbol{G}^{\mathrm{a}}$. Equation (B.7) is maximized when $\boldsymbol{u}^{\mathrm{a}}$ is equal to the eigenvector corresponding to the maximum eigenvalue of $\boldsymbol{G}^{\mathrm{a}}$. For any symmetric and positive semi-definite matrix, $\boldsymbol{G}^{\mathrm{a}}$, the maximum eigenvector represents the direction of the semi-major axis, and its eigenvalue represents the length of the semi-major axis. Clearly, the eigenvector corresponding to the maximum eigenvalue of the outer product term in (B.7) captures the direction of the trembling because it subtracts the constant magnitude and direction representing the gravitational force from the accelerometer readings, and computes the outer product. If $\lambda_{\max}(\cdot)$ denotes the the maximum eigenvalue and $\tilde{\boldsymbol{u}}^{\mathrm{a}}$ denotes the optimal value of $\boldsymbol{u}^{\mathrm{a}}$, then

$$\tilde{\boldsymbol{u}}^{\mathrm{a}} = \text{eigenvector corresponding to } \lambda_{\max}(\boldsymbol{G}^{\mathrm{a}}). \tag{B.8}$$

Next, we fix $\boldsymbol{u}^{\mathrm{a}}$ in (B.6) and minimize the objective function with respect to $\boldsymbol{v}^{\mathrm{a}}$. The minimization problem is formulated as

$$\min_{\boldsymbol{v}^{\mathrm{a}}} \sum_{k\in\Omega_N} \|\boldsymbol{y}_k^{\mathrm{a}} - g\boldsymbol{v}^{\mathrm{a}}\|^2_{\boldsymbol{P}^{\perp}_{\boldsymbol{u}^{\mathrm{a}}}}\,. \tag{B.9}$$

Taking the partial derivative of (B.9) with respect to $\boldsymbol{v}^{\mathrm{a}}$ and equating to zero we get

$$-2g \sum_{k\in\Omega_N} \boldsymbol{P}^{\perp}_{\boldsymbol{u}^{\mathrm{a}}}(\boldsymbol{y}_k^{\mathrm{a}} - g\boldsymbol{v}^{\mathrm{a}}) = \boldsymbol{0}. \tag{B.10}$$

If $\boldsymbol{P}_{\boldsymbol{u}^{\mathrm{a}}}$ represents the projection matrix that is orthogonal to $\boldsymbol{P}^{\perp}_{\boldsymbol{u}^{\mathrm{a}}}$, then based on the orthogonality of projection matrices, we get $\sum_{k\in\Omega_N}(\boldsymbol{y}_k^{\mathrm{a}} - g\boldsymbol{v}^{\mathrm{a}}) \in \boldsymbol{P}_{\boldsymbol{u}^{\mathrm{a}}}$. This implies that $\sum_{k\in\Omega_N}(\boldsymbol{y}_k^{\mathrm{a}} - g\boldsymbol{v}^{\mathrm{a}}) = \eta\boldsymbol{u}^{\mathrm{a}}$, where $\eta > 0$ is the magnitude of the unit vector in the direction of $\boldsymbol{u}^{\mathrm{a}}$. The choice of $\eta > 0$ can be arbitrary since we are only concerned with the direction of

Algorithm 5 Alternating Minimization

procedure AM
  initialize:
  $i \leftarrow 0$, $C_{(0)} \leftarrow 0$, ϵ, and $\mathrm{MAX_ITER}$
  $\boldsymbol{v}^{\mathrm{a}}_{(0)} \leftarrow \bar{\boldsymbol{y}}^{\mathrm{a}}_k / \left\|\bar{\boldsymbol{y}}^{\mathrm{a}}_k\right\|$, where $\bar{\boldsymbol{y}}^{\mathrm{a}}_k = (1/N)\sum_{k\in\Omega_N} \boldsymbol{y}^{\mathrm{a}}_k$
  while do$(i \leq \mathrm{MAX_ITER})$ and $(|C_{(i)} - C_{(i-1)}| < \epsilon)$
    $\boldsymbol{G}^{\mathrm{a}}_{(i)} \leftarrow \sum_{k\in\Omega_N}\left[(\boldsymbol{y}^{\mathrm{a}}_k - g\boldsymbol{v}^{\mathrm{a}}_{(i-1)})(\boldsymbol{y}^{\mathrm{a}}_k - g\boldsymbol{v}^{\mathrm{a}}_{(i-1)})^{\mathsf{T}}\right]$
    $\tilde{\boldsymbol{u}}^{\mathrm{a}}_{(i)} \leftarrow$ eigenvector corresponding to $\lambda_{\max}(\boldsymbol{G}^{\mathrm{a}}_{(i)})$
    $(\bar{\boldsymbol{y}}^{\mathrm{a}}_k - \bar{\boldsymbol{u}}^{\mathrm{a}}_{(i)}) \leftarrow \frac{1}{N}\sum_{k\in\Omega_N}(\boldsymbol{y}^{\mathrm{a}}_k - \boldsymbol{u}^{\mathrm{a}}_{(i)})$
    $\tilde{\boldsymbol{v}}^{\mathrm{a}}_{(i)} \leftarrow (\bar{\boldsymbol{y}}^{\mathrm{a}}_k - \bar{\boldsymbol{u}}^{\mathrm{a}}_{(i)}) / \left\|\bar{\boldsymbol{y}}^{\mathrm{a}}_k - \bar{\boldsymbol{u}}^{\mathrm{a}}_{(i)}\right\|$
    $C_{(i)} \leftarrow \sum_{k\in\Omega_N}(\boldsymbol{y}^{\mathrm{a}}_k - g\tilde{\boldsymbol{v}}^{\mathrm{a}}_{(i)})^{\mathsf{T}}\boldsymbol{P}^{\perp}_{\tilde{\boldsymbol{u}}^{\mathrm{a}}_{(i)}}(\boldsymbol{y}^{\mathrm{a}}_k - g\tilde{\boldsymbol{v}}^{\mathrm{a}}_{(i)})$
    $i \leftarrow i + 1$
  end while
  return $\hat{\boldsymbol{u}}^{\mathrm{a}} = \tilde{\boldsymbol{u}}^{\mathrm{a}}_{(i)}$ and $\hat{\boldsymbol{v}}^{\mathrm{a}} = \tilde{\boldsymbol{v}}^{\mathrm{a}}_{(i)}$
end procedure

the unit vector $\boldsymbol{v}^{\mathrm{a}}$. Here, we choose $\eta = 1$. Therefore, we get

$$\sum_{k\in\Omega_N}(\boldsymbol{y}^{\mathrm{a}}_k - g\boldsymbol{v}^{\mathrm{a}}) = \boldsymbol{u}^{\mathrm{a}}. \tag{B.11}$$

Solving for $\boldsymbol{v}^{\mathrm{a}}$ and ignoring the scale parameter, we get

$$\boldsymbol{v}^{\mathrm{a}} = \frac{1}{N}\sum_{k\in\Omega_N}(\boldsymbol{y}^{\mathrm{a}}_k - \boldsymbol{u}^{\mathrm{a}}) = (\bar{\boldsymbol{y}}^{\mathrm{a}}_k - \bar{\boldsymbol{u}}^{\mathrm{a}}). \tag{B.12}$$

In (B.12), the trembling axis is subtracted from every sample of the accelerometer to obtain the direction of the gravitational vector. Let $\tilde{\boldsymbol{v}}^{\mathrm{a}}$ denote the unit norm vector in the direction of $\boldsymbol{v}^{\mathrm{a}}$. In Algorithm 5, we summarize the steps of the alternating minimization approach to find the MLE of $\boldsymbol{u}^{\mathrm{a}}$ and $\boldsymbol{v}^{\mathrm{a}}$. Substituting $\hat{\boldsymbol{u}}^{\mathrm{a}}$ and $\hat{\boldsymbol{v}}^{\mathrm{a}}$ in (B.5), we get

$$L_{1,2}(\hat{\boldsymbol{\alpha}}^{\mathrm{a}}, \hat{\boldsymbol{u}}^{\mathrm{a}}, \hat{\boldsymbol{v}}^{\mathrm{a}} | \boldsymbol{y}^{\mathrm{a}}) = c - \frac{1}{2\sigma^2_{\mathrm{a}}}\sum_{k\in\Omega_N}\left\|\boldsymbol{y}^{\mathrm{a}}_k - g\hat{\boldsymbol{v}}^{\mathrm{a}}\right\|^2_{\boldsymbol{P}^{\perp}_{\hat{\boldsymbol{u}}^{\mathrm{a}}}}. \tag{B.13}$$

Substituting (B.2) and (B.13) in (B.1), we get

$$\ln L_{\mathrm{D}_1}(\boldsymbol{y}_k^{\mathrm{a}}) = \frac{1}{2\sigma_{\mathrm{a}}^2} \sum_{k \in \Omega_N} \|\boldsymbol{y}_k^{\mathrm{a}} - g\hat{\boldsymbol{v}}^{\mathrm{a}}\|^2_{\boldsymbol{P}^{\perp}_{\hat{\boldsymbol{u}}^{\mathrm{a}}}}. \tag{B.14}$$

The test statistic, $T_{\mathrm{D}_1}(\boldsymbol{y}^{\mathrm{a}}) = (2/N) \ln L_{\mathrm{D}_1}(\boldsymbol{y}^{\mathrm{a}})$, is given as

$$T_{\mathrm{D}_1}(\boldsymbol{y}^{\mathrm{a}}) = \frac{1}{N} \sum_{k \in \Omega_N} \left\{ \frac{1}{\sigma_{\mathrm{a}}^2} \|\boldsymbol{y}_k^{\mathrm{a}} - g\hat{\boldsymbol{v}}^{\mathrm{a}}\|^2_{\boldsymbol{P}^{\perp}_{\hat{\boldsymbol{u}}^{\mathrm{a}}}} \right\} \overset{\mathcal{H}_{1,2}}{<} \gamma'_{\mathrm{D}_1}, \tag{B.15}$$

where $\gamma'_{\mathrm{D}_1} = (2/N) \ln \gamma_{D_1}$.

B.2 Derivation of Detector-II

Let $\boldsymbol{y}^{\omega}$, $\boldsymbol{u}^{\omega}$, and $\boldsymbol{\beta}^{\omega}$ denote the concatenation of the observed gyroscope signal vector, direction of the gyroscope vector, and magnitude of the gyroscope vector, respectively. Then,

$$\begin{aligned}
\boldsymbol{y}^{\omega} &= [(\boldsymbol{y}_k^{\omega})^{\mathsf{T}}, \ldots, (\boldsymbol{y}_{k+N-1}^{\omega})^{\mathsf{T}}]^{\mathsf{T}} \in \mathbb{R}^{3N \times 1}, \\
\boldsymbol{u}^{\omega} &= [(\boldsymbol{u}_k^{\omega})^{\mathsf{T}}, \ldots, (\boldsymbol{u}_{k+N-1}^{\omega})^{\mathsf{T}}]^{\mathsf{T}} \in \mathbb{R}^{3N \times 1}, \\
\boldsymbol{\beta}^{\omega} &= [\beta_k^{\omega}, \ldots, \beta_{k+N-1}^{\omega}]^{\mathsf{T}} \in \mathbb{R}^{N \times 1}.
\end{aligned}$$

where $\boldsymbol{s}_k^{\omega} = \beta_k^{\omega} \boldsymbol{u}_k^{\omega}$, β_k^{ω} is the magnitude of the angular velocity vector, and $\boldsymbol{u}_k^{\omega}$ is a unit vector in the direction of the angular velocity vector. Let $\boldsymbol{y} = [(\boldsymbol{y}^{\mathrm{a}})^{\mathsf{T}}, (\boldsymbol{y}^{\omega})^{\mathsf{T}}]^{\mathsf{T}}$ denote the concatenation of the accelerometer and gyrocope signal. Under $\mathcal{H}_1$, the conditional probability

density function of $\boldsymbol{y}$, denoted as $f_1\left(\boldsymbol{y}|\boldsymbol{v}^{\mathrm{a}}\right)$ factors as

$$f_1\left(\boldsymbol{y}|\boldsymbol{v}^{\mathrm{a}}\right) = \prod_{k\in\Omega_N} \mathcal{N}(g\boldsymbol{v}^{\mathrm{a}}, \sigma_{\mathrm{a}}^2\boldsymbol{I}_3) \times \mathcal{N}(\boldsymbol{0}, \sigma_{\omega}^2\boldsymbol{I}_3).$$

Under $\mathcal{H}_2$, the conditional probability density function of $\boldsymbol{y}$, denoted as $f_2\left(\boldsymbol{y}|\boldsymbol{\alpha}^{\mathrm{a}}, \boldsymbol{u}^{\mathrm{a}}, \boldsymbol{v}^{\mathrm{a}}, \boldsymbol{\beta}^{\omega}, \boldsymbol{u}^{\omega}\right)$ factors as

$$f_2\left(\boldsymbol{y}|\boldsymbol{\alpha}^{\mathrm{a}}, \boldsymbol{u}^{\mathrm{a}}, \boldsymbol{v}^{\mathrm{a}}, \boldsymbol{\beta}^{\omega}, \boldsymbol{u}^{\omega}\right) = \prod_{k\in\Omega_N} \mathcal{N}(\alpha_k^{\mathrm{a}}\boldsymbol{u}^{\mathrm{a}} + g\boldsymbol{v}^{\mathrm{a}}, \sigma_{\mathrm{a}}^2\boldsymbol{I}_3) \times \mathcal{N}(\beta_{\omega}^k\boldsymbol{u}_k^{\omega}, \sigma_{\omega}^2\boldsymbol{I}_3).$$

Let $L_2(\boldsymbol{\alpha}^{\mathrm{a}}, \boldsymbol{u}^{\mathrm{a}}, \boldsymbol{v}^{\mathrm{a}}, \boldsymbol{\beta}^{\omega}, \boldsymbol{u}^{\omega}|\boldsymbol{y})$ and $L_1(\boldsymbol{v}^{\mathrm{a}}|\boldsymbol{y})$ denote the loglikelihood of the probability distribution functions under $\mathcal{H}_2$ and $\mathcal{H}_1$, respectively. Let $L_{\mathrm{D}_2}(\boldsymbol{y})$ denote the likelihood ratio, and $\hat{\boldsymbol{\alpha}}^a$, $\hat{\boldsymbol{u}}^a$, $\hat{\boldsymbol{v}}^a$, $\hat{\boldsymbol{\beta}}^a$, and $\hat{\boldsymbol{u}}^{\omega}$ are the maximum likelihood estimates of the unknown parameters, then the GLRT based detector can be written as

$$\ln L_{\mathrm{D}_2}(\boldsymbol{y}) = \max_{\boldsymbol{\alpha}^{\mathrm{a}}, \boldsymbol{u}^{\mathrm{a}}, \boldsymbol{v}^{\mathrm{a}}, \boldsymbol{\beta}^{\omega}, \boldsymbol{u}^{\omega}} L_2(\boldsymbol{\alpha}^{\mathrm{a}}, \boldsymbol{u}^{\mathrm{a}}, \boldsymbol{v}^{\mathrm{a}}, \boldsymbol{\beta}^{\omega}, \boldsymbol{u}^{\omega}|\boldsymbol{y}) - \max_{\boldsymbol{v}^{\mathrm{a}}} L_1(\boldsymbol{v}^{\mathrm{a}}|\boldsymbol{y}) \underset{\mathcal{H}_1}{\overset{\mathcal{H}_2}{\gtrless}} \ln \gamma_{\mathrm{D}_2}. \tag{B.16}$$

The loglikelihood function, $L_2(\boldsymbol{\alpha}^{\mathrm{a}}, \boldsymbol{u}^{\mathrm{a}}, \boldsymbol{v}^{\mathrm{a}}, \boldsymbol{\beta}^{\omega}, \boldsymbol{u}^{\omega}|\boldsymbol{y})$, under the hypothesis $\mathcal{H}_2$, is

$$L_2(\boldsymbol{\alpha}^{\mathrm{a}}, \boldsymbol{u}^{\mathrm{a}}, \boldsymbol{v}^{\mathrm{a}}, \boldsymbol{\beta}^{\omega}, \boldsymbol{u}^{\omega}|\boldsymbol{y}) = c' - \sum_{k\in\Omega_N} \left[\frac{1}{2\sigma_{\mathrm{a}}^2} \left\| \boldsymbol{y}_k^{\mathrm{a}} - \alpha_k^{\mathrm{a}}\boldsymbol{u}^{\mathrm{a}} - g\boldsymbol{v}^{\mathrm{a}} \right\|^2 + \frac{1}{2\sigma_{\omega}^2} \left\| \boldsymbol{y}_k^{\omega} - \beta_k^{\omega}\boldsymbol{u}_k^{\omega} \right\|^2 \right].$$

where c' is a normalizing constant. The minimization of the third term with respect to α_k^{a}, $\boldsymbol{u}^{\mathrm{a}}$, and $\boldsymbol{v}^{\mathrm{a}}$ follows the same steps as in Appendix B.1. In the fourth term, the parameters, β_k^{ω} and $\boldsymbol{u}_k^{\omega}$, that describe the gyroscope vector are unknown and goes to the minimum value when the norm in the fourth term of (B.16) goes to zero. Hence, the maximum of the

$L_2(\boldsymbol{\alpha}^{\mathrm{a}}, \boldsymbol{u}^{\mathrm{a}}, \boldsymbol{v}^{\mathrm{a}}, \boldsymbol{\beta}^{\omega}, \boldsymbol{u}^{\omega}|\boldsymbol{y})$ is,

$$\max_{\boldsymbol{\alpha}^{\mathrm{a}}, \boldsymbol{u}^{\mathrm{a}}, \boldsymbol{v}^{\mathrm{a}}, \boldsymbol{\beta}^{\omega}, \boldsymbol{u}^{\omega}} L_2(\boldsymbol{\alpha}^{\mathrm{a}}, \boldsymbol{u}^{\mathrm{a}}, \boldsymbol{v}^{\mathrm{a}}, \boldsymbol{\beta}^{\omega}, \boldsymbol{u}^{\omega}|\boldsymbol{y}) = c' - \frac{1}{2\sigma_{\mathrm{a}}^2} \sum_{k \in \Omega_N} \|\boldsymbol{y}_k^{\mathrm{a}} - g\hat{\boldsymbol{v}}^{\mathrm{a}}\|^2_{\boldsymbol{P}^{\perp}_{\hat{\boldsymbol{u}}^{\mathrm{a}}}}. \tag{B.17}$$

The loglikelihood function, $L_1(\boldsymbol{v}^{\mathrm{a}}|\boldsymbol{y})$, under the hypothesis $\mathcal{H}_1$, is

$$L_1(\boldsymbol{v}^{\mathrm{a}}|\boldsymbol{y}) = c' - \sum_{k \in \Omega_N} \left[\frac{1}{2\sigma_{\mathrm{a}}^2} \|\boldsymbol{y}_k^{\mathrm{a}} - g\boldsymbol{v}^{\mathrm{a}}\|^2 + \frac{1}{2\sigma_{\omega}^2} \|\boldsymbol{y}_k^{\omega}\|^2 \right].$$

If $\hat{\boldsymbol{v}}^{\mathrm{a}}$ represents the maximum likelihood estimate of $\boldsymbol{v}^{\mathrm{a}}$, then,

$$\hat{\boldsymbol{v}}^{\mathrm{a}} = \frac{\bar{\boldsymbol{y}}^{\mathrm{a}}}{\|\bar{\boldsymbol{y}}^{\mathrm{a}}\|}, \quad \text{where} \quad \bar{\boldsymbol{y}}^{\mathrm{a}} = \frac{1}{N} \sum_{k \in \Omega_N} \boldsymbol{y}_k^{\mathrm{a}}. \tag{B.18}$$

Hence, the maximum of $L_1(\boldsymbol{v}^{\mathrm{a}}|\boldsymbol{y})$ is given as

$$\max_{\boldsymbol{v}^{\mathrm{a}}} L_1(\boldsymbol{v}^{\mathrm{a}}|\boldsymbol{y}) = c' - \sum_{k \in \Omega_N} \left[\frac{1}{2\sigma_{\mathrm{a}}^2} \left\| \boldsymbol{y}_k^{\mathrm{a}} - g\frac{\bar{\boldsymbol{y}}^{\mathrm{a}}}{\|\bar{\boldsymbol{y}}^{\mathrm{a}}\|} \right\|^2 + \frac{1}{2\sigma_{\omega}^2} \|\boldsymbol{y}_k^{\omega}\|^2 \right]. \tag{B.19}$$

Substituting (B.17) and (B.19) into (B.16), we get

$$\ln L_{\mathrm{D}_2}(\boldsymbol{y}) = \sum_{k \in \Omega_N} \left[\frac{1}{2\sigma_{\mathrm{a}}^2} \left\| \boldsymbol{y}_k^{\mathrm{a}} - g\frac{\bar{\boldsymbol{y}}^{\mathrm{a}}}{\|\bar{\boldsymbol{y}}^{\mathrm{a}}\|} \right\|^2 - \frac{1}{2\sigma_{\mathrm{a}}^2} \|\boldsymbol{y}_k^{\mathrm{a}} - g\hat{\boldsymbol{v}}^{\mathrm{a}}\|^2_{\boldsymbol{P}^{\perp}_{\hat{\boldsymbol{u}}^{\mathrm{a}}}} + \frac{1}{2\sigma_{\omega}^2} \|\boldsymbol{y}_k^{\omega}\|^2 \right]. \tag{B.20}$$

If loglikelihood ratio is denoted as $L_{\mathrm{D}_2}(\boldsymbol{y})$, then the test statistic, $T_{\mathrm{D}_2}(\boldsymbol{y}) = (2/N) \ln L_{\mathrm{D}_2}(\boldsymbol{y})$, is given as

$$T_{\mathrm{D}_2}(\boldsymbol{y}) = \frac{1}{N} \sum_{k \in \Omega_N} \left\{ \frac{1}{\sigma_{\omega}^2} \|\boldsymbol{y}_k^{\omega}\|^2 + \frac{1}{\sigma_2^{\mathrm{a}}} \left[\left\| \boldsymbol{y}_k^{\mathrm{a}} - g\frac{\bar{\boldsymbol{y}}^{\mathrm{a}}}{\|\bar{\boldsymbol{y}}^{\mathrm{a}}\|} \right\|^2 - \|\boldsymbol{y}_k^{\mathrm{a}} - g\hat{\boldsymbol{v}}^{\mathrm{a}}\|^2_{\boldsymbol{P}^{\perp}_{\hat{\boldsymbol{u}}^{\mathrm{a}}}} \right] \right\} \overset{\mathcal{H}_1}{<} \gamma'_{\mathrm{D}_2}, \tag{B.21}$$

where $\gamma'_{\mathrm{D}_2} = (2/N) \ln \gamma_{\mathrm{D}_2}$.

Appendix C

C.1 Derivation of Navigation Mechanization Equations

Let $\boldsymbol{r}^{\mathrm{a}} \in \mathbb{R}^{3\times 1}$ denote a position vector in the a-frame, $\boldsymbol{r}^{\mathrm{i}} \in \mathbb{R}^{3\times 1}$ denote a position vector in the i-frame, and $\boldsymbol{u}^{\mathrm{i}} \in \mathbb{R}^{3\times 1}$ be a vector pointing from origin in the i-frame to the origin of the a-frame. Then,

$$\boldsymbol{r}^{\mathrm{i}} = \boldsymbol{R}^{\mathrm{i}}_{\mathrm{a}} \cdot \boldsymbol{r}^{\mathrm{a}} + \boldsymbol{u}^{\mathrm{i}}. \tag{C.1}$$

Taking the first derivative we get

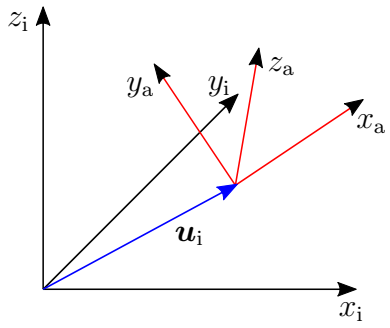

Figure C.1: Transformation of $\boldsymbol{r}^{\mathrm{i}}$ to $\boldsymbol{r}^{\mathrm{a}}$.

$$\dot{\boldsymbol{r}}^{\mathrm{i}} = \frac{d\boldsymbol{r}^{\mathrm{i}}}{dt} = \boldsymbol{R}^{\mathrm{i}}_{\mathrm{a}}\dot{\boldsymbol{r}}^{\mathrm{a}} + \dot{\boldsymbol{R}}^{\mathrm{i}}_{\mathrm{a}}\boldsymbol{r}^{\mathrm{a}} + \dot{\boldsymbol{u}}^{\mathrm{i}}.$$

Taking the second derivative with respect to time, we get

$$\ddot{\boldsymbol{r}}^{\mathrm{i}} = \frac{d^2\boldsymbol{r}^{\mathrm{i}}}{dt^2} = \boldsymbol{R}^{\mathrm{i}}_{\mathrm{a}}\ddot{\boldsymbol{r}}^{\mathrm{a}} + 2\dot{\boldsymbol{R}}^{\mathrm{i}}_{\mathrm{a}}\dot{\boldsymbol{r}}^{\mathrm{a}} + \ddot{\boldsymbol{R}}^{\mathrm{i}}_{\mathrm{a}}\boldsymbol{r}^{\mathrm{a}} + \ddot{\boldsymbol{u}}^{\mathrm{i}},$$

where

$$\begin{aligned}
\dot{\boldsymbol{R}}^{\mathrm{i}}_{\mathrm{a}} &= \boldsymbol{R}^{\mathrm{i}}_{\mathrm{a}}\boldsymbol{\Omega}^{\mathrm{a}}_{\mathrm{ia}}, \quad \text{and} \\
\ddot{\boldsymbol{R}}^{\mathrm{i}}_{\mathrm{a}} &= \boldsymbol{R}^{\mathrm{i}}_{\mathrm{a}}\dot{\boldsymbol{\Omega}}^{\mathrm{a}}_{\mathrm{ia}} + \dot{\boldsymbol{R}}^{\mathrm{i}}_{\mathrm{a}}\boldsymbol{\Omega}^{\mathrm{a}}_{\mathrm{ia}} = \boldsymbol{R}^{\mathrm{i}}_{\mathrm{a}}\left(\boldsymbol{\Omega}^{\mathrm{a}}_{\mathrm{ia}}\boldsymbol{\Omega}^{\mathrm{a}}_{\mathrm{ia}} + \dot{\boldsymbol{\Omega}}^{\mathrm{a}}_{\mathrm{ia}}\right).
\end{aligned}$$

Thus,

$$\ddot{\boldsymbol{r}}^{\mathrm{i}} = \boldsymbol{R}^{\mathrm{i}}_{\mathrm{a}}\ddot{\boldsymbol{r}}^{\mathrm{a}} + 2\boldsymbol{R}^{\mathrm{i}}_{\mathrm{a}}\boldsymbol{\Omega}^{\mathrm{a}}_{\mathrm{ia}}\dot{\boldsymbol{r}}^{\mathrm{a}} + \boldsymbol{R}^{\mathrm{i}}_{\mathrm{a}}\left(\boldsymbol{\Omega}^{\mathrm{a}}_{\mathrm{ia}}\boldsymbol{\Omega}^{\mathrm{a}}_{\mathrm{ia}} + \dot{\boldsymbol{\Omega}}^{\mathrm{a}}_{\mathrm{ia}}\right)\boldsymbol{r}^{\mathrm{a}} + \ddot{\boldsymbol{u}}^{\mathrm{i}}.$$

Using $\ddot{\boldsymbol{r}}^{\mathrm{i}} = \boldsymbol{s}^{\mathrm{i}} + \boldsymbol{g}^{\mathrm{i}}$ from (2.1) and multiply with $\boldsymbol{R}^{\mathrm{a}}_{\mathrm{i}}$ on both sides, we get

$$\boldsymbol{s}^{\mathrm{a}} + \boldsymbol{g}^{\mathrm{a}} = \ddot{\boldsymbol{r}}^{\mathrm{a}} + 2\boldsymbol{\Omega}^{\mathrm{a}}_{\mathrm{ia}}\dot{\boldsymbol{r}}^{\mathrm{a}} + \left(\boldsymbol{\Omega}^{\mathrm{a}}_{\mathrm{ia}}\boldsymbol{\Omega}^{\mathrm{a}}_{\mathrm{ia}} + \dot{\boldsymbol{\Omega}}^{\mathrm{a}}_{\mathrm{ia}}\right)\boldsymbol{r}^{\mathrm{a}} + \ddot{\boldsymbol{u}}^{\mathrm{a}}.$$

If we assume that we navigate over small area with low speed, and denote the navigation frame the with superscript n, then

$$\boldsymbol{s}^{\mathrm{n}} + \boldsymbol{g}^{\mathrm{n}} = \ddot{\boldsymbol{r}}^{\mathrm{n}} + 2\boldsymbol{\Omega}^{\mathrm{n}}_{\mathrm{in}}\dot{\boldsymbol{r}}^{\mathrm{n}} + \left(\boldsymbol{\Omega}^{\mathrm{n}}_{\mathrm{in}}\boldsymbol{\Omega}^{\mathrm{n}}_{\mathrm{in}} + \dot{\boldsymbol{\Omega}}^{\mathrm{n}}_{\mathrm{in}}\right)\boldsymbol{r}^{\mathrm{n}} + \ddot{\boldsymbol{u}}^{\mathrm{n}}.$$

We assume earth's rotation to be constant angular velocity, and thus, the navigation plane moves with at a constant speed. Therefore, $\ddot{\boldsymbol{u}}^{\mathrm{n}} \approx \boldsymbol{0}$, and the above equation can be simplified

as:

$$\begin{aligned}\boldsymbol{s}^{\mathrm{n}} + \boldsymbol{g}^{\mathrm{n}} &= \ddot{\boldsymbol{r}}^{\mathrm{n}} + 2\boldsymbol{\Omega}_{\mathrm{in}}^{\mathrm{n}}\dot{\boldsymbol{r}}^{\mathrm{n}} + \left(\boldsymbol{\Omega}_{\mathrm{in}}^{\mathrm{n}}\boldsymbol{\Omega}_{\mathrm{in}}^{\mathrm{n}} + \dot{\boldsymbol{\Omega}}_{\mathrm{in}}^{\mathrm{n}}\right)\boldsymbol{r}^{\mathrm{n}}, \\ &= \ddot{\boldsymbol{r}}^{\mathrm{n}} + 2\boldsymbol{\omega}_{\mathrm{in}}^{\mathrm{n}} \times \boldsymbol{v}^{\mathrm{n}} + \boldsymbol{\omega}_{\mathrm{in}}^{\mathrm{n}} \times \boldsymbol{\omega}_{\mathrm{in}}^{\mathrm{n}} \times \boldsymbol{r}^{\mathrm{n}}.\end{aligned}$$

Because the navigation plane is attached to the surface of the earth and is also stationary, $\boldsymbol{\omega}_{\mathrm{in}}^{\mathrm{n}} = \boldsymbol{\omega}_{\mathrm{ie}}^{\mathrm{n}}$. Substituting $\boldsymbol{\omega}_{\mathrm{in}}^{\mathrm{n}} = \boldsymbol{\omega}_{\mathrm{ie}}^{\mathrm{n}}$ in the above equation, we get

$$\boldsymbol{s}^{\mathrm{n}} + \boldsymbol{g}^{\mathrm{n}} = \ddot{\boldsymbol{r}}^{\mathrm{n}} + \underbrace{2\boldsymbol{\omega}_{\mathrm{ie}}^{\mathrm{n}} \times \boldsymbol{v}^{\mathrm{n}}}_{\text{Coriolis acceleration}} + \underbrace{\boldsymbol{\omega}_{\mathrm{ie}}^{\mathrm{n}} \times \boldsymbol{\omega}_{\mathrm{ie}}^{\mathrm{n}} \times \boldsymbol{r}^{\mathrm{n}}}_{\text{Centrifugal acceleration}}.$$

The centrifugal acceleration depends on the location of the point on earth. The magnitude of the centrifugal acceleration, which is the cross-product term in the above equation can be approximated as

$$\left\|\boldsymbol{\omega}_{\mathrm{ie}}^{\mathrm{n}} \times \boldsymbol{\omega}_{\mathrm{ie}}^{\mathrm{n}} \times \boldsymbol{r}^{\mathrm{n}}\right\| \leq \left\|\boldsymbol{\omega}_{\mathrm{ie}}^{\mathrm{n}}\right\| \left\|\boldsymbol{\omega}_{\mathrm{ie}}^{\mathrm{n}}\right\| \left\|\boldsymbol{r}^{\mathrm{n}}\right\|.$$

The magnitude of $\boldsymbol{\omega}_{\mathrm{ie}}$ is 7.29×10^{-5}rad/s and the average radius of the earth is 6371km. The overall magnitude of the centrifugal acceleration is less than or equal to $3.39 \times 10^{-2}\mathrm{m/s^2}$. If the experiment takes place at the equator, then the error introduced by neglecting the centrifugal acceleration for pedestrian navigation systems is minimal, i.e., 0.5% of the total distance traveled. Further, the Coriolis acceleration also depends on the speed of the sensor. For example, if we consider a person walking at a speed of 5km/h, then the magnitude of the Coriolis acceleration is approximately $2.04 \times 10^{-4}\mathrm{m/s^2}$. In addition, in some cases, the Coriolis acceleration gets canceled out when the pedestrian changes direction. The overall impact of the Coriolis acceleration is relatively small when compared with the inertial acceleration. Thus, neglecting the centrifugal acceleration and Coriolis acceleration, the

specific force measured for pedestrian navigation systems in the navigation frame can be approximated as

$$\boldsymbol{s}^{\mathrm{n}} + \boldsymbol{g}^{\mathrm{n}} \approx \ddot{\boldsymbol{r}}^{\mathrm{n}}.$$

If $\boldsymbol{s}^{\mathrm{b}}$ represents the specific force measurements in the body frame, then

$$\dot{\boldsymbol{p}}^{\mathrm{n}} = \boldsymbol{v}^{\mathrm{n}}, \tag{C.2}$$

$$\dot{\boldsymbol{v}}^{\mathrm{n}} = \boldsymbol{R}_{\mathrm{b}}^{\mathrm{n}} \boldsymbol{s}^{\mathrm{b}} + \boldsymbol{g}^{\mathrm{n}}, \tag{C.3}$$

where $\boldsymbol{v}^{\mathrm{n}}$ and $\boldsymbol{p}^{\mathrm{n}}$ are the position and velocity estimates, respectively, $\boldsymbol{R}_{\mathrm{b}}^{\mathrm{n}}$ is the rotation matrix from body frame to navigation frame, and $\boldsymbol{g}^{\mathrm{n}}$ is the gravitational acceleration.

C.2 Perturbation Analysis

Let $\delta\boldsymbol{s}^{\mathrm{b}}$ and $\delta\boldsymbol{\omega}_{\mathrm{ib}}^{\mathrm{b}}$ denote the errors in specific force and angular velocity measurements, respectively, then

$$\tilde{\boldsymbol{s}}^{\mathrm{b}} = \boldsymbol{s}^{\mathrm{b}} - \delta\boldsymbol{s}^{\mathrm{b}},$$

$$\tilde{\boldsymbol{\omega}}_{\mathrm{ib}}^{\mathrm{b}} = \boldsymbol{\omega}_{\mathrm{ib}}^{\mathrm{b}} - \delta\boldsymbol{\omega}_{\mathrm{ib}}^{\mathrm{b}}.$$

Let $\boldsymbol{\epsilon} \in \mathbb{R}^{3\times 1}$ be the small angles that aligns the true and computed rotation matrix, then

$$\hat{\boldsymbol{R}}_{\mathrm{b}}^{\mathrm{n}} = (\boldsymbol{I} - \boldsymbol{\Omega}_{\boldsymbol{\epsilon}})\boldsymbol{R}_{\mathrm{b}}^{\mathrm{n}}, \tag{C.4}$$

where $\hat{\boldsymbol{R}}_{\mathrm{b}}^{\mathrm{n}}$ is the rotation matrix with error measurements and $\boldsymbol{R}_{\mathrm{b}}^{\mathrm{n}}$ is the rotation matrix with ideal measurements. Equation (C.4) follows from the discretization of the time-derivative property. If $\tilde{\boldsymbol{\Omega}}_{\mathrm{nb}}^{\mathrm{b}}$ and $\delta\boldsymbol{\Omega}_{\mathrm{nb}}^{\mathrm{b}}$ denote skew-symmetric matrices with perturbed angular velocity measurements and perturbations in the angular velocities, respectively, then $\dot{\hat{\boldsymbol{R}}}_{\mathrm{b}}^{\mathrm{n}}$ is given as

$$\begin{aligned}
\dot{\hat{\boldsymbol{R}}}_{\mathrm{b}}^{\mathrm{n}} &= \hat{\boldsymbol{R}}_{\mathrm{b}}^{\mathrm{n}}\tilde{\boldsymbol{\Omega}}_{\mathrm{nb}}^{\mathrm{b}} \\
\implies \frac{d}{dt}(\boldsymbol{I}-\boldsymbol{\Omega}_{\boldsymbol{\epsilon}})\boldsymbol{R}_{\mathrm{b}}^{\mathrm{n}} &= (\boldsymbol{I}-\boldsymbol{\Omega}_{\boldsymbol{\epsilon}})\boldsymbol{R}_{\mathrm{b}}^{\mathrm{n}}\tilde{\boldsymbol{\Omega}}_{\mathrm{nb}}^{\mathrm{b}} \\
\implies -\dot{\boldsymbol{\Omega}}_{\boldsymbol{\epsilon}}\boldsymbol{R}_{\mathrm{b}}^{\mathrm{n}} + (\boldsymbol{I}-\boldsymbol{\Omega}_{\boldsymbol{\epsilon}})\dot{\boldsymbol{R}}_{\mathrm{b}}^{\mathrm{n}} &= (\boldsymbol{I}-\boldsymbol{\Omega}_{\boldsymbol{\epsilon}})\boldsymbol{R}_{\mathrm{b}}^{\mathrm{n}}(\boldsymbol{\Omega}_{\mathrm{nb}}^{\mathrm{b}} + \delta\boldsymbol{\Omega}_{\mathrm{nb}}^{\mathrm{b}}) \\
\implies -\dot{\boldsymbol{\Omega}}_{\boldsymbol{\epsilon}}\boldsymbol{R}_{\mathrm{b}}^{\mathrm{n}} + (\boldsymbol{I}-\boldsymbol{\Omega}_{\boldsymbol{\epsilon}})\dot{\boldsymbol{R}}_{\mathrm{b}}^{\mathrm{n}} &= (\boldsymbol{I}-\boldsymbol{\Omega}_{\boldsymbol{\epsilon}})\boldsymbol{R}_{\mathrm{b}}^{\mathrm{n}}\boldsymbol{\Omega}_{\mathrm{nb}}^{\mathrm{b}} + (\boldsymbol{I}-\boldsymbol{\Omega}_{\boldsymbol{\epsilon}})\boldsymbol{R}_{\mathrm{b}}^{\mathrm{n}}\delta\boldsymbol{\Omega}_{\mathrm{nb}}^{\mathrm{b}} \\
\implies \dot{\boldsymbol{\Omega}}_{\boldsymbol{\epsilon}}\boldsymbol{R}_{\mathrm{b}}^{\mathrm{n}} &= -\boldsymbol{R}_{\mathrm{b}}^{\mathrm{n}}\delta\boldsymbol{\Omega}_{\mathrm{nb}}^{\mathrm{b}} + \boldsymbol{\Omega}_{\boldsymbol{\epsilon}}\boldsymbol{R}_{\mathrm{b}}^{\mathrm{n}}\delta\boldsymbol{\Omega}_{\mathrm{nb}}^{\mathrm{b}}
\end{aligned}$$

The second term in the above equation, i.e., $\boldsymbol{\Omega}_{\epsilon}\boldsymbol{R}_{\mathrm{b}}^{\mathrm{n}}\delta\boldsymbol{\Omega}_{\mathrm{nb}}^{\mathrm{b}}$, is a second-order term. Neglecting the higher-order terms, we get

$$\dot{\boldsymbol{\Omega}}_{\boldsymbol{\epsilon}}\boldsymbol{R}_{\mathrm{b}}^{\mathrm{n}} \approx -\boldsymbol{R}_{\mathrm{b}}^{\mathrm{n}}\delta\boldsymbol{\Omega}_{\mathrm{nb}}^{\mathrm{b}}. \tag{C.5}$$

To estimate the perturbed orientation angles, equation (C.5) is a matrix with three-degrees of freedom, nonlinear, and cannot be directly substituted into the Kalman filter. To further simplify, let $\boldsymbol{a} \in \mathbb{R}^{3\times 1}$. Post-multiplying (C.5) with $\boldsymbol{R}_{\mathrm{b}}^{\mathrm{n}}\boldsymbol{a}$ on both sides. Then,

$$\dot{\boldsymbol{\Omega}}_{\boldsymbol{\epsilon}}\boldsymbol{a} = \boldsymbol{R}_{\mathrm{b}}^{\mathrm{n}}\delta\boldsymbol{\Omega}_{nb}^{b}\boldsymbol{R}_{\mathrm{b}}^{\mathrm{n}}\boldsymbol{a} \tag{C.6}$$

$$\implies \dot{\boldsymbol{\epsilon}} \times \boldsymbol{a} = \boldsymbol{R}_{\mathrm{b}}^{\mathrm{n}}(\delta\boldsymbol{\omega}_{\mathrm{nb}}^{\mathrm{n}} \times (\boldsymbol{R}_{\mathrm{b}}^{\mathrm{n}}\boldsymbol{a})). \tag{C.7}$$

Rewriting the above equation, we get

$$\dot{\boldsymbol{\epsilon}} \times \boldsymbol{a} = |\boldsymbol{R}_{\mathrm{b}}^{\mathrm{n}}|(\boldsymbol{R}_{\mathrm{b}}^{\mathrm{n}})^{-T}(\delta\boldsymbol{\omega}_{\mathrm{nb}}^{\mathrm{b}} \times (\boldsymbol{R}_{\mathrm{b}}^{\mathrm{n}}\boldsymbol{a})). \tag{C.8}$$

Using the following identity: $\boldsymbol{M}\boldsymbol{a} \times \boldsymbol{M}\boldsymbol{b} = |\boldsymbol{M}|\boldsymbol{M}^{-T}(\boldsymbol{a} \times \boldsymbol{b})$, equation (C.8) can be further simplified as

$$\dot{\boldsymbol{\epsilon}} \times \boldsymbol{a} = (\boldsymbol{R}^{\mathrm{n}}_{\mathrm{b}} \delta \boldsymbol{\omega}^{\mathrm{b}}_{\mathrm{nb}}) \times \boldsymbol{a} \implies \dot{\boldsymbol{\epsilon}} = \boldsymbol{R}^{\mathrm{n}}_{\mathrm{b}} \delta \boldsymbol{\omega}^{\mathrm{b}}_{\mathrm{nb}}. \tag{C.9}$$

Let $\hat{\boldsymbol{v}}^{\mathrm{n}}$ and $\hat{\boldsymbol{p}}^{\mathrm{n}}$ denote the perturbed velocity and position estimates, where the perturbations are denoted with $\delta \boldsymbol{v}^{\mathrm{n}}$ and $\delta \boldsymbol{p}^{\mathrm{n}}$, respectively. Based on the navigation equations, the perturbed inertial acceleration estimate is given as:

$$\begin{aligned}
\dot{\hat{\boldsymbol{v}}}^{\mathrm{n}} &= \hat{\boldsymbol{R}}^{\mathrm{n}}_{\mathrm{b}} \tilde{\boldsymbol{s}}^{\mathrm{b}} + \boldsymbol{g}^{\mathrm{n}} \\
\implies \dot{\boldsymbol{v}}^{\mathrm{n}} - \delta \dot{\boldsymbol{v}}^{\mathrm{n}} &= (\boldsymbol{I} - \boldsymbol{\Omega}_{\boldsymbol{\epsilon}}) \boldsymbol{R}^{\mathrm{n}}_{\mathrm{b}} (\boldsymbol{s}^{\mathrm{b}} - \delta \boldsymbol{s}^{\mathrm{b}}) + \boldsymbol{g}^{\mathrm{n}} \\
\implies \dot{\boldsymbol{v}}^{\mathrm{n}} - \delta \dot{\boldsymbol{v}}^{\mathrm{n}} &= \boldsymbol{R}^{\mathrm{n}}_{\mathrm{b}} \boldsymbol{s}^{\mathrm{b}} + \boldsymbol{g}^{\mathrm{n}} - \boldsymbol{R}^{\mathrm{n}}_{\mathrm{b}} \delta \boldsymbol{s}^{\mathrm{b}} - \boldsymbol{\Omega}_{\boldsymbol{\epsilon}} \boldsymbol{R}^{\mathrm{n}}_{\mathrm{b}} \boldsymbol{s}^{\mathrm{b}} + \boldsymbol{\Omega}_{\boldsymbol{\epsilon}} \boldsymbol{R}^{\mathrm{n}}_{\mathrm{b}} \delta \boldsymbol{s}^{\mathrm{b}}.
\end{aligned}$$

Neglecting the second-order terms, we get

$$\delta \dot{\boldsymbol{v}}^{\mathrm{n}} \approx \boldsymbol{R}^{\mathrm{n}}_{\mathrm{b}} \delta \boldsymbol{s}^{\mathrm{b}} + \boldsymbol{\Omega}_{\epsilon} \boldsymbol{R}^{\mathrm{n}}_{\mathrm{b}} \boldsymbol{s}^{\mathrm{b}}.$$

The second term in the above equation can be further simplified as

$$\boldsymbol{\Omega}_{\boldsymbol{\epsilon}} \boldsymbol{R}^{\mathrm{n}}_{\mathrm{b}} \boldsymbol{s}^{\mathrm{b}} = \boldsymbol{\Omega}_{\boldsymbol{\epsilon}} \boldsymbol{s}^{\mathrm{n}} = \boldsymbol{\epsilon} \times \boldsymbol{s}^{\mathrm{n}} = -\boldsymbol{s}^{\mathrm{n}} \times \boldsymbol{\epsilon} = -\boldsymbol{\Omega}_{\boldsymbol{s}^{\mathrm{n}}} \boldsymbol{\epsilon},$$

where $\boldsymbol{\Omega}_{\boldsymbol{s}^{\mathrm{n}}}$ is the skew-symmetric matrix containing specific forces, $\boldsymbol{s}^{\mathrm{n}}$. The perturbation equation for inertial acceleration can be written as

$$\delta \dot{\boldsymbol{v}}^{\mathrm{n}} = \boldsymbol{R}^{\mathrm{n}}_{\mathrm{b}} \delta \boldsymbol{s}^{\mathrm{b}} - \boldsymbol{\Omega}_{\boldsymbol{s}^{\mathrm{n}}} \boldsymbol{\epsilon}.$$

Therefore, the perturbation equations or error model for the navigation equations in (4.8)-(4.10) can be written as

$$\begin{aligned}
\delta\dot{\boldsymbol{p}}^{\mathrm{n}} &= \delta\boldsymbol{v}^{\mathrm{n}}, \\
\delta\dot{\boldsymbol{v}}^{\mathrm{n}} &= \boldsymbol{R}_{\mathrm{b}}^{\mathrm{n}}\delta\boldsymbol{s}^{\mathrm{b}} - \boldsymbol{\Omega}_{\boldsymbol{s}^{\mathrm{n}}}\boldsymbol{\epsilon}, \\
\dot{\boldsymbol{\epsilon}} &= \boldsymbol{R}_{\mathrm{b}}^{\mathrm{n}}\delta\boldsymbol{\omega}_{\mathrm{nb}}^{\mathrm{b}}.
\end{aligned}$$

Appendix D

D.1 Derivation of Point-Process Filter

In this section, we derive the stochastic state point process filter when the observation model follows a binomial distribution. The derivation follows similar steps to those stated in [96]. We approximate the posterior distribution in (5.9) to a Gaussian distribution. Under this approximation, the mean and variance of the one-step predication density in (5.10) are computed from the posterior density in the previous time interval as

$$\boldsymbol{\theta}_{k|k-1} = \boldsymbol{F}_k \boldsymbol{\theta}_{k-1|k-1},$$
$$\boldsymbol{J}_{k|k-1} = \boldsymbol{F}_k \boldsymbol{J}_{k-1|k-1} \boldsymbol{F}_k^T + \boldsymbol{Q}_k.$$

The posterior distribution in the time interval $((k-1)\Delta, k\Delta]$ is approximated as a Gaussian distribution with parameters $\boldsymbol{\theta}_{k|k}$ and $\boldsymbol{J}_{k|k}$ as the mean and variance, respectively. Let $L(\boldsymbol{\theta}_k)$ denote the loglikelihood of the posterior distribution without the normalizing constant, i.e., $L(\boldsymbol{\theta}_k) = \ln\left(P(b_k|\boldsymbol{\theta}_k, \boldsymbol{H}_k) P(\boldsymbol{\theta}_k|\boldsymbol{H}_k)\right)$. The second order expansion of the logarithm about a

point $\hat{\boldsymbol{\theta}}_k$ gives

$$L(\boldsymbol{\theta}_k) \approx L(\hat{\boldsymbol{\theta}}_k) + L'(\hat{\boldsymbol{\theta}}_k)(\boldsymbol{\theta}_k - \hat{\boldsymbol{\theta}}_k) + \frac{1}{2}(\boldsymbol{\theta}_k - \hat{\boldsymbol{\theta}}_k)^T L''(\hat{\boldsymbol{\theta}}_k)(\boldsymbol{\theta}_k - \hat{\boldsymbol{\theta}}_k) \tag{D.1}$$

$$= c'' + \frac{1}{2}\left[\boldsymbol{\theta}_k - \left\{\hat{\boldsymbol{\theta}}_k - [L''(\hat{\boldsymbol{\theta}}_k)]^{-1} L'(\hat{\boldsymbol{\theta}}_k)\right\}\right]^T \times L''(\hat{\boldsymbol{\theta}}_k)\left[\boldsymbol{\theta}_k - \left\{\hat{\boldsymbol{\theta}}_k - [L''(\hat{\boldsymbol{\theta}}_k)]^{-1} L'(\hat{\boldsymbol{\theta}}_k)\right\}\right]. \tag{D.2}$$

The posterior is approximated as a Gaussian, distributed with $\boldsymbol{\theta}_{k|k}$ and $\boldsymbol{J}_{k|k}$ as the mean and variance, respectively, and is given as

$$\begin{aligned} \boldsymbol{\theta}_{k|k} &= \hat{\boldsymbol{\theta}}_k - [L''(\hat{\boldsymbol{\theta}}_k)]^{-1} L'(\hat{\boldsymbol{\theta}}_k) \\ \boldsymbol{J}_{k|k} &= -[L''(\hat{\boldsymbol{\theta}}_k)]^{-1}. \end{aligned} \tag{D.3}$$

By evaluating (D.3) at $\hat{\boldsymbol{\theta}}_k = \boldsymbol{\theta}_{k|k-1}$, we get the posterior state equations. The first partial derivative of the loglikelihood function of the posterior distribution is given as:

$$L'(\boldsymbol{\theta}_k) = \frac{\partial}{\partial \boldsymbol{\theta}_k}\left[\ln \binom{B}{b_k} + b_k \ln p_k + (B - b_k)\ln(1 - p_k) - \frac{1}{2}(\boldsymbol{\theta}_k - \boldsymbol{\theta}_{k|k-1})^T (\boldsymbol{J}_{k|k-1})^{-1}(\boldsymbol{\theta}_k - \boldsymbol{\theta}_{k|k-1})\right] \tag{D.4}$$

$$= \left[\frac{b_k}{p_k}\frac{\partial p_k}{\partial \boldsymbol{\theta}_k} + \frac{B - b_k}{1 - p_k}\frac{\partial(1 - p_k)}{\partial \boldsymbol{\theta}_k}\right] - (\boldsymbol{J}_{k|k-1})^{-1}(\boldsymbol{\theta}_k - \boldsymbol{\theta}_{k|k-1}). \tag{D.5}$$

From the definition of the p_k, which represents a sigmoid function, we obtain the following identities:

$$\frac{1}{p_k}\frac{\partial p_k}{\partial \boldsymbol{\theta}_k} = (1 - p_k)\frac{\partial \lambda_k(\boldsymbol{\theta}_k)}{\partial \boldsymbol{\theta}_k} \tag{D.6}$$

$$\frac{1}{1 - p_k}\frac{\partial(1 - p_k)}{\partial \boldsymbol{\theta}_k} = -p_k \frac{\partial \lambda_k(\boldsymbol{\theta}_k)}{\partial \boldsymbol{\theta}_k}. \tag{D.7}$$

Substituting (D.6) and (D.7) into (D.5) we get

$$L'(\boldsymbol{\theta}_k) = (b_k - Bp_k)\frac{\partial \lambda_k(\boldsymbol{\theta}_k)}{\partial \boldsymbol{\theta}_k} - (\boldsymbol{J}_{k|k-1})^{-1}(\boldsymbol{\theta}_k - \boldsymbol{\theta}_{k|k-1}). \tag{D.8}$$

Taking the second derivative of (D.8), we get

$$L''(\boldsymbol{\theta}_k) = -(\boldsymbol{J}_{k|k-1})^{-1} + (b_k - Bp_k)\frac{\partial^2 \lambda_k(\boldsymbol{\theta}_k)}{\partial \boldsymbol{\theta}_k \partial \boldsymbol{\theta}_k^T} - \frac{\partial \lambda_k(\boldsymbol{\theta}_k)}{\partial \boldsymbol{\theta}_k} Bp_k(1-p_k)\frac{\partial \lambda_k(\boldsymbol{\theta}_k)}{\partial \boldsymbol{\theta}_k}^T \tag{D.9}$$

Therefore, substituting the expressions of the first and second partial derivatives of the loglikelihood function in (D.8) and (D.9) into (D.3), and evaluating at $\boldsymbol{\theta}_k = \boldsymbol{\theta}_{k|k-1}$, we get

$$\begin{aligned}
\boldsymbol{\theta}_{k|k} &= \boldsymbol{\theta}_{k|k-1} + \boldsymbol{J}_{k|k}\left[(b_k - Bp_k)\frac{\partial \lambda_k(\boldsymbol{\theta}_k)}{\partial \boldsymbol{\theta}_k}\right]_{\boldsymbol{\theta}_{k|k-1}}, \\
(\boldsymbol{J}_{k|k})^{-1} &= (\boldsymbol{J}_{k|k-1})^{-1} + \left[(Bp_k - b_k)\frac{\partial^2 \lambda_k(\boldsymbol{\theta}_k)}{\partial \boldsymbol{\theta}_k \partial \boldsymbol{\theta}_k^T} + Bp_k(1-p_k)\frac{\partial \lambda_k(\boldsymbol{\theta}_k)}{\partial \boldsymbol{\theta}_k}\frac{\partial \lambda_k(\boldsymbol{\theta}_k)}{\partial \boldsymbol{\theta}_k}^T\right]_{\boldsymbol{\theta}_{k|k-1}}.
\end{aligned}$$

The analysis of the convergence of the point-process filter is presented in [97].

D.2 Summary: PID TT027

In this section, we demonstrate the performance of the FI [66] and pFOG method for PID TT027, who demonstrated the greatest number of FOG events (24 in total). Because the list of balance assessment tasks involved in place and sharp 180° turns, we overlay the DL, MDL, and FAL regions detected on the yaw angle plot provided by the inertial navigation system. The sum of the regions identified as DL and MDL represent the FOG region detected in the video data.

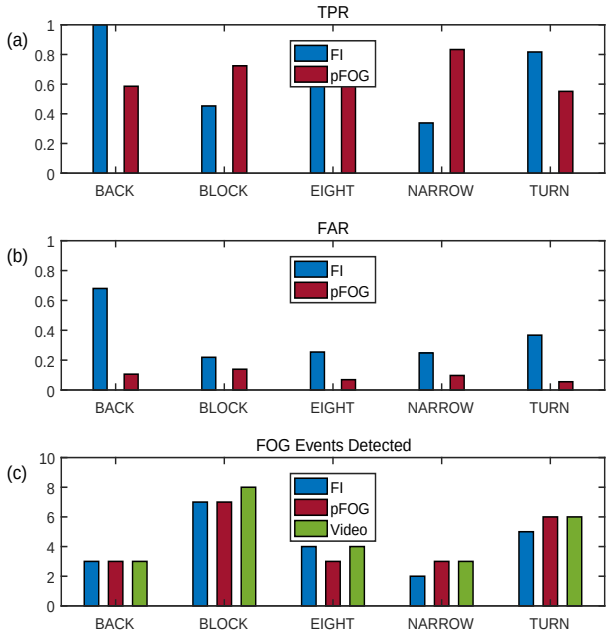

Figure D.1: Summary of TT027. (a) TPR, (b) FAR, and (c) FOG events detected.

For PID TT027, we choose the BLOCK task to obtain the FI-threshold and the kernel parameter because the participant demonstrated the highest number of FOG events (equal to 8) in this task. We set the FI-threshold to 6.0 and the kernel parameter $\sigma_s = 0.29$ to maximize the number of FOG events detected. In Fig. D.2-D.6, we plot the yaw angle of the left foot with an overlay of the DL, MDL, and FAL regions obtained using the video reference system. We observe that the FI-threshold obtained using the BLOCK task, demonstrates high FAR in the remaining tasks. However, the proposed pFOG method demonstrates an improved accuracy with low FAR.

In Fig. D.1, we summarize the results obtained for PID TT027. The FI-method detected 21/24 (or equivalently 87.5% accuracy) FOG events, whereas the pFOG method detected 22/24 (or equivalently 91.66% accuracy) FOG events. The average values of TPR for FI and pFOG method are respectively 0.67 and 0.65. However, our method demonstrates a lower

Table D.1: Number of FOG events detected for different participants across the gait tasks.

PID	**PARAMETER**		**BACK**		**BLOCK**		**EIGHT**		**NARROW**		**TURN**		**TOTAL**	
	FI	pFOG	FI	pFOG	FI	pFOG	FI	pFOG	FI	pFOG	FI	pFOG	FI	pFOG
TT003	6.56	0.30	(0/0)	(0/0)	(0/1)	(0/1)	(0/0)	(0/0)	(0/0)	(0/0)	(0/0)	(0/0)	(0/1)	(0/1)
TT004	6.56	0.30	(0/2)	(1/2)	(0/6)	(4/6)	(0/0)	(0/0)	(0/0)	(0/0)	(0/0)	(0/0)	(0/8)	(5/8)
TT005	6.56	0.30	(0/1)	(1/1)	(0/0)	(0/0)	(0/0)	(0/0)	(0/1)	(1/1)	(0/0)	(0/0)	(0/2)	(2/2)
TT007	6.56	0.30	(8/8)	(4/8)	(0/0)	(0/0)	(0/1)	(1/1)	(1/1)	(0/1)	(0/0)	(0/0)	(9/10)	(5/10)
TT013	6.56	0.30	(0/0)	(0/0)	(1/3)	(2/3)	(0/0)	(0/0)	(1/2)	(0/2)	(0/0)	(0/0)	(2/5)	(2/5)
TT017	6.56	0.30	(0/0)	(0/0)	(1/1)	(0/1)	(0/0)	(0/0)	(0/0)	(0/0)	(0/0)	(0/0)	(1/1)	(0/1)
TT021	6.56	0.30	(1/1)	(1/1)	(1/3)	(3/3)	(0/2)	(1/2)	(0/0)	(0/0)	(0/1)	(1/1)	(2/7)	(6/7)
TT027	6.56	0.30	(3/3)	(3/3)	(5/8)	(7/8)	(4/4)	(3/4)	(2/3)	(3/3)	(5/6)	(6/6)	(19/24)	(22/24)
TOTAL	6.56	0.30	(12/15)	(10/15)	(8/22)	(16/22)	(4/7)	(5/7)	(4/7)	(4/7)	(5/7)	(7/7)	(33/58)	**(42/58)**

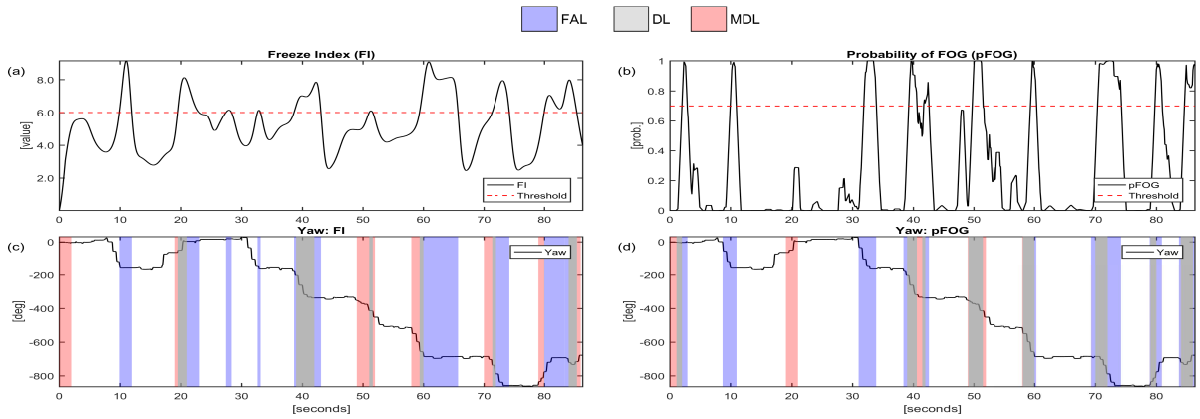

Figure D.2: PID TT027–BLOCK. (a) Freeze-Index plot with FI-threshold set to 6.0. (b) pFOG plot with $\sigma_s = 0.29$. (c) and (d) Yaw angle plot with an overlay of DL, MDL, and FAL. FOG region was marked using video data the following video commentary: Froze when stood up from chair to walk to block. Froze when turning to go back to cones after second trial. Froze during turn in the fourth, fifth, and sixth trials. Questionable left foot freeze in turn for seventh and eighth trials. Froze after trials over while walking away.

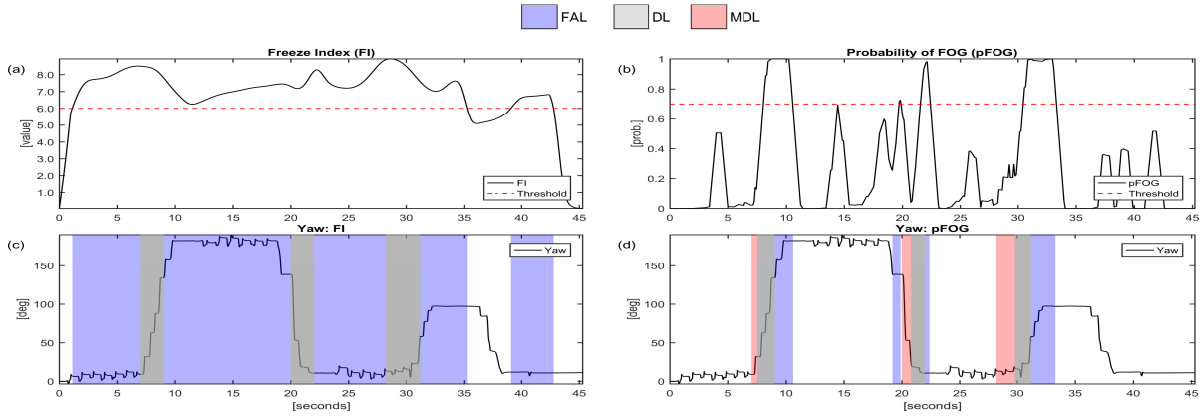

Figure D.3: PID TT027–BACK. (a) Freeze-Index plot with FI-threshold set to 6.0. (b) pFOG plot with $\sigma_s = 0.29$. (c) and (d) Yaw angle plot with an overlay of DL, MDL, and FAL. FOG region marked using the following video commentary: Froze turning after first backward trial. Froze turning after second backward trial. Froze at the end of third backward trial into a turn.

average FAR of 0.09 when compared with the existing method which gives an average FAR of 0.35, indicating a four-fold reduction in the false alarm rate using the proposed method.

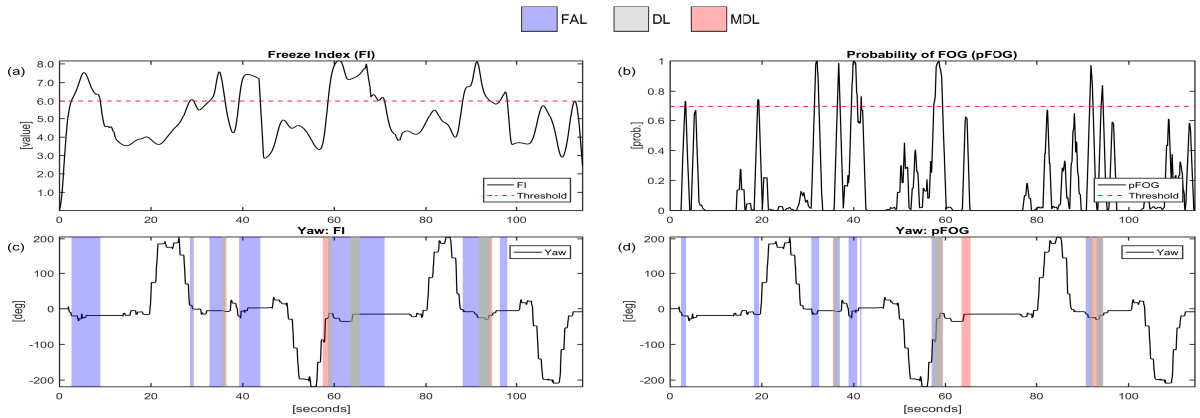

Figure D.4: PID TT027–EIGHT. (a) Freeze-Index plot with FI-threshold set to 6.0. (b) pFOG plot with $\sigma_s = 0.29$. (c) and (d) Yaw angle plot with an overlay of DL, MDL, and FAL. FOG region was marked using the following video commentary: Gait initiation freeze when standing up to start figure EIGHT trial, and first and second figure EIGHT trials. Froze during turn after second figure EIGHT trial. Froze when lining up for third and fourth figure EIGHT trials. The first two FOG events were not recorded in the IMU data.

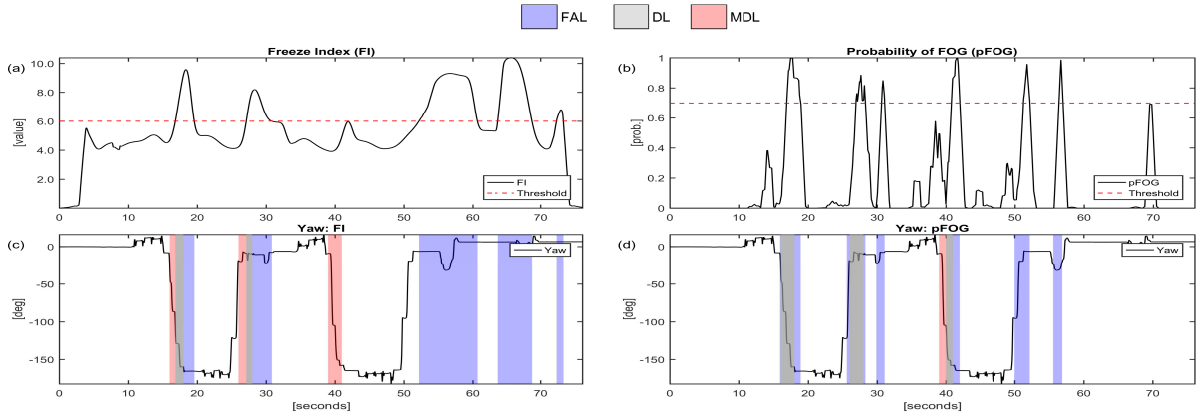

Figure D.5: PID TT027–NARROW. (a) Freeze-Index plot with FI-threshold set to 6.0. (b) pFOG plot with $\sigma_s = 0.29$. (c) and (d) Yaw angle plot with an overlay of DL, MDL, and FAL. FOG region was marked using the following video commentary: Froze when standing up and initiating gait to measure NARROW chair width. Froze during turn after first and third NARROW trials. Froze before side-step to line up for third NARROW trial. The first FOG event was not recorded in the IMU data.

D.3 Experimental Evaluation: Fixed Thresholds

In Table D.1, we analyzed the accuracy of the existing and proposed method across different datasets for a fixed value of FI-threshold and σ_s. These fixed values are obtained by taking the average of the participant-specific FI-threshold and participant-specific kernel parameter in Table 5.2 of Chapter 5. In our analysis, we fix the FI-threshold to 6.56 and $\sigma_s = 0.30$.

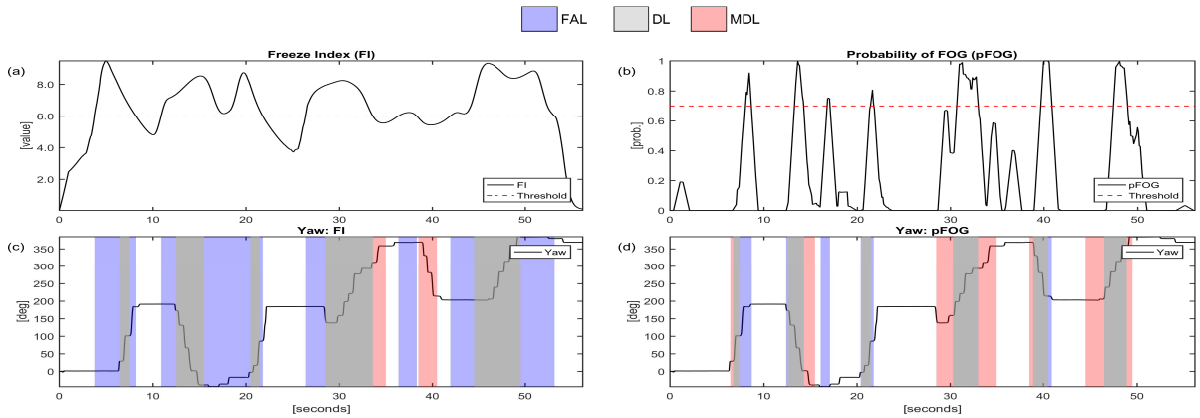

Figure D.6: PID TT027–TURN. (a) Freeze-Index plot with FI-threshold set to 6.0. (b) pFOG plot with $\sigma_s = 0.29$. (c) and (d) Yaw angle plot with an overlay of DL, MDL, and FAL. FOG region was marked using the following video commentary: Froze during first turn, twice during second turn, and third TURN trials. Froze turning wrong way in fourth TURN trial and then froze again turning correct way. Froze in the fifth and sixth TURN trials.

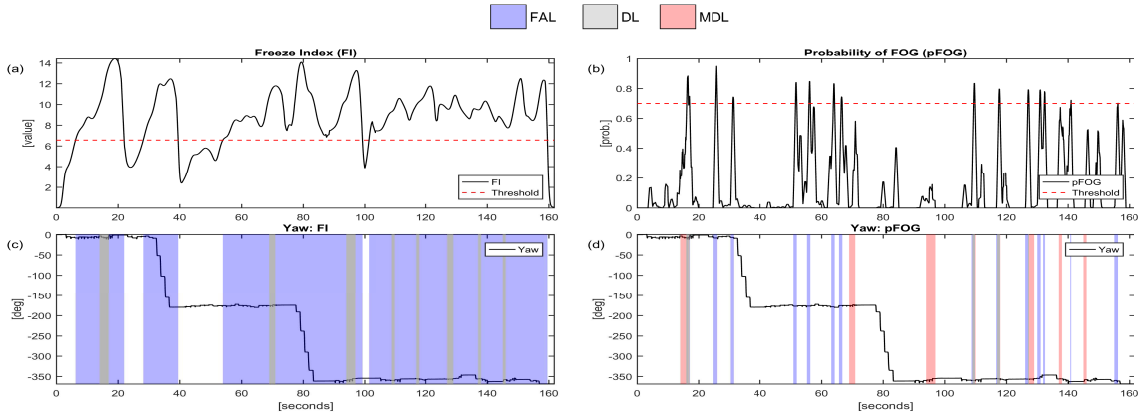

Figure D.7: PID TT007–BACK. (a) Freeze-Index plot with FI-threshold set to 6.56. (b) pFOG plot with $\sigma_s = 0.30$. (c) and (d) Yaw angle plot with an overlay of DL, MDL, and FAL. FOG region marked using the following video commentary: Festination backwards into freeze in the middle of first trial. Festination backwards into freeze at the end of the second trial. Six instances of festination backwards into freeze in the third trial.

Overall, the pFOG method obtained an accuracy of 72.41%, i.e., 42/58 FOG events were detected using a fixed participant-specific kernel parameter (see Table D.1). The FI method obtained an accuracy of 56.68%, i.e., 33/58 FOG events were detected using a fixed FI-threshold. In contrast, when the participant-specific parameters were manually adjusted,

we obtained an accuracy of 70.68% and 81.03% for the FI method and pFOG method, respectively (see Table 5.2).

Table D.2: Detection performance for different types of FOG events..

Event type (No. of events)	(not tuned) FI	(not tuned) pFOG
Turn Freeze (38)	47.36% (18)	76.31% (29)
Initiation/Gait Freeze (12)	58.33% (7)	75.00% (9)
Festination with Freeze (8)	100.00% (8)	50.00% (4)
Overall (58)	56.68% (33)	**72.41**% (42)

In Table D.2, we report the performance of the FI method and proposed approach for a fixed value of the FI-threshold and participant-specific tunable parameter, respectively, across different types of freezing of gait. We notice that the proposed method performs better than the existing approach in detecting all types of freezing, except festination. However, for this particular type of freezing of gait, the false-alarm length detected in the FI method is significantly higher than the proposed approach. In Fig. D.7, we overlay the detection length (DL), missed detection length (MDL), and false alarm length (FAL) regions detected on the yaw angle plot obtained by the foot-mounted inertial navigation system for PID TT007–BACK trial (the only participant who demonstrated festinating gait). We notice that the FI method detects large FAL (represented with blue background) for a fixed value of FI-threshold.

Appendix E

E.1 Module Parameters

Table E.1: Detection module parameters.

Parameters of the detection module	**Assigned value**
Length of the window, N	16 samples
Standard deviation of the accelerometer, σ_{a}	1.0
Standard deviation of the gyroscope, σ_{ω}	0.8
Threshold of Detector-I, γ'_{D_1}	2.0
Threshold of Detector-II, γ'_{D_2}	34.5
Gravity, g	9.8

Table E.2: Navigation module parameters.

Parameters of the navigation module	**Assigned value**
Variance of the errors in the accelerometer, $\tilde{\sigma}^2_{\mathrm{a}}$	0.7
Variance of the errors in the gyroscope, $\tilde{\sigma}^2_{\omega}$	0.017
Variance of the errors in the velocity, σ^2_{v}	0.01
Error covariance matrix, $\boldsymbol{P}_0$	$\mathrm{diag}\{\mathrm{diag}\{10^{-5}\boldsymbol{I}_6\}, \pi/(180)[0.1, 0.1, 0.1]\}$
Initial position, $[\boldsymbol{x}_0]_{1:3}$	$[0, 0, 0]^{\mathsf{T}}$
Initial heading, $[\boldsymbol{x}_0]_9$	0

Table E.3: Validation module parameters.

Parameters of the validation module	**Assigned value**
Cutoff frequency of the low-pass zero-phase filter, ω_0	3.2 Hz
Regularization parameter, λ	0.05
Number of gait cycles used for template generation, M	31
Threshold of the validation module, γ_{G}	0.5

Table E.4: Point-process filter parameters for the pFOG and pFOG-AFS.

Parameters of the point-process filter	**Assigned value**
Width of each bin, Δ	0.125 seconds
Length of each bin, ΔF_{s}	16 samples
Length of the history of spikes, ℓ	8
Background firing rate, α	-15.0
Fixed scaling parameter, β	35.0
State transition matrix, $\boldsymbol{A}_k$	$\boldsymbol{I}_\ell$
Process noise covariance matrix, $\boldsymbol{N}_k$	$10^{-14}\boldsymbol{I}_\ell$
Initial state of the parameter vector, $\boldsymbol{\theta}_{0\|0}$	$0.351\!\!1_\ell$
Initial covariance matrix, $\boldsymbol{J}_{0\|0}$	$10^{-12}\boldsymbol{I}_\ell$
Participant-specific tunable parameter, σ_{s}	0.35

Table E.5: Point-process filter parameters for the pFOG-WA.

Parameters of the point-process filter	**Assigned value**
Width of each bin, Δ	0.125 seconds
Length of each bin, ΔF_{s}	16 samples
Length of the history of spikes, ℓ	8
Initial background firing rate, α_0	-5.5
Fixed scaling parameter, β	1.0
State transition matrix, $\boldsymbol{A}_k$	$\boldsymbol{I}_{\ell+1}$
Process noise covariance matrix, $\boldsymbol{N}_k$	$\mathrm{diag}\{10^{-4}, 10^{-6}\boldsymbol{I}_\ell\}$
Initial state of the parameter vector, $\boldsymbol{\eta}_{0\|0}$	$1.551\!\!1_\ell$
Initial covariance matrix, $\boldsymbol{J}_{0\|0}$	$10^{-4}\boldsymbol{I}_{\ell+1}$
Kernel parameters for pitch	$\mu = 0.0, \tau = 0.10$
Kernel parameters for freeze-index	$\mu = 6.0, \tau = 1.0$